# EXAMINATION OF THE MEMBRANE BINDING DOMAIN OF HUMAN CYCLOOXYGENASE -2 ENZYME USING SITE-DIRECTED SPIN LABELING AND ELECTRON PARAMAGNETIC RESONANCE SPECTROSCOPY

By

Zahra MirAfzali

A DISSERTATION

Submitted to
Michigan State University
in partial fulfillment of the requirements
for the degree of

DOCTOR OF PHILOSOPHY

Department of Chemistry
&
Department of Biochemistry and Molecular Biology

2003

# ABSTRACT

## EXAMINATION OF THE MEMBRANE BINDING DOMAIN OF HUMAN CYCLOOXYGENASE –2 ENZYME USING SITE-DIRECTED SPIN LABELING AND ELECTRON PARAMAGNETIC RESONANCE SPECTROSCOPY

By

Zahra MirAfzali

The widespread use of aspirin, ibuprofen, Celebrex®, Vioxx® and other non-steroidal anti-inflammatory drugs (NSAIDs) has called for a deeper understanding of the physiological systems in which they work. NSAIDs exerts their anti-inflammatory and analgesic effects through the inhibition of cyclooxygenase –1 and –2 (COX-1 and –2). The biological necessity for two COX isozymes is not fully understood as these enzymes have nearly identical catalytic properties. Several evidences support that the COX isozymes have different biological functions. The basis for the differential biological activities is not known, but may relate to differences in their membrane binding domains, which are poorly conserved.

Site-directed spin labeling (SDSL) is a powerful tool for determination of the membrane protein structure and the topology of protein binding to the lipid bilayer. 25 mutant enzymes that contained single reactive cysteines substituted for amino acids within the human COX-2 membrane-binding domain were constructed and spin labeled. The accessibility of each protein-bound spin label with freely diffusing oxygen as a non-polar paramagnetic reagent, and NiEDDA as a polar paramagnetic reagent, was measured

using power saturation EPR spectroscopy. Our results show the accessibility parameter ($\Pi$) for both oxygen and NiEDDA, has a periodicity of 3.6 consistent with an $\alpha$-helical configuration. Furthermore, $\Pi_{oxygen}$ and $\Pi_{NiEDDA}$ both have the same period and phase. Our results indicate that both polar and non-polar paramagnetic relaxers do not access the amino acids located in the membrane-binding domain due to the very low values of $\Pi_{oxygen}$ and $\Pi_{NiEDDA}$. This indicates that the membrane binding domain of hCOX-2 is located in the interfacial region of the membrane and is sandwiched between the main body of the 144 KDa COX dimer and the lipid bilayer. We have identified three amino acids that participate in anchoring the protein to the lipid bilayer. Human COX-2 is the first peripheral membrane protein mapped using site-directed spin labeling.

Another aspect of this dissertation was to study the conformational changes in the mouth of the cyclooxygenase channel. The purpose of this research was to determine whether the COX substrate and inhibitor binding sites are flexible, *e.g.*, can be opened and closed. Ten cysteine double mutants located in the helices that form the opening of the cyclooxygenase active site and membrane binding of human COX-2 were constructed. The dipolar broadening in the presence and absence of NSAIDs, arachidonic acid and heme were compared in detergent. The same experiments were also performed in liposomes. The interspin distance measurements were done using Fourier convolution/deconvolution technique.

Our results indicated that binding of heme, arachidonic acid, and NSAIDs had no significant effect on the conformation of hCOX-2. However, a slight conformational change was observed in the structure of the enzyme in the presence and absence of the lipid bilayer.

# DEDICATION

In the Loving Memory of My Father
Professor
Abolghassem MirAfzali

## ACKNOWLEDGEMENTS

First of all, I would like to thank the person who was the mastermind behind this work and made all of this research possible: Professor David DeWitt, also known as "The Big Boss."

I had a very rough time as a graduate student because my research was based on the work that was supposedly done by the previous graduate student in our lab. It took me almost a year to realize that the previous work was "science fraud" and I found myself in a situation to start the research from scratch. Professor DeWitt helped me tremendously during all those tough and dark days of my life and encouraged me constantly. He not only taught me biochemistry but also taught me many life lessons. He taught me to tolerate difficult people and situations and to concentrate on my goals. He is the best example of a dedicated scientist who spends all his time including weekends, holidays, Christmas and first day of New Year in his lab. He supervised my research EVERY DAY including the weekends. I was always welcome to ask any questions of him and he guided me step by step through this work. I also thank him for supporting me financially to attend various scientific meetings. I have really great memories from the activities that we had outside his lab, such as group lunches, the dinner invitation, the pizza party and the "end of summer" party at his house, the bowling game and our trip to Tahoe City in California.

I would like to thank my chemistry research advisor Professor John McCracken for giving me the opportunity to be a dual major student and work in Professor DeWitt's lab in the Biochemistry Department. Professor McCracken is not only a great scientist but

also a great lecturer. Before joining Professor McCracken's lab I was his teaching assistant in a Physical Chemistry course and I learned a lot from attending his classes. I also enjoyed all the amusing stories that he told us in our group meetings. Professor McCracken accepted me as his student when my former advisor Professor Babcock was seriously ill and gave me the opportunity to start a new project. He also supported me as a research assistant all these years so I could do research without being concerned about teaching duties. When I look back I realize that joining Professor McCracken's lab was the best and the most professional decision that I have ever made in my scientific life.

I would like to Professors Lynmarie A. Posey, Ned Jackson and Honggao Yan for serving in my defense committee.

I would like to thank the members of three cyclooxygenase research laboratories:

In Professor DeWitt's lab I would like to thank Jeffrey Leipprandt for growing bioreactor after bioreactor of cells for me and for tolerating all the frustrating moments in our lab. This research was absolutely impossible without Jeff.

I thank Christi Hemming for being so entertaining and full of life and making me laugh all the time. Christi is one of the most pleasant people that I have ever met in my life.

I thank my dear friend Prashanti Franklin for her friendship and the outstanding undergraduate student Matthew Sekedat for helping me with the liposome incorporation studies of Cox enzyme.

In Professor Smith's lab I would like to thank Professor William Smith for his encouragement and his faith in me. I also thank Jill Rieke, Dr. Cindy DeLong, Jiayan Liu, Dr. Gilad Rimon (Ben Gurion University at Negev, Israel), Dr. Sigal Fleisher (Ben

Gurion University at Negev, Israel), Dr. Byron Wingerd and Dr Dimitry Kuklev for our scientific discussions and also for their friendship. I am still in shock about their lab relocation to the other school down the road, also known as University of Michigan.

In Professor Garavito's lab I would like to thank Professor Mike Garavito for his scientific discussions about lipid bilayer interface and X-ray crystallography and also for introducing the Nebulizer to me which made my life much easier.

I am in debt to Dr. Anne Mulichak who is an outstanding scientist for discussing the crystal structure of COX-2 with me and making the membrane binding domain pictures of COX-2. I would also like to thank Amy Scharmen, Karen Poster-Verrill and Nicole Webb for their friendship.

I would like to thank all the scientists in the MSU Center for Advanced Microscopy.

Thank to Dr. Alicia Pastor Lecha for helping me with the transmission electron microscopy and patiently teaching me this technique. The electron microscopy work was impossible without her. I will never forget all the fun that we had in the dark room and in the microscope room and also the wonderful dinner party at Alicia's new house.

I would like to thank Robert Pcionek for his very genuine friendship and for teaching me how to use the complicated electron microscope instrument. I can't thank him enough.

Another big thanks goes to Ewa Danielewicz for the scanning electron microscopy work on liposomes. I really enjoyed working with Ewa and listening to her amazing stories about her sons.

I would like to acknowledge Dr. Shirley Owens for her impressive confocal laser scanning microscopy work on fluorescence liposomes and also for her kindness and friendship.

I would like to thank Kermit Johnson who is an exceptional technician for teaching me to use the loop-gap resonator. Kermit is my hero.

I thank Dr. Andrew Ichimura for teaching me to use the EPR spectrometer at the beginning of my work in the EPR lab. I really enjoyed my late night talks with Andrew.

I also would like to thank Dr. Joseph Leykam in Macromolecular Structure Sequencing and Synthesis Facility who taught me various techniques including peptide synthesis. I enjoyed talking to Joe and listening to his amusing stories.

I would like to thank the members of the fifth floor labs in Biochemistry building for their wonderful friendship and day-to-day interaction.

I would like to thank my various friends in the Chemistry Department especially Montserrat Rabago-Smith and Chrysoula Vasileiou for their friendship. I will always remember the night that Montserrat made me incredibly drunk with several Tequila shots.

I would like to thank my family especially my mother Dr. Guity Mehr MirAfzali for her encouragement during all these years and my love Michael for making my life so bright especially during the last several months that I was writing my dissertation. I really enjoyed all our "geeky" scientific discussions about magnetic resonance and C programming. Your love and encouragement saved my life. I love you.♥♥

I thank MSU Center for Biological Modeling for the graduate student award for Spring 2001 and also for the travel award.

At last I would like to thank the National Institutes of Health for supporting this "VERY EXPENSIVE" project.

TABLE OF CONTENTS

# LIST OF TABLES

# LIST OF FIGURES

# LIST OF ABBREVIATIONS

| | |
|---|---|
| AA | Arachidonic Acid |
| CLSM | Confocal laser scanning microscopy |
| COX | Cyclooxygenase |
| CW | Continuous wave |
| DEER | Double Electron-Electron Resonance |
| DPPH | α, α'-diphenyl-β- picrylhydrazyl |
| DOPC | 1,2-Dioleoyl-sn-Glycero-3-Phosphocholine |
| DOPS | 1,2-Dioleoyl-sn-Glycero-3-[Phospho-L-Serine] |
| DSDSL | Double Site Directed Spin Labeling |
| EDTA | Ethylene Diamine Tetraacetic Acid |
| EGF | Epidermal Growth Factor |
| ELDOR | ELectron-electron DOuble Resonance |
| EPR | Electron Paramagnetic Resonance |
| ER | Endoplasmic Reticulum |
| FCD | Fourier Convolution Deconvolution |
| FFT | Fast Fourier Transformation |
| FORTRAN | FORmula TRANslation (A programming language) |
| FT | Fourier Transformation |
| MBD | Membrane Binding Domain |
| MOI | Multiplicity of Infection |
| MTSSL | MethaneThioSulfonate Spin Label |
| MLV | MultiLamellar Vesicle |

| | |
|---|---|
| NiAA | Nickel Acetyl Acetonate |
| NiEDDA | Nickel Ethylen Diamine Diacetic Acid |
| NMR | Nuclear Magnetic Resonance |
| NSAID | Non Steroidal Anti Inflammatory Drugs |
| PBS | Phosphate Buffer Saline |
| PDB | Protein Data Bank |
| PG | Prostaglandin |
| $PGG_2$ | Prostaglandin $G_2$ |
| $PGH_2$ | Prostaglandin $H_2$ |
| PGHS | Prostaglandin Endoperoxide $H_2$ Synthase |
| POX | Peroxidase |
| SDSL | Site-Directed Spin Labeling |
| SEM | Scanning Electron Microscopy |
| Sf-21 | Spodoptera Frugiperda |
| TEM | Transmission Electron Microscopy |
| ULV | UniLamellar Vesicle |

# Chapter 1- Literature Review

## Prostaglandins, Prostaglandin Endoperoxide $H_2$ Synthase Isozymes and Nonsteroidal Anti-Inflammatory Drugs

## 1.1. Introduction

Pain is the most significant and costly problem confronting human beings and has a profound impact on the work productivity and the quality of life.

Prostaglandins are a group of physiologically active substances that play a major role in pain, inflammation and chronic inflammatory diseases, such as asthma and rheumatoid arthritis. Cyclooxygenase (COX) isozymes are membrane proteins responsible for the synthesis of prostaglandins. Inhibition of COX with nonsteroidal anti-inflammatory drugs (NSAIDs) acutely reduces inflammation and pain.

In the following review, prostaglandins and their functions in body, the structure and the catalytic mechanism of cyclooxygenase and also different classes of nonsteroidal anti-inflammatory drugs will be discussed.

## 1.2. Prostaglandins

Prostaglandins are a group of physiologically active substances having diverse hormone-like effects in animals. Prostaglandins act in a manner similar to that of hormones, by stimulating target cells into action. However, they differ from hormones in that they act locally, near their site of synthesis, and they are metabolized very rapidly. In terms of chemical structure, prostaglandins are 20-carbon fatty acid derivatives containing a 5-carbon ring (Figure 1.1). They were discovered in human semen in 1935 by Swedish physiologist Ulf Von Euler (*1*), who named them thinking they were secreted by the prostate gland. Prostaglandins are now known to be of widespread occurrence in

animal tissues, where they are formed from polyunsaturated fatty acids and are rapidly metabolized (*2*).

Most prostaglandins are synthesized from arachidonic acid (20:4 $\Delta^{5,8,11,14}$). These are called "series 2" products, because most have two double bonds. However, the triene fatty acid 20:3 $\Delta^{8,11,14}$ can also be used; the products have one fewer double bond than the arachidonic acid derivatives and are called the "series 1" products. Two $\omega^6$ fatty acids, 20:3 $\Delta^{8,11,14}$ and arachidonic acid (20:4 $\Delta^{5,8,11,14}$), are substrates for most prostaglandin biosynthesis, producing the "series 1" and "series 2" products respectively. In addition, the 20:5 $\Delta^{5,8,11,14,17}$ fatty acid, an $\omega^3$ fatty acid, can also be used for prostaglandin biosynthesis. Humans can synthesize $\omega^9$ fatty acids, such as oleic acid and its 20:3 $\Delta^{5,8,11}$ derivative. However, this is ordinarily a minor pathway, and the 20:3 $\Delta^{5,8,11}$ cannot be used to make functional prostaglandins (*2*).

### 1.2.1. Functions of Prostaglandins

Prostaglandins (PG) play critical roles in normal physiological processes. Platelet-derived $TXA_2$ is an important mediator of platelet aggregation and thus hemostasis. During periods of stress, PGs of the E and I series are important regulators of renal blood flow. PGs likewise are important in modulating many aspects of reproductive biology including ovulation, fertilization, fetal development, and parturition. The opposing actions of different PG classes help to maintain bronchial tone. The processes of bone formation and resorption are also subject to regulation by PGs. Macrophage differentiation is also modulated by PGs. PGs are vital to the maintenance of mucosal

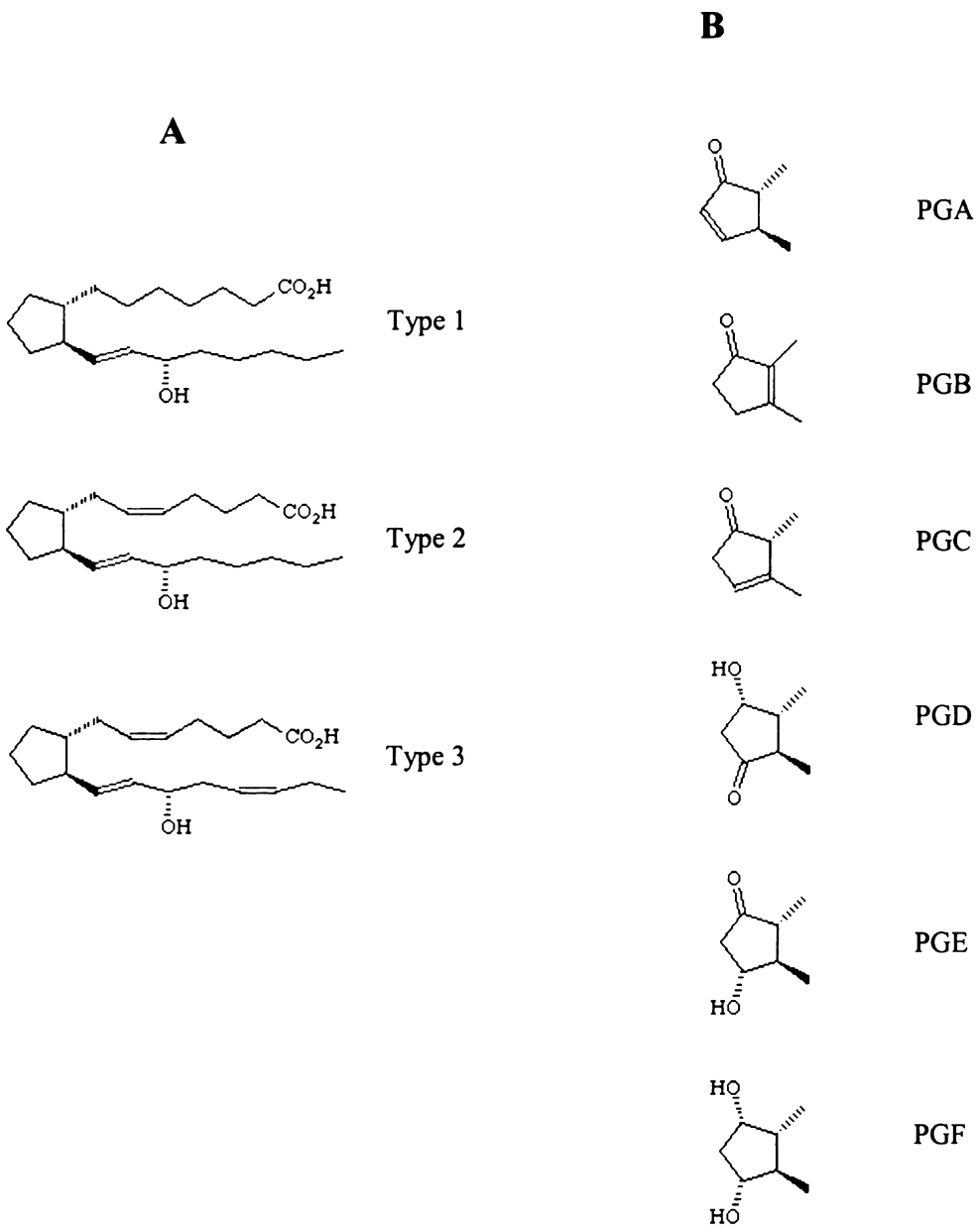


**Figure 1.1.** Nomenclature of prostaglandins

A) The number of carbon-carbon double bonds determines the type of prostaglandin.
B) Letters A to F are designated as the substituents on the cyclopentane ring.

integrity in the gastrointestinal tract and also play a role in the regulation of motility and secretion. PGs also affect immune function in a number of ways (3).

PGs have been implicated in a wide variety of disease processes. The huge annual market for nonsteroidal anti-inflammatory drugs (NSAIDs) which inhibit COX activity is a testament to the role of PGs in acute inflammation and chronic inflammatory diseases, such as asthma, rheumatoid/osteo arthritis, and inflammatory bowel disease (IBD). Epidemiological and animal studies indicate that inhibition of PG synthesis is efficacious in the prevention of coronary artery thrombosis, Alzheimer's disease, gastrointestinal cancer and breast cancer. The properties of PGs that contribute to disease progression include their thrombotic activity, ability to modulate cellular apoptosis and other cell cycle parameters, angiogenic activity and other functions yet to be identified (*3*).

### 1.2.2. Prostanoid Biosynthesis

Prostaglandin formation is a three-step process, which includes:

a) Arachidonic acid release from membrane phospholipids.

b) Conversion of arachidonic acid to $PGH_2$ by cyclooxygenase enzyme.

c) Conversion of $PGH_2$ to specific prostaglandins, followed by their release from the cell.

The overall process in shown in Figure 1.2.

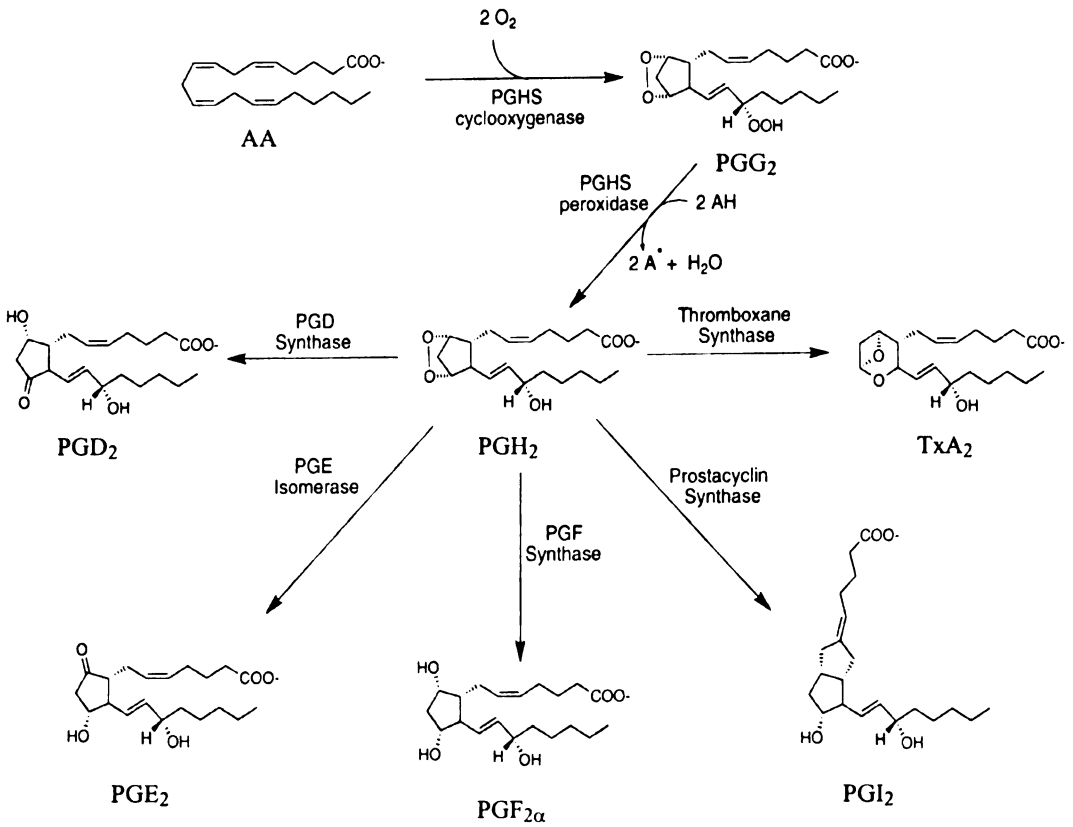


**Figure 1.2.** Biosynthetic pathway for Prostanoid synthesis. Taken from *(4)*. Copyright permission was obtained.

Initially, arachidonic acid is cleaved from membrane phospholipids following hormonal activation of one of the phospholipases $A_2$s ($PLA_2$). Two classes of $PLA_2$ have been shown to be involved in the mobilization of arachidonic acid from phospholipids, cytoplasmic $PLA_2$ ($cPLA_2$) and several secretory $PLA_2$ ($sPLA_2$) (*5*). The $cPLA_2$ is believed to be the major mediator of agonist-induced arachidonic acid released in cells because of its specificity in cleaving. Arachidonic acid is hydrolyzed from the *sn*-2 position of membrane phospholipids. Several $sPLA_2$ have also been shown to mobilize arachidonic acid, and subsequently increase prostanoid production, although specificity for arachidonate cleavage from phospholipids has not been shown as clearly as with $cPLA_2$ (*6*). Release of free arachidonic acid is increased upon activation of $cPLA_2$.

### 1.3. Prostaglandin Endoperoxide $H_2$ Synthases–1 and –2

Cyclooxygenases are N-glycosylated membrane proteins responsible for the synthesis of prostaglandins involved in important physiological processes, such as smooth muscle contraction, inflammation, parturition and platelet aggregation (*7*). Two isoforms have been identified: COX-1 and –2, which are also referred to as Prostaglandin endoperoxide $H_2$ synthases –1 and –2 (PGHS-1 and –2) (*7*). COX-1 and -2 are of particular interest because they are the major targets of nonsteroidal anti-inflammatory drugs (NSAIDs) including aspirin, flurbiprofen, naproxin and new COX-2 inhibitors such as Celebrex®, Vioxx®, Bextra® and Arcoxia®. Inhibition of the COXs with NSAIDs acutely reduces inflammation, pain, and fever. Long term use of these drugs reduces fatal thrombotic events, as well as the development of colon cancer and Alzheimer's

disease. The isozymes are peripheral membrane proteins that catalyze the synthesis of prostaglandins in the arachidonic acid cascade.

The primary structures of both isoforms share a 60% amino acid sequence identity within the species. The major differences in sequence between COX-1 and –2 are in the N-terminal and C-terminal regions of the isozymes. In N-terminal, COX-1 has a sequence of hydrophobic residues within the signal peptide that are lacking completely in COX-2. Conversely, COX-2 contains a highly conserved 18-amino acid cassette at the C-terminus, whose function has not yet been determined.

The theoretical molecular masses of COX-1 and –2 are 66 kDa and 67 kDa respectively. COX-1 has a mass of 72 kDa and COX-2 has both masses of 74 and 72 kDa. The 72 kDa masses can be attributed to the addition of carbohydrate groups at three N-glycosylation sites in both COX-1 and-2 (Asn 68, Asn 144, Asn 410). Glycosylation of all three sites is essential for enzyme activity in both isozymes (*8*). The 74 kDa mass of COX-2 is attributed to an inefficient N-glycosylation at a unique fourth site, Asn580, whose glycosylation has no effect on the enzymatic activity of COX-2 (*8*). Otherwise, the enzymes share a remarkable similarity in sequence within a species, with an epidermal growth factor (EGF) domain, three N-glycosylation sites, and conservation of all catalytically important residues in both COX-1 and COX-2.

The three dimensional structures of ovine 567-amino acid COX-1 complexed with the NSAID flurbiprofen (*9*), with 2-bromoacetoxybenzoic acid (a potent aspirin analogue) (*10*), as well as with iodinated indomethacin and suprofen (*11*), have been determined by X-ray crystallography. X-ray structures of unligated murine COX-2 and COX-2 complexed with flurbiprofen, indomethacin and a selective inhibitor (SC-558)

have also been obtained (*12*). The structure of human COX-2, determined in the presence of a selective inhibitor is similar to that of COX-1 (*13*). The crystal structures revealed the presence of three folding units: an EGF homology domain, a catalytic domain containing both cyclooxygenase and peroxidase catalytic sites and a membrane-binding domain (Figure 1.3). From solubilization and crystallization studies of COXs, it has been shown that the isozymes function as homodimers, forming an interface between EGF homology domain of each monomer.

The crystal structure of COX-1 complexed with flurbiprofen shows the drug localized in a long, hydrophobic channel within the cyclooxygenase active site. The opening of this site begins with the membrane–binding domain and extends into the catalytic domain, with one active site in each monomer. Presumably, the arachidonic acid substrate would be cleaved from the membrane lipids and could directly access the hydrophobic cyclooxygenase active site channel. The crystal structure of $Co^{+3}$-heme ovine COX-1 complexed with arachidonic acid was solved (*14*). This structure revealed specific substrate-enzyme interactions within the cyclooxygenase active site. In the cyclooxygenase reaction, arachidonic acid is positioned in the hydrophobic pocket in an extended L-shaped conformation with the carboxylate group positioned at the base of the channel by virtue of an electrostatic interaction with arginine 120 (*15, 16*). C13 of the arachidonic acid is positioned near tyrosine 385 at the top of the channel (Figure 1.4).

The porphyrin radical of the oxidized heme group, generated by reduction of a hydroperoxide substrate in the peroxidase reaction, abstracts a hydrogen from tyrosine 385 creating a tyrosyl radical (*17, 18*). Next this tyrosyl radical abstracts the 13 pro-S hydrogen from arachidonate creating an arachidonyl radical, which then reacts with a

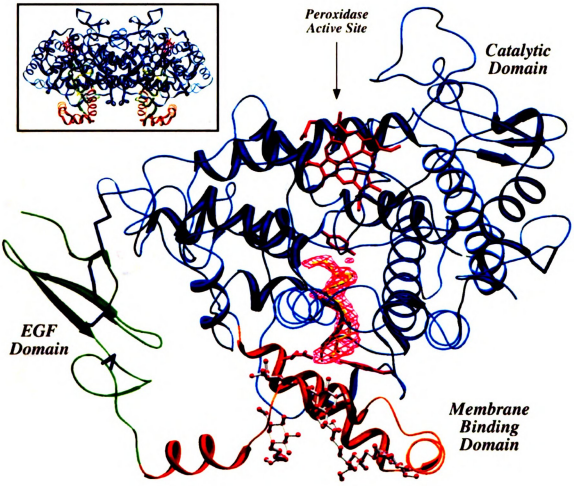


**Figure 1.3.** A ribbon representation of the oCOX-1 monomer with AA bound in the cyclooxygenase channel. The EGF domain, MBD, and catalytic domain are shown in green, orange, and blue, respectively. (Inset) The native dimer with the twofold axis running vertical. Taken from (*14*). Copyright permission was obtained.
Images in this dissertation are presented in color.

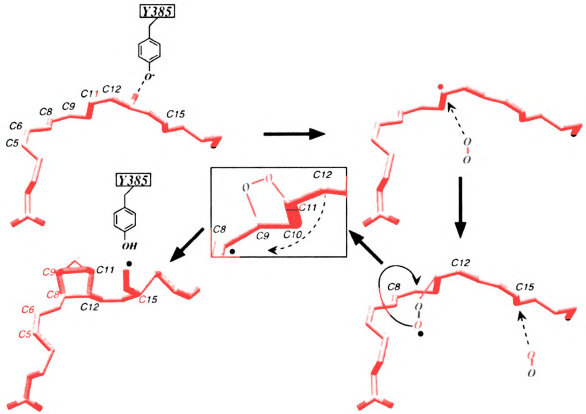


**Figure 1.4.** Mechanistic sequence for converting AA to $PGG_2$.Taken from (14). Copyright permission was obtained. Images in this dissertation are presented in color.

molecule of molecular oxygen at C11. The resulting peroxyl radical next attracts C9 of the fatty acid resulting in an oxygen bridge between C9 and C11, followed by the formation of a cyclopentane ring connecting C8 and C12 (Figure 1.4). Addition of molecular oxygen at C15 and the transfer of the radical back to tyrosine 385 results in the formation of the hydroperoxide $PGG_2$ which exits the cyclooxygenase active site, leaving it primed for another round of catalysis. $PGG_2$ next diffuses to the peroxidase active site, which is a shallow channel containing a heme group and on the opposite face of the enzyme, to undergo the two-electron reduction in the peroxidase active site converting the 15-hydroperoxy group to the 15-alkyl group of $PGH_2$.

X-ray crystallographic studies have demonstrated that neither isozyme contains amino acid sequences of sufficient length and hydrophobicity to function as classical transmembrane domains. Instead, COX-1 and –2 are thought to associate with cellular membranes through a novel, monotopic membrane binding domain that transverses a single leaflet of the lipid bilayer (*9*). The X-ray crystallography shows that projecting from the globular catalytic domain in each monomer are four amphipathic alpha helices (labeled A, B, C and D) (Figure 1.5). Hydrophobic and aromatic residues protrude from these helices and away from the hydrophobic surface of the catalytic domain to create a hydrophobic patch. Chimeric constructs of green fluorescent protein linked to the N-terminal sequences containing the MBD domain from either COX-1 or COX-2 are targeted to the proper membrane location in cells, providing further evidence that these sequences are responsible for membrane localization of the isozymes (*19*). These helices also form the opening to the cyclooxygenase active site and were predicted to facilitate interaction with the lipid bilayer. The substrate of COXs, arachidonic acid, is released

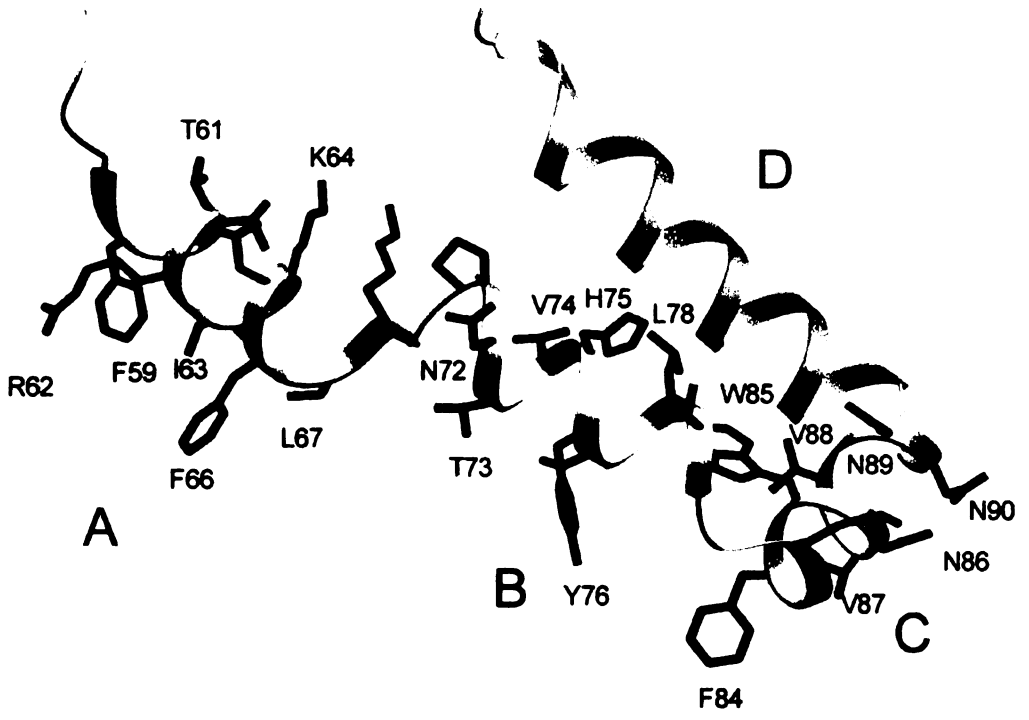


**Figure 1.5.** Side view of the COX-2 membrane binding domain helices
This picture was made by Dr. Anne Mulichak.
Images in this dissertation are presented in color.

from the bilayer and presumably travels through the core of the helices A-D to the cyclooxygenase active site. The membrane-binding domain of COX-1 and COX-2 has the least sequence similarity to each other, sharing only 38% sequence similarity (*7*).

## 1.4. Nonsteroidal Anti-Inflammatory Drugs (NSAIDs)

### 1.4.1. Historical background

The use of medicinal substances to relieve pain and fever dates back to ancient Egypt, where a decoction of dried leaves of myrtle applied to the back and abdomen of patients, was used to expel pains from the womb. Later, in Greece, the bitter extracts from the bark of the poplar tree were used in patients with eye diseases. Extracts of the willow bark were chewed to relieve the pain of childbirth and to reduce fever. These beneficial effects remained largely unknown until the first published report of willow bark was done in England by Reverend Edward Stone in 1763. Later on the active component of willow bark was identified as salicin, which is metabolized to salicylate.

Salicylic acid was synthesized in Germany in 1860 by Kolbe and Lautemann, leading to an extended use as an external antiseptic, an antipyretic, and an antirheumatic drug which caused dyspepsia and tasted bitter when given orally. Salicylic acid has a tendency to cause upset stomach in frequent users, and it was this side effect that inspired Felix Hoffman, a German chemist employed by the Bayer Corporation whose arthritic father used salicylic acid, to synthesize aspirin from the original willow bark compound in 1897. In 1899, Heinrich Dreser named the compound "Aspirin", the "a" referring to the

acetyl grouping and the "spirin" recalling the botanical genus spiraea, from which salicylates could be extracted.

During the beginning of the 20th century, aspirin was recognized as an antipyretic, anti-inflammatory, and an analgesic drug. Later on, the development of other drugs with similar clinical effects, like Phenylbutazone in 1949 and Indomethacin in 1963, inspired pharmacologists and biochemists to search for a common mode of action. Little was known except that they produced an anti-inflammatory effect both quantitatively and qualitatively different from the more potent glucocorticoids (*20-23*).

### 1.4.2. The Problem of Pain

Pain is one of the most significant and costly healthcare problems confronting society today. Pain impacts not only the lives of patients and their families, but also places great strains upon providers as well as the healthcare systems that bear the cost of treatment. Indeed, pain is the single most common reason patients seek medical care, accounting for one-half of all physician office visits. Yet, nearly two-thirds (64%) of pain sufferers report that they only seek medical care when they can endure the pain no longer. A recent survey reports that four of ten adults (42%) experience pain daily, while nine out of ten (89%) experience pain every month. Of the latter, more than 26 million individuals (15%) suffer severe debilitating pain. Forty-three percent of adults - a projected 83 million individuals - report that pain frequently affects their participation in activities. In

the workplace, a significant portion of workdays lost (25%) is due to pain. In hospitalized patients, pain is associated with longer recovery times and poorer patient outcomes. Pain, therefore, has a profound impact on the quality of life, work productivity, and the cost of healthcare (*24*).

### 1.4.3. The Cost of Pain

In U.S the annual cost for healthcare and lost productivity due to the pain is more than 100 billion dollars. The annual cost attributed to back pain, migraines, and arthritis is about 40 billion dollars and the annual cost of the physician visits due to the pain is 40 million dollars. The prescription analgesic market is currently estimated at over $9 billion in the U.S. and $26 billion globally. In the U.S. alone, pain accounts for over 40 million clinical visits per year and 4 billion lost workdays ($65 billion in productivity) (*24, 25*). Despite the large sales numbers, it is widely agreed by practitioners and patients that the market is poorly served by existing therapeutic approaches due mostly to their poor efficacy or debilitating side effects. Because of this unmet need, it is projected that sales of drugs related to pain management will grow by as much as 20% each year for the foreseeable future. One need only look to the short timeframe required for two recently launched pain drugs, OxyContin® (Purdue Pharma) and Celebrex® (Pfizer), to surpass the $1 billion annual sales level, 36 months and 10 months, respectively, to appreciate the market's appetite for new products (*26*).

### 1.4.4. Inhibition of Cyclooxygenase with NSAID

The principal pharmacological effect of NSAIDs is due to their ability to inhibit prostaglandin synthesis by blocking the cyclooxygenase activity of both COX-1 and COX-2. Their therapeutic effectiveness as analgesics, antipyretics, anti-inflammatories and anti-thrombogenics is due to their inhibition of prostanoid synthesis, which also accounts for their side-effect profile.

Traditional NSAIDs can be grouped into four classes based on their modes of inhibition of COX:

**Class I:** Simple, competitive, reversible inhibitors that compete with arachidonic acid for binding to the COX active site.

Included in this class are: Ibuprofen (Advil®, Mortin®); Piroxican (Feldene®); Sulindac sulfide (Clinoril®); Flufenamate; Mefenamic acid (Ponstel®) and Naproxen (Naprosyn®).

**Class II:** Competitive, time-dependent, reversible inhibitors that bind to the COX active site in a first phase, to form reversible enzyme-inhibitor complexes.

Included in this class are: Indomethacin (Indocin®); Flurbiprofen (Ansaid®), Meclofenamic acid (Meclomen®) and Diclofenac (Voltarol®).

**Class III:** Competitive, time-dependent, irreversible inhibitors that form an enzyme inhibitor complex after a covalent conformational change in the protein.

Included in this class is: Aspirin.

The acetylation of COX-1 by aspirin is an irreversible process that inhibits COX activity but not the peroxidase activity.

**Class IV:** Time-dependent COX-2 inhibitors. These drugs have larger side groups to occupy extra side pocket in COX-2.

Included in this class: Celecoxib (Celebrex®); Rofecoxib (Vioxx®); Valdecoxib (Bextra®), Etoricoxib (Arcoxia®) and SC58125.

Table 1.1 lists the generic and brand names of common NSAIDs.

### 1.4.5. COX-2 Selective Inhibition

The original NSAIDs have long been known for their lethal side-effects. As reported in the American Journal of Medicine (*27*), over 100,000 people are hospitalized each year and at least 16,500 die each year from gastrointestinal (GI) bleeding in United States. These figures are considered conservative, and they are only figures for NSAIDs being used to treat arthritis. It also doesn't include the number of people who die of other complications from NSAID use such as congestive heart failure. A true analysis of the number of deaths world wide from NSAIDs would be overwhelming.

The discovery that COX-2 is involved in inflammation, fever, and pain has led to the development of a new class of inhibitors that acts selectively on this isozyme. COX-2 has a larger active site and a side pocket into which the new specific bulkier inhibitors fit. Crystal structures of COX-2/inhibitor complexes (*13*) and (*12*) reveal that selective COX-2 inhibitors utilize the side pocket created by I523V and I434V substitutions in COX-1 (Figure 1.6).

**Table 1.1.** Generic and brand names of common NSAIDs

| GENETIC NAME | BRAND NAME |
|---|---|
| Aceclofenac | Preservex |
| Acematacin | Emflex |
| Azapropazone | Rheumox |
| Benoxaprofen | Oraflex, Operen |
| Bromfenac | Duract |
| Celecoxib | Celebrex |
| Diclofenac | Voltaren, Rhumalgan, Diclomax, Motifene 75 |
| Diflunisal | Dolobid |
| Etodolac | Lodine |
| Etoricoxib | Arcoxia |
| Fenbufen | Lederfen |
| Fenoprofen | Naflon, Fenopron, Progesic |
| Floctafenine | Idarac |
| Flurbiprofen | Ocufen, Froben, Ansaid |
| Ibuprofen | Advil, Haltran, Trendar, Nuprin, Motrin, Aches-N-Pain, Brufen, Nurofen, Actiprofen, ACT-3, Rafen |
| Indomethacin | Indocid, Indocin, Indoflex, Indameth, Rheumacin LA, Flexin, Nisiad |
| Ketoprofen | Orudis, Oruvail, Ketovail, Ketocid, Alrheumat |
| Ketorolac | Toradol, Acular |
| Meclofenamate | Meclomen |
| Mefenamic Acid | Ponstan, Mefic, Ponstel, Meflam, Dysman, Opustan |
| Meloxicam | Mobic |
| Nabumetone | Relafen, Relifex |
| Naproxen | Naprosyn, Anaprox, Naprelan, Synflex, Nycopren, Arthroxen, Laraflex |
| Naproxen sodium | Aleve |
| Oxaprozin | Daypro |
| Oxyphenbutazone | Oxalid, Tandearil |
| Phenylbutazone | Butazolidin, Azolid, Butacote, Butatab |
| Piroxicam | Feldene, Larapam, Piroflam, Flamatrol |
| Rofecoxib | Vioxx |
| Sulindac | Clinoril |
| Suprofen | Suprol |
| Tenoxicam | Tilcotil, Mobiflex |
| Tiaprofenic acid | Surgam |
| Tolfenamic | Clotem |
| Tolmetin | Tolectin |
| Valdecoxib | Bextra |

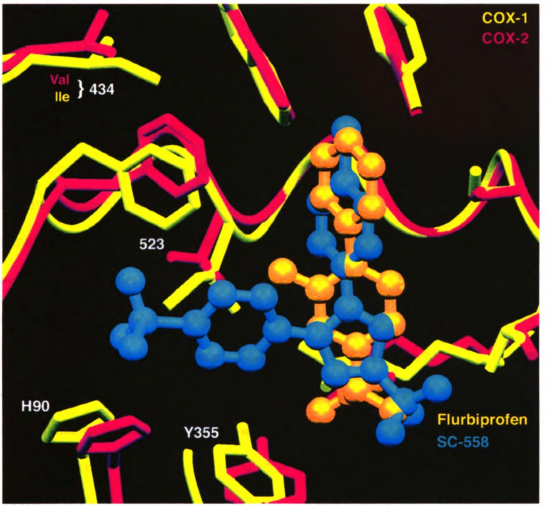


**Figure 1.6.** Isoform-selective inhibitor binding.
The COX-1 and COX-2 active sites are shown superimposed (COX-1, yellow; COX-2 pink). Two inhibitors are seen; flurbiprofen (orange), a nonselective inhibitor, and SC-558 (blue), a COX-2 –selective inhibitor, NSAIDs achieve COX inhibition by occupying the upper portion of the active site channel, preventing the fatty acid substrate from gaining access to the active site tyrosine seen at the upper right. The COX-2 selective inhibitor projects leftward into a side pocket that is not exploited by the nonselective inhibitor. Taken from (*28*).
Images in this dissertation are presented in color. Copyright permission was obtained.

These "COX-2" inhibitors are able to selectively inhibit COX-2, alleviating pain, fever and inflammation without causing the gastrointestinal problems associated with non-selective NSAIDs (22).

## 1.5. Statement of Problem

The main goal of this dissertation is to characterize the structural interactions of the peripheral membrane protein hCOX-2 with lipid bilayers. COX isozymes do not contain transmembrane sequences. Instead, both isozymes contain four short contiguous amphipathic α-helices that constitute a membrane binding domain thought to interact with a single leaflet of the lipid bilayer (*9*). However, this model has never been confirmed experimentally. Amphipathic α-helices are common structural motifs that previously have been grouped into 7 classes according to their function (*29*). Examples of well characterized roles for these motifs include; cell membrane disruption (mellittin and other transmembrane domains), transportation of lipids (apolipoproteins), membrane insertion (integral proteins containing transmembrane domains), and solvent/protein interfaces (most globular proteins). In COX isozymes amphipathic helices are though to be used for stable association to the membrane.

The COX isozymes have been studied extensively because of their essential and regulatory role in prostaglandin synthesis and also because they are the sites of action of nonsteroidal anti-inflammatory drugs (NSAIDs) such as aspirin and ibuprofen. However very little is known about how the membrane binding domains of COX isozymes interact with the lipid bilayers. The crystal structures of these enzymes can be used to predict how the COXs may interact with membrane, but more direct methods must be used to confirm

or refute these predictions. Furthermore, it is not possible to determine the COX isozymes orientation in a membrane, or to determine lipid binding sites in the COXs from a crystal structure, as few lipid or detergent molecules are visible using X-ray analysis.

The experiments outlined in chapter 3 of this dissertation were designed to answer these important basic questions. The results of the experiments in this chapter might have general applicability to a new class of monotopically-associated peripheral membrane proteins. Sequalene hepone cyclase is another monotopic membrane protein, the only other structurally characterized protein of this new class.

The use of site-directed spin labeling (SDSL) to examine the protein –membrane interaction is a technique that has been pioneered by Wayne L. Hubbell (*30, 31*). In this technique, site directed mutagenesis is used to incorporate single cysteine substitutions at various positions into a series of mutant proteins. These cysteines are then covalently modified with a spin-labeled reagent. The differential collision rates of nitroxides side chains in these proteins with polar and non-polar paramagnetic reagents can be used to determine which of these residues are solvent-exposed or membrane-imbedded. These collision rates are measured using power saturation electron paramagnetic resonance (EPR) spectroscopy. One of the best examples of the use of SDSL has been in the identification of membrane-embedded and solvent accessible amino acids in bacteriorhodopsin. While the crystal structure of bacteriorhodopsin, like the COXs, was known beforehand, these experiments were necessary to determine the orientation of this structure within the membrane. SDSL combined with EPR spectroscopy has provided essential information about the membrane interactions of several other proteins including; diphtheria toxin (*32-34*), colicin E1 (*35, 36*) lactose permease (*37-39*), KcsA potassium

channel (*40*), αA-Crystallin (*41-43*), phospholipase $A_2$ (*44, 45*), T4 lysozyme (*46*), tear lipocalin (*47, 48*) and FepA (*49-51*).

In the research described in chapter three, 25 mutant enzymes that contained single reactive cysteines substituted for amino acids within the hCOX-2 membrane-binding domain were constructed and spin labeled. The accessibility of each spin label with freely diffusing oxygen, a non-polar paramagnetic reagent, and NiEDDA, a polar paramagnetic reagent was measured using power saturation EPR spectroscopy.

These studies require the incorporation of purified COX enzyme into artificial cell membranes or liposomes. An increasing number of techniques for preparation of proteoliposomes have been published, because the approach to the incorporation of a new protein into liposomes is still an empirical one. It has been impossible until now to predict which conditions are necessary for a particular protein to be incorporated into the liposomes.

In chapter 2 of this dissertation the incorporation of hCOX-2 into preformed liposome is discussed. The goal of this research is to optimize the method for reconstitution of active hCOX-2 in liposomes and increase the protein content of these proteoliposomes. The shape and size of the liposomes and proteoliposomes have been extensively studied by electron microscopy. To directly detect the hCOX-2 protein molecules, gold labeled anti bodies were attached to the proteins and the gold particles were directly observed by transmission electron microscopy.

In chapter 4 of this dissertation, the conformational changes in the mouth of the cyclooxygenase channel are studied by double site directed spin labeling technique. The purpose of this research was to determine whether the COX substrate and inhibitor

binding sites are flexible, *e.g.*, can be opened and closed, and whether binding of substrate and/or inhibitor locks these enzymes in a static position. One unexplained feature of the enzymology of the COX isozymes is the mechanism whereby certain nonsteroidal anti-inflammatory drugs (NSAIDs) inhibit these enzymes in a time-dependent manner. Upon incubation, NSAIDs such as indomethacin and flurbiprofen form very tight non-covalent, but essentially irreversible complexes with COX isozymes. Presumably, these complexes result from time-dependent conformational changes in the enzymes upon inhibitor binding. NSAID-induced conformational changes in doubly labeled COXs would be observable as shifts in the spin coupled nitroxide lineshape. The mechanism for time-dependent inhibition of the COXs is of considerable practical importance because newly developed NSAIDs that are selective for COX-2 owe their selectivity to the fact that they are time-dependent inhibitors of COX-2 and only simple competitive inhibitors of COX-1 (*52*). Thus, being able to measure conformational changes in the enzyme structure may increase our understanding of the dynamics of enzyme catalysis as well as provide information about mechanism of drug inhibition.

Ten cysteine double mutants located in the helices that form the opening of the cyclooxygenase active site and membrane-binding domain of hCOX-2 were constructed. The dipolar broadening in the presence and absence of NSAIDs, in the presence and absence of heme and in the presence and absence of arachidonic acid were compared in detergent. The same experiments were also performed in liposomes. The distances between the two spin labels were also measured in various samples of hCOX-2. The interspin distance measurements were done using the Fourier convolution/deconvolution technique (*53*).

## 1.6. References


1. von Euler, U. S. (1936) *Journal of Physiology 88*, 213-34.

2. Rocca, B., and FitzGerald, G. A. (2002) *International Immunopharmacology 2*, 603-630.

3. Funk, C. D. (2001) *Science 294*, 1871-1875.

4. Goodwin, D. C., Landino, L. M., and Marnett, L. J. (1999) *Faseb Journal 13*, 1121-1136.

5. Clark, J. D., Schievella, A. R., Nalefski, E. A., and Lin, L. L. (1995) *Journal of Lipid Mediators and Cell Signalling 12*, 83-117.

6. Murakami, M., Shimbara, S., Kambe, T., Kuwata, H., Winstead, M. V., Tischfield, J. A., and Kudo, I. (1998) *Journal of Biological Chemistry 273*, 14411-14423.

7. Smith, W. L., DeWitt, D. L., and Garavito, R. M. (2000) *Annual Review of Biochemistry 69*, 145-182.

8. Otto, J. C., Dewitt, D. L., and Smith, W. L. (1993) *Journal of Biological Chemistry 268*, 18234-18242.

9. Picot, D., Loll, P. J., and Garavito, R. M. (1994) *Nature 367*, 243-249.

10. Loll, P. J., Picot, D., and Garavito, R. M. (1995) *Nature Structural Biology 2*, 637-643.

11. Loll, P. J., Picot, D., Ekabo, O., and Garavito, R. M. (1996) *Biochemistry 35*, 7330-7340.

12. Kurumbail, R. G., Stevens, A. M., Gierse, J. K., McDonald, J. J., Stegeman, R. A., Pak, J. Y., Gildehaus, D., Miyashiro, J. M., Penning, T. D., Seibert, K., Isakson, P. C., and Stallings, W. C. (1996) *Nature 384*, 644-648.

13. Luong, C., Miller, A., Barnett, J., Chow, J., Ramesha, C., and Browner, M. F. (1996) *Nature Structural Biology 3*, 927-933.

14. Malkowski, M. G., Ginell, S. L., Smith, W. L., and Garavito, R. M. (2000) *Science 289*, 1933-1937.

15. Bhattacharyya, D. K., Lecomte, M., Rieke, C. J., Garavito, R. M., and Smith, W. L. (1996) *Journal of Biological Chemistry 271*, 2179-2184.

16. Rieke, C. J., Mulichak, A. M., Garavito, R. M., and Smith, W. L. (1999) *Journal of Biological Chemistry 274*, 17109-17114.

17. Hsi, L. C., Hoganson, C. W., Babcock, G. T., Garavito, R. M., and Smith, W. L. (1995) *Biochemical and Biophysical Research Communications 207*, 652-660.

18. Tsai, A. L., Hsi, L. C., Kulmacz, R. J., Palmer, G., and Smith, W. L. (1994) *Journal of Biological Chemistry 269*, 5085-5091.

19. Li, Y., Smith, T., Grabski, S., and DeWitt, D. L. (1998) *Journal of Biological Chemistry 273*, 29830-29837.

20. Donahue, K. E. S. (1996) *The Watermark 19*, 80-83.

21. Gartrell, D. (1997), UCLA multimedia website.

22. Liebeskind, J. C., and Meldrum, Marcia L. (1997) in *Proceedings of the Eighth World Congress on Pain (Progress in Pain Research and Management)* (T. S. Jensen, J. A. T., and Z. Wiesenfeld-Hallin, Ed.), IASP Press, Seattle.

23. Meldrum, M. L. (1999) *American Pain Society Bulletin 9*.

24. http://www.ampainsoc.org/.

25. Chase, M. (1998) *Wall Street Journal.*

26. http://www.ims-global.com/.

27. Singh, G. (1998) *The American Journal of Medicine July 27*, 31S.

28. FitzGerald, G. A., and Loll, P. (2001) *Journal of Clinical Investigation 107*, 1335-1337.

29. Segrest, J. P., Deloof, H., Dohlman, J. G., Brouillette, C. G., and Anantharamaiah, G. M. (1990) *Proteins-Structure Function and Genetics 8*, 103-117.

30. Hubbell, W. L., and Altenbach, C. (1994) *Current Opinion in Structural Biology 4*, 566-573.

31. Hubbell, W. L., Gross, A., Langen, R., and Lietzow, M. A. (1998) *Current Opinion in Structural Biology 8*, 649-656.

32. Oh, K. J., Zhan, H. J., Cui, C., Altenbach, C., Hubbell, W. L., and Collier, R. J. (1999) *Biochemistry 38*, 10336-10343.

33. Oh, K. J., Zhan, H. J., Cui, C., Hideg, K., Collier, R. J., and Hubbell, W. L. (1996) *Science 273*, 810-812.

34. Zhan, H. J., Oh, K. J., Shin, Y. K., Hubbell, W. L., and Collier, R. J. (1995) *Biochemistry 34*, 4856-4863.

35. Salwinski, L., and Hubbell, W. L. (1999) *Protein Science 8*, 562-572.

36. Salwinski, L., Levinthal, C., Levinthal, F., and Hubbell, W. L. (1993) *Biophysical Journal 64*, A183-A183.

37. Sun, J. Z., Voss, J., Hubbell, W. L., and Kaback, H. R. (1999) *Biochemistry 38*, 3100-3105.

38. Voss, J., Hubbell, W. L., HernandezBorrell, J., and Kaback, H. R. (1997) *Biochemistry 36*, 15055-15061.

39. He, M. M., Voss, J., Hubbell, W. L., and Kaback, H. R. (1997) *Biochemistry 36*, 13682-13687.

40. Gross, A., Columbus, L., Hideg, K., Altenbach, C., and Hubbell, W. L. (1999) *Biochemistry 38*, 10324-10335.

41. Koteiche, H. A., and McHaourab, H. S. (2002) *Febs Letters 519*, 16-22.

42. Koteiche, H. A., and McHaourab, H. S. (1999) *Journal of Molecular Biology 294*, 561-577.

43. Berengian, A. R., Parfenova, M., and McHaourab, H. S. (1999) *Journal of Biological Chemistry 274*, 6305-6314.

44. Frazier, A. A., Roller, C. R., Havelka, J. J., Hinderliter, A., and Cafiso, D. S. (2003) *Biochemistry 42*, 96-105.

45. Frazier, A. A., Wisner, M. A., Malmberg, N. J., Victor, K. G., Fanucci, G. E., Nalefski, E. A., Falke, J. J., and Cafiso, D. S. (2002) *Biochemistry 41*, 6282-6292.

46. McHaourab, H. S., Kalai, T., Hideg, K., and Hubbell, W. L. (1999) *Biochemistry 38*, 2947-2955.

47. Gasymov, O. K., Abduragimov, A. R., Yusifov, T. N., and Glasgow, B. J. (1997) *Biochemical and Biophysical Research Communications 239*, 191-196.

48. Glasgow, B. J., Gasymov, O. K., Abduragimov, A. R., Yusifov, T. N., Altenbach, C., and Hubbell, W. L. (1999) *Biochemistry 38*, 13707-13716.

49. Klug, C. S., Eaton, S. S., Eaton, G. R., and Feix, J. B. (1998) *Biochemistry 37*, 9016-9023.

50. Klug, C. S., and Feix, J. B. (1998) *Protein Science 7*, 1469-1476.

51. Klug, C. S., Su, W. Y., and Feix, J. B. (1997) *Biochemistry 36*, 13027-13033.

52. DeWitt, D. L. (1999) *Molecular Pharmacology 55*, 625-631.

53. Rabenstein, M. D., and Shin, Y. K. (1995) *Proceedings of the National Academy of Sciences of the United States of America 92*, 8239-8243.

# Chapter 2

# Incorporation of Cyclooxygenase Isozymes into Preformed Liposomes and Electron Microscopy Studies of Liposomes and Proteoliposomes

## 2.1. Abstract

The site-directed spin labeling technique requires the incorporation of the purified COX enzyme into the liposomes. Therefore the goal of the research described in this chapter is to optimize the method for reconstitution of active hCOX-2 into liposomes and increase the protein content of these proteoliposomes.

In this research unilamellar vesicle liposome (ULV) is used as the artificial cell membrane model and direct incorporation technique is used to incorporate hCOX-2 into the liposomes. The size and shape of the liposomes including ULV and multilamellar vesicles (MLV) and proteoliposomes were extensively studied by negative staining transmission electron microscopy. In negative staining technique, the background and surroundings are stained to increase the contrast in the sample. In order to directly detect the hCOX-2 protein molecules, gold-labeled antibodies were attached to the proteins and the gold particles were directly observed by transmission electron microscopy. Scanning electron microscopy technique was also used to observe the 3–dimensional images of liposomes and proteoliposomes.

In section 2.2 of this chapter factors effecting incorporation of an isolated protein into the liposomes are discussed. In section 2.3 an overview of various incorporation techniques will be given. Section 2.4 briefly describes various electron microscopy techniques. Section 2.5 provides all the protocols that were used for the experiments in this chapter and finally in section 2.6 the results will be discussed.

## 2.2. Reconstitution of Membrane Proteins into Lipid Vesicles

Six years after the description of liposome formation by Alec Bangham in 1965 (*1*), the reconstitution of a membrane protein into liposomes was first reported by Kagawa and Racker in 1971 (*2*). Since then a large number of membrane proteins have been isolated and re-incorporated into the artificial cell membranes, where they often exhibit their normal biological activity.

An increasing number of techniques for preparation of such proteoliposomes has been published (*3, 4*), and the reason for this is that the approach to the incorporation of a new protein into the liposomes is still an empirical one. It has been impossible until now to predict which conditions are necessary for a particular protein to be incorporated into the liposomes. So one just has to try to find which method works best. According to E. Racker's comment in his book " Reconstitutions of Transporters, Receptors and Pathological State" (page 38) " ... if nothing works, invent a new reconstitution procedure..."

### 2.2.1. Factors Affecting Incorporation

One of the most important factors is the incorporation of an isolated protein into the liposome is the physical state of the lipids. Natural membranes are normally fluid, *i.e.* in the liquid crystalline phase above the phase transition temperature $T_m$. Many proteins are known to be incorporated more readily into lipid bilayers above $T_m$ and are even sometimes found to be excluded from gel-state lipids (*5*). Other proteins are incorporated

into membranes only over a narrow range around $T_m$ *e.g.* glucagon (*6*). A third group of proteins interacts with phospholipids over a wide range of temperature exhibiting preferential interaction with lipids in the gel phase (*7*).

The molecular basis for interaction of proteins with the lipid membranes near the phase transition or with gel-state lipids is thought to be due to point or line defects facilitating protein-lipid interactions as well as protein-protein interactions along such defects. The spontaneous incorporation of membrane proteins into vesicles by freeze thawing probably relies on the conditions that induce packing defects. The importance of the physical state for the incorporation of proteins into liposomes becomes obvious from the observation that M13 virus coat protein shows a maximum incorporation near the phase transition. The protein assembles into the exterior liposome surface well below the phase transition temperature $T_m$ above this temperature there is almost no incorporation.

In general three types of lipid-protein interactions are distinguished:

1) Electrostatic interaction
2) A mixture of electrostatic and hydrophobic interaction
3) Hydrophobic interaction

The second important factor in the incorporation of an isolated protein into the liposome is the composition of the lipids chosen for the incorporation of a protein. As an example, charged lipids often have a marked effect on the incorporation. The use of charged lipids certainly reinforces electrostatic interactions, but this is not the only effect. It has been shown that negatively charged lipids (phosphatidic acid, phosphatidylinositol,

cardiolipin) also improve the incorporation of the acidic proteins *e.g.* cytochrome oxidase (*8*).

The ionic strength of the buffer is the third important factor in the incorporation of the proteins into the lipid vesicles. The ionic strength of the buffer has an influence on lipid-protein interactions, especially when electrostatic interactions are important. Cations such as ($Mg^{2+}$, $Ca^{2+}$) enhance incorporation at certain concentrations, higher concentrations of these cations often being inhibitory (*9*). Also the pH of the buffer can have a high influence on the incorporation.

Other factors that may influence the incorporation are the type and size of the liposomes. Some proteins *e.g.* cytochrome $b_5$ favor small vesicles (20 nm) over large vesicles (100 nm) by a factor of about 200 probably due to the looser packing of the polar head groups of phospholipids in small vesicles (*10*). On the other hand, cytochrome c oxidase incorporates readily into multilamellar liposomes, but less or not at all into small unilamellar liposomes.

## 2.3. Incorporation Techniques

There are essentially four presently known mechanisms for incorporating, *i.e.*, and reconstituting, proteins into liposome:

1) Methods involving the use of an organic solvent.
2) Methods involving the use of the mechanical means.
3) Methods involving the use of detergents.
4) Direct incorporation of the protein into the preformed liposomes.

These techniques will be described briefly in the following sections.

### 2.3.1. Organic Solvent-Mediated Reconstitution

Organic solvents have been used widely to prepare large liposomes in procedures including ethanol injection, ether infusion and reverse-phase evaporation. However, the usefulness of these techniques is limited because exposure of membrane proteins to the organic solvents, which often denature them.

The only suitable method reported to date for organic solvent-mediated reconstitution of membrane proteins is the reverse phase evaporation. Szoka and Papahadjopoulos (*11*) developed a technique for the incorporation of membrane proteins into large unilamellar liposomes after extraction into a hydrocarbon solvent together with phospholipids. The membrane protein was added to a suspension of lipids in a suitable buffer then a solvent e.g. hexane, pentane, diisopropyl ether, and diethyl ether was added and the mixture was sonicated for a few minutes under argon. After the removal of the organic solvent in a rotary evaporator, the large unilamellar liposomes of about 1 μm are formed. Critical aspects of this technique are the selection of the organic solvent as well as the volume ratio of aqueous to non-aqueous phase (*12*).

### 2.3.2. Reconstitution by Mechanical Means

Second method uses mechanical means to produce large and small unilamellar vesicles (ULV) from multilamellar vesicles (MLV) by swelling of the dry phospholipid films in excess buffer. Such mechanical means include sonication of MLVs and forcing multilamellar lipid vesicles through a French press. Sonication and freeze-thawing of a mixed suspension of lipids and isolated proteins has been widely used in earlier stages of membrane protein reconstitution to demonstrate the function of these purified proteins for which detergent dialysis was insufficient (*13*).

### 2.3.3. Reconstitution by Using Detergents

Of the several different methods used to remove detergent from a mixture of detergent, phospholipid and protein, the dialysis procedure has proved highly successful. In such a method, the proteins and phospholipids are cosolubilized in a detergent to form micelles. The detergent is then removed, resulting in the spontaneous formation of bilayer vesicles with the protein incorporated therein. The detergent is incorporated into liposome as well the protein and thus, these methods require removal of the detergent by methods such as dialysis, gel exclusion chromatography or absorption on hydrophobic resins. The methods that use detergent are very slow because detergent removal must be as complete as possible. Also a phase change that take place during this process slows detergent removal even further. Another disadvantage is that one cannot control the orientation of protein incorporated into the liposomes using the detergent methods (*14*).

### 2.3.4. Direct Incorporation of Proteins into Preformed Liposomes

The forth process involves the direct incorporation of proteins into preformed liposomes. One of the key features for successful incorporation of the delipidated proteins into preformed lipid bilayers appear to be the state of organization of the bilayer. Bilayer conducive to spontaneous incorporation of large membrane proteins are achieved by incorporating 'impurities', such as fatty acids, lysophospholipids, mixtures of structurally different phospholipids, cholesterol, detergent and membrane bound proteins. The putative effect of impurities is the formation of 'organizational defects' that act as sites for fusion of vesicles, not only with other vesicles, but also with proteins (*15*) .

## 2.4. Electron Microscopy

### 2.4.1. Transmission Electron Microscopy

The 1986 Nobel Prize in Physics was awarded jointly to Ernst Rusko, Gerd Binnig, and Heinrich Rohrer. Rusko was recognized for his work on electron optics and the original design of the transmission electron microscope in the 1930s. Binnig and Rohrer were acknowledged for their design of the scanning tunneling microscope a half century later in the 1980s. In presenting the award, the Nobel Prize committee noted the significance of the electron microscopes in all areas of science, calling them " one of the most important inventions of this century (*16*)."

The transmission electron microscope (TEM) was developed after the effective role of wavelength on theoretical resolution was apparent. Green light, which is used for light microscope, has a wavelength of 500 nm and therefore has a theoretical resolution of about 200 nm. As you move down the electromagnetic spectrum to shorter wavelengths, you will pass blue and violet into the range of the ultraviolet (<400 nm). An ultraviolet microscope with a theoretical resolution of 50 nm could be used. But ultraviolet light is absorbed by glass, so the lenses would have to be made of quartz. This would make the microscope extremely expensive and fragile for only a moderate increase in resolution. X-ray microscopes would have a vastly superior increase in resolution, but x-rays can not easily be refracted to form an image. Electron waves offered the best alternative. The electron being a charged particle could be easily refracted in a magnetic field. Also, it could be accelerated by an electrical potential. The stronger the potential the faster the electron will move, and according to the De Broglie relationship the shorter the wavelength therefore the better resolution. In fact a typical electron microscope at an accelerating voltage of 75000 V would have a wavelength less than 5 picometer. This makes the theoretical resolution about 100,000 times better than that of light, well worth undertaking the engineering effort. Unfortunately, this theoretical resolution has never come even close to being attained. The basic draw back is that magnetic fields can not be manipulated, shaped and grouped the way an optical engineer does with glass lenses.

Electron microscopy is used in a variety of ways in biology, medicine, and the material sciences. Examples in the biological sciences include diagnosis of human, animal, and plant diseases; development of disease pathology; study of morphological and developmental aspects of organisms, tissues, and cells; identification of pollen,

viruses, bacteriophage, and diatoms; visualization of subcellular components and structures such as DNA; subcellular localization of elements, enzymes, and proteins; in situ hybridization of gene products; and confirmation of biological, physiological, and biochemical data (*17*).

### 2.4.2. Anatomy of Transmission Electron Microscopy

The ray of electrons is produced by pin-shaped cathode heated up with current. The electrons are vacuumed up by a high voltage at the anode. The acceleration voltage is between 50000 and 150000 V. The higher it is the shorter the electron wavelength and the higher the resolution. The accelerated ray of electrons passes a drill-hole at the bottom of the anode. Its following was in analogous to that of a ray of light in a light microscope. The lens systems consist of electronic coils generating an electromagnetic field. The condenser first focuses the ray. It then passes through the object, where it is partially deflected. The degree of deflection is dependent on the electron density of the object. The greater the mass of the atoms, the greater is the degree of deflection. Biological objects have only weak contrast since they consist mainly of atoms with low atomic numbers (C, H, N, and O). Consequently it is necessary to treat the preparation with special contrast enhancing chemicals (heavy atoms) to get at least some contrast. Additionally they should not be thicker than 100 nm. After the electron beam passes through the object, the scattered electrons are collected by an objective electromagnet lens to form an image. This image is subsequently enlarged by an additional lens system call projective. The formed image is made visible on fluorescent screen or is documented

on photographic material. Photos taken with electron microscope are always black and white. Color itself is a function of visible light, and no visible light is used to generate images in an electron microscope (*17*).

### 2.4.3. Staining

In light microscopy the selective absorption of colored dyes by biological structures enables the detail of a thin section to be seen more clearly. In electron microscopy the equivalent technique uses the absorption of heavy metal atoms to produce differential electron scattering and hence increased contrast in samples. Organic materials consist mainly of elements of low atomic numbers, *e.g.*, hydrogen (Z=1), carbon (Z=6), nitrogen (Z=7), oxygen (Z=8), phosphorus (Z=15), sulfur (Z=16), which have a low electron-scattering power. Hence the contrast in an image of untreated material is low. Staining by soaking in solutions containing tungsten (Z=74), osmium (Z=76), lead (Z=82) or uranium (Z=92) results in sites of high electron-scattering power, and consequently images with more clearly visible specimen detail.

If the specimen is particulate, *e.g.*, viruses, macromolecules or cellular fragments, there is an alternative staining technique, negative staining. In positive staining the heavy metal is absorbed by the tissue or particle itself, whereas in negative staining it is the surroundings and background which are stained, leaving the particle itself unstained and clearly visible against them. This is a very good technique to reveal fine surface structures on particles. Negative staining transmission electron microscopy was used on liposomes and proteoliposomes in this chapter (*18*).

### 2.4.4. Scanning Electron Microscopy

The Scanning Electron Microscope (SEM) is one of the most versatile and widely used tools of modern science as it allows the study of both morphology and composition of biological and physical materials.

By scanning an electron probe across a specimen, 3-D high-resolution images of the morphology or topography of a specimen, with great depth of field, at very low or very high magnifications can be obtained. Size, shape, and distribution as well as statistical analyses of these parameters, may be performed.

In scanning electron microscope, the electron gun, produces a stream of monochromatic electrons. The stream is condensed by the first condenser lens. This lens is used to both form the beam and limit the amount of current in the beam. It works in conjunction with the condenser aperture to eliminate the high-angle electrons from the beam. The beam is then constricted by the condenser aperture, eliminating some high-angle electrons. The second condenser lens forms the electrons into a thin, tight, coherent beam. An objective aperture further eliminates high-angle electrons from the beam. A set of coils then "scan" or "sweep" the beam in a grid fashion, dwelling on points for a period of time determined by the scan speed (usually in the microsecond range). The final lens, the objective, focuses the scanning beam onto the part of the specimen desired. When the beam strikes the sample (and dwells for a few microseconds) interactions occur inside the sample and are detected with various instruments. Before the beam moves to its next dwell point these instruments count the number of interactions

and display a pixel on a cathode ray tube (CRT), whose intensity is determined by this number (the more reactions the brighter the pixel). This process is repeated until the grid scan is finished and then repeated, the entire pattern can be scanned 30 times per second (*17*).

## 2.5. Materials and Methods

**Materials.** 1,2-Dioleoyl-sn-Glycero-3-Phosphocholine (DOPC) and 1,2- Dioleoyl -sn-Glycero-3-[Phospho-L-Serine] (Sodium Salt) (DOPS) were obtained from Avanti Polar Lipids Inc. (Alabaster, Alabama). Oleic acid ≥ 99% was purchased from Fluka. All restriction enzymes and DNA modifying enzymes were purchased from New England Biolabs (Beverly, Massachusetts). Ni-NTA was purchased from Qiagen Inc. (Valencia, California). Specially purified aqueous detergent solution (10% solution) of Tween® 20 was obtained from Pierce (Rockford, Illinois). Arachidonic acid was obtained from Cayman Chemicals (Ann Arbor, Michigan). Nanogold® - antirabbit (NFR) was purchased from Nanoprobes Inc. (Yaphank, New York). Uranyl acetate was from Fluka. Other chemicals were purchased from Sigma.

**Site-directed mutagenesis.** A histidine-tagged version of the human COX-2 protein with cysteines 299 and 526 mutated to serines was subcloned into the pFastbac plasmid (Life technologies Inc.). All of the COX-2 mutants were made using Quick Change Mutagenesis method (Stratagene) using complementary 30-40 nucleotide long primers containing the desired mutations. The mutations were confirmed by the dideoxynucleotide sequencing method. Recombinant baculovirus expressing the mutant

COX-2 protein was generated using the Bac-to-Bac® baculovirus expression system (Life technologies, Inc.).

**Expression of recombinant COX protein in SF21 insect cells.** *Spodoptera frugiperda* (*Sf*21) insect cells were purchased from Invitrogen Corporation (Carlsbad, California) and cultured at 27°C in HyQ-SFX-Insect serum –free insect cell media from HyClone (Logan, Utah) supplemented with 0.1% Pluronic F-68 (Life Technologies, Inc.), 1x Lipid concentrate (Sigma), and 0.2% glucose in four- 2800 ml Fernbach flasks (Bellco Biotechnology Inc., Vineland, NJ) each containing one liter of culture. The shakers were rotated at 120 rpm using an Innova® model 4000 benchtop gyrotory incubator shaker (New Brunswick Scientific Co. Inc,. Edison, NJ).

When cells reached a density of 1.5-2 million cells per milliliter, recombinant baculovirus were added at an M.O.I of 0.01-0.1 and the infection was allowed to proceed for 72 to 96 hours. Cells were harvested, washed with PBS, and then stored as pellets at -80°C.

**Purification of His-tagged COX from baculovirus-infected SF21 insect cells.** SF21 cell pellets were resuspended in 3 ml/g wet weight of Nickel-homogenization buffer (25 mM $NaPO_4$, 100 mM NaCl, 20 mM Imidazole, pH=7.4). The Tween® 20 detergent was added (1% v/v) to the suspended cells. The cells were disrupted by Bioneb® cell disruption system (Glas-Col, Terre Haute, Indiana). After low speed (10,000 x g for 1 hour) centrifugation to pellet cell debris, the supernant was poured into cramp-seal ultracentrifuge tubes. The insoluble material was removed by ultracentrifugation at 100,000 x g for 2 hour. The solubilized extract was next incubated with Fast-flow Ni-

NTA resin for overnight at 4°C with rocking. The resin was poured into a column and washed with 5 volume of Nickel-homogenization buffer containing 0.1% Tween®. Next the resin was washed with 3 volume of Nickel-wash buffer (25 mM $NaPO_4$, 300 mM NaCl, 20 mM Imidazole, pH=7.4) containing 0.1% Tween® 20. The protein was eluted with Nickel-elusion buffer (25 mM $NaPO_4$, 100 mM NaCl, 200 mM Imidazole, pH=7.4) containing 0.2% Tween® 20. Fractions with high specific cyclooxygenase activity were pooled and concentrated in Amicon® Ultra centrifugal filter device with 30000 molecular weight cutoff (Millipore Co., Bedford, MA).

**Cyclooxygenase assay.** Cyclooxygenase activities were measured at 37°C by observing the initial rate of oxygen consumption with an $O_2$ electrode (YSI Inc., Yellow Springs, OH) (*19*).

**Protein determinations.** Protein concentrations were measured using Bicinchoninic acid method (Pierce, Rockford, Illinois) with bovine serum albumin as standard.

**Preparation of large unilamellar vesicles (*20*).** Large unilamellar vesicles (LUVs) were prepared with a DOPC: DOPS ratio of 3:7 and various amounts of oleic acid (0%, 1.25%, 2.47%, 4.82%, 9.2%, 16.8%, 28.8% and 44.7% (w/w)) by mixing the appropriate aliquots of lipids and fatty acid in chloroform and drying the solution under a stream of nitrogen. The dried film of the phospholipids was dissolved in 0.5 ml of hexane and the organic solvent was removed again under a stream of nitrogen. The resulting film was hydrated in a buffer of 25 mM Tris-Cl and 50 mM KCl pH 7.4 for 1 h, vortexed thoroughly and

extruded through a polycarbonate filter with a 0.1 μm pore diameter using a hand-held Mini-Extruder (Avanti Polar Lipids, Birmingham, AL). Lipids were extruded at a total concentration of approximately 38 mM. This process resulted into a transparent milky suspension.

**Incorporation of COX into the preformed liposomes (*20*).** The COX protein was added to the preformed liposomes. Three different protein: lipid molar radio was used (1:250, 1:500 and 1:1000). The solution contained 25 mM Tris-Cl and 50 mM KCl pH 7.4. The mixture was incubated for 20 minutes at 37 C.

**Separation of unincorporated proteins from the proteoliposome (*21*).** 0.5 ml of liposome suspension was mixed with 1 ml of 30% (w/v) Ficoll in 25 mM Tris-Cl and 50 mM KCl pH 7.4 to give a final concentration of 20% (w/v) Ficoll. The liposome suspension was transferred to an ultracentrifuge tube. 3 ml of 10% (w/v) Ficoll was gently layered on top of the liposome suspension. The upper Ficoll layer was covered with a solution of in 25 mM Tris-Cl and 50 mM KCl pH 7.4 (0% Ficoll). The swing-out rotor (Beckman SW 50.1) was used for 30 min at 100,000 g at 20 C. The liposomes and proteoliposomes are separated at the interface between the 0% Ficoll and 10% Ficoll layers. The unincorporated protein will remain in the 30% Ficoll layer.

**Determination of total phosphorus:** The total amount of phosphorus was measured by ascorbic acid method of Ammon and Hinsberg, (*22*) modified by Lowry et al (*23*).

**Gold Labeling.** About 100 µl of proteoliposomes are placed into Eppendorf tube and 10 µl of primary antibody is added to them. The mixture is incubated for 30 minutes in room temperature with occasional shaking. The non-attached primary antibodies are separated from the complex of proteoliposomes-primary antibodies using the Ficoll gradient technique, which was described previously. The liposomes and the complex of proteoliposomes-primary antibodies are separated at the interface between the 0% Ficoll and 10% Ficoll layers. The unattached antibody will remain in the 30% Ficoll layer. The complex of proteoliposomes-primary antibodies are placed into a Eppendorf tube and about 100 µl of gold immunoprobe NANOGOLD®-anti rabbit (NRF) (1.4 nm particle attached to affinity-purified Fab' fragment, raised in goat, against rabbit IgG (whole molecule)) is added to the tube and is incubated for 30 minutes in room temperature with occasional shaking. The non-attached gold-labeled secondary antibodies are separated from the complex of proteoliposomes-primary antibodies-gold labeled secondary antibodies using the Ficoll gradient technique. The liposomes and the complex of proteoliposomes-primary antibodies-gold labeled secondary antibodies are separated at the interface between the 0% Ficoll and 10% Ficoll layers. The unattached gold-labeled secondary antibody will remain in the 30% Ficoll layer. The transmission electron microscopy was done on the sample as described using a diluted stain (0.1-0.2 % solution of uranyl acetate). Because the NANOGOLD® particles are small, over staining with uranyl acetate may tend to obscure direct visualization of individual NANOGOLD® particles. Therefore a diluted stain was used.

**Transmission electron microscopy of liposomes and proteoliposomes.** A JEOL transmission electron microscope (model 100CXII, Tokyo, Japan) operating at 100 kV under the vacuum was used. Formvar (polyvinylformaldehyde) - carbon coated copper grids G-300 mesh (Electron microscopy sciences, Inc., Fort Washington, PA), were employed. A drop of liposome solution (concentration about 5 mM of lipid) was placed on the grid and after 1 minute the excess was removed with a Whatman filter paper #1. A thin film was left on the grid and allowed to air dry. Negative staining with one drop of a 1% solution of uranyl acetate was performed. After 1 minute this drop was again removed with the filter paper, and the resulting stained film was dried in a dust free place.

**Scanning electron microscopy of liposomes and proteoliposomes.** The liposomes and proteoliposomes with total lipid concentration between 15 mM to 38 mM were mixed with an equal volume of 4% gluteraldehyde in 0.1 M sodium phosphate buffer, pH 7.0, for 1 h at room temperature. After fixation one drop of the suspension was placed on the coverslip previously coated with poly –L-lysine (Sigma) and allowed to stand for 5 minutes. The coverslip was then carefully washed with several drops of distilled water, followed by dehydration in ethanol. The coverslips were dried using a Balzers critical point dryer (Balzers CPD, FL-9496, Balzers, Liechtenstein) with liquid carbon dioxide as the transitional fluid. Coverslips were mounted on metal stubs and coated with a 25-30 nm gold layer in an Emscope sputter coater (Emscope Laboratories Ltd., Ashford, Kent, U.K.). The liposomal structures were observed with a JEOL scanning microscope (model JSM-6300F, Tokyo, Japan) at 7 mm working distance using an accelerating voltage of 13 kV.

**Solid Phase EPR measurements**. All EPR measurements were recorded on a Bruker ESP 300E X-band spectrometer equipped with a $TE_{102}$ Bruker rectangular cavity. 200 µl of samples were loaded into a 4-mm OD clear fused quartz sample tubes (Wilmad-labglass, New Jersey). The first derivative absorption spectra of the samples at 183 ± 2K were obtained by averaging 4 scans at a scan width of 110 Gauss and each scan time of 4 minutes. The temperature was controlled with Bruker BVT 2000 liquid nitrogen temperature controller. The microwave power was kept at 1 mW to avoid the saturation of the EPR lines.

**Quantitation of EPR signal and the measurement of incorporation yield (*24*).** In order to measure the incorporation yield of COX enzyme into the preformed liposome, single cysteine spin labeled *h*COX-2 (H75C) was used. The incorporation yield can be measured by dividing the total number of moles of spin labeled protein sample added to the liposomes to total number of moles of the isolated spin labeled proteoliposome band after Ficoll gradient. In spin counting experiment Fremy's salt ($K_2$ $(SO_3)_2$) NO) is used as a standard and is quantified optically ($\varepsilon_{248}$=1690 and $\varepsilon_{545}$= 20.8). Because spin quantitation by EPR is somewhat prone to error, we have used a detailed protocol for our quantitation procedure. First, we have shown that both Fremy's salt and the nitroxide spin label signal are linear in square root of applied microwave power to at least 5 mW. Consequently, we choose 1 mW power for our quantitation studies. Second, the linear relationship between $H_1$ modulation amplitude and the area under the EPR absorption curve, even under condition of mild over modulation, provides a convenient means by

which to increase the accuracy of the determinations. Thus, we carried out a double integration of the first derivative EPR signal of the Fremy's salt and the spin labeled protein samples. By plotting the area vs. the modulation amplitude we were able to extract a least-squares value for area/gauss of modulation amplitude for the known and unknown species. Four different modulation amplitudes were used: 1.0080 G, 1,424 G, 1.793 G and 2.013 G. Typical data for nitroxide spin label are shown in Figure 2.1. Finally, from this value and the known concentration of ($K_2$ ($SO_3$) $_2$) NO), we can determine the nitroxide spin label concentration using the following equation.

$$[x] = \frac{A_x (B_m)_{Std}}{A_{Std} (B_m)_x} [Std] \qquad 2.1$$

where A is the measured area under the absorption curve, $B_m$ is the modulation amplitude in mT.

**Figure 2.1.**

A) Stack-plot of EPR spectra of H75C spin labeled proteoliposomes. Each EPR spectrum was acquired using a different modulation amplitude.

*B)* The plot of intensity of each spectra in Figure 2.1.A versus the modulation amplitude. The slope of this line is used in equation 2.1.

A

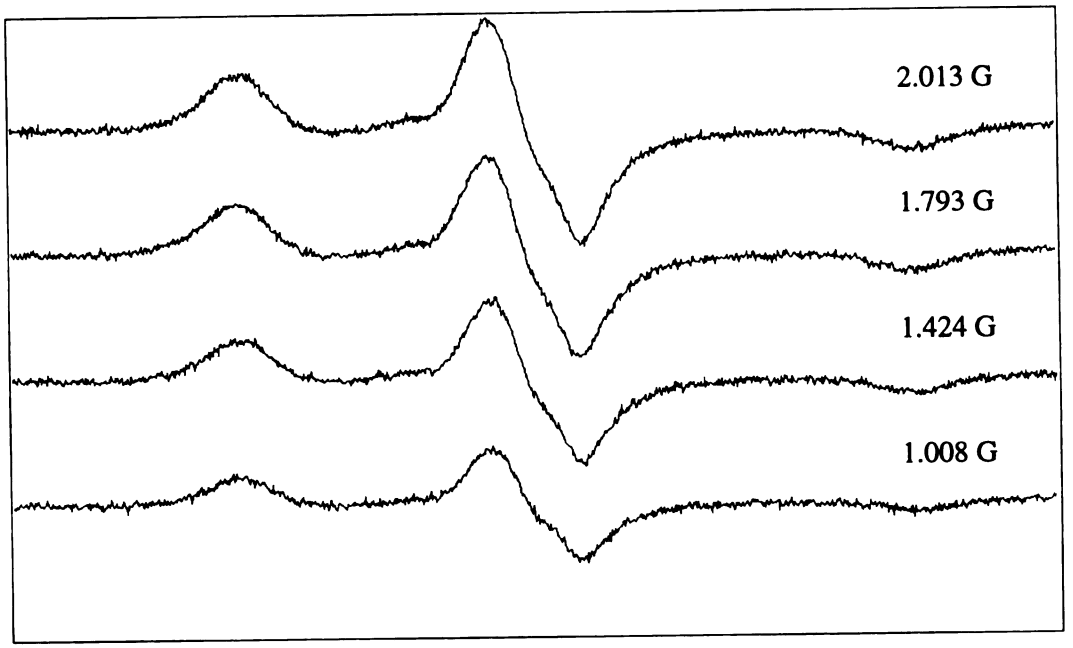
2.013 G
1.793 G
1.424 G
1.008 G

B

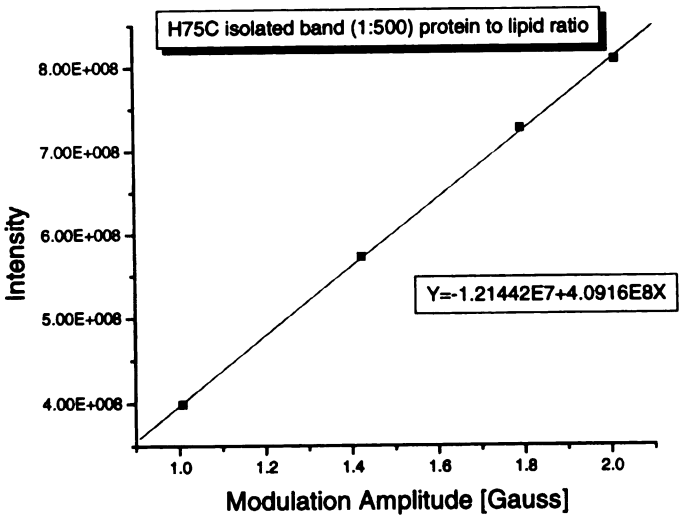
H75C isolated band (1:500) protein to lipid ratio
8.00E+008
7.00E+008
6.00E+008
5.00E+008
4.00E+008
Intensity
Y=-1.21442E7+4.0916E8X
1.0
1.2
1.4
1.6
1.8
2.0
Modulation Amplitude [Gauss]

## 2.6. Results and Discussions

To study the effect of oleic acid concentration on the incorporation yield of COX enzymes into the preformed liposome different amounts of oleic acid (0, 1.25, 2.47, 4.82, 9.2, 16.8, 28.8 and 44.7 % (w/w)) were added to DOPC: DOPS (7:3) molar ratio aliquots of lipids in chloroform and dried under the stream of nitrogen and hydrated in Tris buffer (pH=7.4). COX enzyme was added to the various samples of preformed liposomes. The molar ratio of protein to lipid was about 1/500 and the mixture was incubated for 20 minutes at 37 °C. The unincorporated protein was separated from the proteoliposomes using a Ficoll density gradient. The activity of the isolated proteoliposome band and the activity of the mixture of protein and liposomes before separation by density gradient was measured at 37 °C by observing the initial rate of oxygen consumption with an $O_2$ electrode. The concentration of lipid was determined by measuring the concentration of phosphorous. The incorporation yield was determined by dividing the total activity of the isolated band to the total activity of the protein and liposome mixture before separation by density gradient. Our results show that there is a significant increase in the incorporation yield upon adding the oleic acid. The optimum amount of oleic acid to yield the highest incorporation is between 4.8 and 9.2 % (w/w) (See table 2.1 and 2.2).

To examine the effect of the ratio of the protein to lipid on the incorporation yield of COX enzyme into preformed liposomes different protein to lipid ratios were used (1:250, 1:500 and 1:1000). 1:500 protein to lipid ratio gave the highest incorporation yield (data is not shown).

The incorporation efficiency and the specific activity of the incorporated hCOX-2 was studied using spin counting and electron paramagnetic resonance spectroscopy. In this experiment a single Cys mutant (H75C) of hCOX-2 was purified, spin labeled and incorporated into the liposomes. The total number of moles of spin labeled protein were counted in a sample before separation by density gradient and in an isolated proteoliposome band after density gradient. The incorporation yield was determined by dividing the total number of moles of protein in an isolated band to the total number of moles of protein in a protein and liposome mixture before separation by the density gradient. In another experiment the incorporation yield for H75C mutant into preformed liposomes was measured using an oxygen electrode as previously described. From the spin counting experiments the total amount of protein before Ficoll gradient and the amount of the protein in the isolated proteoliposome band after gradient were found to be 1.48E-7 mole and 8.037E-8 mole respectively. From the specific activity measurements the total amount of protein before Ficoll gradient and the amount of the protein in the isolated proteoliposome band after gradient were found to be 1.50E-7 mole and 8.369E-8 mole respectively. The spin counting experiment indicated 54% incorporation and oxygen assay experiment indicate 55% incorporation. These experiments show a good correlation between the two techniques.

These experiments also indicate that there is no significant change in the specific activity of the protein in the detergent versus the specific activity of the incorporated protein in the liposomes.

**Table 2.1.** The effect of oleic acid concentration on incorporation of hCOX-2 into preformed liposomes.

| % Oleic Acid in DOPC:DOPS (7:3) | % Protein Incorporated | Molar Ratio (Lipid:Protein) |
|---|---|---|
| 0 | 8.1 | 1810 |
| 1.25 | 37.5 | 1400 |
| 2.47 | 44.7 | 1300 |
| 4.82 | 42.6 | 1310 |
| 9.2 | 54.8 | 950 |
| 16.8 | 34.9 | 1450 |
| 28.8 | 23.5 | 1650 |
| 44.7 | 22.5 | 1650 |

**Table 2.2.** The effect of oleic acid concentration on incorporation of oCOX-1 into preformed liposomes.

| % Oleic acid in DOPC:DOPS (7:3) | % Protein Incorporated | Molar Ratio (Lipid:Protein) |
|---|---|---|
| 0 | 0 | NA |
| 1.25 | 37 | 1450 |
| 2.47 | 39 | 1580 |
| 4.82 | 51 | 810 |
| 9.2 | 53.8 | 1000 |
| 16.8 | 56.7 | 993 |

The liposomes (unilamellar vesicles and unilamellar vesicles) and proteoliposomes were extensively studied by transmission electron microscopy (TEM) and scanning electron microscopy (SEM).

Multilamellar and unilamellar vesicles can be generated by a variety of techniques, which lead to systems with differing lamellarity, size, trapped volume and solute distribution. The straightforward hydration of lipid to produce multilamellar vesicles (MLVs) results in systems, which exhibit low-trapped volumes. Figure 2.2 represents the negative stain electron micrograph of multilamellar vesicles. The onion layer structure of MLVs is clearly shown in this micrograph.

Unilamellar vesicles (ULVs) can be produced directly from MLVs by extrusion or sonication. Unilamellar vesicles were used as the artificial cell membrane models for protein incorporation in this dissertation. Figure 2.3 (B) represents the negative stain electron micrograph of unilamellar vesicles (ULVs). Figure 2.3 (A) shows the negative stain electron micrograph of isolated proteoliposome band and Figure 2.4 (B) is a scanning electron micrograph of isolated proteoliposomes band. Distributions of various liposome sizes were observed. The diameter of about 90 liposomes were measured. The average diameter was 100 $\pm$ 15 nm. Scanning electron microscopy reveals the 3-D structure of liposomes. Figure 2.4 (A) shows the 3-D spherical shape of the liposome.

In order to directly observe proteins in a proteoliposome, the hCOX-2 enzyme was gold labeled using a gold immunoprobe. Figure 2.5. shows the gold labeled proteins incorporated into a liposome. COX isozymes exist as dimer. Therefore there will be two gold labeled antibody per each molecule. However because of the resolution limitation it

is not possible to observe two particles per molecule. We believe that each black dot on the electron micrograph represents one protein molecule.

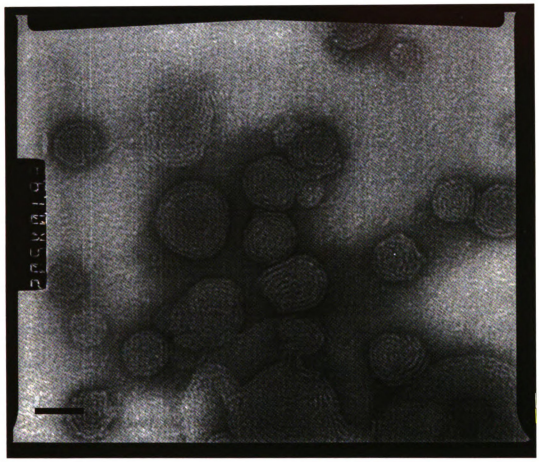

**Figure 2.2** Representative negative stain electron micrograph of multilamellar lipid membranes. (3:7 molar ratio of DOPS:DOPC and 9.2 % (w/w) oleic acid liposome was used).
Bar=48.8 nm
(Magnification =205,000)

**Figure 2.3**

A) Representative negative stain electron micrograph of proteoliposome (3:7 molar ratio of DOPS:DOPC and 9.2 % (w/w) oleic acid liposome was used).

Bar=150 nm

(Magnification = 67,000)

B) Representative negative stain electron micrograph of plain liposome (3:7 molar ratio of DOPS:DOPC and 9.2 % (w/w) oleic acid)

Bar=200 nm

(Magnification = 50,000)

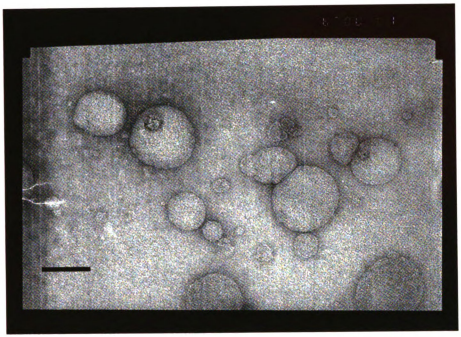

A

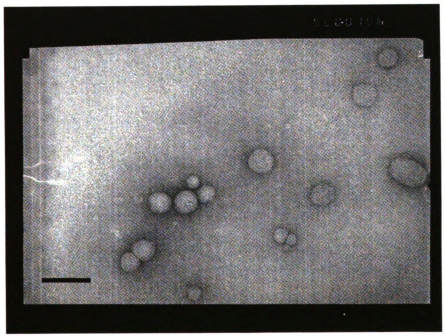

B

**Figure 2.4.**

A) Scanning electron micrograph of a liposome. The background of the picture is the gold plated cover slips.

B) Low magnification scanning electron micrograph of liposomes.

Bar= 250 nm

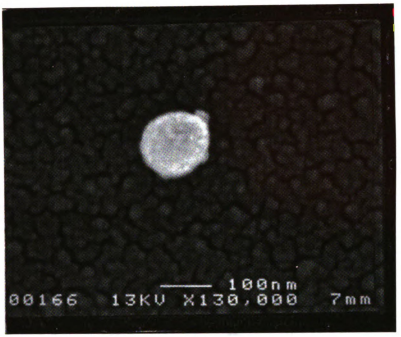


A

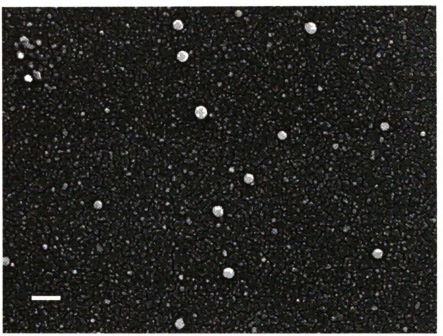

B

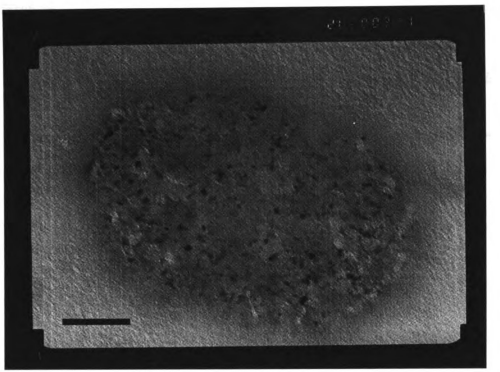

**Figure 2.5.** Representative negative stain electron micrograph of gold labeled proteins incorporated into a liposome (3:7 molar ratio of DOPS:DOPC and 9.2 % (w/w) oleic acid liposome was used).
Bar=50 nm

(Magnification = 200,000)

## 2.7. References


1. Bangham A.D., S., M.M, and Watkins, J.C. (1965) *Journal of Molecular Biology 13*, 238-52.

2. Kagawa, Y., and Racker, E. (1971) *Journal of Biological Chemistry 246*, 5477-&.

3. Rigaud, J. L., Levy, D., Mosser, G., and Lambert, O. (1998) *European Biophysics Journal with Biophysics Letters 27*, 305-319.

4. Rigaud, J. L., Pitard, B., and Levy, D. (1995) *Biochimica Et Biophysica Acta-Bioenergetics 1231*, 223-246.

5. Mateu, L., Caron, F., Luzzati, V., and Billecocq, A. (1978) *Biochimica Et Biophysica Acta 508*, 109-121.

6. Epand, R. M., Boni, L. T., and Hui, S. W. (1982) *Biochimica Et Biophysica Acta 692*, 330-338.

7. Epand, R. M., and Sturtevant, J. M. (1984) *Biophysical Chemistry 19*, 355-362.

8. Eytan, G. D., and Racker, E. (1977) *Journal of Biological Chemistry 252*, 3208-3213.

9. Navarro, J., Chabot, J., Sherrill, K., Aneja, R., Zahler, S. A., and Racker, E. (1985) *Biochemistry 24*, 4645-4650.

10. Greenhut, S. F., Bourgeois, V. R., and Roseman, M. A. (1986) *Journal of Biological Chemistry 261*, 3670-3675.

11. Szoka, F., and Papahadjopoulos, D. (1978) *Proceedings of the National Academy of Sciences of the United States of America 75*, 4194-4198.

12. Batzri, S., and Korn, E. D. (1973) *Biochimica Et Biophysica Acta 298*, 1015-1019.

13. Racker, E. (1979) *Methods of Enzymology 55*, 699-711.

14. Holloway, E. T., and Bohr, D. F. (1973) *Circulation Research 33*, 678-685.

15. Jain, M. K., and Zakim, D. (1987) *Biochimica Et Biophysica Acta 906*, 33-68.

16. http://www.nobel.se/.

17. Flegler S.L., H. J. W., and Klomparens K.L. (1993) *Scanning and transmission electron microscopy: an introduction*, W.H. Freeman, New York.

18. Hayat M.A. (2000) *Principles and Techniques of Electron Microscopy*, Cambridge University Press, Cambridge.

19. Laneuville, O., Breuer, D. K., Dewitt, D. L., Hla, T., Funk, C. D., and Smith, W. L. (1994) *Journal of Pharmacology and Experimental Therapeutics 271*, 927-934.

20. Singh, P. (2001) in *PCT Int. App. WO 2001041740*, USA.

21. New, R. R. C. (1990) *Liposomes a Practical Approach*, Oxford University Press, New York.

22. Ammon, R. H., K. (1936) *Z. physiol. Chem. 239*, 207-216.

23. Lowry, O. H. R., N.R.; Leiner, K. Y.; Wu, M.L.; Farr, A. L.,. (1954) *Ibid 207.*

24. Weil J.A., B. J. R., Wertz J.E. (1994) *Electron Paramagnetic Resonance*, John Wiley & Sons Inc., New York.

# Chapter 3

## Electron Paramagnetic Resonance Spectroscopy and Site Directed Spin Labeling

## 3.1. Abstract

Although the catalytic domain of COX isozymes has been extensively studied, very little is known about how the putative membrane binding domain of COX isozymes interacts with the lipid bilayers. X-ray crystallographic studies (*1*) have demonstrated that neither isozymes contain amino acid sequences of sufficient length and hydrophobicity to function as classical transmembrane domains. Instead, COX-1 and –2 are thought to associate with cellular membrane through a novel, monotopic membrane-binding domain that associates with a single leaflet of the lipid bilayer, which would allow orientation of residues in the COX-1 helices paralleled to the lipid/water interface of the membrane. The crystal structures of these isozymes can be used to predict how COXs interact with membranes, but more direct methods must be used to confirm or refute these predictions. Furthermore, it is not possible to orient the COXs in a membrane, or to determine lipid binding sites in the COXs from a crystal structure, as few lipid or detergent molecules are visible using X-ray analysis. The experiments outlined in this chapter were designed to begin mapping the topology of COX-membrane interactions. The results of the experiments in this chapter shall have general applicability to a new class of monotopically-associated peripheral membrane proteins. Squalene hopene cyclase is another monotopic membrane protein, the only other structurally characterized protein of this type (*2*).

Site-directed spin labeling (SDSL) is a powerful tool for determination of membrane protein structure and the topology of protein binding to the lipid bilayer (*3, 4*). The strategy of SDSL involves the introduction of a nitroxide side-chain at a selected site

in a protein. This is usually accomplished by cysteine substitution mutagenesis, followed by modification of the unique sulfhydryl group with a selective nitroxide reagent. Nitroxide scanning experiments provide sequence-correlated data that identify regular secondary structures and their orientation by virtue of periodicity in sequence position.

In this work, 25 mutant enzymes that contained single reactive cysteines substituted for amino acids within the hCOX-2 membrane-binding domain were constructed and spin labeled. The accessibility of each spin label to freely diffusing oxygen as a non-polar paramagnetic reagent and NiEDDA as a polar paramagnetic reagent was measured using power saturation EPR spectroscopy and the orientation of the membrane binding domain with respect to the lipid bilayer surface was determined.

Section 3.2 of this chapter will give an overview of various structural biology methods. In sections 3.3, 3.4 and 3.5, principles of EPR spectroscopy, the structure of the EPR spectrometer and resonators and the spectral properties of nitroxide free radicals will be discussed respectively. Section 3.6 will give a detailed description of the site directed spin labeling technique and finally in the last two sections of this chapter, 3.7 and 3.8, the experiments and the results will be discussed.

## 3.2. Structural Studies of Biomolecules

Structural biology is the science of biological phenomena at the molecular level. The task of explaining biological function at a molecular level requires knowledge of the composition and structure of the biological system. As genome research rapidly increases the number of proteins known, the requirement for obtaining structural information will

increase dramatically (*5*). The techniques used to gain structural information are physical chemistry methods that can be applied to biological problems. These techniques include X-ray diffraction, neutron diffraction, electron diffraction, nuclear magnetic resonance spectroscopy (NMR), electron paramagnetic resonance spectroscopy (EPR), fluorescence spectroscopy, Raman spectroscopy, infrared spectroscopy, ultraviolet spectroscopy, circular dichroism spectroscopy and X-ray absorption spectroscopy. Each physical method provides a different perspective of the system, and multiple methods are needed to achieve a full view.

In this present discussion, the following classes of techniques will be discussed: High (atomic) resolution techniques, low resolution techniques, and techniques using probes. High-resolution techniques use either X-ray crystallography or NMR and yield molecular structures at atomic resolution. Low resolution techniques, such as electron microscopy, atomic force microscopy and electron diffraction yields the overall shape of the biomolecule at less than atomic resolution. Techniques involving probes are fluorescence spectroscopy, spin label electron paramagnetic resonance spectroscopy and certain NMR isotopic labeling experiments. These techniques do not result in atomic resolution structure, but instead they yield information about specific parts of the biomolecule. For example, probes can be used to measure the distance between two parts of a complex, or to learn about the dynamics of specific parts of biomolecules.

X-ray crystallography and NMR spectroscopy are excellent techniques for providing high resolution structural information (*6, 7*). X-ray diffraction can yield interatomic distances for the form of the protein that is present in the crystal. When the sample is cryo- cooled, resolution for proteins may approach 0.9 Å. NMR can yield an

average solution structure or the structure in solid state based on multiple measurements of short (<5-6 Å) interproton distances. However they both have limitations. Both methods are limited by sample requirements. Many samples do not crystallize and even if they do, the crystal may not diffract well or their phases may not be solvable. NMR requires relatively concentrated samples of molecules that are small in molecular weight. Consequently, membrane proteins are difficult to study by either technique. Only very few membrane proteins structures have been solved by X-ray crystallography or solid state NMR (*8, 9*).

Because membrane proteins do not easily yield to crystallization or NMR, they have been studied using lower resolution methods. Electron diffraction, a technique that requires two-dimensional crystals, yields low resolution information in which helices can often be resolved. Furthermore, membrane proteins are well suited to study by electron diffraction (*10, 11*).

Electron microscopy provides a lower resolution structure without the need for two-dimensional crystals. High-resolution electron micrographs show the overall shape of molecules or complexes, but do not give atomic detail. Often, low-resolution data is complementary to high-resolution data. For instance, GroEL-GroES complexes were observed by electron microscopy before their crystal structures were solved. When the crystal structures of GroEL and GroES (*12-15*) were solved several years later, the electron micrographs were useful in defining how the two proteins interact.

The third class of biophysical techniques is those involving probes. For these methods, the biomolecules are labeled with an unnatural probe that slightly changes the molecular structure, and the probes are studied using spectroscopic methods. The

information that the probe yields is then used to make inferences about the structure, dynamics, or environment of the molecule. Advantages of probes are that they can simplify complicated systems, they do not require crystals, and often the sample quantity and concentration requirements are much lower than for other techniques.

In fluorescence labeling the distance between two fluorophores can be measured using Fluorescence Resonance Energy Transfer (FRET). This method is based on Föster energy transfer theory. One fluorophore, the donor, transfers the energy to the acceptor without emission of a photon. Fluorescence energy transfer can yield distances between naturally fluorescent sites or added labels if all of the angles that define the relative orientations of the axes of the donor and the acceptor are known or average values are assumed. Distances of up to 80 Å can be measured if suitable donors and acceptors are chosen (*16*).

Site directed spin labeling has emerged as a powerful technique for determining the structure of the biomolecules. By incorporating two spin labeled side chains, distances between elements of secondary structure can be determined by quantitation of spin-spin interaction between the nitroxide probes using EPR spectroscopy (*17*).

Exogenous spin labels have been routinely criticized as " perturbing" the "real" structure. Although researchers always have to be sensitive to the relationship between reality in living systems and their observations, spin labeling is not more perturbing than other physical methodologies. Any method that modifies the biomolecules with a probe is subject to the concern of whether the studied features of the biomolecule are significantly perturbed by the added probe. This is an important question also for X-ray crystallography, for example, when a heavy metal is added to aid in scattering, in

fluorescence labeling when a fluorescent label is attached and in spin labeling when a nitroxide spin label is attached. For the specific case of nitroxide spin labels, there have been several inquiries into the extent to which the label perturbs the structure of the proteins. Spin labels attached to three of the amino acids in myoglobin (His-12, Tyr-103, and Tyr-151) were shown not to affect the properties of heme or the conformation and stability of he protein (*18*). Similarly, studies of spin labeled T4 lysozyme have revealed minimal perturbation in the structure (*19*).

## 3.3. Principles of Electron Paramagnetic Resonance Spectroscopy

### 3.3.1. Zeeman Interaction

Electron paramagnetic resonance spectroscopy (EPR) is very similar in concept to nuclear magnetic resonance spectroscopy (NMR). Both deal with the interaction of the electromagnetic radiation with the magnetic moment. In the case of EPR, the magnetic moments arise from electrons, but in NMR the magnetic moments arise from nuclei. EPR spectroscopy is applicable to systems in a paramagnetic state. The paramagnetic state is a state having net electron spin angular momentum. The origin of EPR spectroscopy lies in the spin of the electron and its associated magnetic moment (μ). The component of electron magnetic moment along the direction of the external magnetic field (z-axis) is:

$$\mu_Z = -g_e \beta_e M_s \qquad 3.1$$

and, $\beta_e = \frac{eh}{4\pi m_e}$ where $m_e$ is the mass of electron and $g_e$ is the free electron g-factor and is equal to 2.0023 and $M_s = \pm\frac{1}{2}$.

In the absence of an external magnetic field, the energy levels of the magnetic moment are degenerate. In the presence of an external magnetic field, there is an interaction between the external magnetic field ($B_0$) and the magnetic moment ($\mu$), which is called the Zeeman interaction, and the energy levels will be separated. The Zeeman interaction energy for the electron is:

$$E = -(\mu_z)_e B_0 = g_e \beta_e B_0 M_s = \pm\frac{1}{2} g_e \beta_e B_0 \qquad 3.2$$

and in the similar manner for nuclei spin $\frac{1}{2}$, *e.g.* $^1$H, the Zeeman interaction energy is:

$$E = -(\mu_z)_n B_0 = -g_n \beta_e B_0 M_I = \pm\frac{1}{2} g_n \beta_n B_0 \qquad 3.3$$

and $\beta_n = \frac{eh}{4\pi m_p}$, where $m_p$ is the mass of proton and $M_I = \pm\frac{1}{2}$.

The ratio of the electron magnetic moment to the $^1$H magnetic moment is :

$$\frac{|\mu_e|}{|\mu_n|} = \frac{g_e m_p}{g_n m_e} = 659 \qquad 3.4$$

where for $^1H$, $g_n$ = 5.5857. Therefore the magnetic moment of the electron is 659 times larger than the magnetic moment of $^1H$ and also the gap between the energy levels for electron is 659 times larger than $^1H$. The transition energy between electron Zeeman energy levels is in the microwave frequency ($10^9$ Hz) range and for nuclear Zeeman energy level is in the radio frequency range ($10^6$ Hz)(*20*).

### 3.3.2. The Resonance Condition

In the presence of an external magnetic field the energy levels for an electron spin are separated. This separation increases linearly with $B_0$. It means that if the magnetic field is stronger, the separation between the two energy levels is more. If the energy of the microwave matches the difference between the two energy states, a transition in the population between the two energy levels happens and the spectra is obtained. The frequency for the microwave radiation is in the range of 1-100 GHz. The difference between the energy levels is expressed as:

$$\Delta E = h\nu = g_e \beta_e B_0 \qquad 3.5$$

where h is Planck's constant and ν is the resonance frequency. This equation describes the "resonance" condition for electron paramagnetic resonance spectroscopy.

Each molecule has a thermal energy equal to kT. At ambient temperature this energy is 208 $cm^{-1}$. The energy difference between the electron spin states is typically 0.3

$cm^{-1}$. Since the thermal energy of a molecule is more than the difference between the two energy levels, at ambient temperature the electron spins populate both energy levels.

Due to Boltzmann law:

$$\frac{N_u^e}{N_l^e} = \exp\frac{-(E_u - E_l)}{kT} = \exp\frac{-g_e\beta_e B_0}{kT} = \exp\frac{-0.3}{208} = 0.9986 \approx 1 \qquad 3.6$$

where $N_u^e$ is the number of electrons in the upper state and $N_l^e$ is the number of electrons in the lower state, k is the Boltzmann constant and T is the temperature in Kelvin.

After irradiating the molecule with microwave energy, there is a transition between the population of spins in the two energy levels. The net transition is from lower state to upper state. The spins do not remain in the excited state and after a brief time the spins emit their energy and return to the ground state. This is a spontaneous emission and the spins lose their energy, in other words, they exchange their energy with the surroundings, which is called lattice. The time that takes for the spins to transfer their energy to lattice and relax to the ground state is called $T_1$ or spin-lattice relaxation time.

In addition to spin-lattice relaxation, there is another phenomenon that describes an interaction between spins, called the spin-spin relaxation, $T_2$. The more efficient relaxation pathway will predominate over the other and will have the greatest affect on the EPR linewidth of the EPR absorbance. In solution, for an organic free radical such as the nitroxide free radical, the spin-lattice relaxation time is much greater than the spin-spin relaxation time. The reciprocal of the spin-lattice relaxation time, $1/T_1$, is very small

in comparison to the spin-spin relaxation time, $1/T_2$. So the spin-spin relaxation time determines the linewidth of the EPR spectrum. In these cases, the spin-spin relaxation time is defined by the central linewidth, $\Delta B$, in the first derivative spectrum (*20*).

$$\frac{1}{T_2} = (\frac{\sqrt{3}}{2})\Delta B \qquad 3.7$$

### 3.4. The Electron Paramagnetic Resonance Experiment

Most EPR spectrometers operate at a fixed frequency, usually in the microwave region, and the resonance condition is met by sweeping the applied magnetic field, $B_z$. The electron paramagnetic resonance spectrometer used throughout this study was operated with the microwave field at approximately 9.3E9 Hz, designated X-band, with the resonant field being approximately 3300 Gauss.

#### 3.4.1. The EPR Spectrometer

A simplified diagram of an EPR spectrometer is shown in Figure 3.1. During operation, the microwave energy from the klystron (A) travels down the wave conduit (B) into a resonator (C), containing the sample in a special cavity (D). The electromagnet (E) applies an external magnetic field (I) to the sample in order to create the excited and

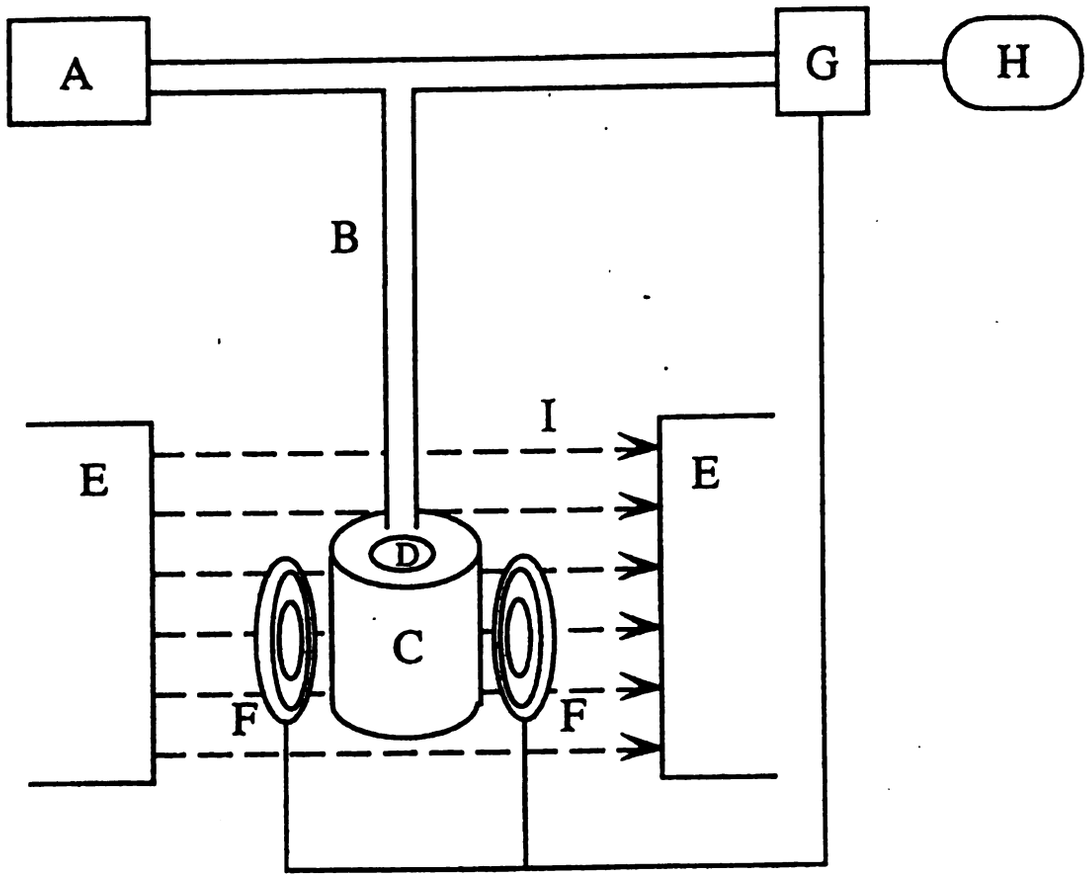


**Figure 3.1.** The EPR spectrometer

A: Klystron B: Wave guide conduit C: Resonator D: Sample cavity E: Electromagnet
F: Helmholtz coils G: Detector H: Computer I: Magnetic field.
Taken from (*21*)

ground spin states for the free radical electron. The microwave energy interacts with the sample and returns into the wave-guide. The microwave signal returning from the sample is routed by a circulator to a detector that measures its incident power. To enhance sensitivity, the magnetic field at the resonator is modulated by Helmholtz coils (F) to encode a new frequency of 100 kHz on any EPR absorption signals that may occur. The modulation amplitude must be kept below the linewidth of the EPR absorption in order to avoid linewidth distortion of these resonances in the derivative spectrum. The EPR signal is fed from the detector (G) to a 100 kHz lock in amplifier detection of the modulated signal. The modulated signal appears as the first derivative of the absorption spectrum and the signal is output to a computer or recording device (H).

### 3.4.2. The Loop-Gap Resonator

The resonator cavity is critical for determining EPR sample conditions and signal strength. The loop-gap resonator is shown in Figure 3.2. The microwave energy from the wave guide conduit (not pictured) reaches the resonator through the transmission line (A). The capacitance of the wire coupling loop (C) is adjusted with the coupling adjustment (B) in order to match the transmission line impedance to the impedance of the resonator circuit containing the sample tube in the sample cavity (D). The central core of the resonator is made of a ceramic material and coated with a thin layer of silver. The flux return loop (E) and the sample loop (G) are actually cylindrical holes bored in this ceramic material and connected by a narrow gap (F). The configuration of these loops and the thin gap between them is designed to optimize the magnetic component of the

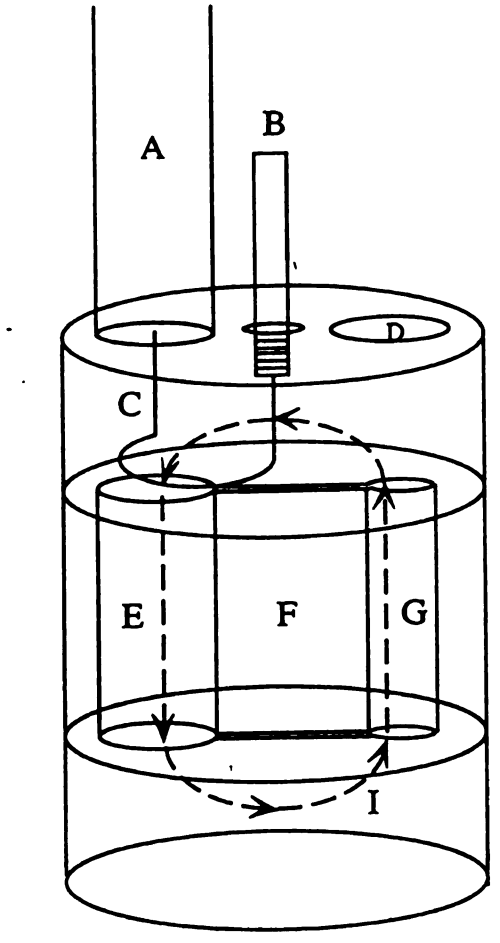


**Figure 3.2.** The two loop one gap resonator

A: Transmission line B: Coupling adjustment C: Wire coupling loop D: Sample cavity
E: Flux return loop G: Sample loop F: Gap.
Taken form (*21*)

microwave signal in the sample loop and minimize the electric component. This provides the highest possible microwave magnetic field (I) density across the sample cavity (22).

### 3.4.3. Rectangular Box Cavity (TE102)

TE102 resonator is the most commonly used EPR cavity. This resonator was used for the double site directed spin labeling studies on frozen samples (Chapter 4). Figure 3.3 shows the structure of this resonator. The sample is placed in the middle of the resonator where the magnetic field density is maximum and the electric filed density is minimum.

## 3.5. Nitroxide Free Radicals

Paramagnetic species are rarely found naturally, therefore to investigate biological phenomena using electron paramagnetic resonance, spectroscopists incorporated stable free radical spin probes into the biological system of interest. Site directed mutagenesis is used to substitute cysteine residues at specific amino acids of the interest and a sulfhydryl specific nitroxide spin label is attached to the mutated cysteine (Figure 3.4). A standard nitroxide free radical containing an $^{14}N$ nucleus will give a characteristic three line spectrum as seen with the 1-oxy-2,2,5,5-tetramethylpyrrolinyl-3-methyl)-methanethiosulfonate spin label (MTSSL). This structure is stabilized by the four adjacent methyl groups which exert a protective effect on the free radical and make this spin label, and ones like it, stable and inert.

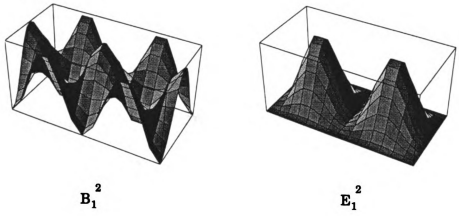


**Figure 3.3.** The structure of TE102 rectangular box cavity. The Picture was taken from ESP 300e EPR spectrometer manual.

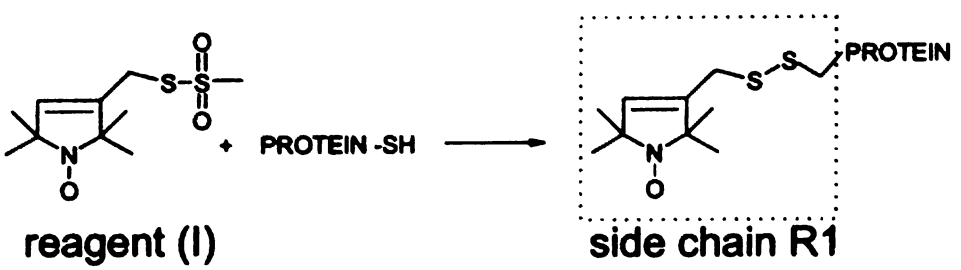


**Figure 3.4.** The methanethiosulfonate spin label (MTSSL) reacts exclusively with the free sulfhydryl group on the introduced cysteine residue. Taken form (*23*). Copyright permission was obtained.

Depending on the questions the investigator wishes to answer (s)he may choose one of several sulfhydryl-reactive label reagents that have been synthesized. Each of these reagents is usually composed of two functional parts: 1) a sulfhydryl reactive group that provides the means of attachment to a cysteine residue and 2) a nitroxide moiety. Variation in the means of attachment or in the geometry of the nitroxide group provides the researcher with many options to explore scientific questions.

The typical free radical spin probe has two resonance structures that contribute to the overall nitroxide structure (Figure 3.5). The resonance contributing form A that localizes the radical electron on the nitrogen also places a negative charge on the oxygen. Environments which stabilize the negative charge on the oxygen in this contributing form, such as polar solvents, would increase the unpaired electron density at the nitrogen and consequently increase the hyperfine coupling constant $a_0$ between the resonance induced by the nitrogen spin. This trend is observed in nitroxide spectra in solvents of varying polarity.

In addition, measurement of the three dimensional components of the hyperfine tensor indicate that the radical electron is located primarily along the molecular axis perpendicular to the plane of the three nitroxide bonds. The hyperfine tensor components are determined by examining the spectra of a nitroxide in a solid crystal under different magnetic field orientations. These values indicate that the electron primarily occupies a p orbital on the nitrogen atom oriented perpendicular to the nitrogen bond plane (*24*).

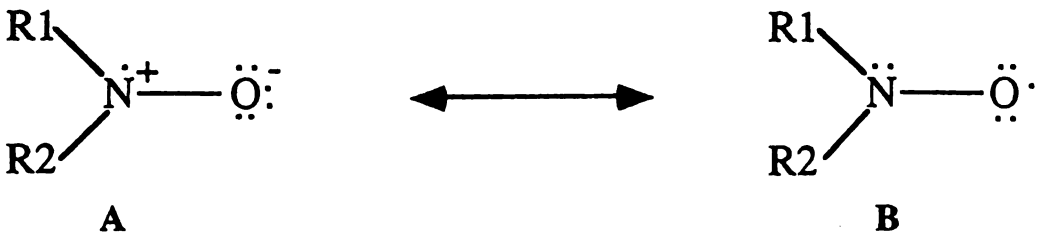


**Figure 3.5.** Two resonance structures of nitroxide

### 3.5.1. Nitroxide Radical Spectrum

The total Hamiltonian for a system with one electron and one $^{14}N$ atom is:

$$H = H_e + H_n + H_{HF} + H_Q \qquad 3.8$$

where $H_e$, $H_n$, $H_{HF}$ and $H_Q$ are electron Zeeman, nuclear Zeeman, hyperfine interaction and nuclear quadrupole interaction Hamiltonians respectively. For simplicity the effect of the nuclear quadrupole interaction in neglected.

$$H = g_e \beta_e B_0 S_z - g_n \beta_n B_0 I_z + hAS_z I_z \qquad 3.9$$

If the hyperfine interaction (A) is positive then the energy levels are:

$$\begin{aligned} E_1 &= \langle -\frac{1}{2}, 1 | g_e \beta_e B_0 S_z - g_n \beta_n B_0 I_z + hAS_z I_z | -\frac{1}{2}, 1 \rangle \\ E_1 &= -\frac{1}{2} g_e \beta_e B_0 - g_n \beta_n B_0 - \frac{1}{2} hA \\ E_1 &= -\frac{1}{2} h\upsilon_e - h\upsilon_n - \frac{1}{2} hA \end{aligned} \qquad 3.10$$

$$E_2 = \langle -\frac{1}{2}, 0 | g_e \beta_e B_0 S_z - g_n \beta_n B_0 I_z + hAS_z I_z | -\frac{1}{2}, 0 \rangle$$

$$E_2 = -\frac{1}{2} g_e \beta_e B_0 \qquad 3.11$$

$$E_2 = -\frac{1}{2} h\upsilon_e$$

$$E_3 = \langle -\frac{1}{2}, -1 | g_e \beta_e B_0 S_z - g_n \beta_n B_0 I_z + hAS_z I_z | -\frac{1}{2}, -1 \rangle$$

$$E_3 = -\frac{1}{2} g_e \beta_e B_0 + g_n \beta_n B_0 + \frac{1}{2} hA \qquad 3.12$$

$$E_3 = -\frac{1}{2} h\upsilon_e + h\upsilon_n + \frac{1}{2} hA$$

$$E_4 = \langle \frac{1}{2}, -1 | g_e \beta_e B_0 S_z - g_n \beta_n B_0 I_z + hAS_z I_z | \frac{1}{2}, -1 \rangle$$

$$E_4 = \frac{1}{2} g_e \beta_e B_0 + g_n \beta_n B_0 - \frac{1}{2} hA \qquad 3.13$$

$$E_4 = \frac{1}{2} h\upsilon_e + h\upsilon_n - \frac{1}{2} hA$$

$$E_5 = \langle \frac{1}{2}, 0 | g_e \beta_e B_0 S_z - g_n \beta_n B_0 I_z + hAS_z I_z | \frac{1}{2}, 0 \rangle$$

$$E_5 = \frac{1}{2} g_e \beta_e B_0 \qquad 3.14$$

$$E_5 = \frac{1}{2} h\upsilon_e$$

$$E_6 = \langle \frac{1}{2}, 1 | g_e \beta_e B_0 S_z - g_n \beta_n B_0 I_z + hAS_z I_z | \frac{1}{2}, 1 \rangle$$

$$E_6 = \frac{1}{2} g_e \beta_e B_0 - g_n \beta_n B_0 + \frac{1}{2} hA \qquad 3.15$$

$$E_6 = \frac{1}{2} h\upsilon_e - h\upsilon_n + \frac{1}{2} hA$$

The hyperfine interaction is larger than the nuclear Zeeman interaction. The energy level diagram is shown in Figure 3.6. The EPR transitions are governed by the selection rules $\Delta m_s = \pm 1$ and $\Delta m_I = 0$.

### 3.5.2. The Spectrum of the Non-Oriented Systems (Solid Phase)

The EPR spectra of spin labels in solid phase can be described by this Hamiltonian:

$$H = \beta_e B_0 \cdot g_e \cdot S - g_n \beta_n B_0 \cdot I + S \cdot A \cdot I \qquad 3.16$$

$g_e$ is the electronic Zeeman interaction matrix, $g_n$ the nuclear g-factor, $B_0$ is the external magnetic field, $S$ and $I$ the electron and nuclear spin operators, respectively, and $A$ the electron nucleus hyperfine interaction matrix. The principle axes of the $g_e$ matrix defining field orientation are shown in Figure 3.7, with the x-axes lying along the N-O bond, z-axis parallel to the nitrogen, $2p_z$ orbital and the y-axis perpendicular to the x,z-plane.

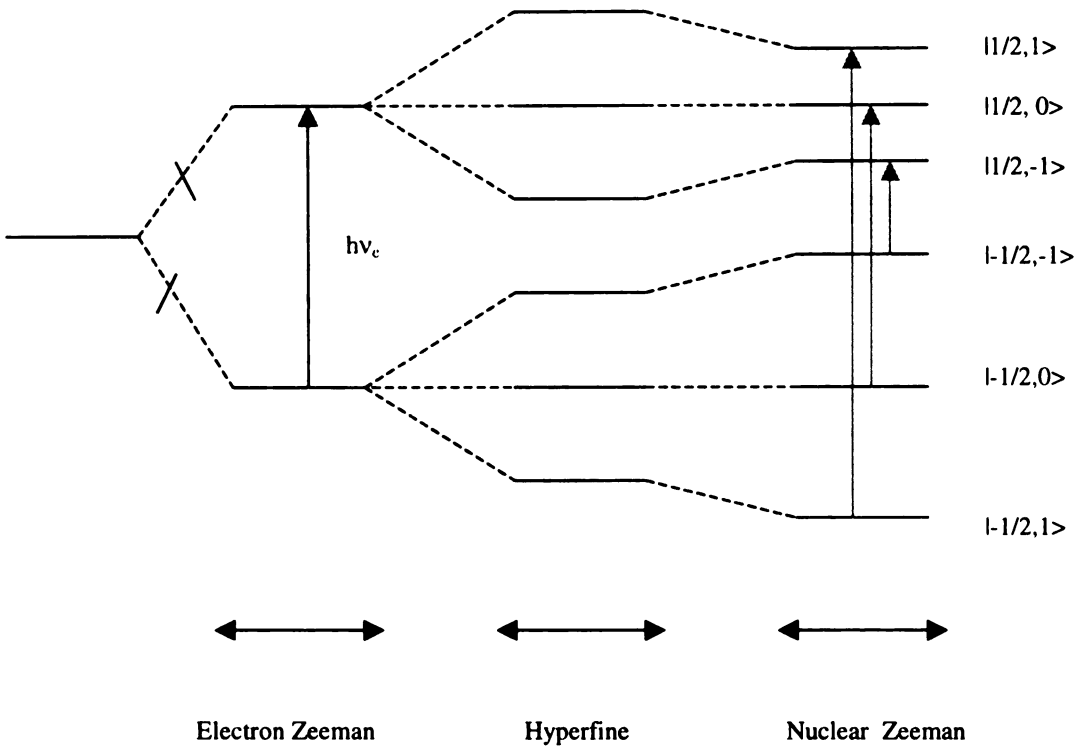


**Figure 3.6.** The energy level diagram for a system with one electron and one $^{14}N$ atom.

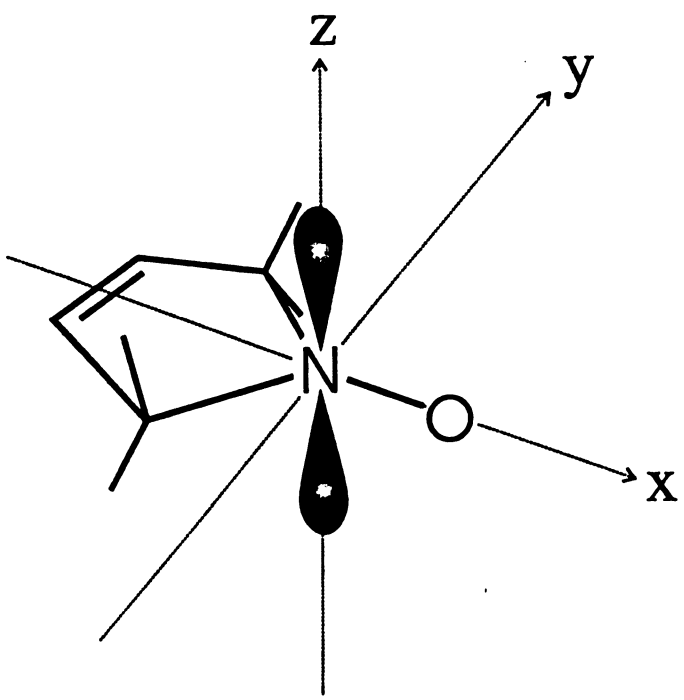


**Figure 3.7.** Principle axes of the $g_e$ matrix of nitroxide spin label. Taken from (*25*)

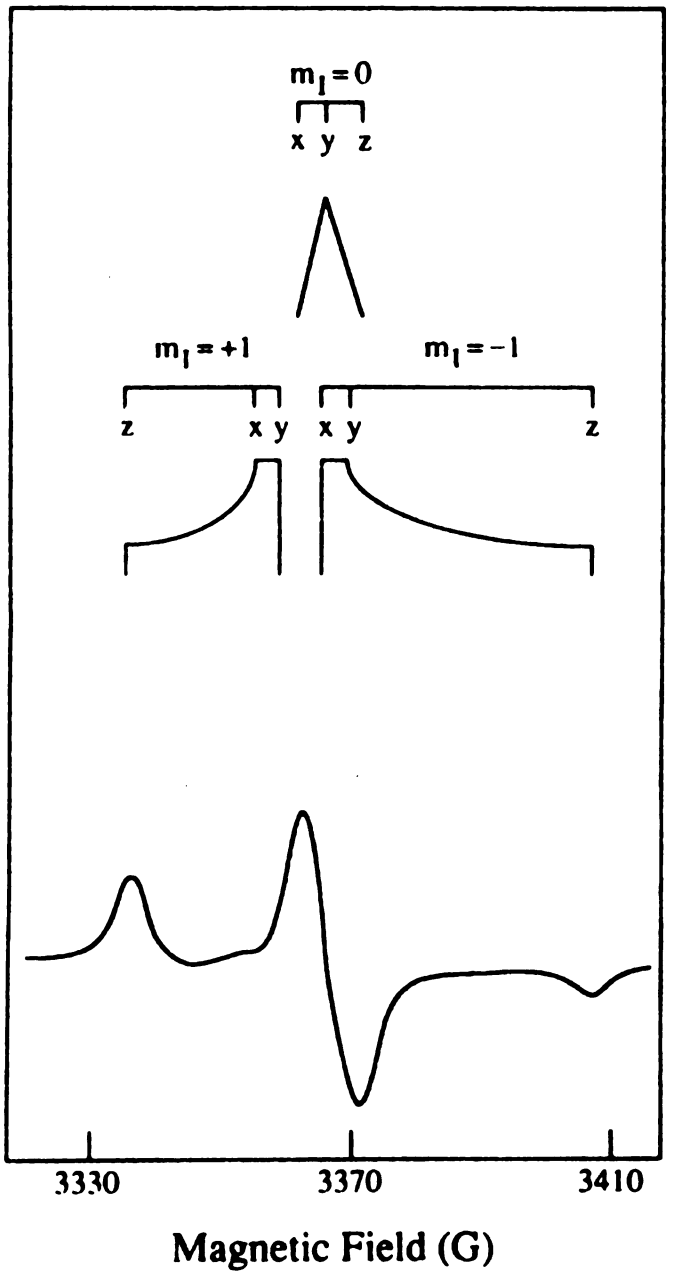


**Figure 3.8.** Schematic diagram of the rigid limit EPR powder pattern of MTSSL.

Taken from (*26*). Copyright permission was obtained.

In Figure 3.8, the EPR spectrum of a spin labeled sample at low temperature (solid phase) is shown. The EPR spectrum is equivalent to a powder in the rigid limit of polycrystalline sample. The spectrum is composite of spectra of molecules differing by their projection of the $^{14}N$ nuclear moment into the external magnetic field $B_0$ designated by the values of $m_I = +1$, 0 and $-1$. $^{14}N$ hyperfine contribution to the spectrum produce three step shoulders at magnetic fields $B_z = \frac{h\upsilon - m_I A_z}{g_z \beta_e}$ and six divergences at $B_{x,y} = \frac{h\upsilon - m_I A_{x,y}}{g_{x,y} \beta_e}$ (*24*).

### 3.5.3. Spectral Anisotropy

In a nitroxide radical, the unpaired electron is localized to a p-type orbital that is not spherically symmetric. In this situation, interactions between the unpaired electron and the nitrogen nucleus and between the unpaired electron and the applied magnetic field are sensitive to the orientation of the molecule relative to the applied field. In other words, the position of the resonant field (g-value) and the magnitude of the hyperfine splitting (A-value) are dependent on the orientation of the magnetic field relative to the nitroxide molecular axes. Using a Cartesian coordinate system, the principle axes for the nitroxide are diagramed in Figure 3.7. The z-axis is defined by the nitrogen 2p$\pi$-orbital that is associated with the unpaired electron and the x-axis is defined by the NO bond. The y-axis is orthogonal to the x and z-axes. The molecular coordinate system for the nitroxide is used to define the direction of the applied magnetic field relative to the

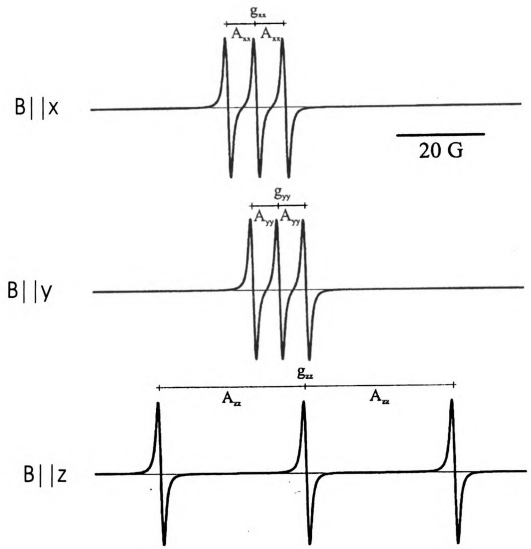


**Figure 3.9.** Orientation dependence of the EPR spectrum of a nitroxide. Simulated spectra of a monocrystal sample with the external magnetic field B directed along the principle axes of **g** and **A** tensors. Taken from (*25*)

nitroxide. The orientation-dependent effect of the nitroxide g- and A- values relative to the applied magnetic field is diagramed in Figure 3.9, which shows the spectra for a nitroxide in a highly ordered crystal that is oriented such that the applied magnetic field is parallel to each of the principle molecular axes, as noted in the figure. To described the anisotropic nature of g and a, they may be characterized by second-rank tensors, **g** and **A**. These tensors are diagonal in the nitroxide molecular axis system with principle values: $g_{xx}$, $g_{yy}$, $g_{zz}$, and $A_{xx}$, $A_{yy}$, $A_{zz}$. The magnetic interactions between an applied magnetic field and the unpaired electron for any other nitroxide orientation can be described by arithmetic combinations of the principle values. As can be seen in Figure 3.9, the nuclear hyperfine coupling is maximal when the $2p\pi$ orbital is parallel to the applied magnetic field, leading to $A_{zz}$ having the largest splitting values. As will be seen in section 3.5.4, the above anisotropies may be partially or totally averaged if molecular motion is rapid relative to the EPR timescale.

### 3.5.4. The Effect of Nitroxide Motion on EPR Lineshapes

Extraction of motional data from the EPR spectra of nitroxides is arguably the most widespread use for spin labels. An EPR spectrometer has an effective time interval for collecting data ($1/\nu$). If molecular motion is much faster than $1/\nu$, all of the spectral anisotropies will be averaged and single g- and A- values will be observed. Nitroxide attached to macromolecules are usually characterized by longer rotational correlation times where averaging of the **g** and **A** anisotropies is incomplete. These effects are

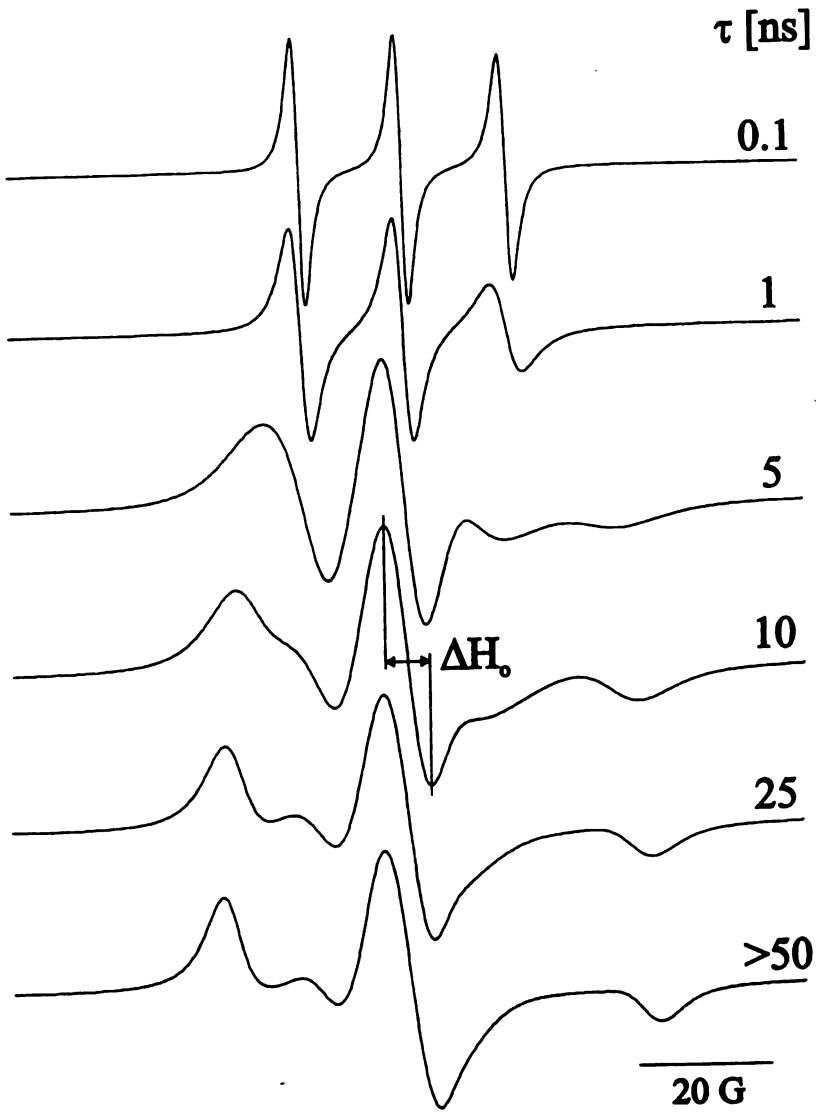


**Figure 3.10.** Motion dependence of the EPR spectrum of a nitroxide. Simulated spectra of a nitroxide tumbling in solution with the rotational correlation time τ. No significant changes in the spectral line shape are observed at τ exceeding 50 ns. Taken from (*25*).

illustrated in Figure 3.10, which demonstrates the correlation between the rate of isotropic nitroxide tumbling and the resulting EPR spectra. For an ensemble of nitroxides with very fast reorientation rates, all of the spectral anisotropies will be averaged and single g- and A- values will be observed. This is the case for the spectrum at the top of Figure 3.10, where the correlation time for the nitroxide is less than 0.1 ns. However, if molecular motion is slow relative to the above criteria (bottom spectrum in Figure 3.10), the nitroxide will appear to be motionless and the resulting spectrum is what one would expect from the superposition of spectra from a sample of nitroxides frozen in all possible orientations, often referred to as a 'powder spectrum'. For intermediate amounts of motion, various degrees of averaging will be observed (middle spectra in Figure 3.10). The spectra in Figure 3.10 represent simple isotropic tumbling. However, in biological systems, nitroxide motion is often anisotropic. In these situations, the principle **g** and **A** tensors are not averaged equally. Nitroxide motion at any particular site is directly related to its local environment and is reflected in its EPR spectrum.

The mobility of a nitroxide side chain depends on the structural features of its local environment. One of the goals of SDSL is to relate the EPR spectrum for a nitroxide side chain to its motion, and thus, to the structure of its local environment. This information is readily achievable at a semi-quantitative level. For example, a convenient measure of motion is the peak-to-peak first derivative width of the central ($m_I$=0) resonance ($\Delta B_0$ also known as $\Delta H_0$ in Figure 3.10). The numerical value for $\Delta B_0$ is primarily dependent on the degree of averaging of the anisotropic **g** tensor. Structure-dependent variations in $\Delta B_0$

have been employed to map topology in many proteins by simple distinction between buried and surface sites.

The ability to correlate a nitroxide's EPR lineshape with its motion and then to correlate that motion to a specific structural environment is one of the primary goals in SDSL studies. A nitroxide side chain motion is the result of three contribution factors: 1) $\tau_R$, the rotational correlation time for the entire protein; 2) $\tau_B$, the effective correlation time due to local backbone flexibility; 3) $\tau_S$, the effective correlation time due to isomerizations about the bonds that link the nitroxide to the backbone. The resulting EPR spectrum reflects the sum of each of these contributions. Therefore, how local structure contributes to each of these is a subject of great interest for spin labeling studies (*27, 28*).

### 3.6. Accessibility Determination Using Power Saturation

A significant amount of information about a protein's structure can be derived from the degree of solvent exposure of its side chains. A nitroxide side chain introduced at any region of interest can report on solvent exposure using the power saturation technique. The technique exploits changes in $T_1$ relaxation pathways by Heisenberg spin exchange with diffusible, fast-relaxing paramagnetic species. The rate of exchange is proportional to the frequency of encounters and thus the degree of side chain exposure. A brief introduction to the physical nature of this phenomenon and its experiment utility in spin-labeling studies is described below.

### 3.6.1. Continuous Wave Saturation EPR (CWS-EPR)

CWS-EPR is one of the methods to measure the $T_1$. CWS-EPR can be performed on a conventional EPR spectrometer, preferably fitted with a loop-gap resonator. The loop-gap resonator is a recent development and is important in that it provides a sufficient microwave energy density to saturate the nitroxide resonance.

A convenient experimental parameter determined from CWS-EPR is $P_{1/2}$. $P_{1/2}$ is the microwave power required to saturate the signal to one-half the amplitude it would have if it did not saturate at all. Changes in the $P_{1/2}$ are related to the exchange rate ($W_x$):

$$\Delta P_{1/2} = P_{1/2} - P_{1/2}^0 \propto \frac{1}{T_1 T_2} - \frac{1}{T_1^0 T_2^0} \approx \frac{1}{T_2^0}\left(\frac{1}{T_1} - \frac{1}{T_1^0}\right) = \frac{2W_x}{T_2^0} \qquad 3.17$$

As indicated, this relationship is approximate and assumes that $T_2$ is independent of the exchange rate. This is generally the case for nitroxides on membrane-bound proteins where $T_2$ is much less than $T_1$ and also the concentration of the exchange reagent is such that $W_x \ll \frac{1}{T_2}$.

The amplitude of an EPR signal is proportional to the square root of the microwave power. Also, the amplitude of the signal is a linear function of the square root of the power:

$$A = N\Lambda P^{1/2} \qquad 3.18$$

where $A$ is the peak to peak amplitude, $N$ is the normalization factor, $\Lambda$ is the instrumental calibration factor. So, by increasing the power, a signal with larger amplitude is obtained.

For higher microwave powers the amplitude of the signal is not a linear function of the square root of the power and the equation in modified to:

$$A = \frac{N\Lambda P^{1/2}}{S^{3/2}} \qquad 3.19$$

where $S = 1 + \Lambda^2 P \gamma^2 T_1 T_2$ and $\gamma$ is the magnetogyric ratio given by $\gamma = \frac{2\pi g_0 \beta_e}{h}$.

The value of $P_{1/2}$ is found from the intersection of $A = \frac{N\Lambda P^{1/2}}{S^{3/2}}$ and $A = \frac{N\Lambda P^{1/2}}{2}$ (Figure 3.11):

$$P_{1/2} = \frac{(2^{2/3} - 1)}{\Lambda^2 \gamma^2 T_1 T_2} \qquad 3.20$$

and substituting this equation in 3.19 gives:

$$A = \frac{N\Lambda P^{1/2}}{[1+(2^{2/3}-1)P/P_{1/2}]^{3/2}} \qquad 3.21$$

Equation 3.21 can be modified as:

$$A = \frac{IP^{1/2}}{[1+(2^{1/\varepsilon}-1)P/P_{1/2}]^{\varepsilon}} \qquad 3.22$$

where $I = N\Lambda$ and $\varepsilon = 3/2$.

$\varepsilon$ is an adjustable parameter and measures the homogeneity of the saturation of the resonance line. For the homogeneous and inhomogeneous saturation limits, $\varepsilon = 1.5$ and $\varepsilon = 0.5$ respectively. Under the nitrogen (in the absence of any other paramagnetic relaxers) $\varepsilon$ is always very close to 1.5 and indicates the homogeneous saturation (*29, 30*).

### 3.6.2. Site-Directed Spin Labeling

Eduard G. Rozantsev and Harden M. McConnell are the two pioneers in the spin labeling technique who contributed seminally to this branch of science. Eduard Rozantsev developed a broad range of nitroxyl compounds and reagents and Harden McConnell's foresight into the areas of biological structure and function brought the

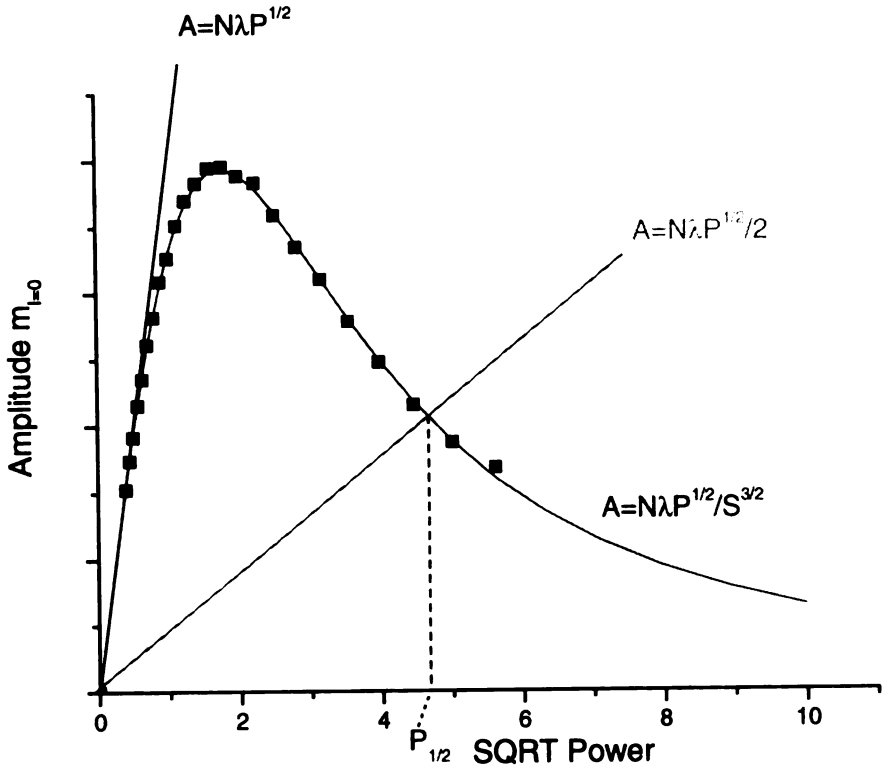


**Figure 3.11.** A typical power saturation curve

world the broad leadership that guided this technique to where it is today. McConnell's lab was located in the Physical Chemistry Laboratories of the Department of Chemistry at Stanford University, where his research prior to that point had been heavily involved in areas of chemical physics, solid-state physics, and theoretical aspects of spin physics. Rozantsev's lab, then at the Institute of Chemical Physics, USSR Academy of sciences, Moscow, was publishing extensively on the chemistry, synthesis and physical chemistry of broad range of nitroxyl compounds (coined iminoxyl at the time). Rozantsev's research was published mainly in Russian academy journals. Since it was difficult to obtain samples from " behind the iron curtain", a major synthetic effort was launched in the McConnell lab to reproduce compounds synthesized in the Rozantsev's lab and to develop analogues of protein modification reagents.

Site directed spin labeling (SDSL) consists of

a) Manipulating the system of interest so that it contains a single reactive amino acid residue or in the case of double site directed spin labeling (DSDSL) two reactive amino acid residues, usually a cysteine, that may be selectively modified with an appropriate spin label usually a sulfhydryl specific nitroxide reagent.
b) Selectively labeling the site
c) Examining the functional viability of the mutants, preferably before and after spin labeling.
d) Characterizing the spin-labeled site by a variety of EPR techniques.

This approached was first introduced by Wayne Hubbell (a former student of Harden McConnell), who recognized that the rapid advancement in the site-directed mutagenesis could solve a problem that had plagued spin labeling since its inception- the lack of

proteins containing unique reactive cysteines. Indeed its relatively low abundance makes cysteine the residue of choice in SDSL studies (*24*).

### 3.6.3. The Theory of Site-Directed Spin Labeling

The small molecules in a membrane/water system are partitioned between the water and the fluid hydrophobic phase of the bilayer according to their polarity. Polar molecules preferentially partition into the aqueous phase, and the non-polar molecules preferentially partition into the membrane phase. The bilayer interior is non-uniform with gradients of the polarity and fluidity along the direction of the bilayer normal. Thus, there are expected to be gradients in both concentration and diffusion coefficient of small molecules in equilibrium with the aqueous phase.

According to Henry's law:

$$C_{i,m}(x) = C_{i,w} \exp(\frac{\mu_{i,w}^0}{RT}) \exp(\frac{-\mu_{i,m}^0}{RT}) \qquad 3.23$$

where $C_{i,m}(x)$ is the concentration of species $i$ in the bilayer at the distance x from the interface, $C_{i,w}(x)$ is the uniform concentration of neutral species $i$ inside the water and membrane respectively.

The nitroxide attached to the protein are expected to have a depth-dependent collision rate with a paramagnetic reagent in the membrane.

The Heisenberg exchange rate $W_x$ with a hydrophobic reagent that freely diffuses into the lipid phase is proportional to collision rate and is expressed as:

$$W_x = 4\pi\rho g d D_m(x) C_m(x) \qquad 3.24$$

where $\rho$ is the exchange probability and is equal to 1, g is the steric factor, d is the collision diameter, $D_m(x)$ is the position-dependent relative diffusion coefficient and $C_m(x)$ is the position-dependent concentration given by equation 3.23.

According to equation 3.17,

$$P_{1/2} - P_{1/2}^0 = \Delta P_{1/2} \propto \frac{W_x}{T_2} \qquad 3.25$$

where $P_{1/2}$ and $P_{1/2}^0$ are the value in the presence and absence of the paramagnetic reagent.

From equations 3.23-25, it follows that the logarithm of the ratio of saturation is directly related to the difference in standard state chemical potentials of reagents at any depth, since $T_2$ cancels out.

$$\Phi = \ln[\frac{\Delta P_{1/2}(1)}{\Delta P_{1/2}(2)}] = \frac{-[\mu_1^0(x) - \mu_2^0(x)]}{RT} + cons \qquad 3.26$$

Usually compound 1 is the paramagnetic molecule, which can easily diffuse inside the membrane (*e.g.* $O_2$) and compound 2 is the paramagnetic molecule which can easily diffuse in the water and not inside the membrane (*e.g.* NiEDDA, NiAA, $CrOx^{-3}$).

To obtain equation 3.26, it is assumed that $T_2$ is independent of the rate of exchange, an approximation and it is desirable to make $\Delta P_{1/2}$ independent of $T_2$. Since the peak to peak first derivative line width $\Delta B$ is proportional $\frac{1}{T_2}$ then a quantity $\Delta P'_{1/2}$ is defined as:

$$\Delta P'_{1/2} = \frac{\Delta P_{1/2}}{\Delta B} \propto W_x \qquad 3.27$$

$\Delta P'_{1/2}$ is independent of $T_2$, but it depends on the Q factor of the resonator used in the EPR spectrometer. To obtain a quantity independent of this factor, dimensionless accessibility parameter, $\Pi$ is defined

$$\Pi = \frac{\Delta P'_{1/2}}{P'_{1/2}(DPPH)} \qquad 3.28$$

where $P'_{1/2}(DPPH)$ is the value determined for a sample of crystalline 2,2-diphenyl-1-picrylhydrazyl.

In Figure 3.12 model helices with different topographies and corresponding idealized behavior of accessibility parameter $\Pi$, is shown.

### 3.7. Materials and Methods

**Material.** The nitroxide spin label (1-oxyl-2,2,5,5-tetramethylpyrroline-3-methyl)-methanethiosulfonate (MTSSL) was purchased from Reanal Fine Chemical (Budapest, Hungary). NiEDDA was prepared as follows: equimolar amounts of $Ni(OH)_2$ (464 mg) and EDDA (881 mg) were mixed in 100 ml of 50% methanol in water. The mixture was stirred for 24 hr at room temperature and an additional 24 hr at 60°C. The resulting blue solution was filtered, and the solvent was evaporated to give 1.12 g of a blue powder. Mass spectroscopy showed 1 peak at 231 Da (molecular ion $[NiEDDA - 1H]^-$).

**Sample preparation.** Protein expression, purification and reconstitution into the liposomes were described in chapter 2.

**Spin labeling.** The purified single cysteine mutant of COX-2 (4 mg/ml) was incubated in a 20-fold molar excess of MTSSL overnight at 4°C. Unreacted spin labels were removed by dialysis. Dialysis was performed at 4°C against 4 liter of liposome buffer (25 mM Tris-Cl and 50 mM KCl pH=7.4) using Slide-A-Lyzer® with 10,000 molecular weight cut off (Pierce, Rockford, Illinois). The dialysis buffer was changed 4 times every 6 h. The spin labeled protein was concentrated to 15-20 mg/ ml.

**CW EPR power saturation measurements**: Continuos wave (CW) EPR spectroscopy was performed on a Bruker ESP 300E spectrometer at room temperature (23±2 C)

equipped with a two loop one gap resonator (Medical Advances, Milwaukee, Wisconsin). Samples were loaded into a gas permeable TPX capillary (Jagmar Ltd., Krakpw, Poland) with total volume of 4 µl. Power saturation experiments were carried out using 2 Gauss modulation amplitude and varying microwave power (typically 0.1-36 mW). The scan range of all spectra was 100 Gauss and the final spectra was obtained by signal averaging 8, 16 or 32 scans using the digitizer. The peak to peak amplitude of the first derivative $m_{I=0}$ resonance line (A) was measured and plotted against the square root of the incident microwave power. The data points were then fit to the expression:

$$A_{pp}(0) = \frac{IP^{1/2}}{\left[1+(2^{-\varepsilon}-1)\,P/P_{1/2}\right]^{\varepsilon}}$$

using Microcal Origin ® (Microcal Software, Inc., Northampton, Massachusetts). Here $I$ is a scaling factor, $P_{1/2}$ is the microwave power required to reduce the resonance amplitude to half of its unsaturated value, and $\varepsilon$ is a measure of the homogeneity of the saturation of the resonance. In this fit, $I$, $\varepsilon$ and $P_{1/2}$ are adjustable parameters and yield a characteristic $P_{1/2}$. Values for $P_{1/2}$ are then generated for each sample under three different conditions: (1) equilibrated with nitrogen; (2) equilibrated with 20% oxygen (air); and (3) equilibrated with nitrogen in the presence of 50 mM NiEDDA. The proteoliposome samples were added to a freeze-dried aliquot of NiEDDA. From these values of $P_{1/2}$, a collision parameter for $O_2$ ($\Pi^{oxy}$) was determined according to

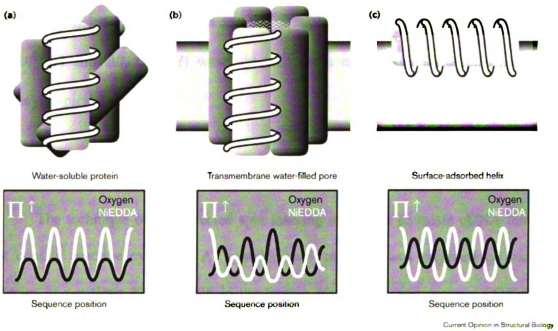


**Figure 3.12.** Model helices and idealized behavior of the accessibility parameter. Taken from (*23*). Copyright permission was obtained.

$$\Pi^{oxy} = \frac{\Delta P'_{1/2}(O_2)}{P'_{1/2}(DPPH)} = \frac{[P_{1/2}(O_2) - P_{1/2}(N_2)]/\Delta B_{pp}}{P_{1/2}(DPPH)/\Delta B_{pp}(DPPH)}$$

$\Delta B_{pp}$ is the peak-to-peak line width for the central resonance of the EPR spectra. A similar expression can be written for $\Pi^{NiEDDA}$, the collision parameter for NiEDDA. $P_{1/2}(DPPH)$ and $\Delta B_{pp}(DPPH)$ were obtained for a crystal sample of DPPH (α, α'-diphenyl-β-picrylhydrazyl).

### 3.8. Results

The technique of site-directed spin labeling requires a template cDNA that does not contain reactive cysteines. A "cysteine-less" template was prepared by mutating cysteins at positions 229 and 526 in the human histidine-tagged enzyme COX-2. The cysteine-less template retained 70% of the cyclooxygenase and peroxidase activities of the native Histidine-tagged COX-2, indicating that cysteins 299 and 526 are not required for catalysis and that these substitutions only minimally distort the structure of the protein.

Four helices (A-D) form the membrane-binding domain in the mouth of the cyclooxygenase active sites. Helices A, B and C were studied by site directed spin labeling in this chapter. By using the cysteine-less template, 25 single cysteine mutants were constructed (Table 3.1). The histidine-tagged mutant proteins were expressed in *sf-21* cells using baculovirus constructs and purified using nickel affinity chromatography as described in detail in chapter 2. All of the single cysteine mutants retained significant

cyclooxygenase activities (10-70% of the native). Conjugation of the cysteines with the spin label MTSSL had no effect on cyclooxygenase activity. These results demonstrated that the cysteine substitutions and subsequent conjugation with the spin label did not grossly disrupt the native structure of the enzyme.

Each of the 25 single mutant proteins were purified, spin labeled and concentrated to ≈20 mg/ml (≈280 μM) and incorporated into preformed liposomes. The unincorporated protein was separated from the proteoliposomes using a Ficoll density gradient. The proteoliposomes were concentrated using ultracentrifugation. The proteoliposomes were loaded into a gas permeable TPX capillary with total volume of 4 μl. Continuous wave (CW) EPR spectroscopy was performed on a Bruker ESP 300E spectrometer at room temperature (23±2 °C) equipped with a two loop one gap resonator. Power saturation experiments were carried out using 2 Gauss modulation amplitude and varying microwave power (typically 0.1-36 mW). The scan-range of all spectra was 100 Gauss. The noise level of each spectrum was filtered using Bruker's WinEPR software. (See Appendix A). The peak to peak amplitude of the first derivative $m_{I=0}$ resonance line (A) was measured and plotted against the square root of the incident microwave power. The data points then were fit to the following equation:

$$pp(0)=I\sqrt{P}\left[1+(2^{-\varepsilon}-1)\frac{P}{P_{1/2}}\right]^{-\varepsilon}$$

Values for $P_{1/2}$ are then generated for three different samples of each mutant: 1) The spin labeled proteoliposome equilibrated with nitrogen; 2) The spin labeled proteoliposome

**Table 3.1.** Relative cyclooxygenase activities of the single substituted *h*COX-2 cysteine mutants.

| Samples | Activity before labeling [a] | Activity after labeling |
|---|---|---|
| Native COX-2 | 100 | NA[c] |
| Cys[-b] | 70 | NA |
| E58C | 50 | 50 |
| F59C | 50 | 50 |
| L60C | 70 | 70 |
| T61C | 60 | 60 |
| R62C | 50 | 50 |
| I63C | 70 | 70 |
| K64C | 70 | 70 |
| L65C | 70 | 70 |
| F66C | 50 | 50 |
| L67C | 40 | 40 |
| N72C | 60 | 60 |
| T73C | 40 | 40 |
| V74C | 60 | 60 |
| H75C | 70 | 70 |
| Y76C | 70 | 70 |
| I77C | 60 | 60 |
| L78C | 30 | 30 |
| G83C | 35 | 35 |

| | | |
|---|---|---|
| F84C | 50 | 50 |
| W85C | 10 | 10 |
| N86C | 50 | 50 |
| V87C | 30 | 30 |
| V88C | 30 | 30 |
| N89C | 30 | 30 |
| N90C | 20 | 20 |

[a] Cyclooxygenase activity determined by oxygen electrode as described previously on purified enzyme before and after conjugation with MTSSL. All activities are normalized to the specific activity of the His-Tagged native COX-2.

[b] $Cys^-$ : human COX-2 mutant in which cysteines at positions 299 and 526 were substituted with serines.

[c] NA: Not Applicable

equilibrated with 20% oxygen (air); 3) The spin labeled proteoliposome in the presence of 50 mM NiEDDA equilibrated with nitrogen. In order to equilibrate the samples with the gas, the loop-gap resonator was connected to nitrogen and air cylinders. The sample was purged with the gas for at least 20 minutes before performing the measurements. The resonator remained connected to the gas during the measurements.

*Power Saturation Experiments:*

In the absence of any relaxer, the energy levels are saturated and homogeneity factor (ε) is close to 1.5. (See section 3.6.1 for detail theory discussion about power saturation curves). The presence of other paramagnetic species can affect $P_{1/2}$. For example, the presence of a nearby fast-relaxing transition metal ion will enhance the rate at which MTSSL radical electrons relax from the high-energy to low-energy state, thus increasing the microwave power that can be absorbed before the transition saturates. On the other hand very high microwave powers distort the line shapes and the data for the peak to peak amplitude of the signals obtained at very high powers are not useful. Therefore in the presence of relaxers the power saturation curves don't roll over significantly. The homogeneity factor (ε) for power saturation curves in the presence of relaxers, especially the metal relaxer is about 0.5. However the value of $P_{1/2}$ is not significantly affected by the homogeneity of the saturation curves because what determines the $P_{1/2}$ value of the curve is the initial slope of the curve.

*EPR spectra: Mobility of the nitroxide side chains*

Figures 3.13-15 show the room temperature EPR spectra of nitroxide spin label side chain (R1) at sites 58-67, 72-78 and 83-90 in 30% sucrose. 30% w/v sucrose is used in order to reduce the rotary diffusion rate of the protein. Sucrose at this concentration does not affect the rotational mobility of the side chain.

The shape of spin label EPR spectrum reflects the degree of reorientational motion of the nitroxide side-chain. This residual motion depends on the secondary and tertiary structure of the spin label binding site and its vicinity. Three distinct types of structural classes can be assigned based on mobility. The first class consists of sites where the spectral line shape indicates rapid motions. These sites occur generally in loops or at the solvent-exposed surfaces of helices where R1 is not in contact with protein tertiary structure. Weak interaction between the nitroxide and the rest of the protein results in the high degree of mobility. In this case, the apparent hyperfine splitting and the line width are small, as found for the spectra of I63R1 and F66R1 in helix A, V87R1 in helix C and E58R1 in the loop which connects the EGF domain to helix A. In turn, if residual motion is restricted due to strong interaction of the nitroxide group with neighboring side-chains or backbone atoms, the apparent hyperfine splitting and the line width are increased. This is obvious for the spectra of V74R1 and I77R1 in helix B and F84R1, W85R1 and N86R1 in helix C, which clearly show the restricted motion of nitroxide spin label. The line shapes in this second class are characterized by the presence of resolved outer splittings indicating partial averaging of the A tensor. The broad central line is also consistent with partial averaging of the g tensor. None of the residues in helix A shows a restricted nitroxide motion. This reveals a loosely packed environment around

helix A, which is in agreement with the X-ray crystallographic structure (*1*). The third class shows an intermediate degree of averaging which occurs at sites: F59R1, L60R1, T61R1, R62R1, K64R1, L65R1 and L67R1 in helix A, T73R1, H75R1, Y76R1 and I78R1 in helix B and G83R1, V88R1, N89R1 and N90R1 in Helix C.

In order to extract dynamics data from an EPR spectrum, a spectral parameter that is sensitive to changes in mobility is needed. The inverse central line widths ($\Delta B^{-1}$ also known as $\Delta H^{-1}$) are widely used as indicators of mobility. However $\Delta B^{-1}$ measurements can be erroneous due to the sharp features of the central peak ($m_{I=0}$) in proteins which have fast rotational motion in solutions. 30% w/v sucrose is used in order to reduce the rotary diffusion rate of the protein. But even in 30% w/v sucrose solution the $\Delta B^{-1}$ measurement is not very accurate. The peak to peak amplitude of the $m_{I=0}$ of a normalized spectra (normalized to the total number of spins) is used as a more sensitive indicator of mobility. In a normalized spectrum if spectral lineshape is narrow then the peak to peak amplitude is large and if the lineshape is broad then the peak to peak amplitude is small.

For this technique the noise level in spectrum is filtered using Bruker's WinEPR software and the spectrum is normalized to the total number of spin (area underneath the spectrum) using Origin software. The peak to peak amplitudes of the normalized spectra are measured and plotted as a function of the amino acid sequence (Figures 3.19-21 B). A periodicity of 3.6 is observed in these plots which is consistent with an α-helical configuration of the backbone.

*Accessibilities to Oxygen and Nickel Ethylene Diamine Diacetic Acid (NiEDDA)*

The solvent exposure of a nitroxide spin label attached to a cysteine residue in a protein can be measured by examining its collision frequency with another paramagnetic reagent such as NiEDDA in solution. The collision frequency of a nitroxide probe with paramagnetic relaxers depends on the product of its translational diffusion coefficient and its local concentration. Molecular oxygen and water-soluble NiEDDA have been found to be ideally suited because of the sizes and solubility properties. Molecular oxygen has a low concentration in the tightly packed protein interior, whereas both the solubility and the diffusion coefficient are high in the bilayer. Therefore, the collision frequency between oxygen and spin labels in the interior of the protein is low, whereas it is high, if the spin label side-chain faces the bilayer. The relative collision frequencies were determined by the method of continuos wave power saturation. The increase in $P_{1/2}$ that occurs in the presence of NiEDDA or air is converted into a dimensionless accessibility parameter $\Pi$ (*31*). $\Pi$ is proportional to the collision frequency of the nitroxide with the respective reagent.

The accessibility parameter values in the presence of NiEDDA or with the sample in equilibrium with air were plotted as a function of sequence position (See Table 3.2 and Figures 3.19-21 A). The highest values of $\Pi_{NiEDDA}$ and hence the highest collision frequency with NiEDDA is revealed for the side-chains attached to positions L60R1, T61R1, K64R1 in helix A (Figure 3.19), H75R1, Y76R1 in helix B (Figure 3.20) and V87R1 in helix C (Figure 3.21). The residues showing the largest collision frequency must be oriented towards the aqueous phase, while those with low values of $\Pi_{NiEDDA}$ face

the protein or the bilayer. The accessibility parameter $\Pi_{oxygen}$ and the width of the central absorption peak (or the normalized amplitude of the center peak ($m_{I=0}$)) allow discrimination between these cases. Low values of normalized amplitude of the center peak ($m_{I=0}$) and low oxygen accessibility is typical of the location of the nitroxide side-chain buried inside the protein. The oxygen accessibility is lowest for positions F59R1, K62R1 in helix A, V74R1 in helix B and G83R1, F84R1, W85R1, V88R1, N89R1 and N90R1 in helix C and all these positions have a relative low values of normalized amplitude of the center peak ($m_{I=0}$). On the other hand, high motional freedom and thus narrow EPR lines combined with high oxygen accessibility are characteristic of the nitroxide in contact with the lipid bilayer. This is the case for E58R1, F66R1 and L67R1, which show high accessibility to air and lower accessibility to NiEDDA and have narrow EPR lineshapes.

As it is shown in Figures 3.19-21 A and B, there is a qualitative agreement in the patterns of $\Pi$ and the normalized amplitude. The solvent –accessible nitroxides, which display high $\Pi$ values, are likely to enjoy high mobility, which in turn will lead to high values of the normalized amplitude of $m_{I=0}$ peak. This is obvious for L60R1, T61R1, I63R1 and K64R1 in Helix A, H75R1 and Y76R1 in Helix B and V87R1 in Helix C.

The buried sites such as F59R1, R62R1 and L65R1 in helix A; V74R1 and I77R1 in helix B and W85R1 and N89R1 in helix C display low $\Pi$ values and low values of the normalized amplitude of $m_{I=0}$ peak.

**Table 3.2.** Collisional parameters for the membrane binding domain mutants.

| Mutants | $P_{1/2}(N_2)$ | $P_{1/2}$(Air) | $P_{1/2}$ (50 mM NiEDDA) | $\Delta B_{p-p}$ | Π(Air) | Π(NiEDDA) |
|---|---|---|---|---|---|---|
| E58C | 4.69 | 13.23 | 11.21 | 3.05 | 0.281 | 0.214 |
| F59C | 4.61 | 6.93 | 12.61 | 4.64 | 0.0502 | 0.173 |
| L60C | 4.72 | 11.32 | 14.11 | 3.48 | 0.190 | 0.270 |
| T61C | 5.38 | 10.42 | 15.59 | 3.92 | 0.129 | 0.261 |
| R62C | 4.29 | 8.07 | 8.80 | 4.50 | 0.0842 | 0.100 |
| I63C | 4.52 | 9.20 | 11.61 | 4.06 | 0.115 | 0.175 |
| K64C | 4.61 | 9.48 | 12.25 | 3.77 | 0.129 | 0.203 |
| L65C | 4.78 | 9.34 | 12.55 | 3.92 | 0.117 | 0.199 |
| F66C | 4.09 | 8.82 | 7.15 | 3.48 | 0.136 | 0.0880 |
| L67C | 4.42 | 9.60 | 7.28 | 3.05 | 0.170 | 0.0940 |

| Mutants | $P_{1/2}(N_2)$ | $P_{1/2}$(Air) | $P_{1/2}$ (50 mM NiEDDA) | $\Delta B_{p-p}$ | Π(Air) | Π(NiEDDA) |
|---|---|---|---|---|---|---|
| N72C | 3.73 | 7.45 | 6.67 | 4.29 | 0.0869 | 0.0686 |
| T73C | 4.24 | 7.43 | 11.75 | 3.85 | 0.0832 | 0.196 |
| V74C | 5.77 | 7.95 | 13.51 | 4.62 | 0.0472 | 0.168 |
| H75C | 4.58 | 8.03 | 10.12 | 2.86 | 0.121 | 0.194 |
| Y76C | 4.58 | 8.18 | 13.33 | 4.62 | 0.0781 | 0.190 |
| I77C | 5.38 | 8.54 | 12.62 | 4.07 | 0.0708 | 0.178 |
| L78C | 6.02 | 8.85 | 13.14 | 3.63 | 0.0784 | 0.196 |

| Mutants | $P_{1/2}(N_2)$ | $P_{1/2}$(Air) | $P_{1/2}$ (50 mM NiEDDA) | $\Delta B_{p-p}$ | Π(Air) | Π(NiEDDA) |
|---|---|---|---|---|---|---|
| G83C | 3.99 | 6.00 | 10.76 | 4.62 | 0.0435 | 0.147 |
| F84C | 3.66 | 5.88 | 9.29 | 4.95 | 0.0448 | 0.114 |
| W85C | 4.37 | 6.88 | 11.37 | 5.17 | 0.0485 | 0.136 |
| N86C | 3.76 | 6.90 | 11.71 | 4.18 | 0.0754 | 0.191 |
| V87C | 3.43 | 8.55 | 12.13 | 3.08 | 0.167 | 0.283 |
| V88C | 5.64 | 8.17 | 10.02 | 4.4 | 0.0576 | 0.0997 |
| N89C | 3.11 | 6.26 | 5.58 | 4.51 | 0.0480 | 0.0551 |
| N90C | 4.85 | 7.57 | 11.28 | 4.07 | 0.0670 | 0.158 |

$P'_{1/2}$ (DPPH) =9.96

The line shapes for proteoliposomes are significantly broader than proteins in solution (compare Figures 3.13-15 and 3.16-18). This is due to increase of the rotational correlation time ($\tau_R$) for the proteoliposome because the liposomal structures are significantly larger than proteins and rotate much slower in solutions than solubilized proteins.

**3.13.** CW-EPR spectra of COX-2 helix A spin label mutants in 30% w/v sucrose

**Figure 3.14.** CW-EPR spectra of Cox-2 helix B spin label mutants in 30% w/v sucrose.


N72C
Y76C
T73C
I77C
V74C
I78C
H75C

**Figure 3.15.** CW-EPR spectra of Cox-2 helix C spin label mutants in 30% w/v sucrose.

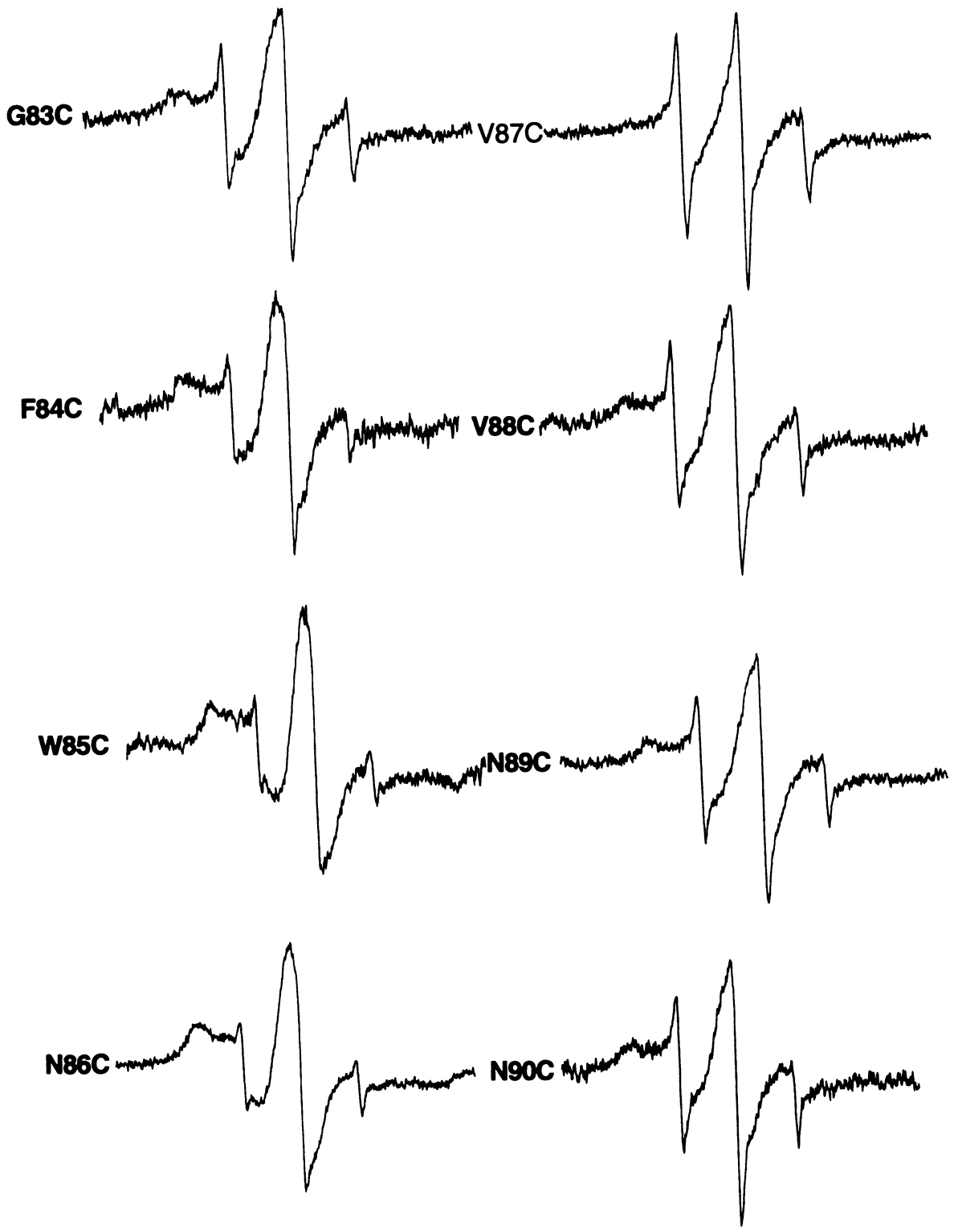
G83C
V87C
F84C
V88C
W85C
N89C
N86C
N90C

**Figure 3.16.** CW-EPR spectra of Cox-2 helix A spin label mutants incorporated into liposome.

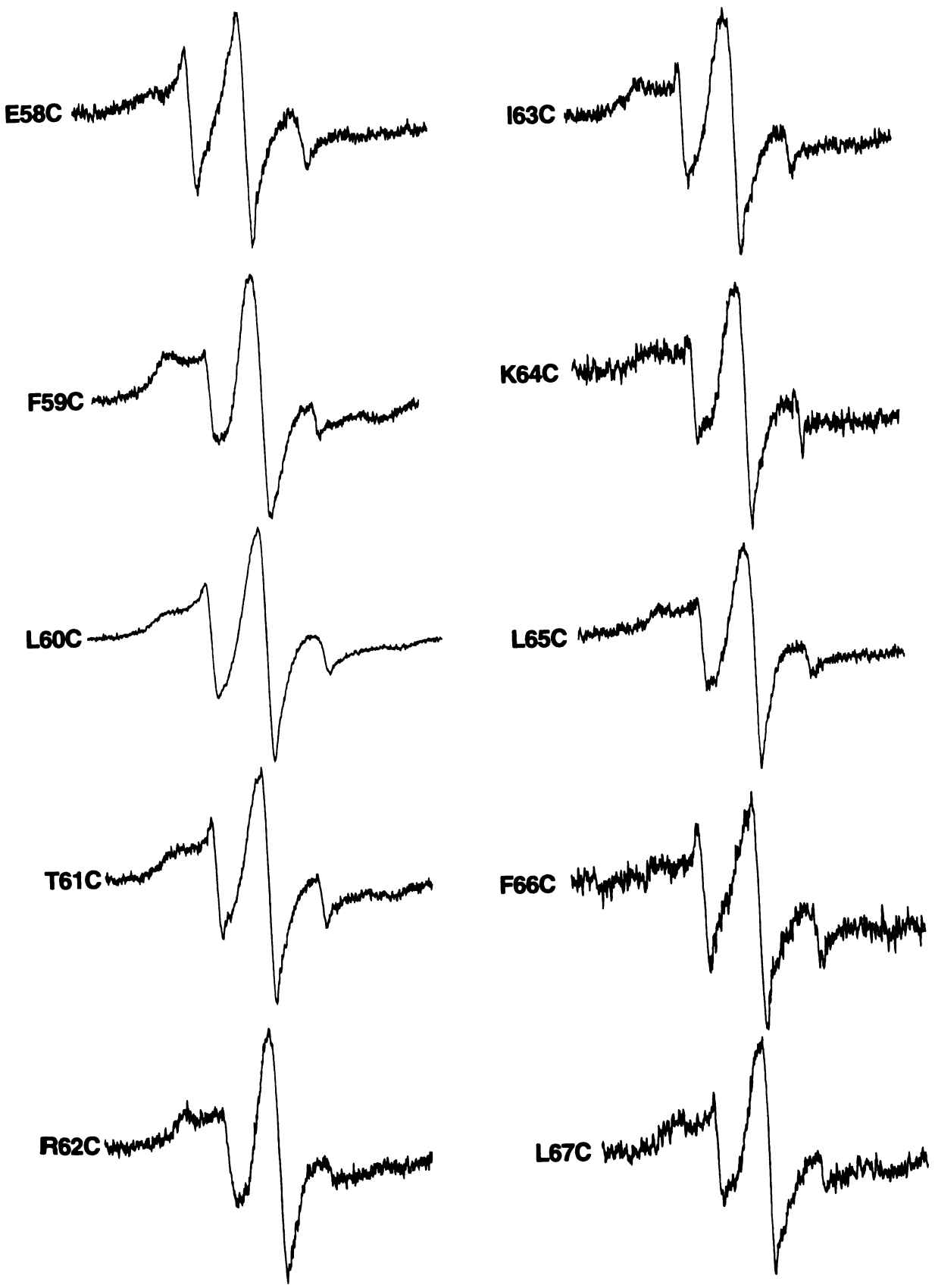
E58C
I63C
F59C
K64C
L60C
L65C
T61C
F66C
R62C
L67C

**Figure 3.17.** CW-EPR spectra of Cox-2 helix B spin label mutants incorporated into liposomes.

**Figure 3.18.** CW-EPR spectra of Cox-2 helix C spin label mutants incorporated into liposomes

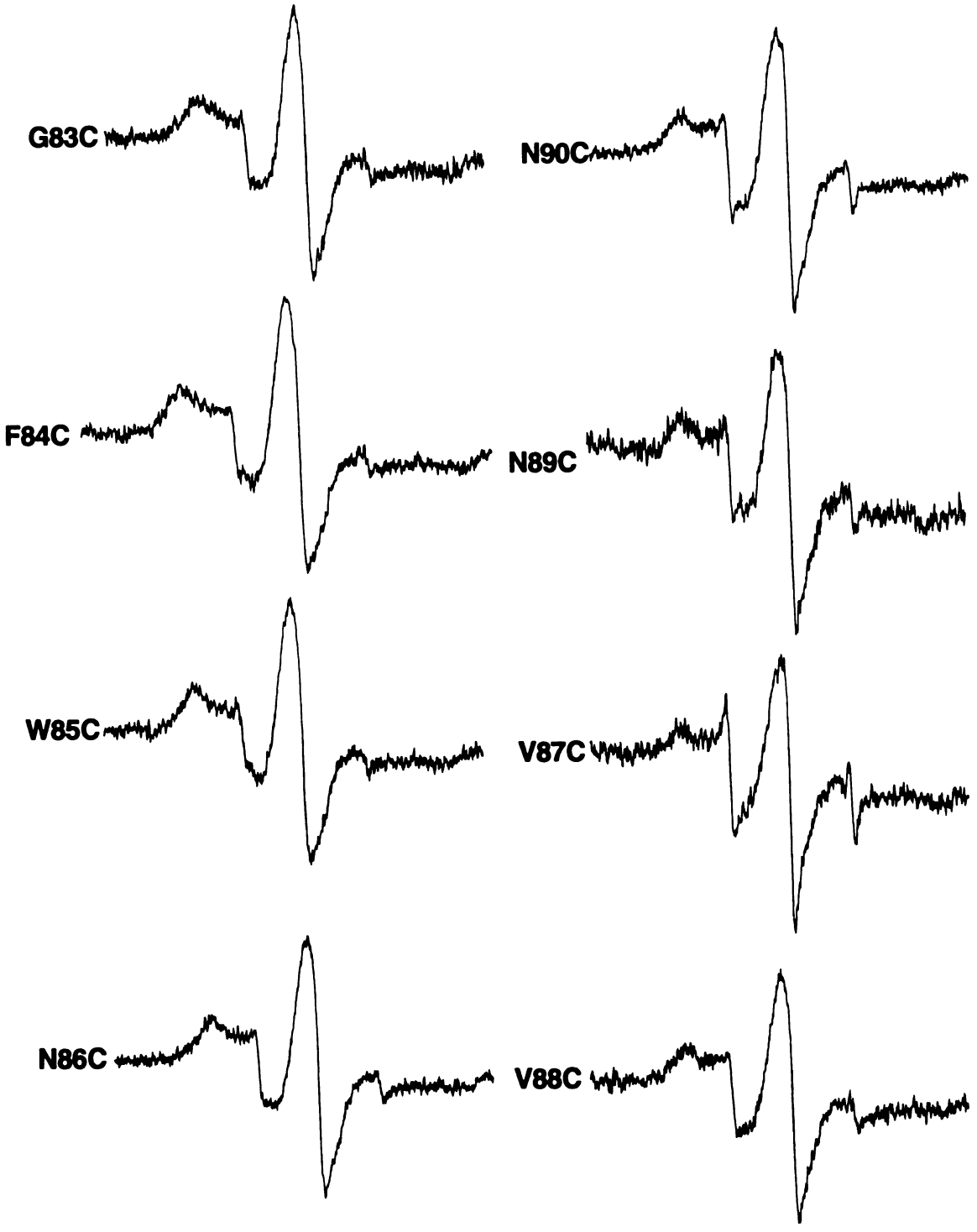
G83C
N90C
F84C
N89C
W85C
V87C
N86C
V88C

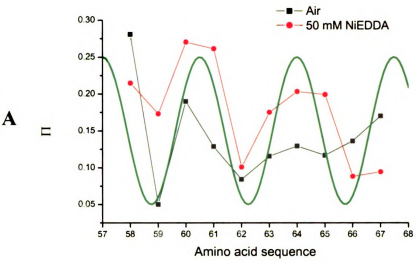


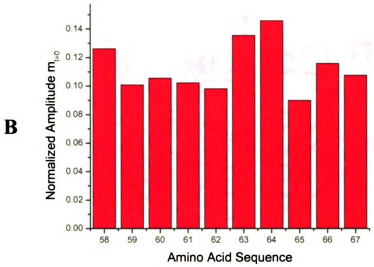


**Figure 3.19.** A) Plot of relative accessibility of Helix A side chains.
B) Plot of mobility of Helix A side chains.

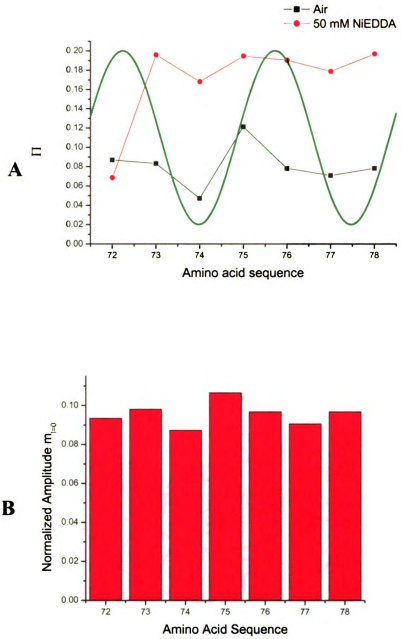


**Figure 3.20.** A) Plot of relative accessibility of Helix B side chains. B) Plot of mobility Helix B side chains.

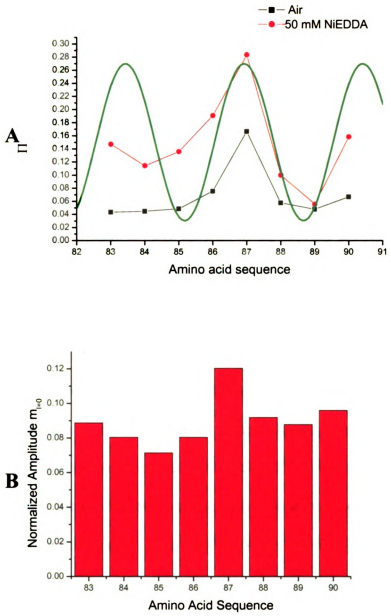


**Figure 3.21.** A) Plot of relative accessibility of Helix C side chains.
B) Plot of mobility of Helix C side chains.

### 3.9. Discussion

Figures 3.19-21 show the sequence-specific variation in $\Pi_{oxygen}$ along helices A-C. Consistent with an α-helical configuration of the backbone, a periodicity of 3.6 is observed as demonstrated from the superimposed sinusoid. The oscillatory behavior continues uninterrupted along the sequence although a shift in phase is detected in the last turn of helix A. $\Pi_{oxygen}$ and $\Pi_{NiEDDA}$ both have the same period and phase. This reveals that one side of the protein is more exposed to the aqueous environment, while the other side is exposed to the interior part of the protein (See Figure 3.12).

Values of $\Pi_{NiEDDA}$ are very low throughout the Helices A, B and C being a maximum $\approx$ 0.3 .The values of $\Pi_{oxygen}$ are also very low throughout the three helices being a maximum $\approx$ 0.2. For reference, in 20 mM NiEDDA, R1 sites exposed to water or lipid or buried in a protein interior have typical $\Pi_{NiEDDA}$ values of $\approx$ 6, <0.1, and 0.01, respectively (*32*). In these experiments 50 mM NiEDDA was used so it is expected to get $\Pi_{NiEDDA}$ values which are even higher than the above mentioned values. Also for reference, R1 at buried sites, water-exposed sites, and lipid-exposed sites have $\Pi_{oxygen}$ $\approx$0.05, 0.45-0.55 and 1, respectively. These low values of accessibility for both $\Pi_{NiEDDA}$ and $\Pi_{oxygen}$ indicate that both polar and non-polar paramagnetic relaxers do not access the aminoacids located in the membrane-binding domain. One possibility is that the membrane-binding domain of hCOX-2 is sandwiched between the main body of the 144 kDa hCOX-2 dimer and the lipid bilayer. The spatial organization of the dimer around the helices in the membrane-binding domain results in an excluded volume that lowers

the diffusion coefficient of oxygen. Our data suggests that the side of the helix, which is accessible to water, is not completely immersed in water. If that was the case, we would have expected to see a $\Pi_{NiEDDA}$ higher than 6 for 50 mM NiEDDA. Instead the maximum $\Pi_{NiEDDA}$ was around 0.3. This reveals that NiEDDA molecules can not diffuse freely. One possibility is that the water-exposed site of the helix is in a close contact with the phosphate head groups at the bilayer interface. The concentration of NiEDDA is much lower in the bilayer interface than in the aqueous phase and this is the reason of such low $\Pi_{NiEDDA}$ values.

E58R1 which is the last amino acid in the loop connecting the EGF domain to helix A has a higher accessibility to oxygen than to NiEDDA. This suggests that this amino acid participates in anchoring the protein to the lipid bilayers. The last two amino acids in helix A F66R1 and L67R1 have higher accessibility to oxygen that to NiEDDA suggest that they may also play a role in membrane binding.

The crystal structure (*33*) shows that in helix A side chains for amino acids F59, R62 and F66 would be exposed to the surface of the of the protein and T61 would be exposed to the interior part of the protein although, our accessibility data and also the data from line shapes reveal that F59, R62 are exposed to the interior part of the protein and T61 is exposed to surface of the protein (See figures 3.22-23).

The crystal structure shows that in helix B the side chain for amino acid H75 would be exposed to the interior part of the protein although, our accessibility data and also the data from the line shapes reveal that H75C is exposed to the surface of the protein (see Figures 3.22-23). The failure to observe oscillation in the $O_2$ or NiEDDA accessibility data are indicative of the helix B environment that is uniformly accessible to

the NiEDDA but interior to the protein. Accessibility data for $O_2$ are also uniform but show that helix B is inaccessible to this relaxation agent.

The crystal structure shows that in helix C side chains for amino acids G83, W85 and N89 would be exposed to the interior part of the protein and V87 would be exposed to the surface of protein. Our accessibility data and also the data from line shapes reveal the same thing. (see Figures 3.22-23).

As it is shown in Figures 3.22 and 23, helices A and B are rotated anti clockwise by several degrees in liposome compare with their structure in crystal. Helix C maintains same structure in both liposome and crystal.

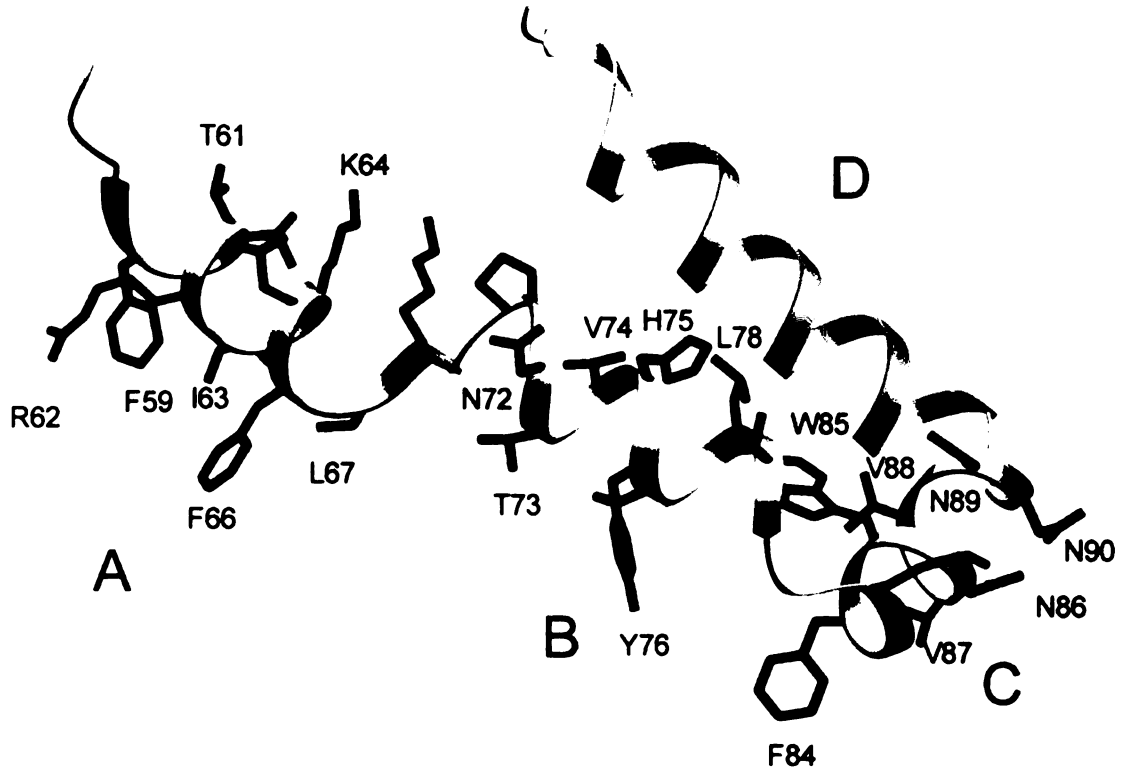


**3.22.** The crystal structure of the membrane-binding domain of hCOX-2.
This picture was made by Dr. Anne Mulichak.
Images in this dissertation are presented in color.

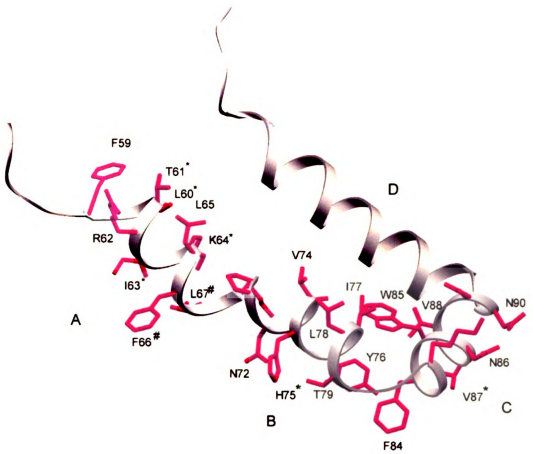


**3.23.** The structure of the membrane-binding domain of hCOX-2 that was proposed by site directed spin labeling.
* Mobile and solvent exposed amino acids
# The lipid exposed amino acids
This picture was made by Dr. Anne Mulichak.
Images in this dissertation are presented in color.

## 3.10. References


1. Picot, D., Loll, P. J., and Garavito, R. M. (1994) *Nature 367*, 243-249.

2. Wendt, K. U., Lenhart, A., and Schulz, G. E. (1999) *Journal of Molecular Biology 286*, 175-187.

3. Hubbell, W. L., and Altenbach, C. (1994) *Current Opinion in Structural Biology 4*, 566-573.

4. Hubbell, W. L., Cafiso, D. S., and Altenbach, C. (2000) *Nature Structural Biology 7*, 735-739.

5. Read, R. J., and Wemmer, D. E. (1999) *Current Opinion in Structural Biology 9*, 591-593.

6. Drenth, J. P. H., Boom, B. W., Toonstra, J., and Vandermeer, J. W. M. (1994) *Archives of Dermatology 130*, 59-65.

7. Georgopoulos, C., Ang, D., Wall, D., Wu, B., vanderVies, S., Richardson, A., Deloche, O., Kelley, W., Keppel, F., Drijard, L., Zuber, U., Liberek, K., Wawrzynow, A., Wojtkowiak, D., Zylicz, M., Szyperski, T., Pellacchia, M., and Wutrich, K. (1996) *Molecular Biology of the Cell 7*, 1954-1954.

8. Michel, J. P. (2003) *Wiener Klinische Wochenschrift 115*, 273-274.

9. Ketchem, R. R., Hu, W., and Cross, T. A. (1993) *Science 261*, 1457-1460.

10. Grigorieff, N., Ceska, T. A., Downing, K. H., Baldwin, J. M., and Henderson, R. (1996) *Journal of Molecular Biology 259*, 393-421.

11. Subramaniam, S., Gerstein, M., Oesterhelt, D., and Henderson, R. (1993) *Embo Journal 12*, 1-8.

12. Lewis, V. A., Hynes, G. M., Dong, Z., Saibil, H., and Willison, K. (1992) *Nature 358*, 249-252.

13. Braig, K., Otwinowski, Z., Hegde, R., Boisvert, D. C., Joachimiak, A., Horwich, A. L., and Sigler, P. B. (1994) *Nature 371*, 578-586.

14. Engel, A., Hayerhartl, M. K., Goldie, K. N., Pfeifer, G., Hegerl, R., Muller, S., Dasilva, A. C. R., Baumeister, W., and Hartl, F. U. (1995) *Science 269*, 832-836.

15. Valencia, A., Hubbard, T. J., Muga, A., Banuelos, S., Llorca, O., Carrascosa, J. L., and Valpuesta, J. M. (1995) *Proteins-Structure Function and Genetics 22*, 199-209.

16. Cantor, J. M., and Haskins, K. (2003) *Faseb Journal 17*, C271-C272.

17. Gross, A., and Hubbell, W. (1998) *Biophysical Journal 74*, A44-A44.

18. Postnikova, G. B. (1996) *Biochemistry-Moscow 61*, 679-693.

19. Langen, R., Oh, K. J., Cascio, D., and Hubbell, W. L. (2000) *Biochemistry 39*, 8396-8405.

20. Weil J.A., B. J. R., Wertz J.E. (1994) *Electron Paramagnetic Resonance*, John Wiley & Sons Inc., New York.

21. Andrews, S. H. (1999) pp 170, Universityof Virginia, Charlottesville.

22. Froncisz, W., and Hyde, J. S. (1982) *Journal of Magnetic Resonance 47*, 515-521.

23. Hubbell, W. L., Gross, A., Langen, R., and Lietzow, M. A. (1998) *Current Opinion in Structural Biology 8*, 649-656.

24. Berliner, L. J. (1998) *Biological Magnetic Resonance*, Vol. 14, Plenum Press, New York.

25. Salwinski, L. (1998) pp 269, UCLA, Los Angles.

26. Berliner, L. J. (1998) *Spin Labeling the next millennium*, Vol. 14, Plenum Press, New York.

27. Boxrud, P. D., and Berliner, L. J. (1996) *Journal of Protein Chemistry 15*, 231-242.

28. Likhtenstein, G. I., Bogatyrenko, V. R., and Kulikov, A. V. (1993) *Applied Magnetic Resonance 4*, 513-521.

29. Altenbach, C., Froncisz, W., Hyde, J. S., and Hubbell, W. L. (1989) *Biophysical Journal 56*, 1183-1191.

30. Altenbach, C., Flitsch, S. L., Khorana, H. G., and Hubbell, W. L. (1989) *Biochemistry 28*, 7806-7812.

31. Altenbach, C., Marti, T., Khorana, H. G., and Hubbell, W. L. (1990) *Science 248*, 1088-1092.

32. Gross, A., Columbus, L., Hideg, K., Altenbach, C., and Hubbell, W. L. (1999) *Biochemistry 38*, 10324-10335.

33. Kurumbail, R. G., Stevens, A. M., Gierse, J. K., McDonald, J. J., Stegeman, R. A., Pak, J. Y., Gildehaus, D., Miyashiro, J. M., Penning, T. D., Seibert, K., Isakson, P. C., and Stallings, W. C. (1996) *Nature 384*, 644-648.

# Chapter 4

# Double Site Directed Spin Labeling Studies

## 4.1. Abstract

The goal of the research described in this chapter is to study conformational changes in the mouth of the cyclooxygenase channel. Formation of the NSAID-COX complexes has been proposed to result in conformational changes in COX (*1*). This hypothesis is supported by studies that show that time-dependent inhibitors protect from proteolytic cleavage at Arg-277, an amino acid located on a peptide loop distant from the inhibitor binding pocket (*2-5*). Heme, which binds at a site separate from the NSAID binding pocket, also protected COX from proteolysis, indicating a global flexibility in the COX isozymes. Despite this circumstantial evidence that the COXs undergo conformational changes, comparison of the X-ray crystal structure of the COX-2 holoenzyme with the structure of COX-1 and –2 co-crystallized with various time-dependent NSAIDs reveals only minor structural differences (*6*). To investigate this controversy, I have examined arachidonic acid, NSAIDs, and heme induced conformation changes of hCOX-2 using site-directed spin labeling and electron paramagnetic resonance spectroscopy.

Ten mutants located in the helices that form the opening of the cyclooxygenase active site and the membrane-binding domain of hCOX-2 were constructed. Each mutant contained the I98C substitution in helix D, and one of five amino acids substitutions in opposing helix B (T73C, V74C, H75C, Y76C and I77C) or one of the five amino acid substitutions in adjacent helix C (F84C, W85C, N86C, V87C and V88C). The dipolar broadenings of the spectra in the presence and absence of NSAIDs, in the presence and absence of heme and in the presence and absence of arachidonic acid were compared in

this chapter a brief review about various interspin distance measurement techniques will be given and then the Fourier convolution/deconvolution technique will be explained in detail. Finally, the experiments and the results will be discussed.

## 4.2. Dipole-Dipole Interaction

The two nitroxide spin labels attached to a biomolecule *e.g.* a protein interact with each other through the electron-electron dipolar interaction (Figure 4.1).

The biradical spin Hamiltonian is expressed as:

$$H=h\Omega_1 \ S_{1Z}+h\Omega_2 S_{2Z}+\frac{h^2\gamma_e^2(1-3Cos^2\theta)(3S_{1Z}S_{2Z}-S_1S_2)}{2R^3}+JS_1\bullet S_2 \qquad (4.1)$$

where $h$ is the Planck's constant, $\gamma_e$ is the electron gyromagnetic ratio, $J$ is the exchange integral, $\theta$ is the angle between the interspin vector and magnetic field z direction, $\Omega_1$ and $\Omega_2$ represent the resonance offsets for electron spins 1 and 2, and $S_{1Z}$ and $S_{2Z}$ are the z direction components of the electron spin angular momentum vectrors $S_1$ and $S_2$ , respectively. The first two terms of equation 4.1 give rise to the EPR spectrum in the absence of the electron-electron dipolar interaction. However, the existence of the electron-electron dipolar interaction perturbs the non- interacting EPR spectrum to give rise to an overall spectral broadening. The electron-electron dipolar interaction is given as

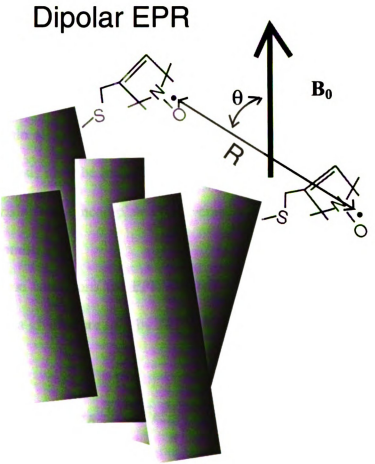


**Figure 4.1.** Dipolar coupling between two spin labels. Taken from (*9*).

the third term of the equation 4.1. The electron-electron dipolar interaction has an $R^{-3}$ dependence on the interspin distance R. Because spin exchange interaction decays exponentially as a function of R, the electron-electron dipolar interaction becomes dominant when R is larger than 7 Å unless there is a through bond interaction. The short-range spin exchange interaction is not considered in Fourier convolution deconvolution (FCD) analysis.

When nitroxides are attached to a biomolecule such as a protein, the flexible nitroxide side chain allows significant degrees of freedom for the magnetic tensors at a given $\theta$. This analysis must be included in the analysis of the spin Hamiltonian. To avoid complications arising from incomplete time averaging of θ the EPR spectra must be taken under a frozen conditions.

Under these conditions the EPR absorption lines at all spectral positions in the magnetic field for a given $\theta$ are split by $2B$ (in Gauss),

$$2B=\frac{(3/2)g_e\beta(3Cos^2\theta-1)}{R^3} \qquad (4.2)$$

where $g_e$ is the free electron g factor, $\beta$ is the electron Bohr magneton. Here it is assumed that the effect of the g anisotropy in negligible at 9 GHz (*9*).

## 4.3. Determination of Electron-Electron Distance from Dipolar Interaction between Two Spin Labels Measured by EPR in Immobilized State

The task of methodology development is to maximize sensitivity of the spectral display to the dipolar interaction and to separate the dipolar interaction from other features of the spectra and thereby extract the distance information from the spectrum. A variety of techniques have been reported for various types of samples and magnitude of dipolar interaction as outlined in the following paragraphs and summarized in Table 4.1 (*9*).

### 4.3.1. Dipolar Splitting is Significant Compared with Linewidths of Spectra for Corresponding Monoradical

When the dipolar splitting (D) is significant relative to the linewidths of the signals in the CW spectra, analysis of the lineshape changes can be used to determine the magnitude of the dipolar interaction. A variety of techniques have been used. Each of these techniques will be briefly discussed in the following sections. The convolution of the lineshapes will be discussed in detail. This technique was used to measure the distances between the two spin labels in various hCOX-2 mutants.

**Table 4.1.** Summary of methods for determining electron-electron distances.

| Method | [a] $R_{Max}$(Å) |
|---|---|
| Simulation of CW lineshape | 20-25 |
| Deconvolution of CW lineshape | 25 |
| Relative intensity of half-field transitions | 12 |
| Ratio of peak heights | 22 |
| 2+1 pulse sequence pulsed ELDOR | 60 |
| 4-pulse DEER | 80 |
| Double-quantum coherence | 80 |

[a] $R_{Max}$ is the maximum values of r that has been proposed as measurable by a particular technique .

#### 4.3.1.1. Analysis of Spectral Lineshapes by Computer Simulation

In principle, computer modeling of the complete spectral lineshape can define both the interspin distance and the orientation of the interspin vector relative to the magnetic axes of both paramagnetic centers, as well as separating dipolar and exchange interactions. The simulated spectral lineshapes depend upon the degree of ordering of the relative orientations of the magnetic axes, therefore, information can be obtained concerning the range of conformations present in the sample (*10*).

#### 4.3.1.2. Lineshape Deconvolution

This technique is extensively explained in chapter 4.4.

#### 4.3.1.3. Relative Intensity of the Half- Field Transition

Anisotropic interaction between two spins (dipolar interaction and anisotropic exchange) shifts the triplet state $m_s = \pm 1$ energy levels relative to the $m_s = 0$ level, and causes the normally forbidden transition probability between the $m_s = -1$ and $m_s = +1$ levels to become non-zero. This transition occurs at half the magnetic field required for the allowed transitions (at constant microwave frequency), and hence is called the "half-field" transitions. If the anisotropic exchange is negligible, and if $r > 4\text{-}5$ Å, the resonant field for the half-field transition is independent of the values of J (exchange interaction) and r (distance). The ratio of the integrated intensity of the half-field transition to the

integrated intensity of the allowed transition is a function of r and independent of J. Therefore, isotropic and anisotropic contributions can be separated by measuring the relative intensity of the half-field transition (*11, 12*).

#### 4.3.1.4. Lineshapes Distortion Determined by the Ratio of Peak Heights

Broadening of the frozen CW EPR solution of a nitroxide spin label due to dipolar interaction with a second nitroxide changes the relative intensities of the center and outer lines of the spectrum. Kokorin et al (*13, 14*) proposed that a ratio of peak heights could be used to estimate the distance between two nitroxide radicals.

### 4.3.2. Dipolar Interaction is Small Compared with Linewidths of Spectra for Corresponding Monoradical

CW techniques for measuring dipolar interaction depend upon the observation of significant broadening of the lineshape due to the interaction. Smaller dipolar interactions can be measured by pulsed techniques than by CW techniques. Thus, the pulse techniques tend to be more useful at longer distances than are accessible by CW techniques.

#### 4.3.2.1. 3-Pulse ELDOR (Electron-Electron Double Resonance)

A spin echo is created by a two-pulse sequence at one microwave frequency. The timing of a pulse at a second microwave frequency is varied. Examples of this technique have been described by Tsvetkov and co-worker (*15*) and are reviewed in Milov et al (*16*).

#### 4.3.2.2. 2+1 Sequence

Raitsiming and co-workers proposed a sequence that is similar to 3-pulse ELDOR, but with all three pulses at the same microwave frequency (*17*). This is a denoted as the "2+1" sequence. The upper limit of distances between nitroxides accessible by this technique is about 60 Å.

#### 4.3.2.3. 4-Pulse DEER (Double Electron-Electron Resonance)

In the 2+1 pulse sequence and in 3-pulse ELDOR experiments there is an inherent experimental dead time that limits the magnitude of the dipolar interaction that can be characterized. Martin and Pannier (*18*) designed a 4-pulse experiment that eliminated that dead time. The interspin distances up to 80 Å can be measured using this technique.

#### 4.3.2.4. Double–Quantum Coherence

Allowed double-quantum coherence (DQC) can be generated in ordered or disordered sample containing pairs of radicals and random distributions or radicals. Pake doublets obtained from DQC can be used to determine distances within pairs of radicals and the decay constants yield concentrations in a distribution. The upper limit of distances between nitroxides accessible by this technique is about 80 Å (*19, 20*).

## 4.4. Fourier Convolution Deconvolution of the Dipolar Coupling in the Spin-Labeled EPR Spectra

### 4.4.1. Theoretical Background

In the following three sections, a brief mathematical background will be provided which is necessary for understanding the Fourier convolution deconvolution of the dipolar coupling in the EPR spectra.

#### 4.4.1.1. Convolution

Mathematically, a convolution is defined as the integral over all space of one function at x times another function at u-x. The integration is taken over the variable x (which may be a 1D or 3D variable), typically from minus infinity to infinity over all the dimensions. So the convolution is a function of a new variable u, as shown in the following equations. The cross in a circle is used to indicate the convolution operation.

$$C(u)=f(x)\otimes g(x)=\int_{Space} f(x)g(u-x)dx \qquad (4.3)$$

$$C(u)=g(x)\otimes f(x)=\int_{Space} g(x)f(u-x)dx \qquad (4.4)$$

It doesn't matter which function is taken first, *i.e.* the convolution operation is commutative. The convolution of two functions is complex. To convolute two functions, the first function must be superimposed on the second at every possible position, and multiplied by the value of the second function at that point. The convolution is the sum of all of these superpositions. Figure 4.2 shows how one can thinks about the convolution, as giving a weighted sum of shifted copies of one function: the weights are given by the function value of the second function at the shift vector. If one of the functions is unimodal (has one peak), as in Figure 4.2, the other function will be shifted by a vector equivalent to the position of the peak, and smeared out by an amount that depends on how sharp the peak is. But if we switch the roles of the two functions, we see that the bimodal function g has doubled the peaks of the unimodal function f.

#### 4.4.1.2. Fourier Transform

The Fourier transform is a mathematical function that performs a conversion between real space and reciprocal space (See Figure 4.3).

The Fourier transform of f (ω) is defined as:

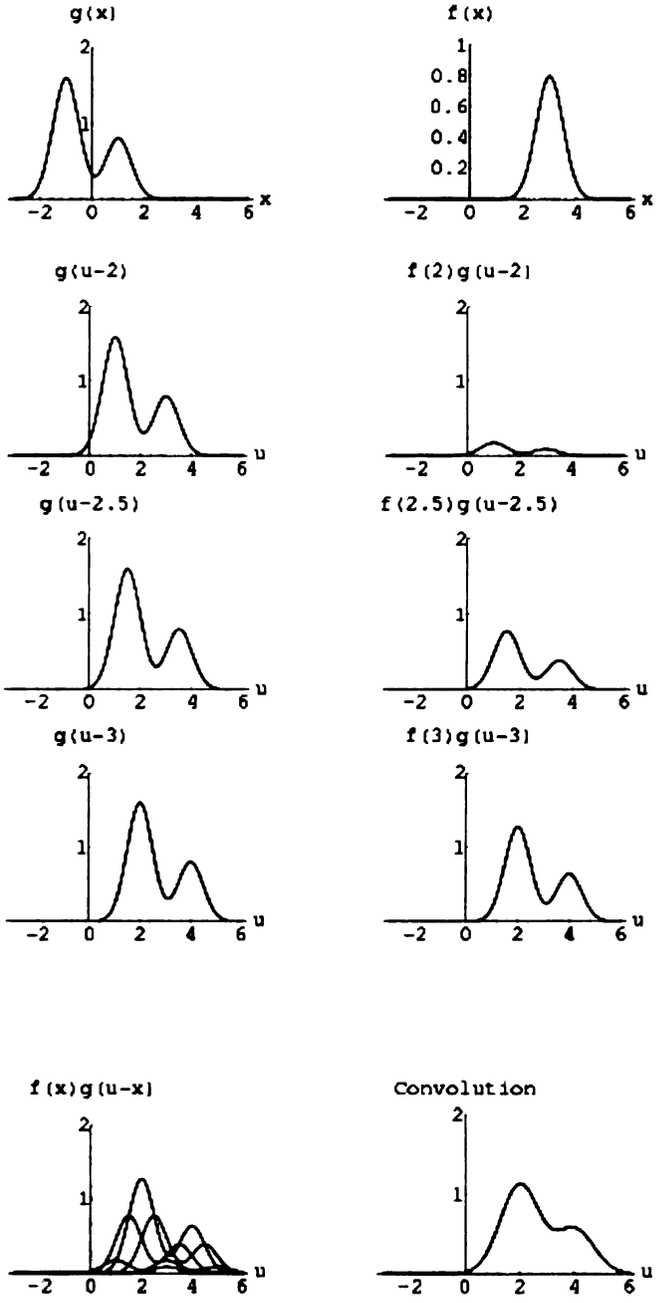


**Figure 4.2.** Convolution of f (x) ⊗ g (x)

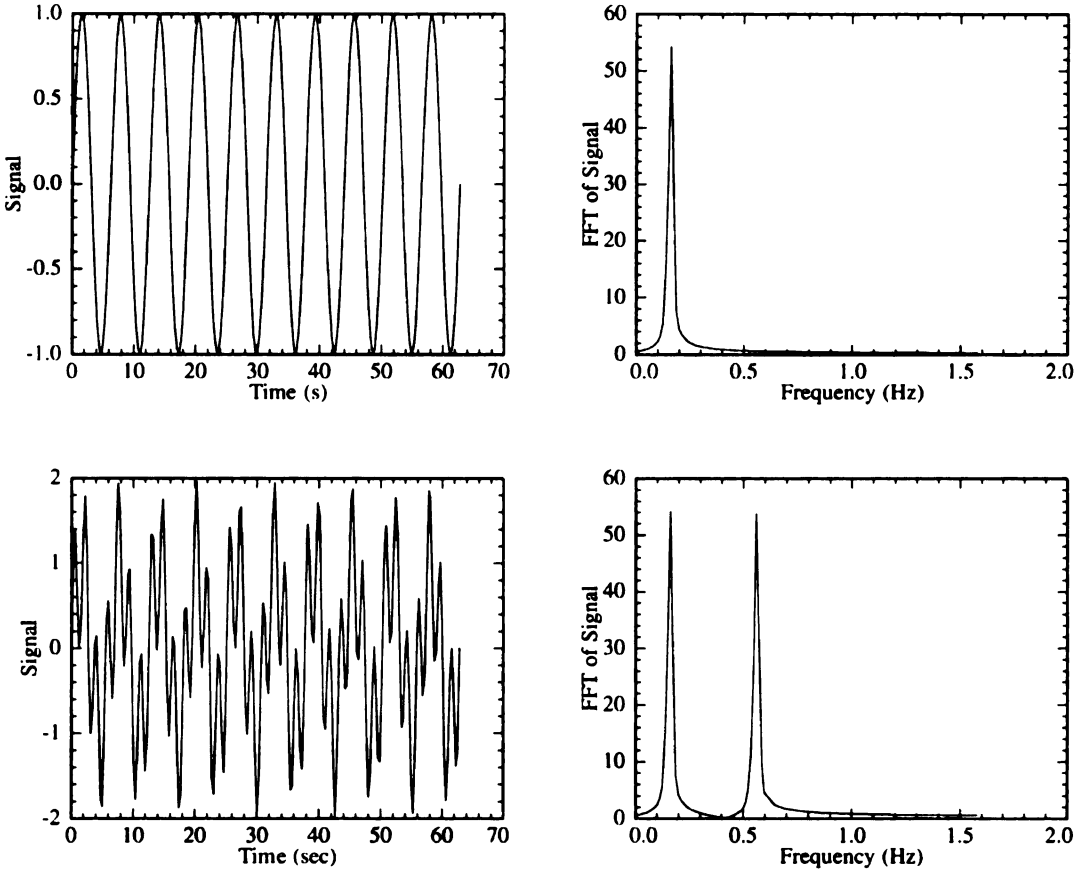


**Figure 4.3.** Fourier transformation of a signal

The picture was kindly made by Professor Michael Romalis (Princeton University) using GenPlot software.

$$F(\omega)=\frac{1}{\sqrt{2\pi}}\int_{-\infty}^{\infty}\exp(2\pi i\omega t)f(t)d\omega \qquad (4.5)$$

where $\omega=1/t$

To avoid confusion, it is customary to write the Fourier transform and its inverse so that they exhibit reversibility:

$$F(t)=\frac{1}{\sqrt{2\pi}}\int_{-\infty}^{\infty}\exp(2\pi i\omega t)f(\omega)dt \qquad (4.6)$$

#### 4.4.1.3 Convolution Theorem

The convolution theorem is one of the most important relationships in Fourier theory, and in its application to x-ray crystallography and spectroscopy.

*Convolution theorem:* The Fourier transform of a convolution of two functions is the product of their Fourier transforms (equations 4.7-9) where the superscript * indicates the Fourier transform function.

$$[C(u)]^{*}=[f(x)\otimes g(x)]^{*} \qquad (4.7)$$

$$[C(u)]^{*}=[\int_{Space} f(x)g(u-x)dx]^{*} \qquad (4.8)$$

$$[C(u)]^{*}=f(\frac{1}{x})^{*}.g(\frac{1}{x})^{*} \qquad (4.9)$$

### 4.4.2. Fourier Convolution Deconvolution of the EPR Dipolar Coupling

In most biological systems, except macroscopically oriented samples, the distribution of θ is isotropic. It is possible then to treat the spectrum of the two interacting spins as the convolution of the non-interacting powder pattern absorption spectrum with a dipolar broadening function D(R,B), known as a Pake pattern. The average splitting <2B> over the distribution D(R,B) is then:

$$<2B>=\frac{(0.75)(3/2)g_e\beta}{R^3} \qquad (4.10)$$

Thus, the EPR spectrum Π(B) for the two nitroxides is described by:

$$\Pi(B)=\int_{-\infty}^{\infty} S(B')D(R,B'-B)dB' \qquad (4.11)$$

where S(B) is the non-interacting EPR spectrum. However, in practice there will be a distribution of interspin distances due to the flexibility of the nitroxide side chain as well as the conformational variation of the macromolecules. In this situation the EPR spectrum is described by:

$$\Pi(B)=\int_{-\infty}^{\infty} S(B')M(B'-B)dB' \qquad (4.12)$$

where M(B) is the weighted sum of the D(R,B) over the distribution of the distances P(R):

$$M(B) = \sum_{R} P(R)D(R,B) \qquad (4.13)$$

According to equation 4.8, equation 4.12 can be written as:

$$\Pi(B) = S(B') \otimes M(B') \qquad (4.14)$$

Since $\Pi$ is approximated by a convolution of S and M in real space, equation 4.14 is simplified in Fourier space using the convolution theorem (equations 4.7-9):

$$\Pi^{*}(\omega) = S^{*}(\omega) \bullet M^{*}(\omega) \qquad (4.15)$$

where $\omega = 1/B$ in units of gauss$^{-1}$.

So:

$$M^{*}(\omega) = \frac{\Pi^{*}(\omega)}{S^{*}(\omega)} \qquad (4.16)$$

M(B) is then obtained from the inverse Fourier transform of the $M^{*}(\omega)$ :

$$M(B)=\frac{1}{\sqrt{2\pi}}\int_{-\infty}^{\infty}\exp(2\pi i\omega B)M^{*}(\omega)d(\omega) \qquad (4.17)$$

if equation 4.16 is substituted to equation 4.17 then:

$$M(B)=\frac{1}{\sqrt{2\pi}}\int_{-\infty}^{\infty}\exp(2\pi i\omega B)\frac{\Pi^{*}(\omega)}{S^{*}(\omega)}d(\omega) \qquad (4.18)$$

The average splitting <2B> for a given P(R) is obtained form the following formula:

$$<2B>=\frac{\int_{-\infty}^{\infty}|2B|.M(B)dB}{\int_{-\infty}^{\infty}M(B)dB} \qquad (4.19)$$

if equation 4.19 in substituted in equation 4.10 then (*9, 21*):

$$<R>=(\frac{0.75(3/2)g_{e}\beta}{<2B>})^{1/3} \qquad (4.20)$$

### 4.4.3. Spectral Analysis

EPR spectra can be analyzed according to the equations 4.14-4.20 using fast Fourier transform routines (Figure 4.4), and the resulting spectra at each step of the analysis are shown in Figure 4.5. Both real and imaginary components of the dipolar

**Figure 4.4.** A flow chart of the algorithm for distance analysis from dipolar spin-spin interaction. Taken from (*9*). Copyright permission was obtained.

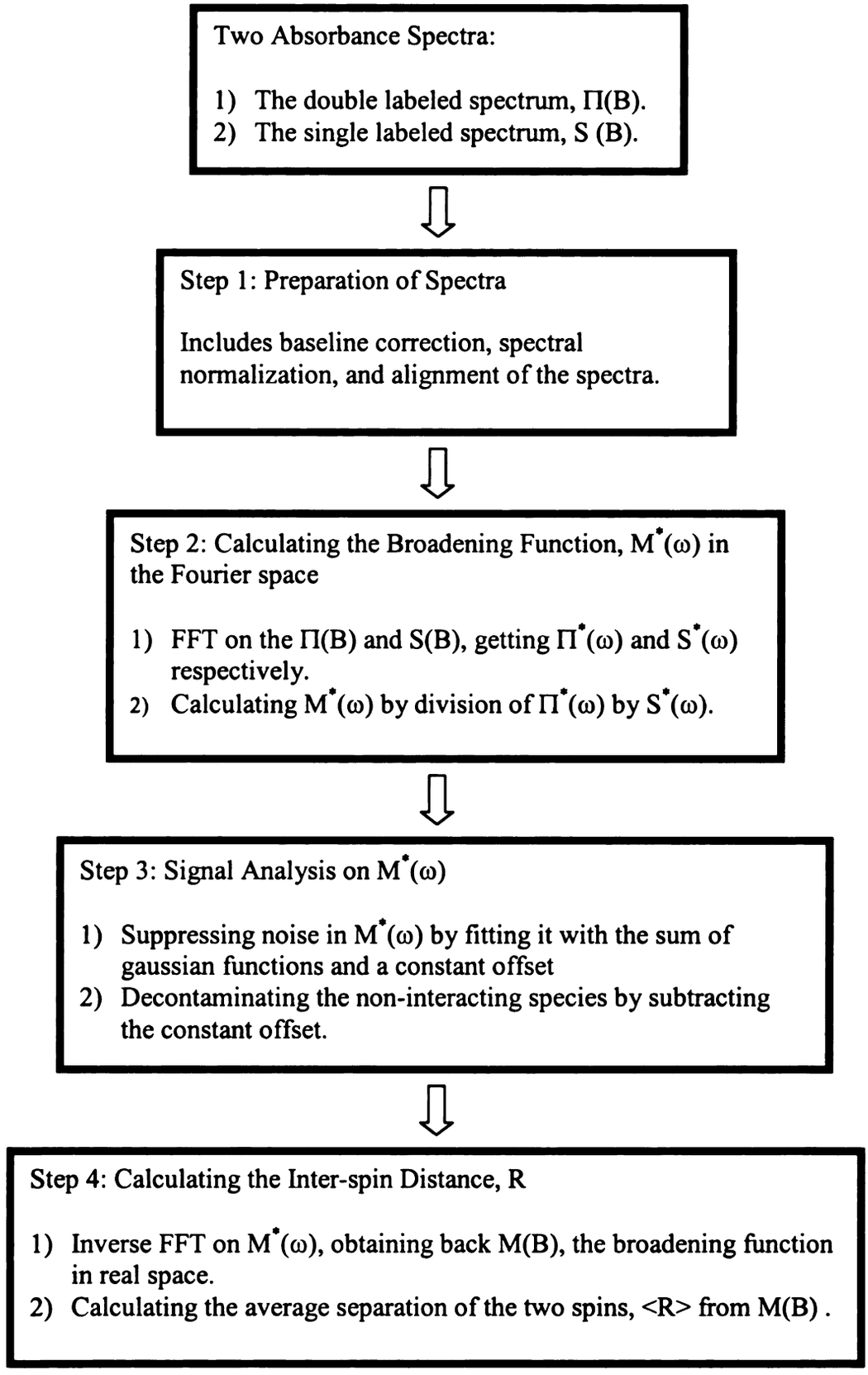
Two Absorbance Spectra:
1) The double labeled spectrum, Π(B).
2) The single labeled spectrum, S (B).
Step 1: Preparation of Spectra
Includes baseline correction, spectral normalization, and alignment of the spectra.
Step 2: Calculating the Broadening Function, M*(ω) in the Fourier space
1) FFT on the Π(B) and S(B), getting Π*(ω) and S*(ω) respectively.
2) Calculating M*(ω) by division of Π*(ω) by S*(ω).
Step 3: Signal Analysis on M*(ω)
1) Suppressing noise in M*(ω) by fitting it with the sum of gaussian functions and a constant offset
2) Decontaminating the non-interacting species by subtracting the constant offset.
Step 4: Calculating the Inter-spin Distance, R
1) Inverse FFT on M*(ω), obtaining back M(B), the broadening function in real space.
2) Calculating the average separation of the two spins, <R> from M(B) .

**Figure 4.5.** The resulting spectra at each step of analysis outlines in Figure 4.4. Taken from (*9*). Copyright permission was obtained.

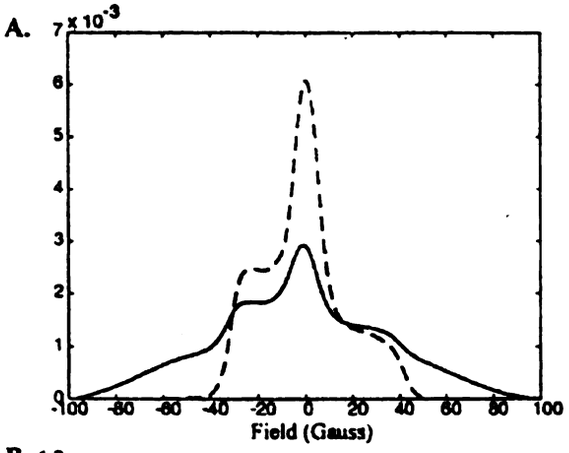


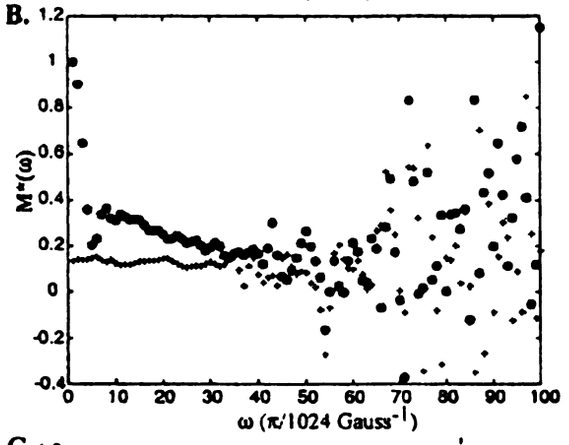


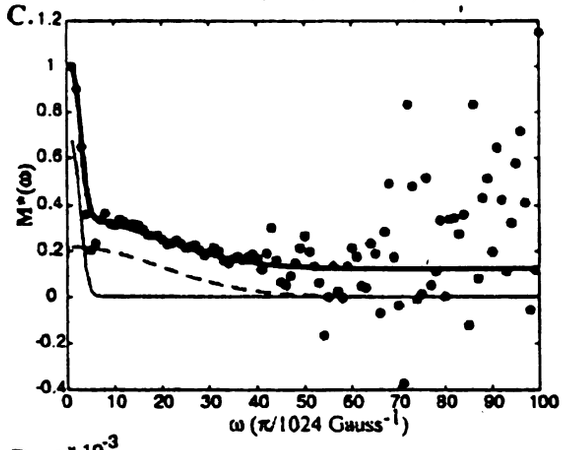


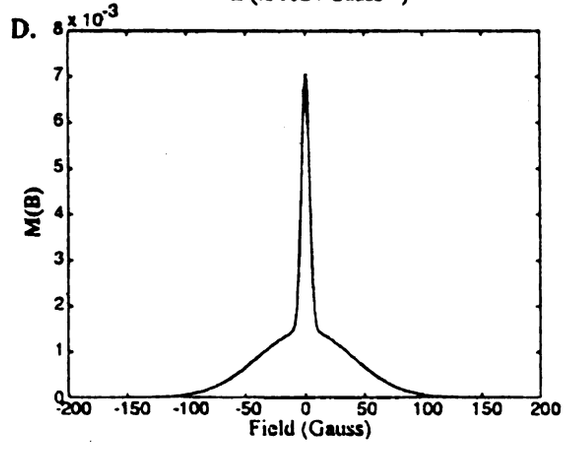


Step 1.

--------  Mono labeled S (B)

━━━━━  Double labeled Π (B)

Step 2.

•  Real part of M*(ω)

+  Imaginary part of M*(ω)

Step 3.

━━━━━  Fitting with two gaussians plus the y-axis offset, with a cut off ω of 60 (π/1024 Gauss $^{-1}$)

———  Separated gaussian components

- - - - - - -

Step 4.

Two gaussians may reflect two distinct spin-spin distances.

spectrum in Fourier space $\frac{\Pi^*(\omega)}{S^*(\omega)}$ contain high amplitude noise at high values of ω (Figure 4.5 B). The noise can be suppressed by fitting the spectral decay in Fourier space with a sum of gaussian functions. In most cases, we have found that it is sufficient to use a sum of only two gaussians. The final dipolar spectrum is obtained by inverse Fourier transformation of the best fitting function. The distribution P(R) of interspin distance leads to broadening functions that are sum of many Pake patterns. This in combination with the EPR line width leads to broadening functions that do not look like Pake patterns. The average distance is calculated using equations 4.18-20 (*9, 21*).

### 4.4.4. Monoradical Impurities

Monoradical impurities due to incomplete spin labeling reactions are a potential problem when analyzing spin-spin interactions. EPR spectra with monoradical contamination can be incorrectly interpreted as showing larger nitroxide-nitroxide distance. The Fourier deconvolution method can separate the dipolar spectrum for the interacting nitroxides from the spectral contribution from the monoradical contaminants. The composite EPR spectrum for a mixture of monoradical and biradicals is given by:

$$\Pi(B)=a\cdot\int_{-\infty}^{\infty} S(B')M(B'-B)dB'+b\cdot S(B) \qquad (4.21)$$

where a is the fraction of the biradical, b is the fraction of the monoradicals with $a+b=1$. Thus after Fourier deconvolution we will have:

$$M'^{*}(\omega)=aM^{*}(\omega)+b \qquad (4.22)$$

in Fourier space and the non-interacting species contributes to the y-axis offset. This y-axis offset b can be subtracted from the dipolar spectrum in the Fourier space (Figure 4.6) (*9, 21*).

## 4.5. Materials and Methods

**Materials.** 1,2-Dioleoyl-sn-Glycero-3-Phosphocholine (DOPC) and 1,2- Dioleoyl -sn-Glycero-3-[Phospho-L-Serine] (Sodium Salt) (DOPS) were obtained from Avanti Polar Lipids Inc. (Alabaster, Alabama). Oleic acid ≥ 99% was purchased from Fluka. All restriction enzymes and DNA modifying enzymes were purchased from New England Biolabs (Beverly, Massachusetts). Ni-NTA was purchased from Qiagen Inc. (Valencia, California). Specially purified aqueous detergent solution (10% solution) of Tween® 20 was obtained from Pierce (Rockford, Illinois). The nitroxide spin label (1-oxyl-2,2,5,5-tetramethylpyrroline-3-methyl)- methanethiosulfonate (MTSSL) was purchased from Reanal Fine Chemical (Budapest, Hungary). Arachidonic acid was obtained from Cayman Chemicals (Ann Arbor, Michigan). Flurbiprofen, Ibuprofen and Naproxen were purchased from Aldrich. The COX-2 selective inhibitor SC-58125 was obtained from Karen Seibert at Pharmacia and other chemicals were purchased from Sigma.

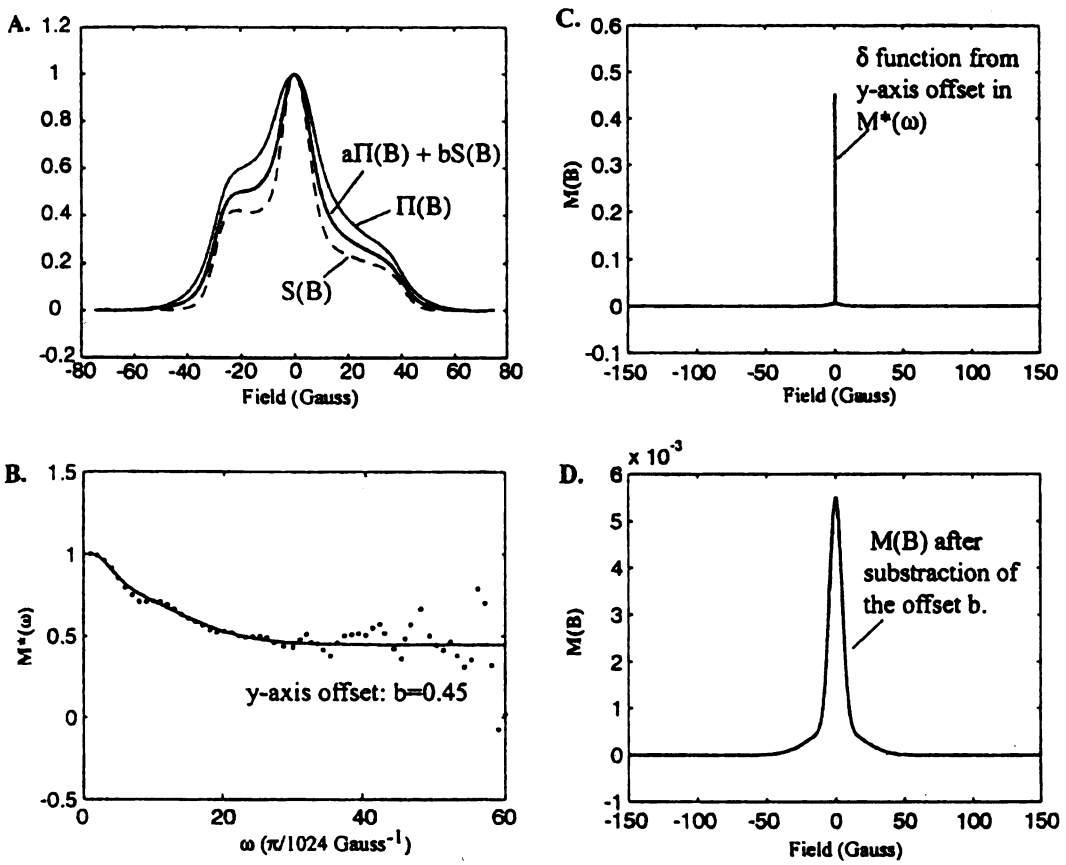


**Figure 4.6.** Analysis of monoradical impurities. Taken from (*9*).

**Sample Preparation.** Protein expressions, purification, spin labeling and liposome incorporation are as described in chapter 3.

**EPR measurements.** All EPR measurements were recorded on a Bruker ESP 300E X-band spectrometer equipped with a TE102 Bruker rectangular cavity. The samples typically 200 μl at concentration of 14 μM labeled protein, were loaded into a 4-mm OD clear fused quartz sample tubes (Wilmad-labglass, New Jersey). The first derivative absorption spectra of the samples at 183 ± 2K were obtained by averaging 4 scans at a scan width of 110 Gauss and each scan time of 4 minutes. The temperature was controlled with Bruker BVT 2000 liquid nitrogen temperature controller. A modulation amplitude of 1 Gauss was used. The microwave power was maintained at 1 milliWatt to avoid the saturation of the EPR spectra.

## 4.6. Results

The site-directed spin labeling technique requires a template cDNA that does not contain reactive cysteines. A "cysteine-less" template was therefore prepared by mutating cysteines at positions 299 and 526 in human histidine-tagged COX-2 to serines. The cysteine-less enzyme retains 70% of the cyclooxygenase activity of the native His-tagged COX-2, indicating that cysteines 299 and 526 are not required for catalysis and these substitutions only minimally distort the structure of the protein. Four helices (A-D) form the membrane-binding domain that is also the mouth of the cyclooxygenase active site (*22*). These helices were chosen as labeling sites because this is the region in which the

most flexibility is observed in the crystal structure of COX (*23, 24*) . By using a cysteine-less template, ten mutants were constructed, each containing the I98C substitution in helix D, and one of five amino acid substitutions in opposing helix B (T73C, V74C, H75C, Y76C and I77C) or one of the five amino acid substitutions in adjacent helix C (F84C, W85C, N86C, V87C and V88C). Nine of the ten double cysteine mutants retained significant cyclooxygenase activities (10-55% of the native) (Table 4.2). One mutation, W85C, reduced cyclooxygenase activity by 95-98%, indicating that this residue plays a critical role in protein structure or catalysis and this mutation significantly alters the COX-2 structure. Conjugation of the cysteines with the spin label MTSSL had no effect on the activity. These results indicate that with one exception the cysteine substitutions and subsequent conjugation with the spin label do not grossly disrupt the native structure of the enzyme. Several studies indicate that the nitroxide spin labels do not perturb the structure and other properties of the biomolecules (*25, 26*).

Each of the ten pair-wise mutant proteins were purified and then reconstituted with 2 molar equivalent of cobalt-protoporphyrin IX. Binding of Co-PPIX to COX is identical to hemin (*27*). Hemin was not used because even a small amount of oxidized Fe (III) in hemin could cause dipole-dipole interaction with the spin labels. Cobalt-PPIX is diamagnetic and will not have any magnetic interaction with the spin labels. Flurbiprofen (time-dependent COX inhibitor), naproxen and ibuprofen (time independent COX inhibitors), SC58125 (COX-2 selective inhibitor) and arachidonic acid (the primary substrate for COX-2) were used to examine conformational changes in COX-2. The inhibitors were added with 20 fold molar excess with respect to protein for each sample. EPR spectra of apoenzymes, holoenzymes, NSAID-treated holoenzymes and arachidonic

acid-bound holoenzymes were recorded at 183 K. The first derivative EPR spectra were integrated (absorbance) and normalized to the same number of spins. The normalized absorbance spectra of solubilized spin-labeled COX-2 holoenzymes were overlaid with the normalized absorbance spectra of the spin-labeled COX-2 complexed with various NSAIDs, with arachidonic acid, or with the spectra of the spin labeled apoenzymes (Appendix C). All the spectra superimposed on each other, indicating that binding of heme, arachidonic acid, and NSAIDs had no significant effect on the conformation of COX-2.

The normalized absorbance spectra of solubilized spin-labeled COX-2 apoenzymes and COX-2 holoenzymes complexed with various NSAIDs or arachidonic acid were overlaid with the normalized absorbance spectra of liposome incorporated spin-labeled COX-2 apoenzymes and COX-2 holoenzymes complexed with various NSAIDs or arachidonic acid (Appendix C). The slight differences in the line broadening of the EPR spectra in the presence and absence of liposomes indicate that the spin-spin interactions in mutants T73C/I98C, V74C/I98C, H75C/I98C, Y76C/I98C, I77C/I98C, F84C/I98C and W85C/I98C were slightly stronger when the proteins were in the detergent. This observation is consistent with the interpretation that there may be a small conformational difference between the COX-2 in the detergent versus the phospholipid bilayer.

In helix C mutants (F84C, W85C, N86C, V87C and V88C), the dipolar line broadening is due to the interaction of each spin labeled residue with the spin labeled I98C residue. The interactions between the two subunits (inter-helix spin-spin coupling) do not contribute to the line broadening because the residues are far apart from each other

(Figures 4.7-4.11). The Fourier convolution/deconvolution method can only be used when the distances between the two spin labels are between 8-25 Å (*21*). The distances between each residue in helix C and I98C are in the range that can be measured by Fourier convolution / deconvolution method. Distances more than 25 Å do not contribute to the line broadening. On the other hand for helix B mutants (T73C, V74C, H75C, Y76C and I77C), the dipolar broadening is due to the interaction of more than two spin labeled residues (Figures 4.12-4.16). Because more than two spin labeled amino acids give rise to the line broadening, it is not possible to measure the distances between the helix B mutants and I98C.

All the mutants in helix B show a stronger spin-spin interaction in the detergent than in the liposomes. This indicates that in liposomes the spin labels are further apart from each other. There are two explanations for this observation.

1) There is a distance increase between the two spin label residues within each monomer *e.g.* an increase in distance between spin labeled-H75C and spin labeled-I98C within a monomer.
2) There is an increase in the distance between the two subunits *i.e.* an increase in the distance between two spin labeled residues between the two monomers.

To determine which explanation is true the distance measurements were done on a series of singly labeled residues in helix B (T73C, V74C, H75C, Y76C and I77C) in detergent and in the liposomes. The normalized absorbance spectra of each mutant in liposome and in detergent were superimposed on each other (Figure 4.17). The superimposition did not show any changes in the line broadening which indicated that there was no distance change between the two spin labeled residues between the two

monomers. The conclusion is that the slight change in the line broadening is due to the increase in distance between the two spin label residues within each monomer.

Fourier convolution deconvolution analysis of the broadening functions resulting from spin-spin interaction of the doubly labeled COX-2 (between helix C mutants and I98C) was used to calculate the molecular distance between the nitroxides by comparing the broadening of the doubly labeled protein to the singly labeled reference spectrum using a FORTRAN program written by Professor Yeon-Kyon Shin for Matlab ® (13) (see Appendix B for the outout of Matlab analysis). In this study the H75C single mutant was used as the reference spectrum. The inter-nitroxide distances between the five mutants in helix C and I98C in helix D in the detergent and in the liposome were calculated (see Table 4.2).

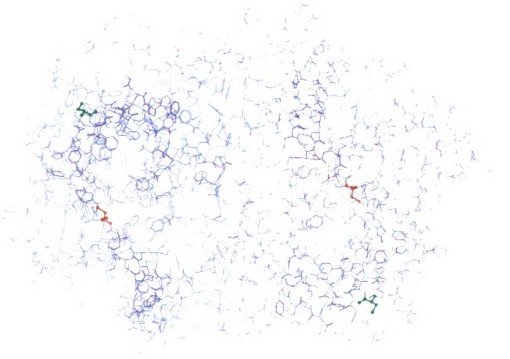

**Figure 4.7.** The X-ray structure of murine holo-COX-2 (5COX) with two cysteine substitution mutations at residues F84and I98.
I98C is shown in green. F84C is shown in red.
The distance between the two Cα s of the two I98C residues in dimer is 66.32 Å.
The distance between the two Cα s of the two F84C residues in dimer is 48.43 Å.
The distance between the Cα of I98C and Cα of F84C within a monomer is 22.01 Å.

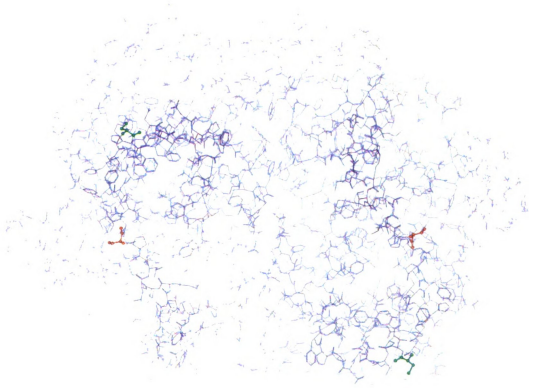

**Figure 4.8.** The X-ray structure of murine holo-COX-2 (5COX) with two cysteine substitution mutations at residues W85 and I98.
I98C is shown in green. W85C is shown in red.
The distance between the two Cα s of the two I98C residues in dimer is 66.32 Å.
The distance between the two Cα s of the two W85C residues in dimer is 52.89 Å.
The distance between the Cα of I98C and Cα of W85C within a monomer is 22.72 Å.

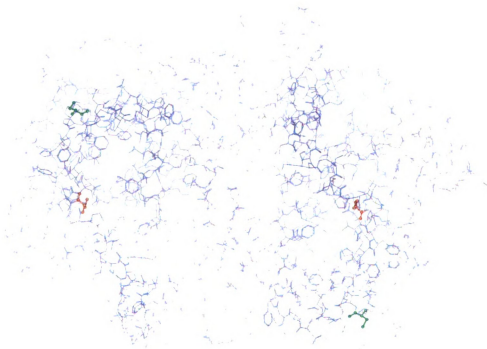

**Figure 4.9.** The X-ray structure of murine holo-COX-2 (5COX) with two cysteine substitution mutations at residues N86 and I98.
I98C is shown in green. N86C is shown in red.
The distance between the two Cα s of the two I98C residues in dimer is 66.32 Å.
The distance between the two Cα s of the two N86C residues in dimer is 51.00 Å.
The distance between the Cα of I98C and Cα of N86C within a monomer is 21.32 Å.

**Figure 4.10.** The X-ray structure of murine holo-COX-2 (5COX) with two cysteine substitution mutations at residues V87 and I98.
I98C is shown in green. V87C is shown in red.
The distance between the two Cα s of the two I98C residues in dimer is 66.32 Å.
The distance between the two Cα s of the two V87C residues in dimer is 58.02 Å.
The distance between the Cα of I98C and Cα of V87C within a monomer is 19.97 Å.

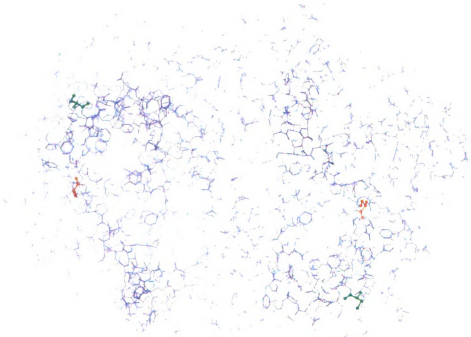

**Figure 4.11.** The X-ray structure of murine holo-COX-2 (5COX) with two cysteine substitution mutations at residues V88 and I98.
I98C is shown in green. V88C is shown in red.
The distance between the two Cα s of the two I98C residues in dimer is 66.32 Å.
The distance between the two Cα s of the two V88C residues in dimer is 57.05 Å.
The distance between the Cα of I98C and Cα of V88C within a monomer is 18.14 Å.

**Figure 4.12.** The X-ray structure of murine holo-COX-2 (5COX) with two cysteine substitution mutations at residues T73 and I98.
I98C is shown in green. T73C is shown in red.
The distance between the two Cα s of the two I98C residues in dimer is 66.32 Å.
The distance between the two Cα s of the two T73C residues in dimer is 44.96 Å.
The distance between the Cα of I98C and Cα of T73C within a monomer is 39.67 Å.

**Figure 4.13.** The X-ray structure of murine holo-COX-2 (5COX) with two cysteine substitution mutations at residues V74 and I98.
I98C is shown in green. V74C is shown in red.
The distance between the two Cα s of the two I98C residues in dimer is 66.32 Å.
The distance between the two Cα s of the two V74C residues in dimer is 44.66 Å.
The distance between the Cα of I98C and Cα of V74C within a monomer is 38.59 Å.

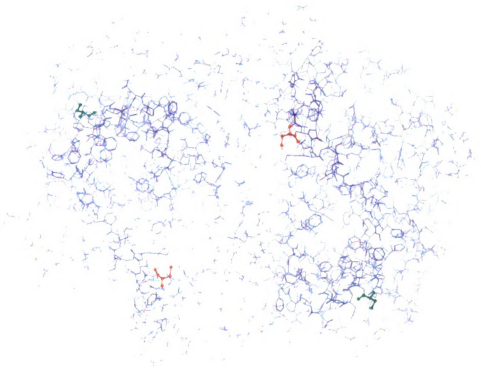

**Figure 4.14.** The X-ray structure of murine holo-COX-2 (5COX) with two cysteine substitution mutations at residues H75 and I98.
I98C is shown in green. H75C is shown in red.
The distance between the two Cα s of the two I98C residues in dimer is 66.32 Å.
The distance between the two Cα s of the two H75C residues in dimer is 37.60 Å.
The distance between the Cα of I98C and Cα of H75C within a monomer is 35.70 Å.

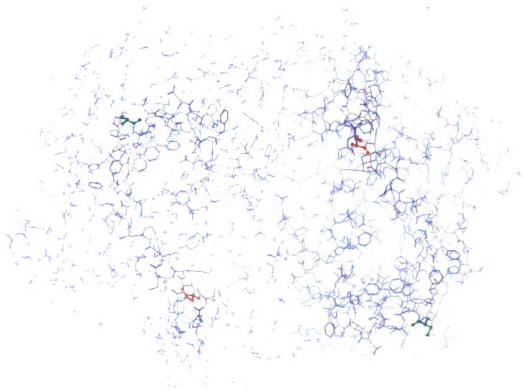

**Figure 4.15.** The X-ray structure of murine holo-COX-2 (5COX) with two cysteine substitution mutations at residues Y76 and I98.
I98C is shown in green. Y76C is shown in red.
The distance between the two Cα s of the two I98C residues in dimer is 66.32 Å.
The distance between the two Cα s of the two Y76C residues in dimer is 40.24 Å.
The distance between the Cα of I98C and Cα of Y76C within a monomer is 34.78 Å.

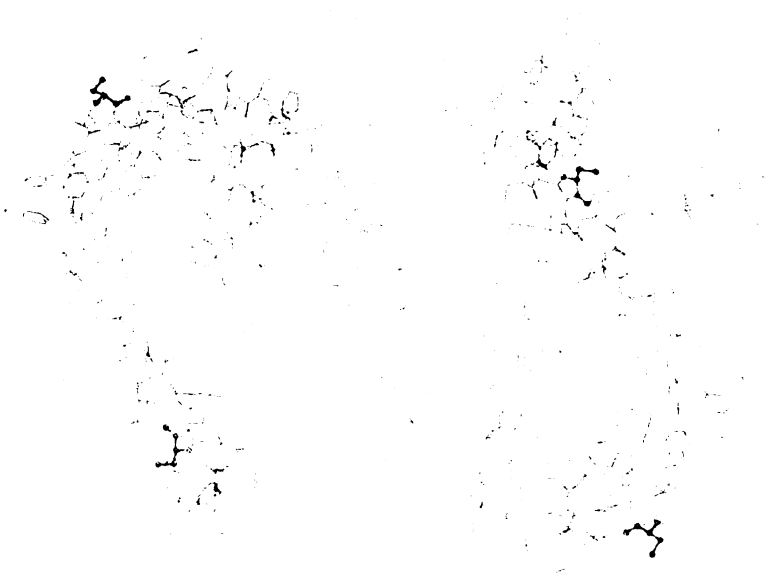

**Figure 4.16.** The X-ray structure of murine holo-COX-2 (5COX) with two cysteine substitution mutations at residues I77 and I98.
I98C is shown in green. I77C is shown in red.
The distance between the two Cα s of the two I98C residues in dimer is 66.32 Å.
The distance between the two Cα s of the two I77C residues in dimer is 45.73 Å.
The distance between the Cα of I98C and Cα of I77C within a monomer is 34.34 Å.

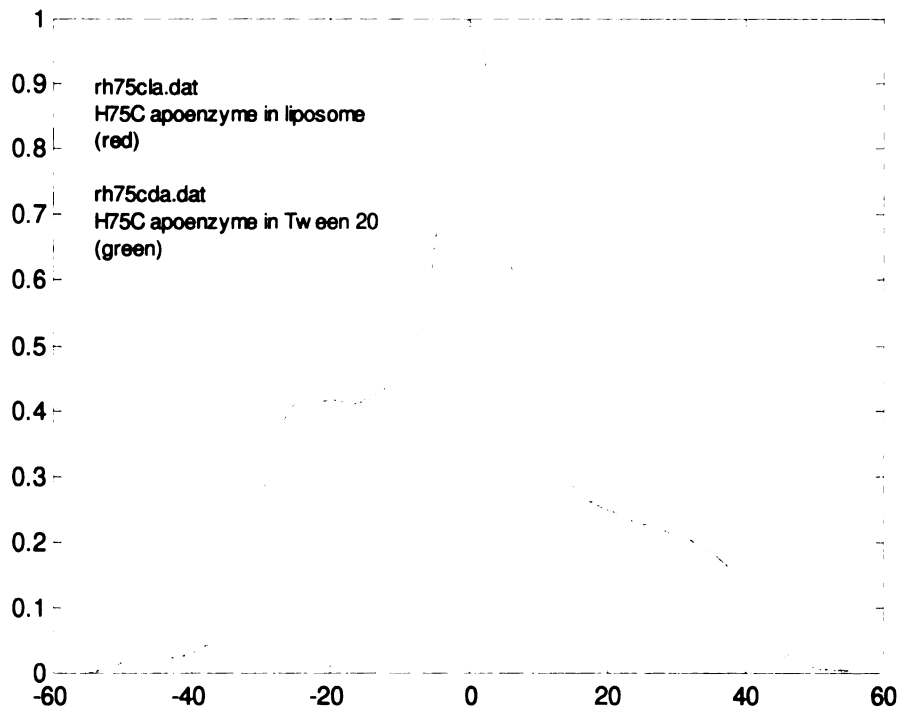


**Figure 4.17.** Overlay of absorbance EPR spectra of H75C in liposome (red) and H75C in Tween 20 (green). The two spectra completely superimpose on each other and show no change in the line broadening.

## 4.7. Discussion

All NSAIDs function by blocking prostaglandin biosynthesis through inhibition of COX, but different drugs achieve this via different mechanisms. Some NSAIDs such as ibuprofen are classical time independent competitive inhibitors, which form reversible enzyme-inhibitor complexes (EI). Other NSAIDs such as flurbiprofen are time dependent, slow tight-binding inhibitors that initially form a reversible EI complex, which is then gradually converted to an inactive form (EI*).

$$E + I \leftrightarrow EI(Time-independent)$$

$$E + I \leftrightarrow EI \leftrightarrow EI^{*}(Time-dependent)$$

The difference between time-dependent and time-independent inhibition is clinically relevant, as it underlies the isoform-specific inhibition seen with selective COX-2 inhibitors. COX-2 selective inhibitors are time-dependent inhibitors of COX-2 forming tight-binding and slowly reversible complexes with this isozyme, but are simple competitive reversible inhibitors of the COX-1 isozyme.

An understanding of the EI→EI* transition associated with time-dependent inhibition should therefore be useful in the rational design of novel therapeutics.

Different hypothesis have been advanced to explain this phenomenon, including the invocation of a structural rearrangement between EI and EI* and the suggestion that time dependent and time-independent inhibitors occupy distinct binding sites (*28-30*).

To gain deeper insight into the mechanism of NSAID binding we have used double site-directed spin labeling combined with EPR spectroscopy. Our results also indicated no detectable conformational changes in the structure of COX.

Thus if the EI→EI* transition corresponds to a conformational rearrangement, it must be small or in the region of COX-2 that we did not observe.

The slight differences in the line broadening of T73C/I98C, V74C/I98C, H75C/I98C, Y76C/I98C, I77C/I98C, F84C/I98C and W85C/I98C mutants in the detergent versus liposome show a small conformational change between the structure of the protein in the detergent and the structure of the protein in the lipid bilayers. This observation is consistent with the interpretation that the mouth of the cyclooxygenase channel in more open in the liposome environment. Previous studies on other proteins have also suggested a slight conformational difference in the structure of membrane proteins in the presence and absence of lipid bilayers (*31*).

**Table 4.2.** EPR determined inter-nitroxide for mutants in Helix C and I98C.

| SAMPLE | INTER NITROXIDE DISTANCE (Å) IN DETERGENT | INTER NITROXIDE DISTANCE (Å) IN LIPOSOME |
|---|---|---|
| F84C/I98C | 15.358 ± 0.420 | 15.536 ± 0.976 |
| W85C/I98C | 16.086 ± 0.231 | 16.734 ± 0.180 |
| N86C/I98C | 14.581 ± 0.481 | 15.188 ± 0.277 |
| V87C/I98C | 16.194 ± 0.352 | 16.489 ± 0.244 |
| V88C/I98C | 14.384 ± 0.301 | 14.226 ± 0.603 |

## 4.8. References


1. Smith, W. L., and DeWitt, D.L. (1996) in *Therapeutic Immunology* (Austen, K. F., Burakoff, S.J., Rosen, F.S., and Storm, T.B., Ed.) pp 119-131, Blackwell Scientific Publications, Inc., Cambridge, MA.

2. Kulmacz, R. J., and Lands, W. E. M. (1982) *Biochemical and Biophysical Research Communications 104*, 758-764.

3. Chen, Y. N. P., Bienkowski, M. J., and Marnett, L. J. (1987) *Journal of Biological Chemistry 262*, 16892-16899.

4. Kalgutkar, A. S., Crews, B. C., and Marnett, L. J. (1996) *Biochemistry 35*, 9076-9082.

5. Kulmacz, R. J. (1989) *Journal of Biological Chemistry 264*, 14136-14144.

6. Selinsky, B. S., Gupta, K., Sharkey, C. T., and Loll, P. J. (2001) *Biochemistry 40*, 5172-5180.

7. Koteiche, H. A., and McHaourab, H. S. (1999) *Journal of Molecular Biology 294*, 561-577.

8. Berengian, A. R., Parfenova, M., and McHaourab, H. S. (1999) *Journal of Biological Chemistry 274*, 6305-6314.

9. Berliner L.J., E. S. S., Eaton G.R. (2000) *Distance Measurements in Biological Systems by EPR*, Vol. 19, Kluwar Academic/Plenum Publishers, New York, New York.

10. Hustedt, E. J., Smirnov, A. I., Laub, C. F., Cobb, C. E., and Beth, A. H. (1997) *Biophysical Journal 72*, 1861-1877.

11. Eaton, S. S., and Eaton, G. R. (1982) *Journal of the American Chemical Society 104*, 5002-5003.

12. Eaton, S. S., More, K. M., Sawant, B. M., and Eaton, G. R. (1983) *Journal of the American Chemical Society 105*, 6560-6567.

13. Kokorin, A. I., and Formazyuk, V. E. (1981) *Molecular Biology 15*, 722-728.

14. Kokorin, V. V., Osipenko, I. A., Polotnyuk, V. V., Zolkina, S. V., and Shirina, T. V. (1982) *Fizika Metallov I Metallovedenie 54*, 48-53.

15. Milov, A. D., and Tsvetkov, Y. D. (1997) *Applied Magnetic Resonance 12*, 495-504.

16. Milov, A. D., Maryasov, A. G., and Tsvetkov, Y. D. (1998) *Applied Magnetic Resonance 15*, 107-143.

17. Raitsimring, A., Peisach, J., Lee, H. C., and Chen, X. (1992) *Journal of Physical Chemistry 96*, 3526-3531.

18. Martin, R. E., Pannier, M., Diederich, F., Gramlich, V., Hubrich, M., and Spiess, H. W. (1998) *Angewandte Chemie-International Edition 37*, 2834-2837.

19. Saxena, S., and Freed, J. H. (1997) *Journal of Chemical Physics 107*, 1317-1340.

20. Saxena, S., and Freed, J. H. (1996) *Chemical Physics Letters 251*, 102-110.

21. Rabenstein, M. D., and Shin, Y. K. (1995) *Proceedings of the National Academy of Sciences of the United States of America 92*, 8239-8243.

22. Picot, D., Loll, P. J., and Garavito, R. M. (1994) *Nature 367*, 243-249.

23. Kurumbail, R. G., Stevens, A. M., Gierse, J. K., McDonald, J. J., Stegeman, R. A., Pak, J. Y., Gildehaus, D., Miyashiro, J. M., Penning, T. D., Seibert, K., Isakson, P. C., and Stallings, W. C. (1996) *Nature 384*, 644-648.

24. Luong, C., Miller, A., Barnett, J., Chow, J., Ramesha, C., and Browner, M. F. (1996) *Nature Structural Biology 3*, 927-933.

25. Langen, R., Oh, K. J., Cascio, D., and Hubbell, W. L. (2000) *Biochemistry 39*, 8396-8405.

26. Postnikova, G. B. (1996) *Biochemistry-Moscow 61*, 679-693.

27. Malkowski, M. G., Ginell, S. L., Smith, W. L., and Garavito, R. M. (2000) *Science 289*, 1933-1937.

28. Copeland, R. A., Williams, J. M., Giannaras, J., Nurnberg, S., Covington, M., Pinto, D., Pick, S., and Trzaskos, J. M. (1994) *Proceedings of the National Academy of Sciences of the United States of America 91*, 11202-11206.

29. Llorens, O., Perez, J. J., Palomer, A., and Mauleon, D. (1999) *Bioorganic & Medicinal Chemistry Letters 9*, 2779-2784.

30. So, O. Y., Scarafia, L. E., Mak, A. Y., Callan, O. H., and Swinney, D. C. (1998) *Journal of Biological Chemistry 273*, 5801-5807.

31. He, M. M., Voss, J., Hubbell, W. L., and Kaback, H. R. (1997) *Biochemistry 36*, 13682-13687.

# Chapter 5

# Conclusion and Future Direction

The cyclooxygenase isozymes have been studied extensively because of their essential and regulatory role in prostaglandin synthesis and also because they are the sites of action of the Nonsteroidal anti-inflammatory drugs (NSAIDs) such as aspirin, flurbiprofen, naproxen and new selective COX-2 inhibitors. However very little is known about how the membrane binding domain of COX isozymes interact with the lipid bilayers. It in not possible to orient the COX isozymes in a membrane, or to determine lipid binding sites in the isozymes from a crystal structure, as few lipid or detergent molecules are visible using X-ray analysis.

The goal of this dissertation is to study the membrane-binding domain of hCOX-2 using site-directed spin labeling technique.

Site-directed spin labeling (SDSL) is emerging as a promising tool for the determination of protein topography. In the research described in chapter 3 of this dissertation, 25 mutant enzymes that contained single reactive cysteines substituted for amino acids within the hCOX-2 membrane-binding domain were constructed and spin labeled. The accessibility of each protein-bound spin label with freely diffusing oxygen as a non-polar paramagnetic reagent, and NiEDDA as a polar paramagnetic reagent, was measured using power saturation EPR spectroscopy. Our results show the accessibility parameter ($\Pi$) for both oxygen and NiEDDA, has a periodicity of 3.6 for helices A and C. These results are where the helix axis lies along an interface with protein. Furthermore, $\Pi_{oxygen}$ and $\Pi_{NiEDDA}$ both have the same period and phase. Our results indicate that both polar and non-polar paramagnetic relaxers do not access the amino acids located in the membrane-binding domain due to the very low values of $\Pi_{NiEDDA}$ and $\Pi_{oxygen}$. This indicates that the membrane binding domain of hCOX-2 is located in the

interfacial region of the membrane and is sandwiched between the main body of the 144 kDa COX dimer and the lipid bilayers. We have identified 3 amino acids that participate in anchoring the protein to the lipid bilayers, but most of the amino acids in the membrane-binding domain are not in contact with the hydrocarbon core of the lipid bilayers. hCOX-2 is the first peripheral membrane protein mapped using site-directed spin labeling. COX isozymes and squalene hopene cyclase are the only members of the new class of monotopically-associated peripheral membrane proteins. The results of the SDSL experiments in this dissertation might have general applicability to this new class.

To fully investigate the MBD of hCOX-2, mutant enzymes that contain single reactive cysteines substituted for amino acids in the loops of hCOX-2 membrane-binding domain need to be constructed and investigated by site-directed spin labeling method.

Another aspect of my project was to study the conformational changes in the mouth of the cyclooxygenase channel. The purpose of this research was to determine whether the COX substrate and inhibitor binding sites are flexible, *e.g.*, can be opened and closed.

In the research described in chapter 4 of this dissertation, 10 cysteine double mutants located in the helices that form the opening of the cyclooxygenase active site and membrane-binding of hCOX-2 were constructed. The dipolar broadening in the presence and absence NSAIDs, arachidonic acid and heme were compared in detergent. The same experiments were also performed in liposomes. The inter-spin distance measurements were done using the Fourier convolution/deconvolution technique.

Our results indicated that binding of heme, arachidonic acid, and NSAIDs had no significant effect on the conformation of hCOX-2. However, a slight conformational change was observed in the structure of the enzyme in the presence of the lipid bilayers.

In order to further investigate the possibility of the conformational change in the mouth of the cyclooxygenase channel, time resolved EPR experiments on liquid samples at room temperature need to be done in the presence and absence of various NSAIDs, arachidonic acid and lipid bilayers.

# Appendix A

## The Data Analysis Procedures for the Experiments Described in Chapter 3.

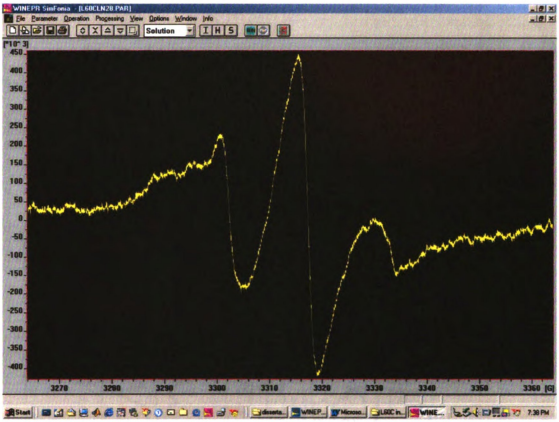


**Figure 1A:**

**Step one**: To open the spectrum with Bruker's SimFonia software.

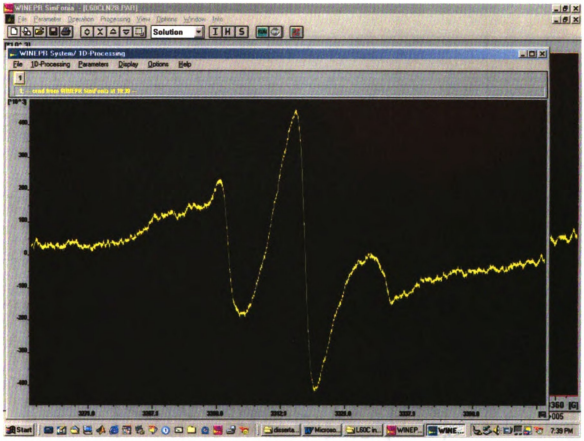


**Figure 2A:**

**Step two:** To export the spectrum to WinEPR software.

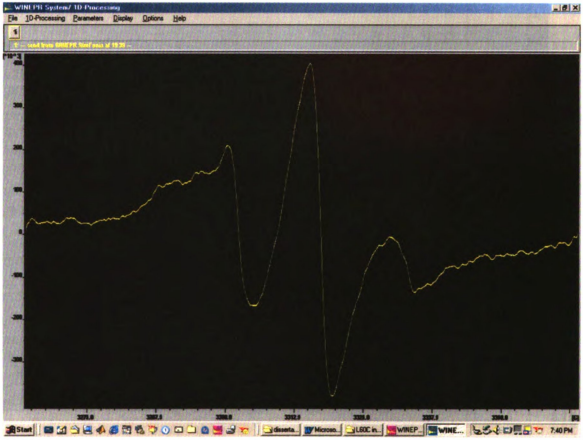


**Figure 3A**:

**Step three:** To filter the noise in the spectrum.

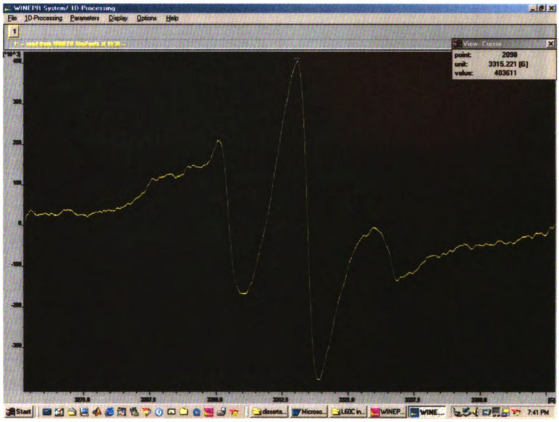


**Figure 4A:**

**Step four:** To measure the peak to peak amplitude.

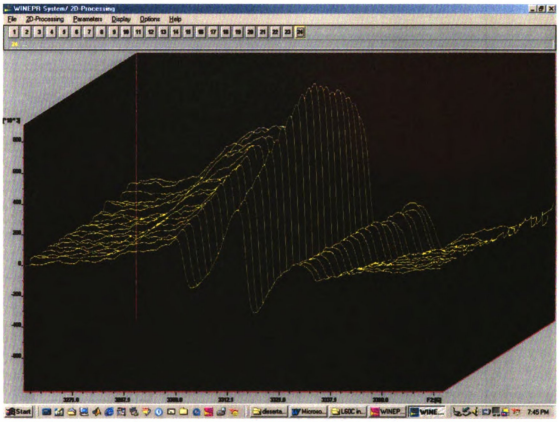


**Figure 5A:**

The stack plot of EPR spectra. Each spectrum was acquired in a different microwave power.

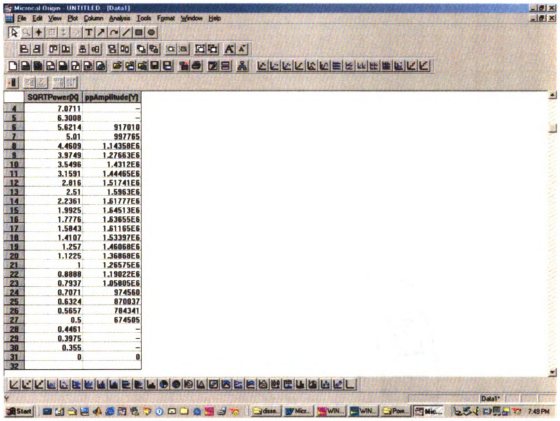


**Figure 6A:**

**Step five:** Peak to peak amplitude $m_{I=0}$ of a first derivative EPR signal is a function of the square root of the incident microwave power.

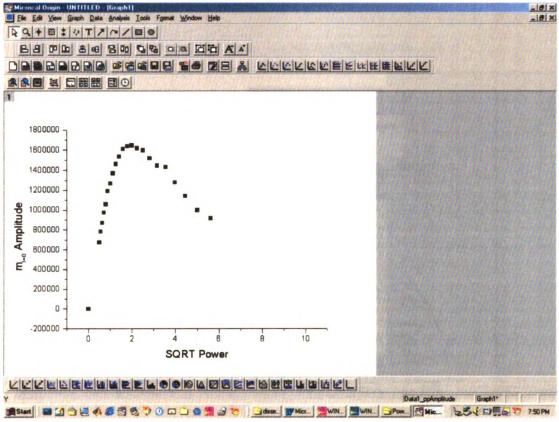


**Figure 7A:**

**Step six**: To plot the peak to peak amplitude of spectra as a function of the square root of the incident microwave power.

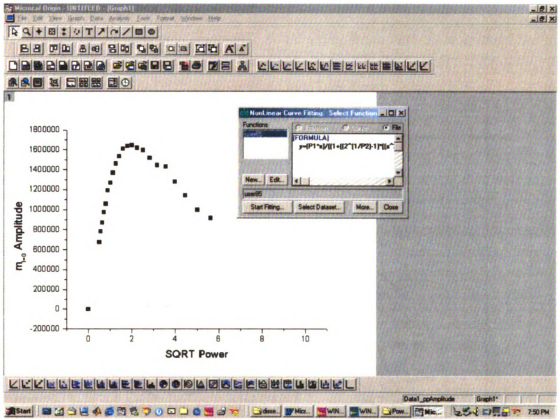


**Figure 8A:**

**Step seven:** Curve fitting the curve to the following equation:

Y=(P1*x)/((1+((2^(1/P2)-1)*((x^2)/P3)))^(P2))

This equation is same as equation 3.22 in chapter 3.

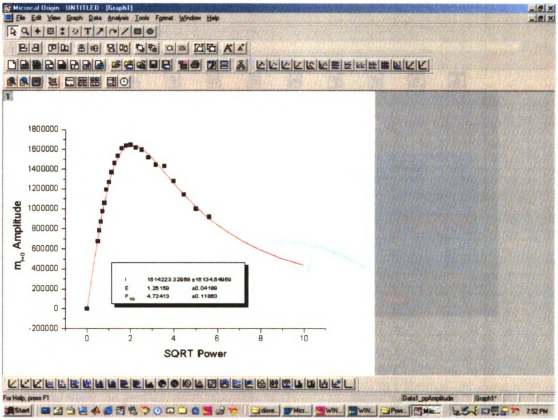


**Figure 9A:**

**Step eight**: To obtain the unknown values.

P1=I (scaling factor), P2=E (spectral homogeneity factor) and P3=$P_{1/2}$.

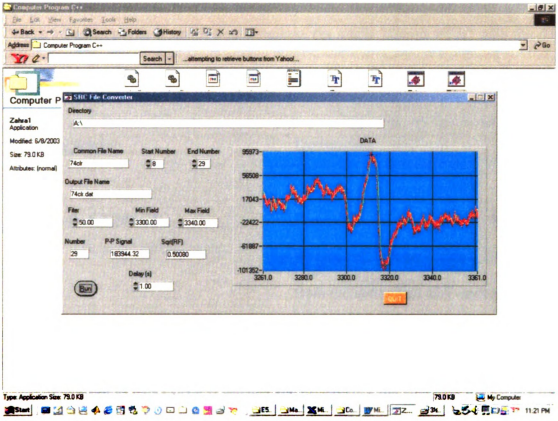


**Figure 10A:**

A new software was recently written in C programming language in collaboration with Professor Michael Romalis in Princeton University.

The software will automatically load the spectra, filter them and measure their peak to peak amplitude $m_{I=0}$ as a function of the square root of the microwave power and save the results in a *.dat file.

# Appendix B

## Application of MATLAB ® Scripts for Measuring the Distance between Two Nitroxide Spin Labels

A FORTRAN program has been written for MATLAB® by Professor Y.K. Shin that can be used for Fourier convolution deconvolution analysis of dipolar spectra. Output of an example analysis that compares the singly labeled H75C with the doubly labeled N86C/I98C mutant is presented below:

| Computer Screen | Explanation |
|---|---|
| EDU» load v8698dh1.dat | Load the spectrum of the double-labeled N86C/I98C mutant. EPR data are saved from the instrument as Y-coordinates only. |
| EDU» load rh75cdh.dat | Load the singly labeled spectrum of H75 used as a reference (Y-coordinate only). |
| EDU» v8698dh1f=eprfile(v8698dh1); | Defines the double mutant data file as an EPR spectrum. The *f* at the end of the file name specifies that the file is used as a function. |
| sweepwidth in Gauss?110 | This is the sweep width of the EPR spectrum. |

| | |
|---|---|
| absorbance(1) or differential(0)?0 | EPR data is usually collected as a first derivative spectrum. |
| Shift Field? Yes:input number of points, No=00 | Do not shift the field. |
| Correct Field? Yes=1, No=01 | This corrects for minor variations in the magnetic field that occur from sample to sample. |
| EDU» rh75cdhf=eprfile(rh75cdh); | Defines the single mutant data file as an EPR spectrum. |
| sweepwidth in Gauss?110 | The sweep width for both single and double mutant should be same. |
| absorbance(1) or differential(0)?0 | EPR data is usually collected as a first derivative spectrum. |
| Shift Field? Yes:input number of points, No=00 | Do not shift the field. |
| Correct Field? Yes=1, No=01 | This corrects for minor variations in the magnetic field that occur from sample to sample. |

| | |
|---|---|
| EDU» specintin=v8698dh1f; | This defines *v8698dh1f* as the doubly labeled spectrum. |
| EDU» specnonin=rh75cdhf; | This defines *rh75cdhf* as the singly labeled reference spectrum. |
| EDU» ftbroadf | This calculates the broadening function for the doubly labeled spectrum over the distribution P(r) and carries out a Fourier transformation to isolate the electron-electron dipolar interaction. |
| what color would you like?'r' | 'Red' is the color of singly labeled absorbance spectrum (See Figure B1). |
| Current plot held | |
| what color would you like?'g' | 'Green' is the color of doubly labeled absorbance spectrum (See Figure B1). |
| Current plot released | The Fourier transformation of the calculated broadening function is plotted. |
| EDU» sweep_width=220; | Input value as 2x the actual sweep width. |

| | |
|---|---|
| EDU» tau=[0.4 6 0.6 60 0]; | Use Figure B3 to determine the biphasic decay components and the offset representing the percentage of monoradical within the sample. |
| EDU» fflowfit | Command to solve for the distance between the nitroxides. |
| What is the cutoff?58 | Value obtained from the Fourier transform where the decay function reverts to noise in Figure B4. |
| Current plot held | The program is plotting the various output displays seen in Figure B5. |
| Current plot released | |
| Current plot held | |
| Current plot released | |

tau = Calculated tau values. The sample was

0.4962 6.9169 0.5031 50.1327 0.0007 monoradical free.

sum_of_components =

1.0000

what color would you like?'r' 'Red'

what color would you like?'r' 'Red'

Current plot held

what color would you like?'r' 'Red'

B_dev =

7.8738

what color would you like?'r' 'Red'

Current plot held

what color would you like?'r' 'Red'

what color would you like?'r' 'Red'

what color would you like?'r' 'Red'

avg_2B = 6.4716 This is the calculated value for

$\langle 2B \rangle$

| | |
|---|---|
| distance =14.7723 | This is the calculated value of r. |
| finish(0)? 0 | End of the calculation. |

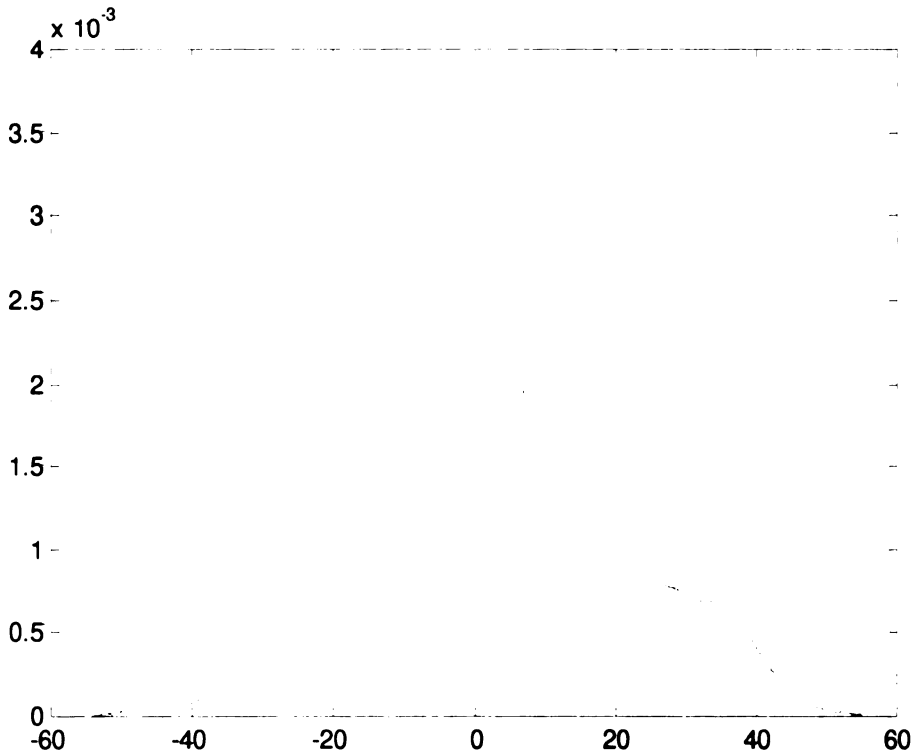


**Figure B1.** Overlaid Absorbance spectra of singly and doubly labeled proteins. The overlay spectra of the singly labeled H75C mutant (red) and the doubly labeled N86C/I98C mutant (green) are shown above.
The spectrum of doubly labeled protein is defines as:

$$\Pi(B) = \int_{-\infty}^{\infty} S(B')M(B'-B)dB'$$

For detail discussion see chapter 4.

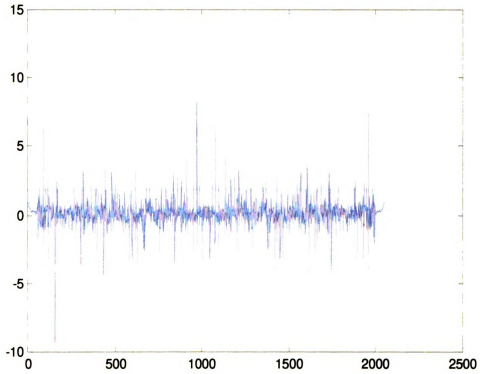


**Figure B2.** Fourier transform of $\Pi^*(\omega)$, the doubly labeled spectrum. Only the ends of this curve contain useful information. A close-up of this is shown in the next figure.

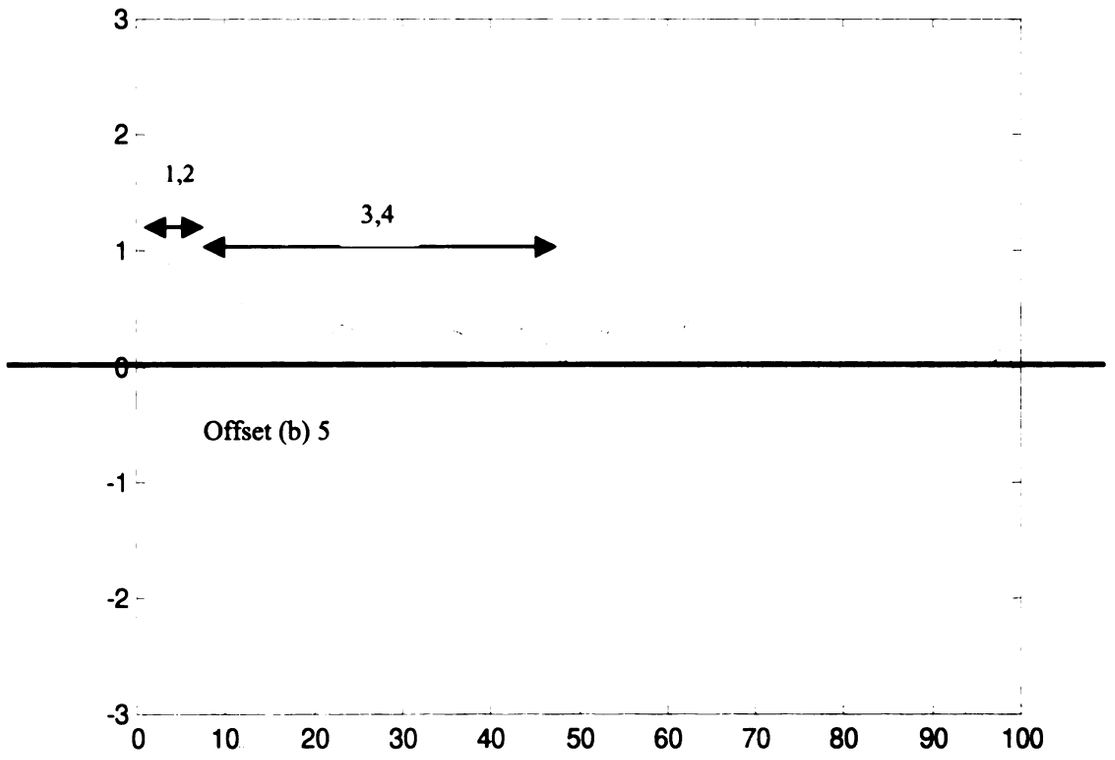


**Figure B3.** Zoom of Fourier transform of doubly labeled spectrum. This figure is used to obtain the five components referred to as the tau. Tau is made up of 5 components [1, 2, 3, 4, 5]. The first two components are the rise and run of the initial decay, the third and fourth components are the rise and run of the second decay and the final component is the offset.

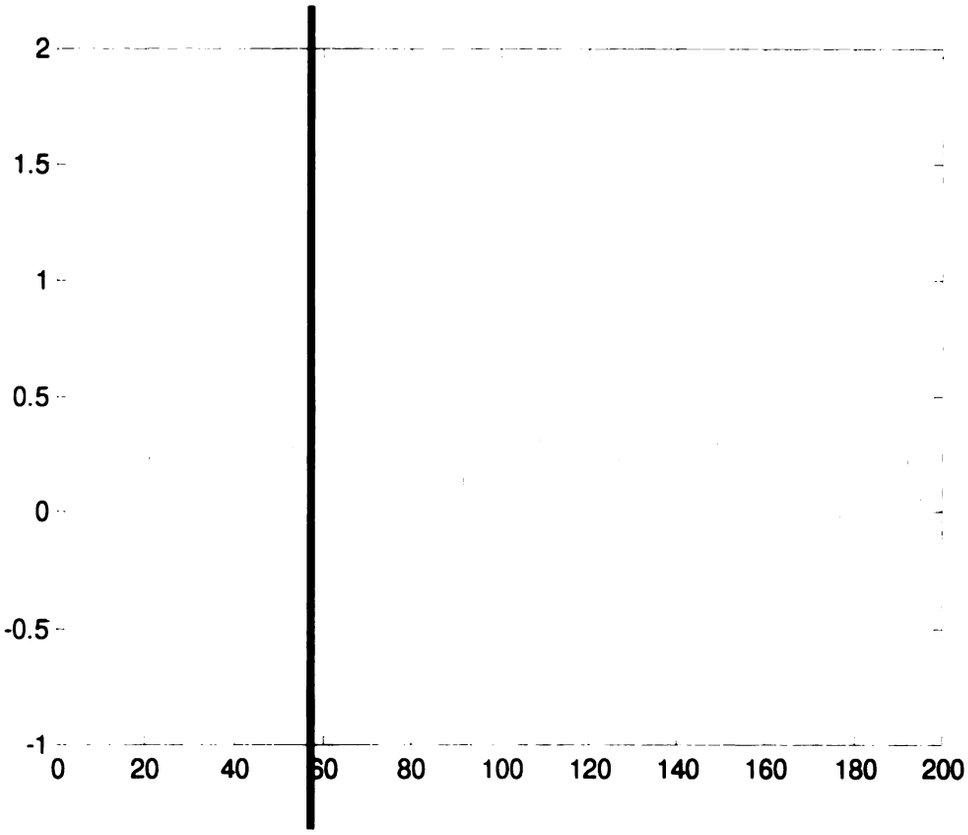


**Figure B4.** Fourier transform using calculated tau components. This figure is used to determine the cut-off for calculations, where the signal is totally overcome with noise. For this measurement, the cutoff of 58 was used (black line).

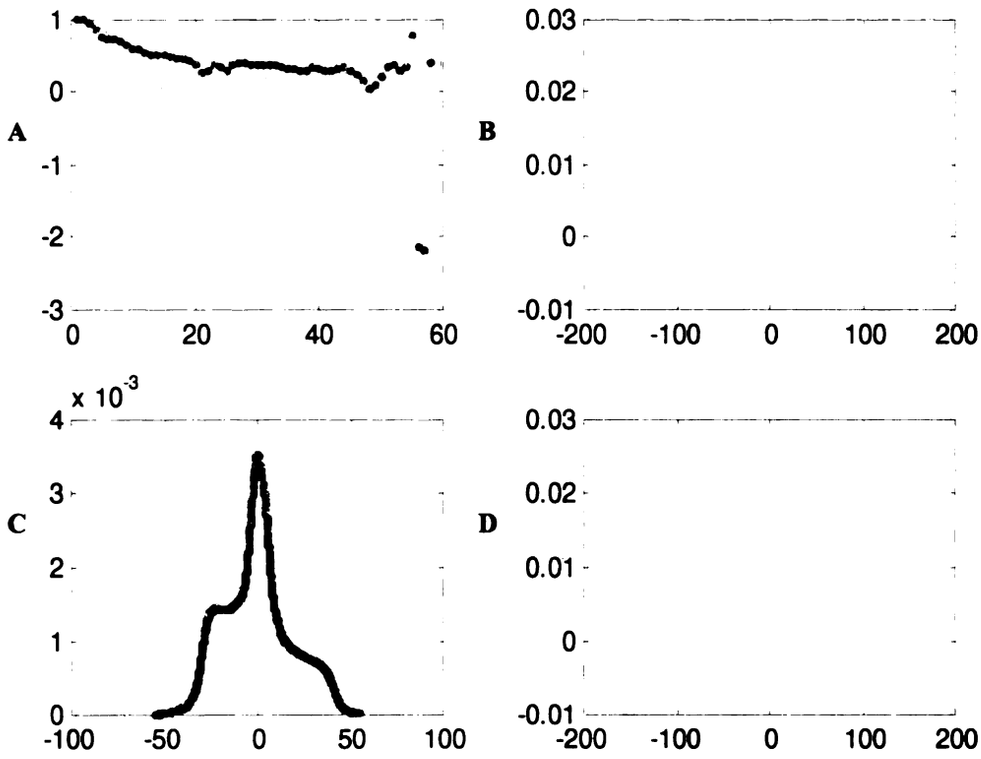


**Figure B5.** Spectra resulting form FCD analysis of dipolar coupling.

**Panel A.** shows the fit of the biphasic decay function, where the green dots are the experimental data, the upper red line is the best fit of the equation and the lower line is the discrepancy between the two.
**Panel B.** shows the inverse Fourier transform of $M^*(\omega)$ fit to 2 gaussians.
**Panel C.** shows the absorbance spectrum of the doubly labeled protein prior to (green line) and after (red line) subtraction of the monoradical component $b \bullet S(B)$.
**Panel D.** shows the inverse Fourier tranform of only the biradical component $aM^*(\omega)$.

# Appendix C

## EPR Spectra of Ten *h*COX-2 Double Mutants

**Figure 1C**. Absorbance EPR spectra of T73C/I98C double mutant in detergent (Tween 20) and liposome and in the presence of Co-PPIX, arachidonic acid and various COX inhibitors.
Spectra were normalized to maximum absorbance and were uncorrected for any contribution by monoradical species.
Images in this dissertation are presented in color.

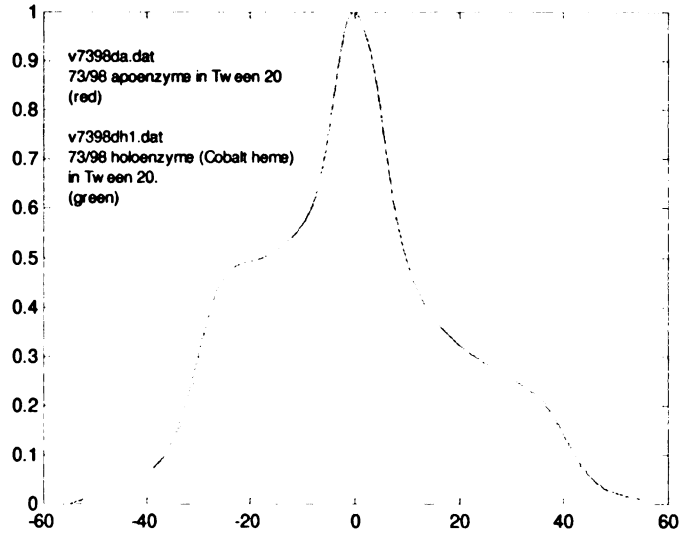
v7398da.dat
73/98 apoenzyme in Tween 20
(red)
v7398dh1.dat
73/98 holoenzyme (Cobalt heme)
in Tween 20.
(green)

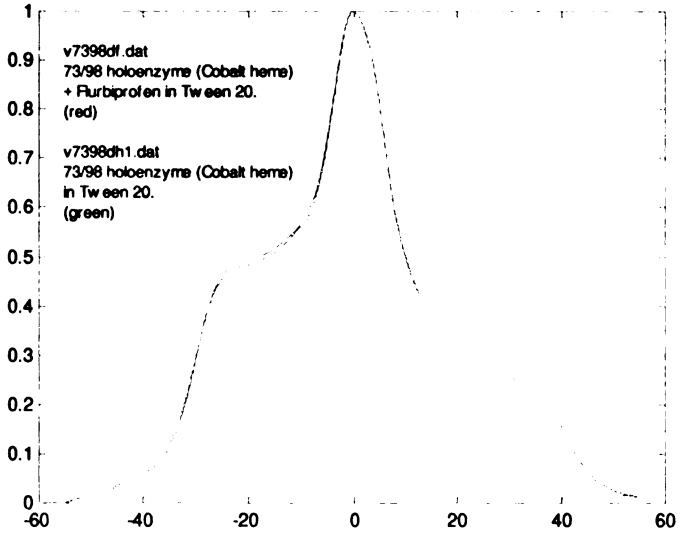
v7398df.dat
73/98 holoenzyme (Cobalt heme)
+ Flurbiprofen in Tween 20.
(red)
v7398dh1.dat
73/98 holoenzyme (Cobalt heme)
in Tween 20.
(green)

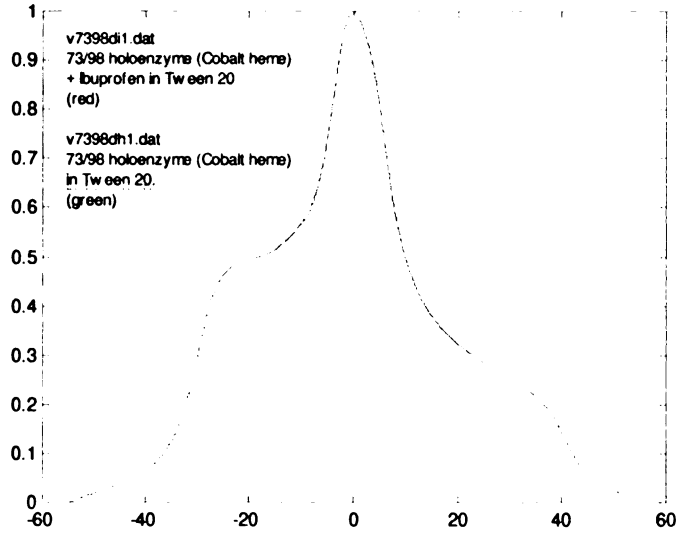
v7398di1.dat
73/98 holoenzyme (Cobalt heme)
+ Ibuprofen in Tween 20
(red)
v7398dh1.dat
73/98 holoenzyme (Cobalt heme)
in Tween 20.
(green)

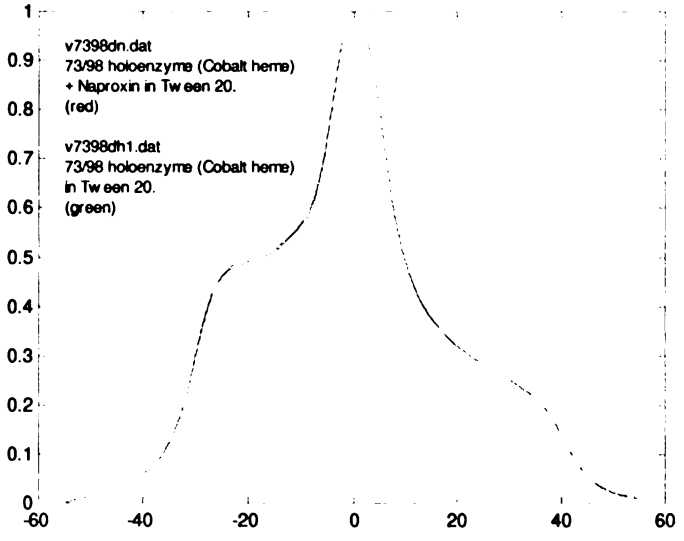
v7398dn.dat
73/98 holoenzyme (Cobalt heme)
+ Naproxin in Tween 20.
(red)
v7398dh1.dat
73/98 holoenzyme (Cobalt heme)
in Tween 20.
(green)

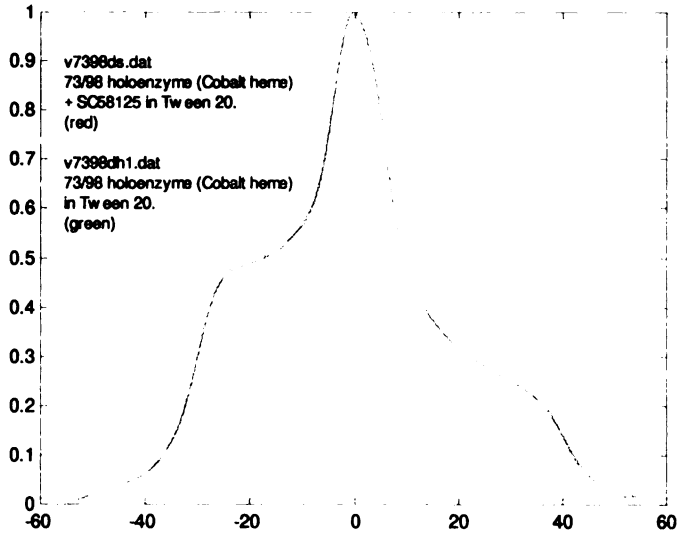
v7398ds.dat
73/98 holoenzyme (Cobalt heme)
+ SC58125 in Tween 20.
(red)
v7398dh1.dat
73/98 holoenzyme (Cobalt heme)
in Tween 20.
(green)

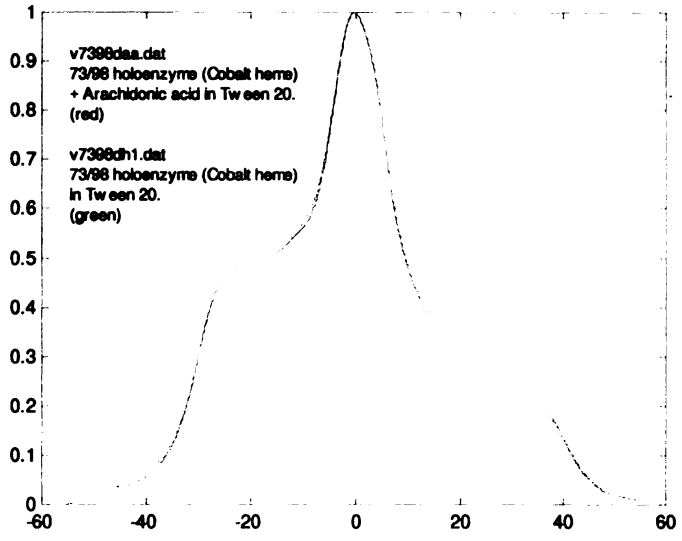
v7398daa.dat
73/98 holoenzyme (Cobalt heme)
+ Arachidonic acid in Tween 20.
(red)
v7398dh1.dat
73/98 holoenzyme (Cobalt heme)
in Tween 20.
(green)

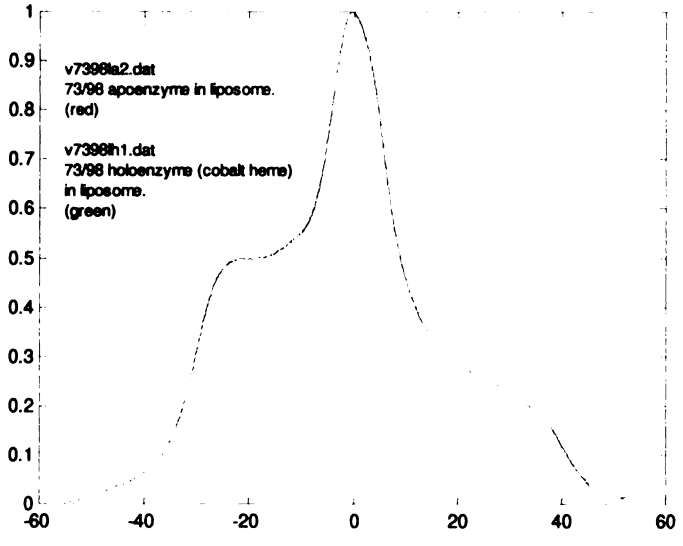
v7398la2.dat
73/98 apoenzyme in liposome.
(red)
v7398lh1.dat
73/98 holoenzyme (cobalt heme)
in liposome.
(green)

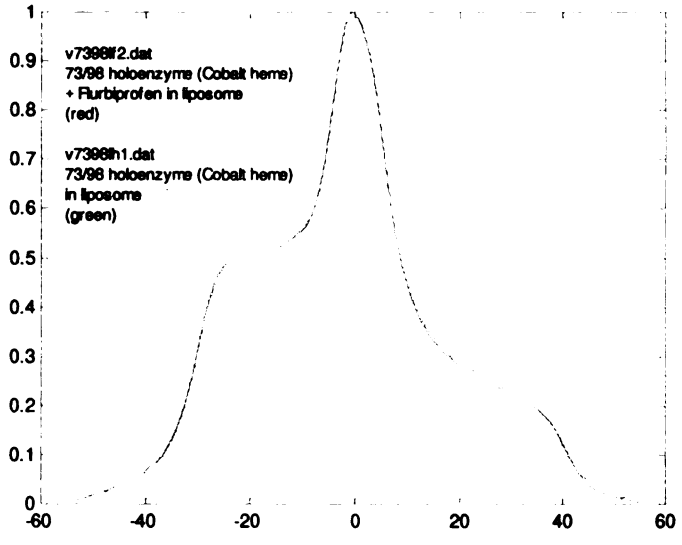
v7398lf2.dat
73/98 holoenzyme (Cobalt heme)
+ Flurbiprofen in liposome
(red)
v7398lh1.dat
73/98 holoenzyme (Cobalt heme)
in liposome
(green)

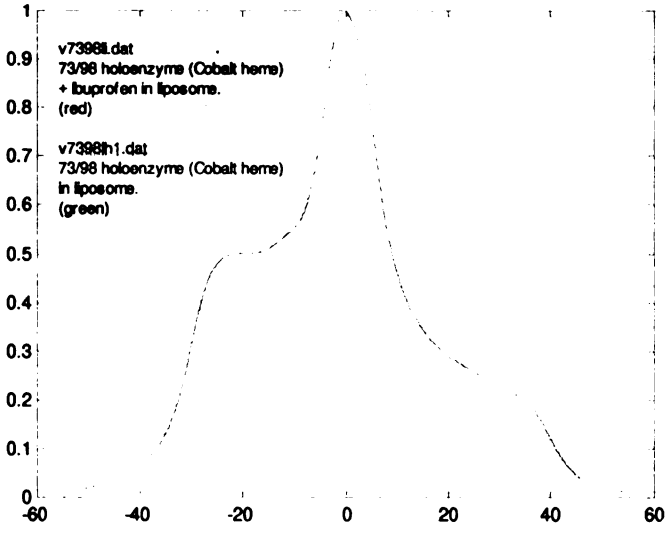
v7398il.dat
73/98 holoenzyme (Cobalt heme)
+ Ibuprofen in liposome.
(red)
v7398lh1.dat
73/98 holoenzyme (Cobalt heme)
in liposome.
(green)

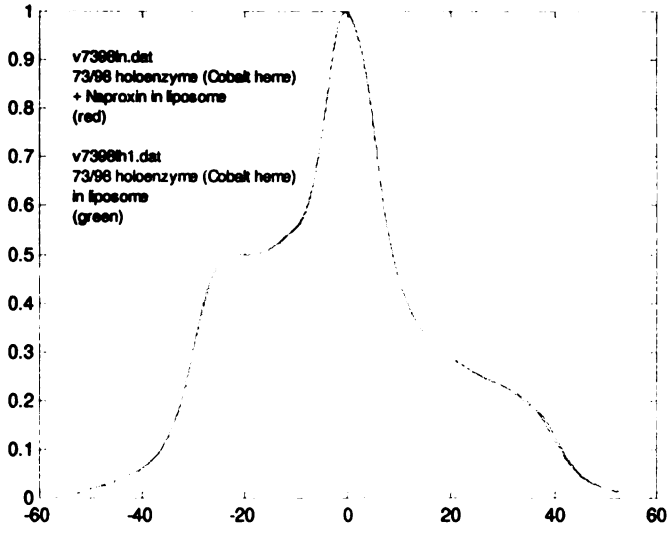
v7398ln.dat
73/98 holoenzyme (Cobalt heme)
+ Naproxin in liposome
(red)
v7398lh1.dat
73/98 holoenzyme (Cobalt heme)
in liposome
(green)

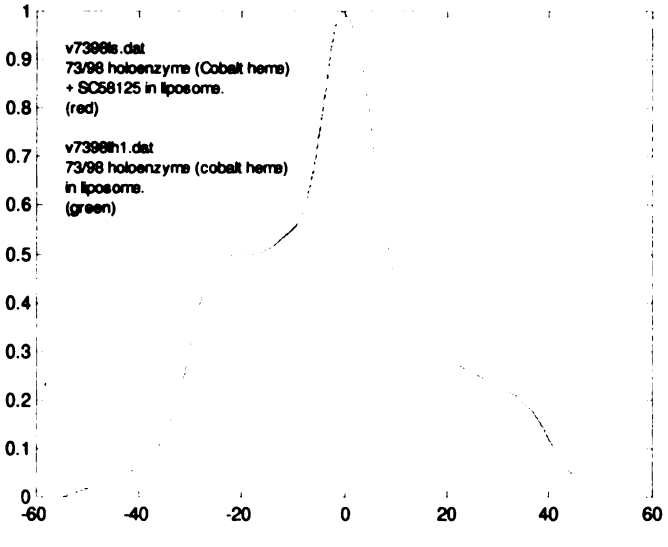
v7398ls.dat
73/98 holoenzyme (Cobalt heme)
+ SC58125 in liposome.
(red)
v7398lh1.dat
73/98 holoenzyme (cobalt heme)
in liposome.
(green)

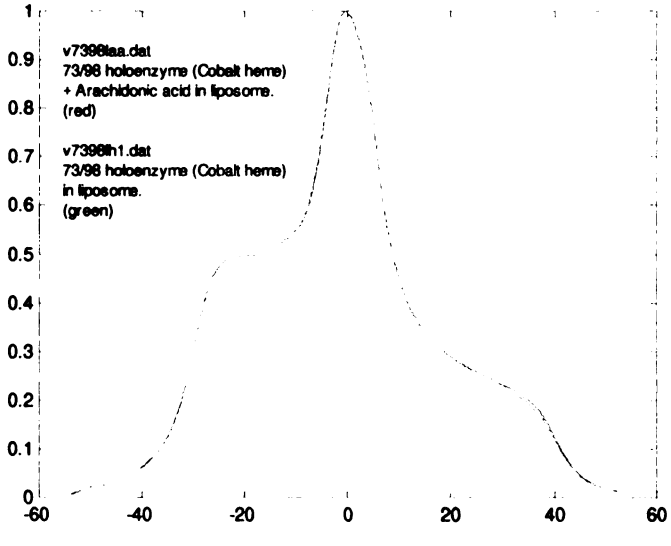
v7398laa.dat
73/98 holoenzyme (Cobalt heme)
+ Arachidonic acid in liposome.
(red)
v7398lh1.dat
73/98 holoenzyme (Cobalt heme)
in liposome.
(green)

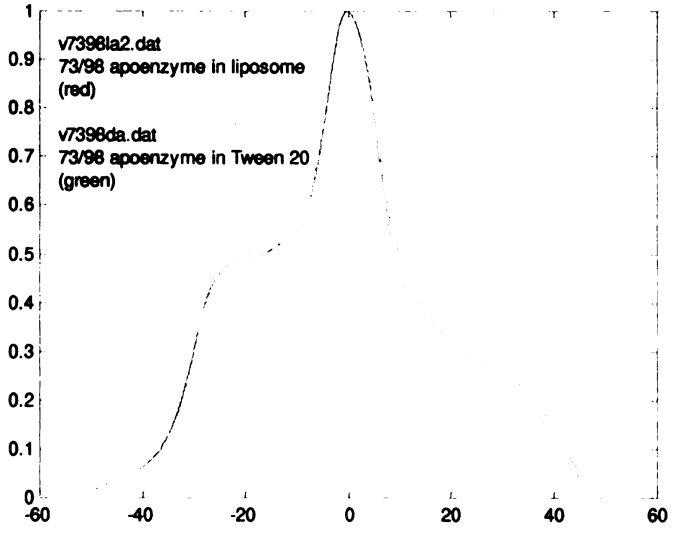
v7398la2.dat
73/98 apoenzyme in liposome
(red)
v7398da.dat
73/98 apoenzyme in Tween 20
(green)

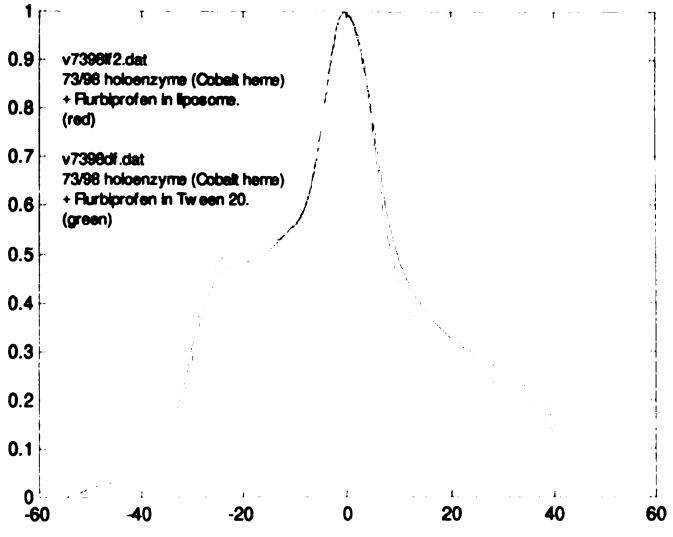
v7398lf2.dat
73/98 holoenzyme (Cobalt heme)
+ Flurbiprofen in liposome.
(red)
v7398df.dat
73/98 holoenzyme (Cobalt heme)
+ Flurbiprofen in Tween 20.
(green)

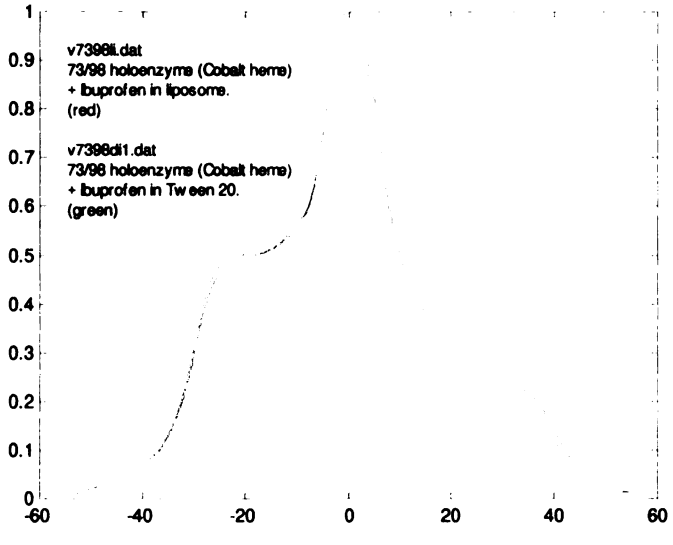
v7398li.dat
73/98 holoenzyme (Cobalt heme)
+ Ibuprofen in liposome.
(red)
v7398di1.dat
73/98 holoenzyme (Cobalt heme)
+ Ibuprofen in Tween 20.
(green)

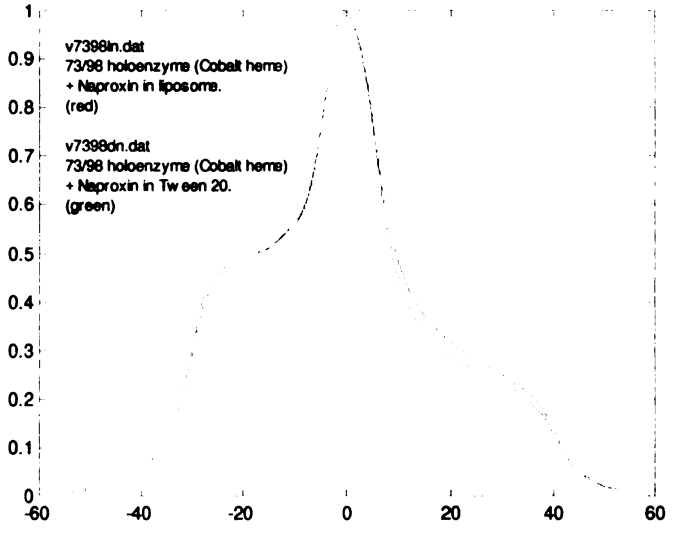
v7398ln.dat
73/98 holoenzyme (Cobalt heme)
+ Naproxin in liposome.
(red)
v7398dn.dat
73/98 holoenzyme (Cobalt heme)
+ Naproxin in Tween 20.
(green)

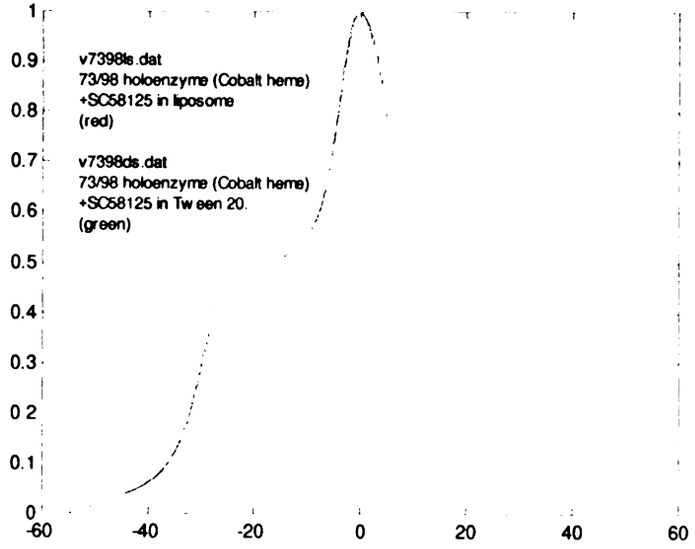
v7398ls.dat
73/98 holoenzyme (Cobalt heme)
+SC58125 in liposome
(red)
v7398ds.dat
73/98 holoenzyme (Cobalt heme)
+SC58125 in Tween 20.
(green)
1
0.9
0.8
0.7
0.6
0.5
0.4
0.3
0.2
0.1
0
-60
-40
-20
0
20
40
60

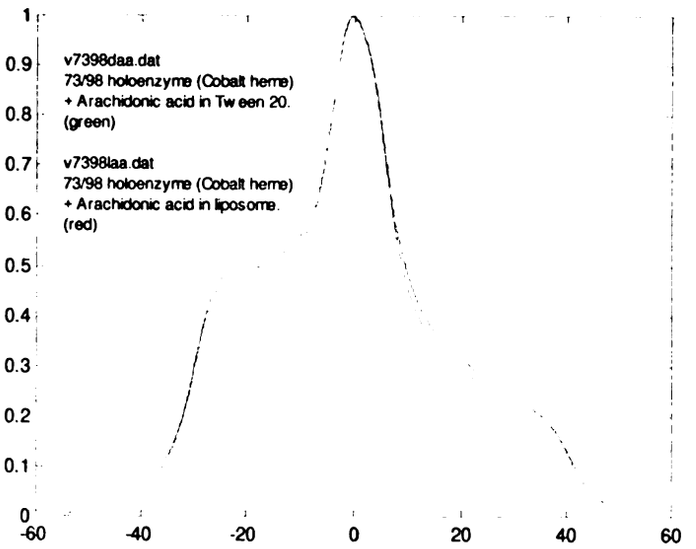
v7398daa.dat
73/98 holoenzyme (Cobalt heme)
+ Arachidonic acid in Tween 20.
(green)
v7398laa.dat
73/98 holoenzyme (Cobalt heme)
+ Arachidonic acid in liposome.
(red)
1
0.9
0.8
0.7
0.6
0.5
0.4
0.3
0.2
0.1
0
-60
-40
-20
0
20
40
60

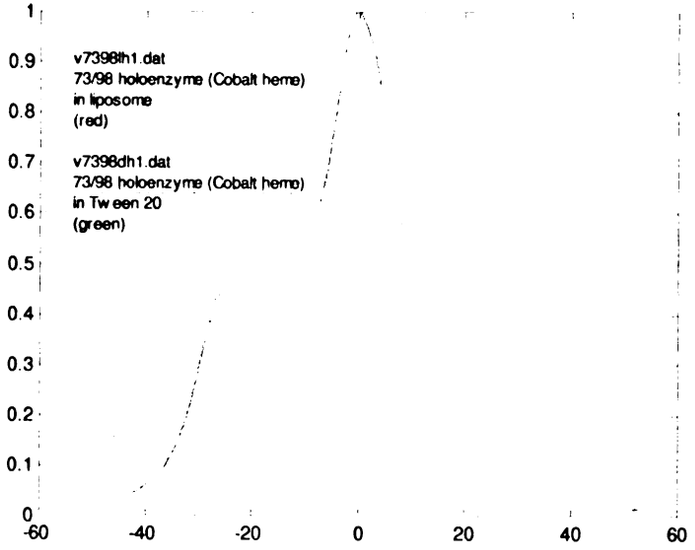
v7398th1.dat
73/98 holoenzyme (Cobalt heme)
in liposome
(red)
v7398dh1.dat
73/98 holoenzyme (Cobalt heme)
in Tween 20
(green)
1
0.9
0.8
0.7
0.6
0.5
0.4
0.3
0.2
0.1
0
-60
-40
-20
0
20
40
60

**Figure 2C**. Absorbance EPR spectra of V74C/I98C double mutant in detergent (Tween 20) and liposome and in the presence of Co-PPIX, arachidonic acid and various COX inhibitors.
Spectra were normalized to maximum absorbance and were uncorrected for any contribution by monoradical species.
Images in this dissertation are presented in color.

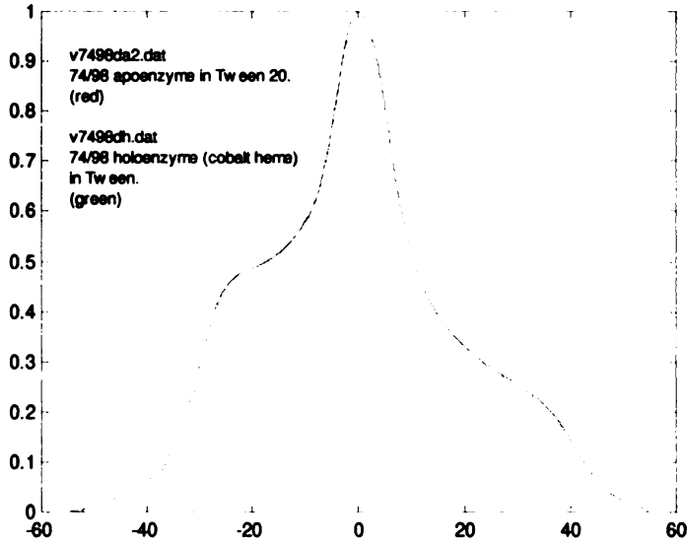
v7498da2.dat
74/98 apoenzyme in Tween 20.
(red)
v7498dh.dat
74/98 holoenzyme (cobalt heme)
in Tween.
(green)

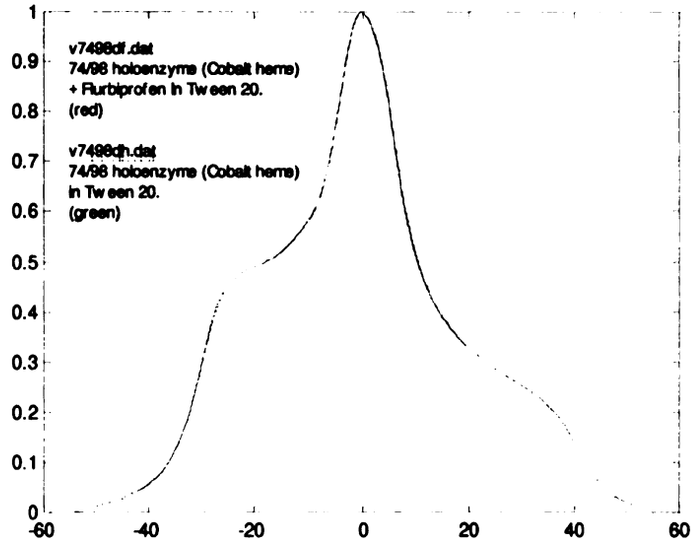
v7498df.dat
74/98 holoenzyme (Cobalt heme)
+ Flurbiprofen in Tween 20.
(red)
v7498dh.dat
74/98 holoenzyme (Cobalt heme)
in Tween 20.
(green)

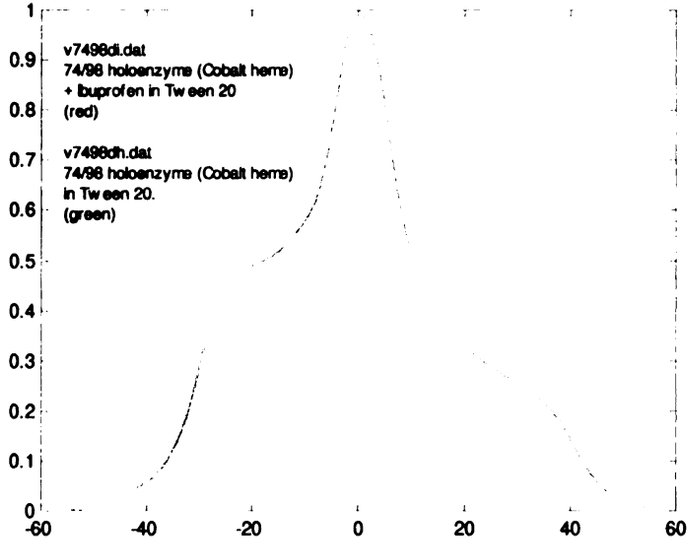
v7498di.dat
74/98 holoenzyme (Cobalt heme)
+ Ibuprofen in Tween 20
(red)
v7498dh.dat
74/98 holoenzyme (Cobalt heme)
in Tween 20.
(green)

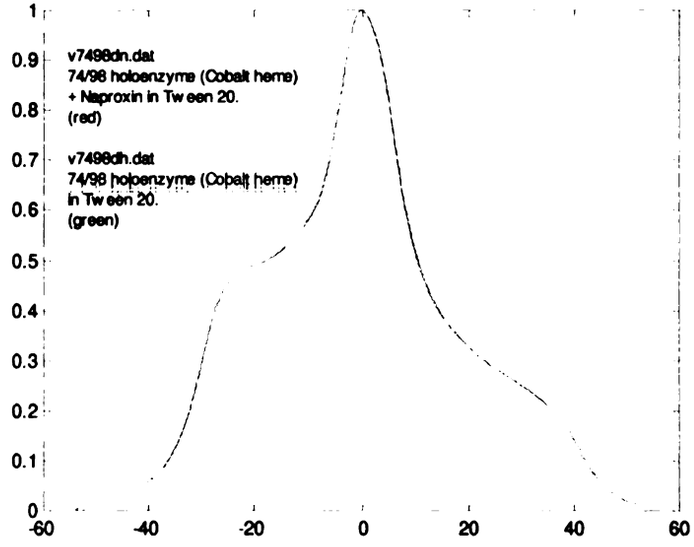
v7498dn.dat
74/98 holoenzyme (Cobalt heme)
+ Naproxin in Tween 20.
(red)
v7498dh.dat
74/98 holoenzyme (Cobalt heme)
in Tween 20.
(green)

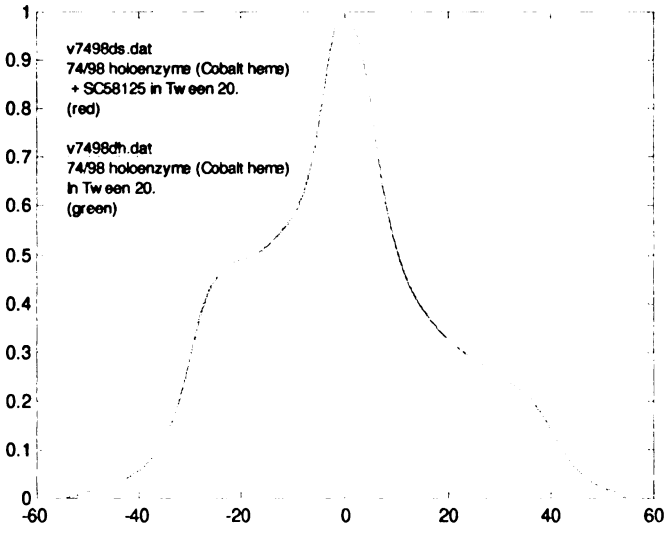
v7498ds.dat
74/98 holoenzyme (Cobalt heme)
+ SC58125 in Tween 20.
(red)
v7498dh.dat
74/98 holoenzyme (Cobalt heme)
In Tween 20.
(green)

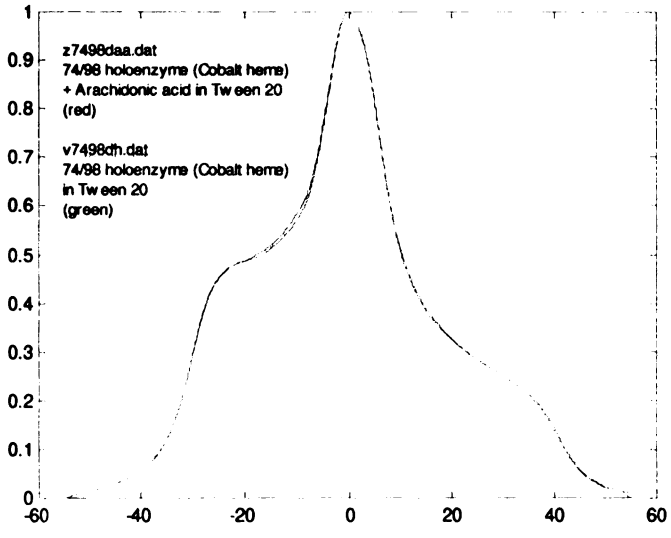
z7498daa.dat
74/98 holoenzyme (Cobalt heme)
+ Arachidonic acid in Tween 20
(red)
v7498dh.dat
74/98 holoenzyme (Cobalt heme)
in Tween 20
(green)

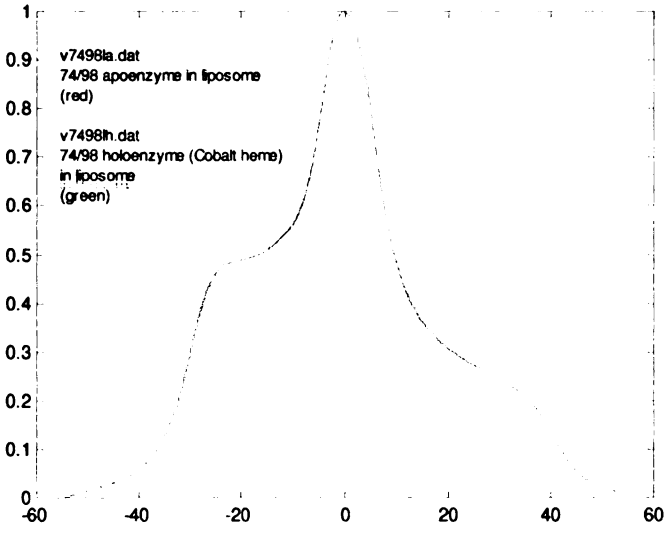
v7498la.dat
74/98 apoenzyme in liposome
(red)
v7498lh.dat
74/98 holoenzyme (Cobalt heme)
in liposome
(green)

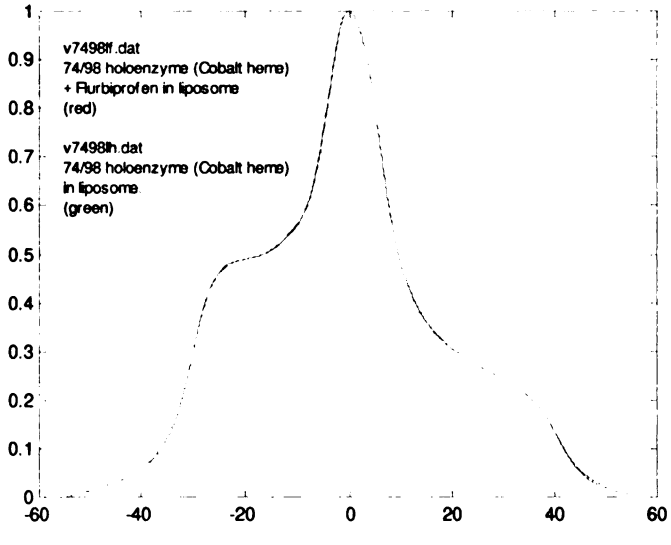
v7498lf.dat
74/98 holoenzyme (Cobalt heme)
+ Flurbiprofen in liposome
(red)
v7498lh.dat
74/98 holoenzyme (Cobalt heme)
in liposome
(green)

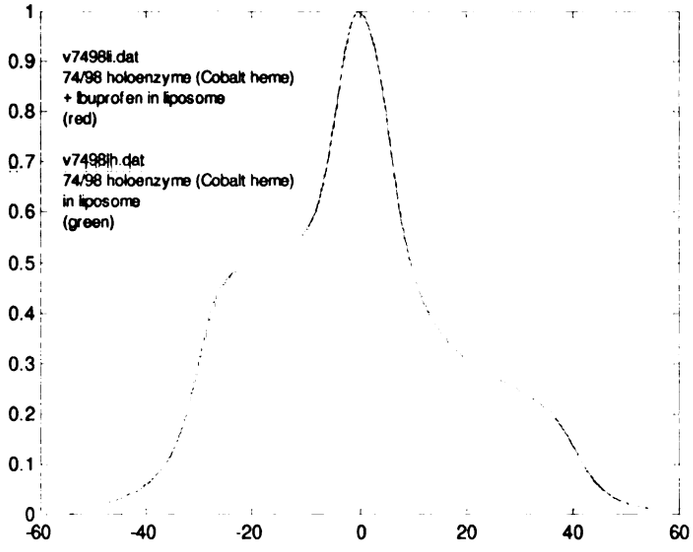
v7498li.dat
74/98 holoenzyme (Cobalt heme)
+ Ibuprofen in liposome
(red)
v7498lh.dat
74/98 holoenzyme (Cobalt heme)
in liposome
(green)

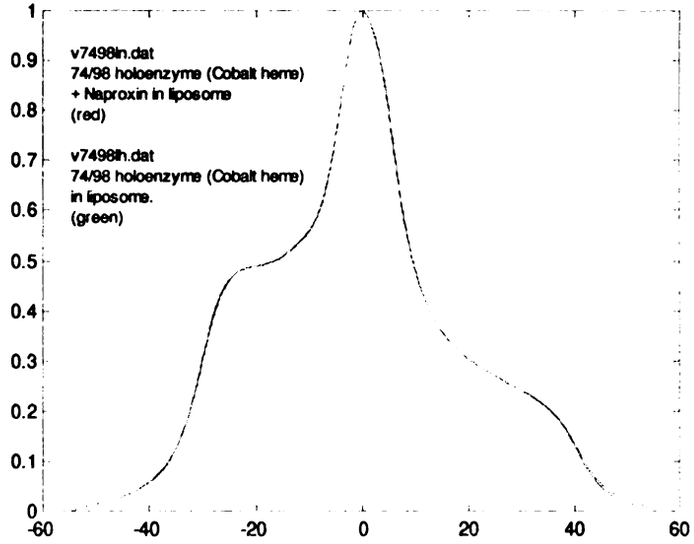
v7498ln.dat
74/98 holoenzyme (Cobalt heme)
+ Naproxin in liposome
(red)
v7498lh.dat
74/98 holoenzyme (Cobalt heme)
in liposome.
(green)

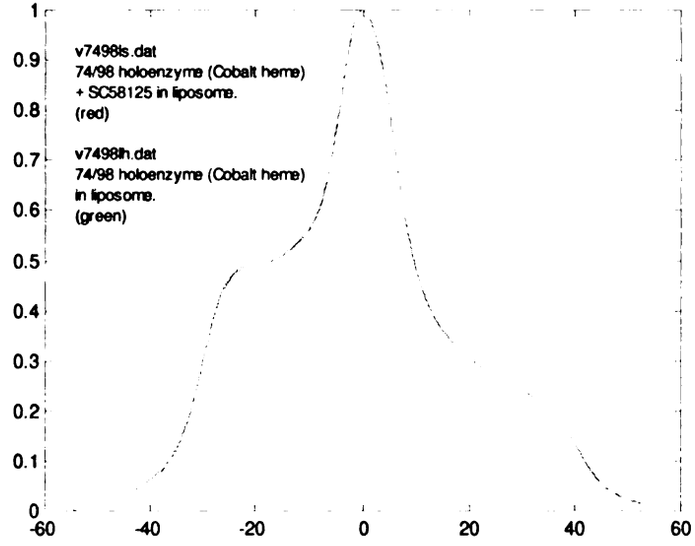
v7498ls.dat
74/98 holoenzyme (Cobalt heme)
+ SC58125 in liposome.
(red)
v7498lh.dat
74/98 holoenzyme (Cobalt heme)
in liposome.
(green)

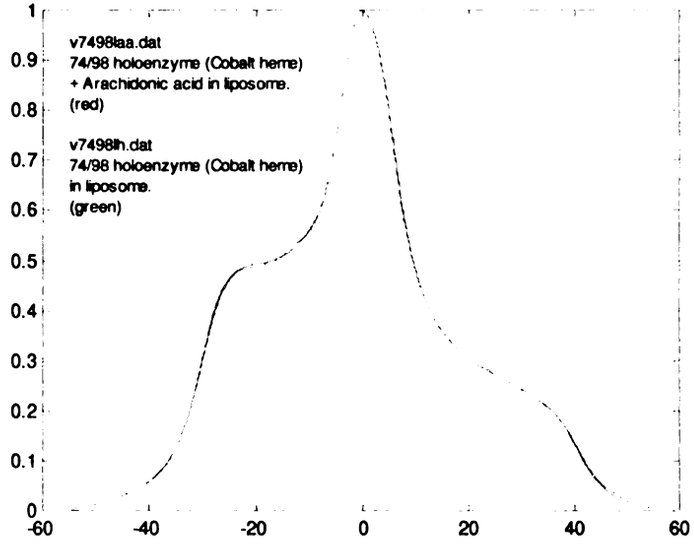
v7498laa.dat
74/98 holoenzyme (Cobalt heme)
+ Arachidonic acid in liposome.
(red)
v7498lh.dat
74/98 holoenzyme (Cobalt heme)
in liposome.
(green)

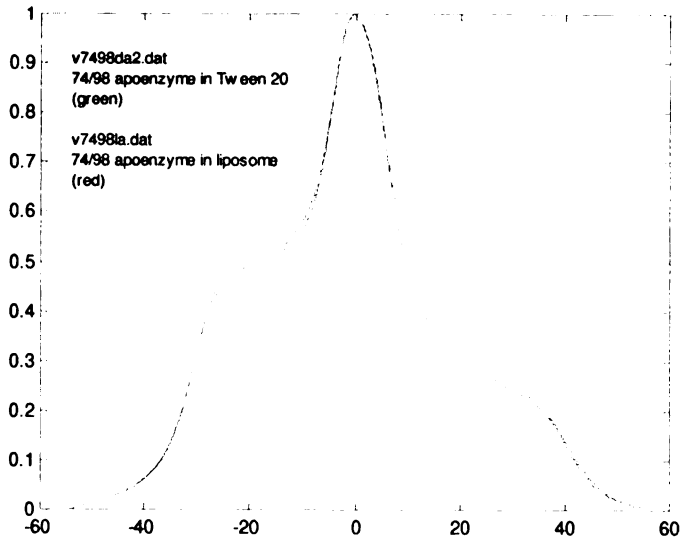
v7498da2.dat
74/98 apoenzyme in Tween 20
(green)
v7498la.dat
74/98 apoenzyme in liposome
(red)

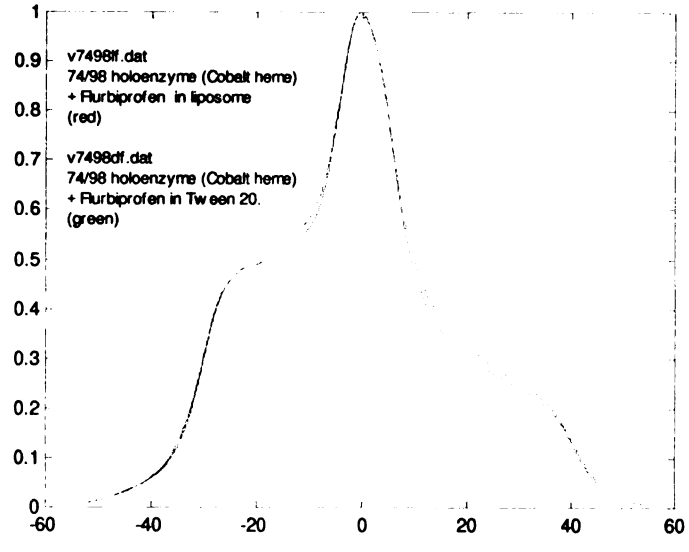
v7498lf.dat
74/98 holoenzyme (Cobalt heme)
+ Flurbiprofen in liposome
(red)
v7498df.dat
74/98 holoenzyme (Cobalt heme)
+ Flurbiprofen in Tween 20.
(green)

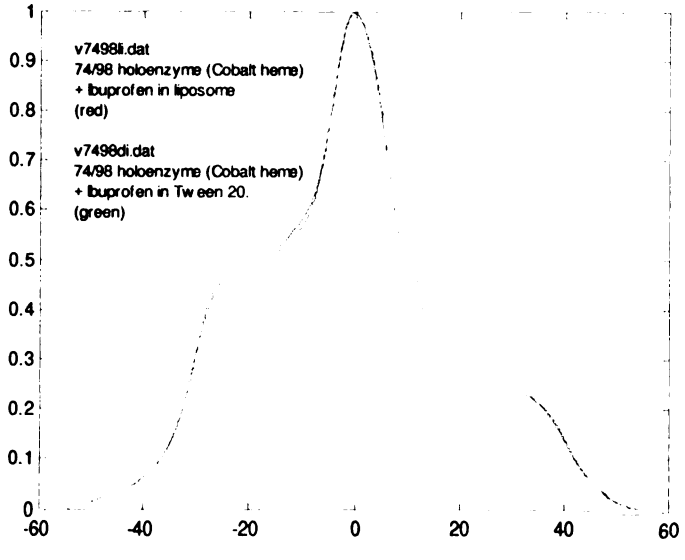
v7498li.dat
74/98 holoenzyme (Cobalt heme)
+ Ibuprofen in liposome
(red)
v7498di.dat
74/98 holoenzyme (Cobalt heme)
+ Ibuprofen in Tween 20.
(green)

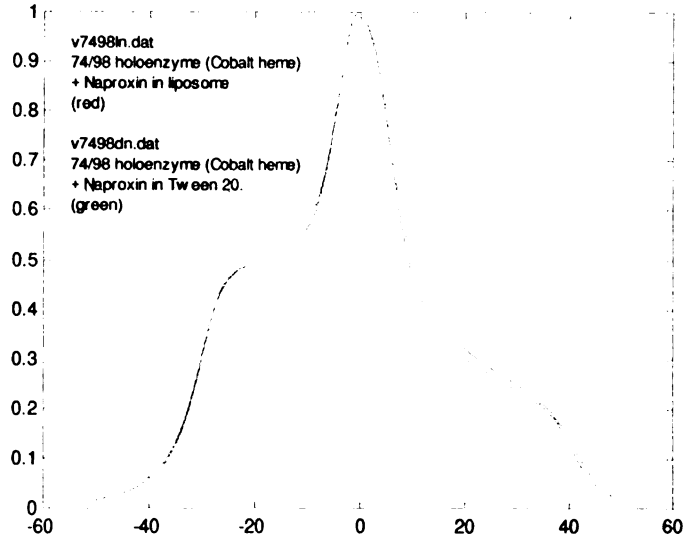
v7498ln.dat
74/98 holoenzyme (Cobalt heme)
+ Naproxin in liposome
(red)
v7498dn.dat
74/98 holoenzyme (Cobalt heme)
+ Naproxin in Tween 20.
(green)

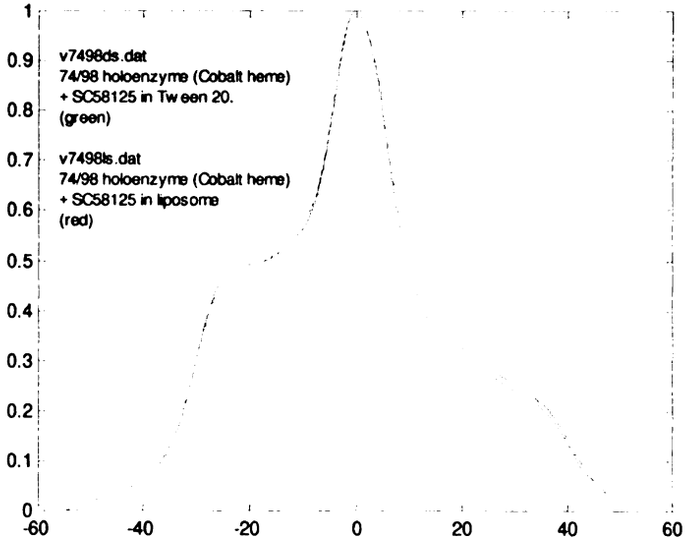
v7498ds.dat
74/98 holoenzyme (Cobalt heme)
+ SC58125 in Tween 20.
(green)
v7498ls.dat
74/98 holoenzyme (Cobalt heme)
+ SC58125 in liposome
(red)

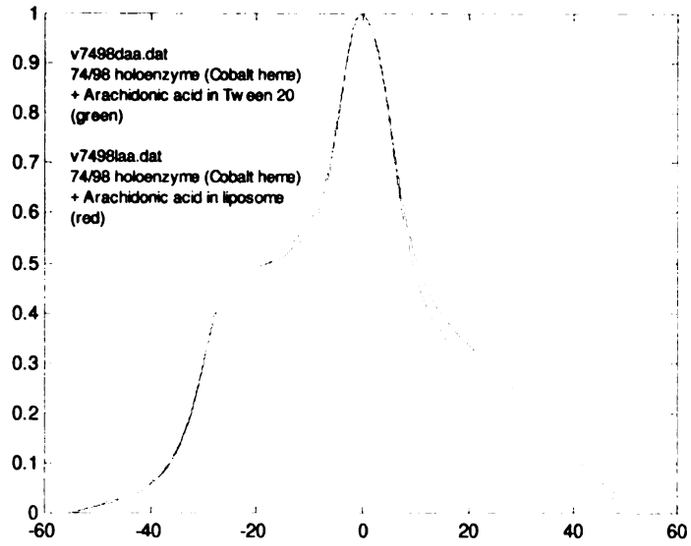
v7498daa.dat
74/98 holoenzyme (Cobalt heme)
+ Arachidonic acid in Tween 20
(green)
v7498laa.dat
74/98 holoenzyme (Cobalt heme)
+ Arachidonic acid in liposome
(red)

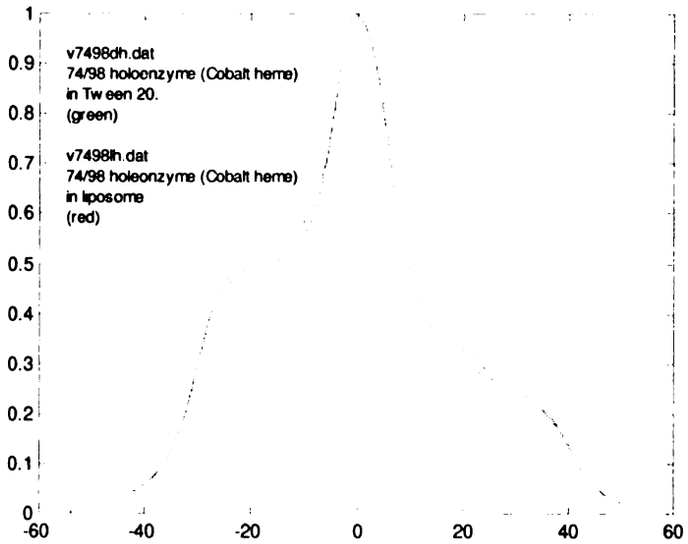
v7498dh.dat
74/98 holoenzyme (Cobalt heme)
in Tween 20.
(green)
v7498lh.dat
74/98 holeonzyme (Cobalt heme)
in liposome
(red)

**Figure 3C**. Absorbance EPR spectra of H75C/I98C double mutant in detergent (Tween 20) and liposome and in the presence of Co-PPIX, arachidonic acid and various COX inhibitors.
Spectra were normalized to maximum absorbance and were uncorrected for any contribution by monoradical species.
Images in this dissertation are presented in color.

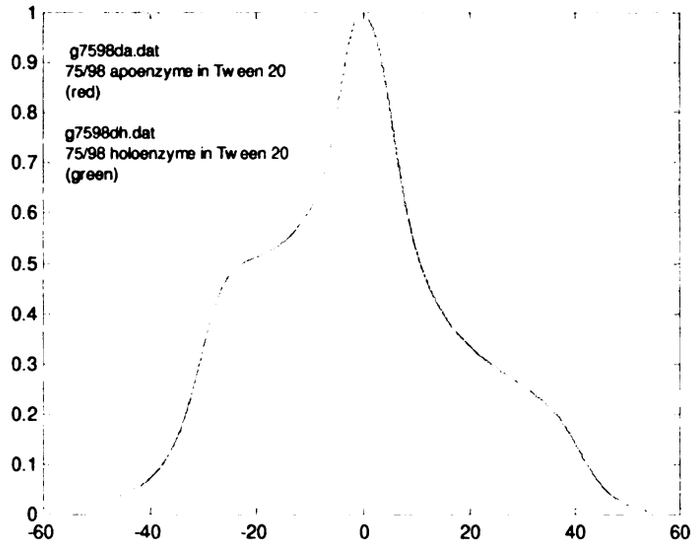
g7598da.dat
75/98 apoenzyme in Tween 20
(red)
g7598dh.dat
75/98 holoenzyme in Tween 20
(green)

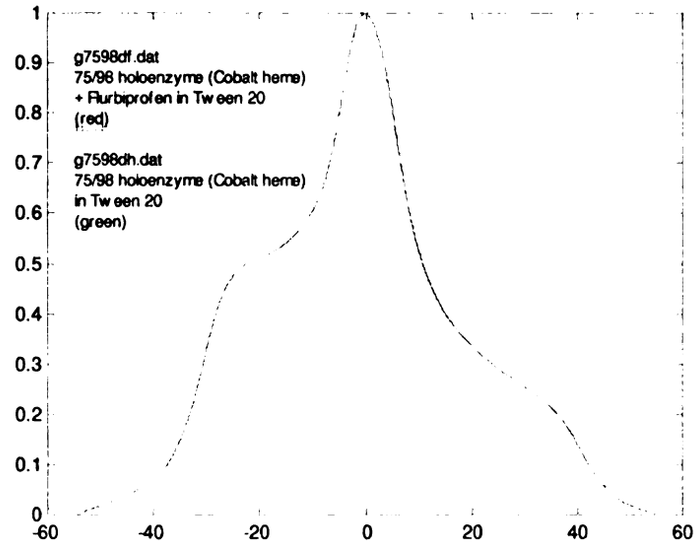
g7598df.dat
75/98 holoenzyme (Cobalt heme)
+ Flurbiprofen in Tween 20
(red)
g7598dh.dat
75/98 holoenzyme (Cobalt heme)
in Tween 20
(green)

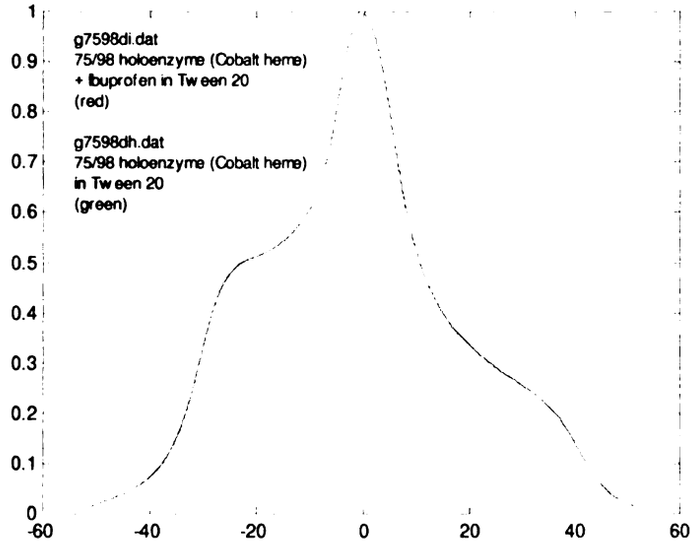
g7598di.dat
75/98 holoenzyme (Cobalt heme)
+ Ibuprofen in Tween 20
(red)
g7598dh.dat
75/98 holoenzyme (Cobalt heme)
in Tween 20
(green)

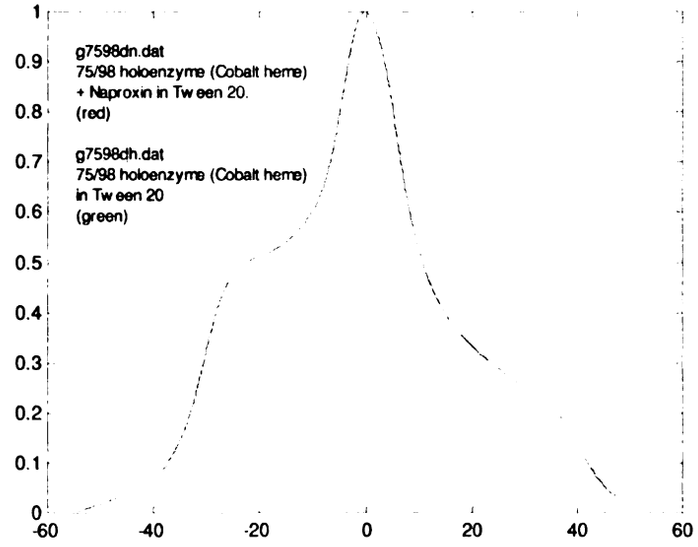
g7598dn.dat
75/98 holoenzyme (Cobalt heme)
+ Naproxin in Tween 20.
(red)
g7598dh.dat
75/98 holoenzyme (Cobalt heme)
in Tween 20
(green)

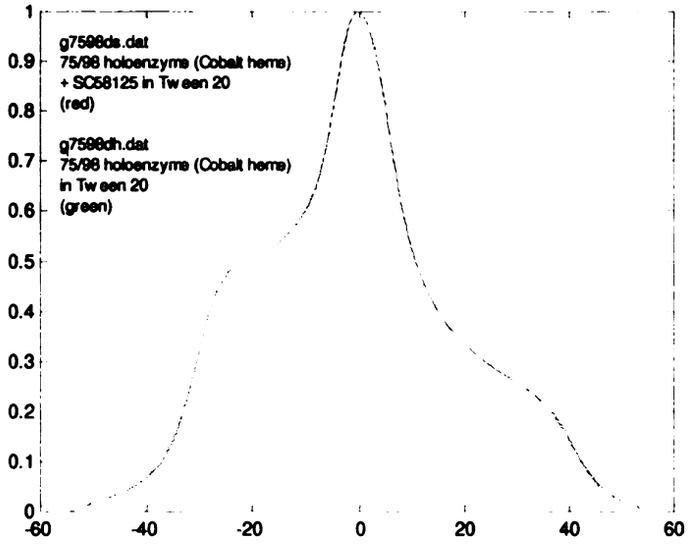
g7598ds.dat
75/98 holoenzyme (Cobalt heme)
+ SC58125 in Tween 20
(red)
g7598dh.dat
75/98 holoenzyme (Cobalt heme)
in Tween 20
(green)

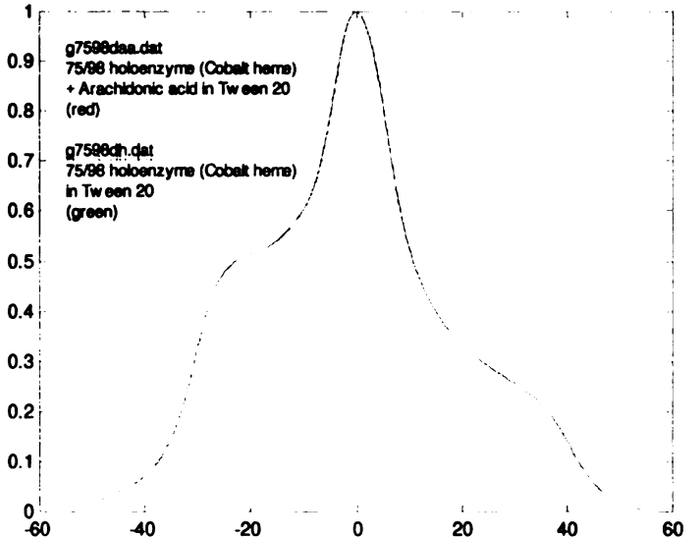
g7598daa.dat
75/98 holoenzyme (Cobalt heme)
+ Arachidonic acid in Tween 20
(red)
g7598dh.dat
75/98 holoenzyme (Cobalt heme)
in Tween 20
(green)

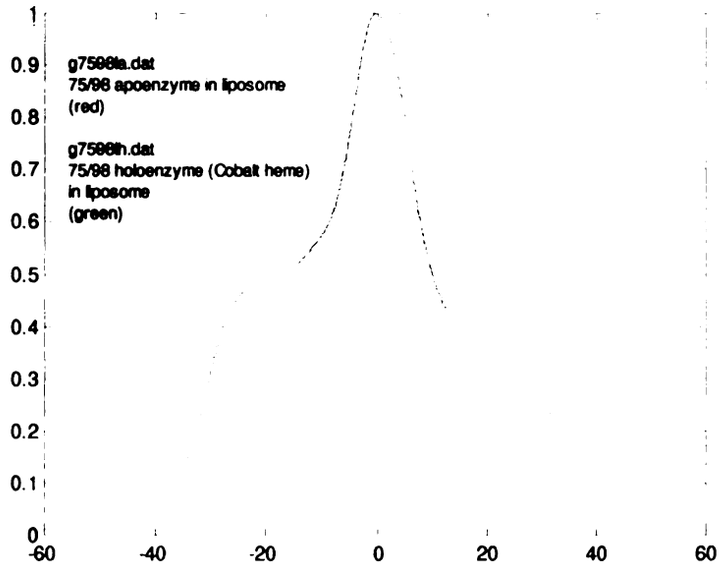
g7598la.dat
75/98 apoenzyme in liposome
(red)
g7598lh.dat
75/98 holoenzyme (Cobalt heme)
in liposome
(green)

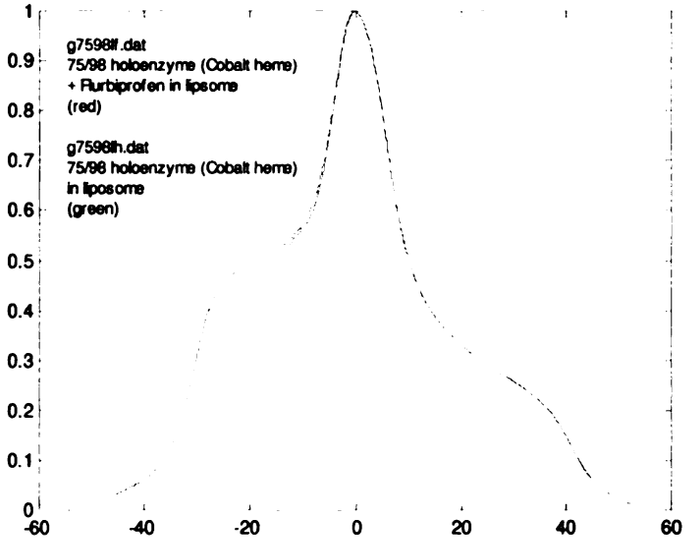
g7598lf.dat
75/98 holoenzyme (Cobalt heme)
+ Flurbiprofen in lipsome
(red)
g7598lh.dat
75/98 holoenzyme (Cobalt heme)
in liposome
(green)

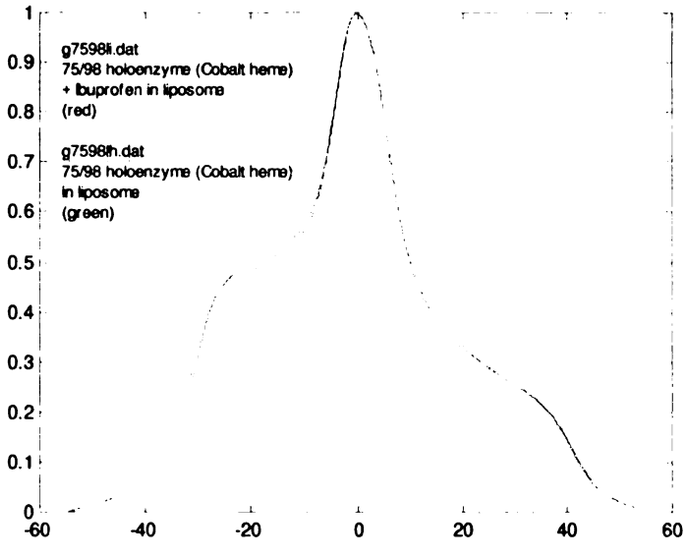
g7598li.dat
75/98 holoenzyme (Cobalt heme)
+ Ibuprofen in liposome
(red)
g7598lh.dat
75/98 holoenzyme (Cobalt heme)
in liposome
(green)

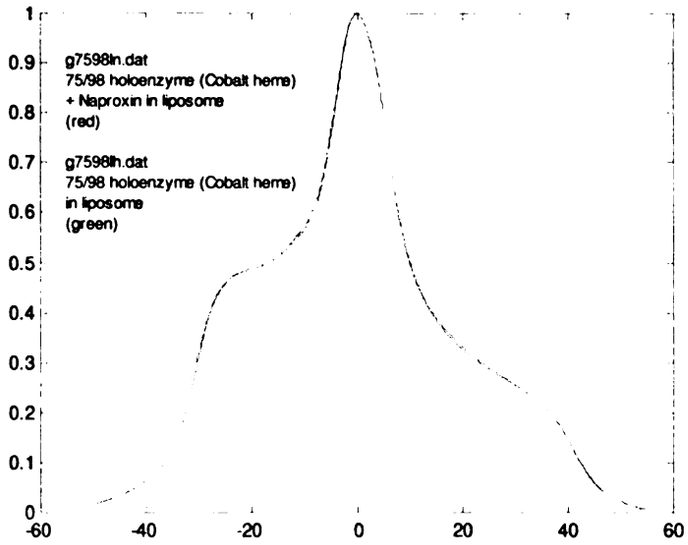
g7598ln.dat
75/98 holoenzyme (Cobalt heme)
+ Naproxin in liposome
(red)
g7598lh.dat
75/98 holoenzyme (Cobalt heme)
in liposome
(green)

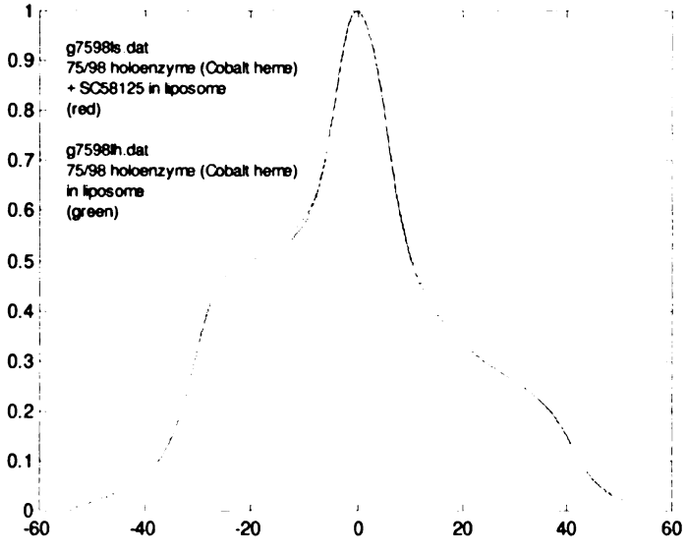
g7598ls.dat
75/98 holoenzyme (Cobalt heme)
+ SC58125 in liposome
(red)
g7598lh.dat
75/98 holoenzyme (Cobalt heme)
in liposome
(green)

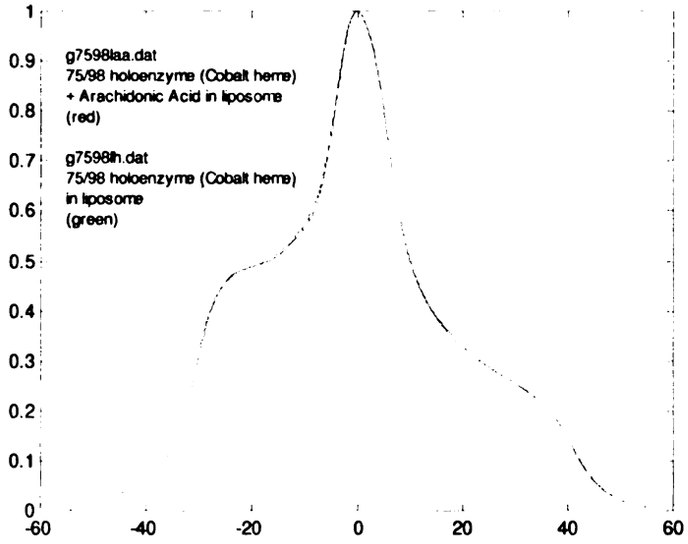
g7598laa.dat
75/98 holoenzyme (Cobalt heme)
+ Arachidonic Acid in liposome
(red)
g7598lh.dat
75/98 holoenzyme (Cobalt heme)
in liposome
(green)

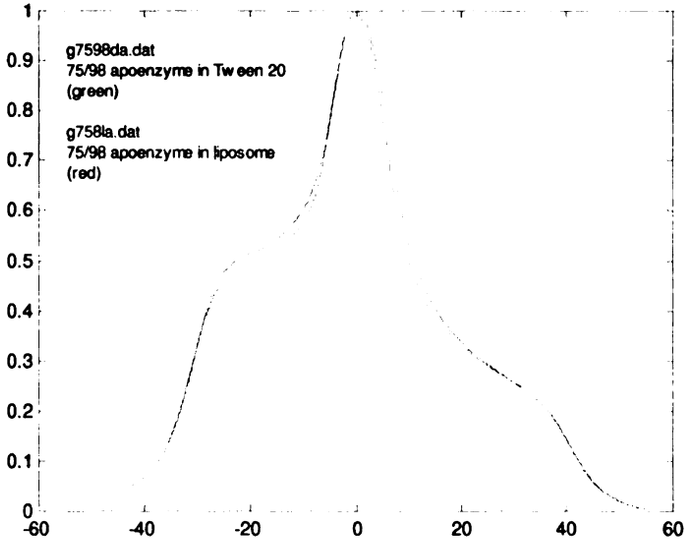
g7598da.dat
75/98 apoenzyme in Tween 20
(green)
g758la.dat
75/98 apoenzyme in liposome
(red)

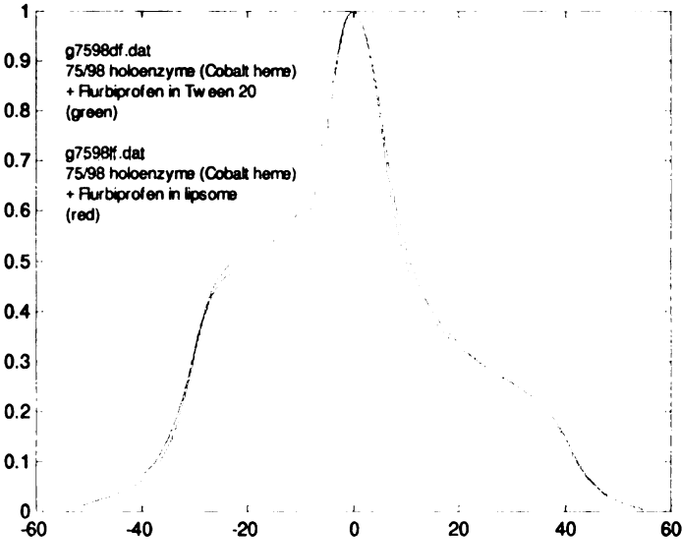
g7598df.dat
75/98 holoenzyme (Cobalt heme)
+ Flurbiprofen in Tween 20
(green)
g7598lf.dat
75/98 holoenzyme (Cobalt heme)
+ Flurbiprofen in lipsome
(red)

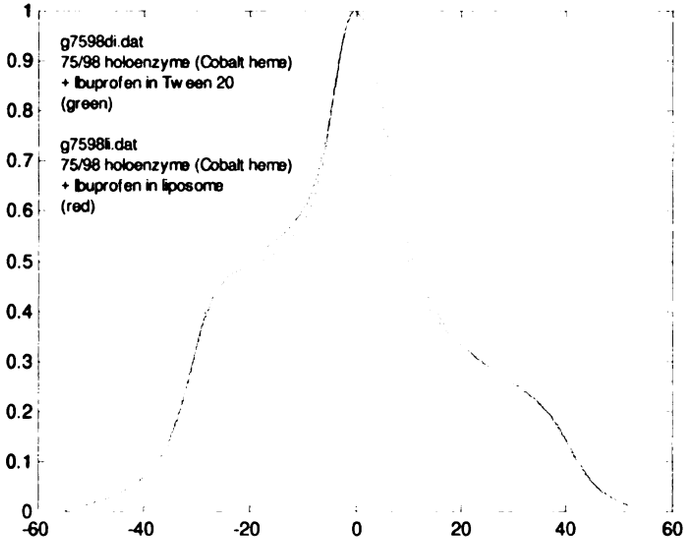
g7598di.dat
75/98 holoenzyme (Cobalt heme)
+ Ibuprofen in Tween 20
(green)
g7598li.dat
75/98 holoenzyme (Cobalt heme)
+ Ibuprofen in liposome
(red)

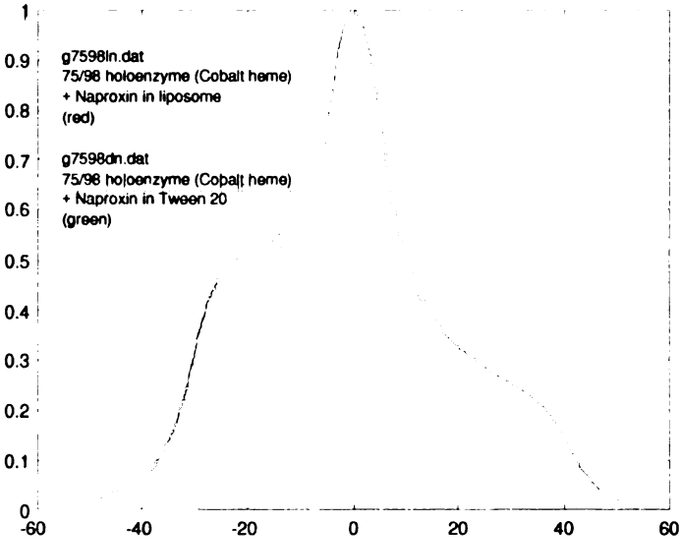
g7598ln.dat
75/98 holoenzyme (Cobalt heme)
+ Naproxin in liposome
(red)
g7598dn.dat
75/98 holoenzyme (Cobalt heme)
+ Naproxin in Tween 20
(green)

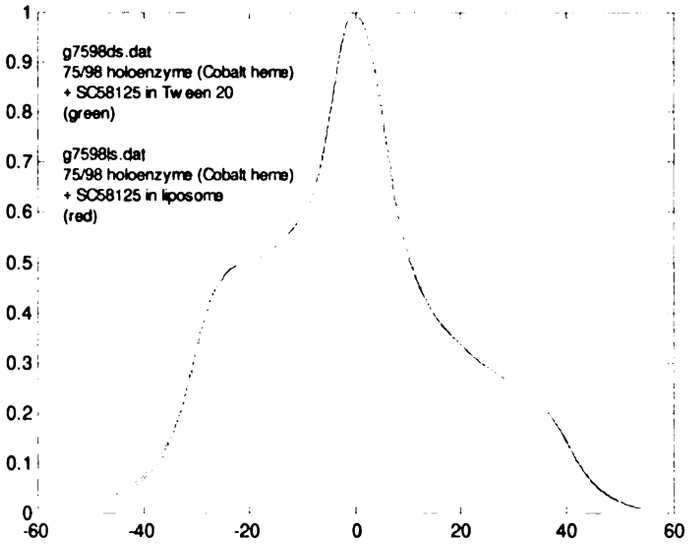
g7598ds.dat
75/98 holoenzyme (Cobalt heme)
+ SC58125 in Tween 20
(green)
g7598ls.dat
75/98 holoenzyme (Cobalt heme)
+ SC58125 in liposome
(red)
1
0.9
0.8
0.7
0.6
0.5
0.4
0.3
0.2
0.1
0
-60
-40
-20
0
20
40
60

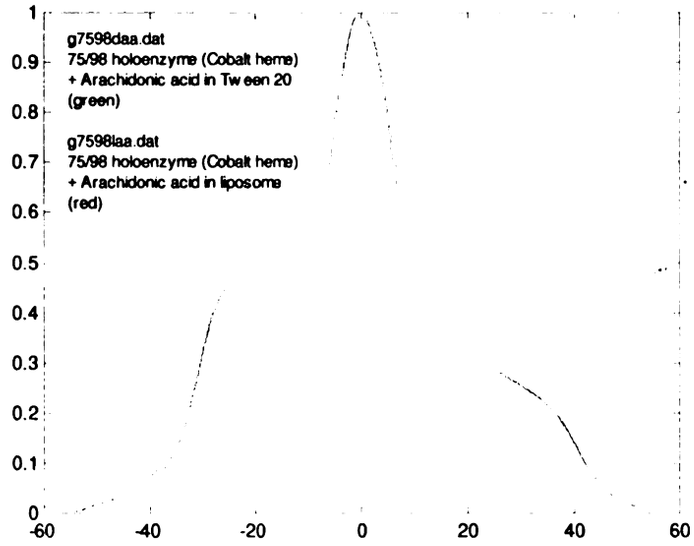
g7598daa.dat
75/98 holoenzyme (Cobalt heme)
+ Arachidonic acid in Tween 20
(green)
g7598laa.dat
75/98 holoenzyme (Cobalt heme)
+ Arachidonic acid in liposome
(red)
1
0.9
0.8
0.7
0.6
0.5
0.4
0.3
0.2
0.1
0
-60
-40
-20
0
20
40
60

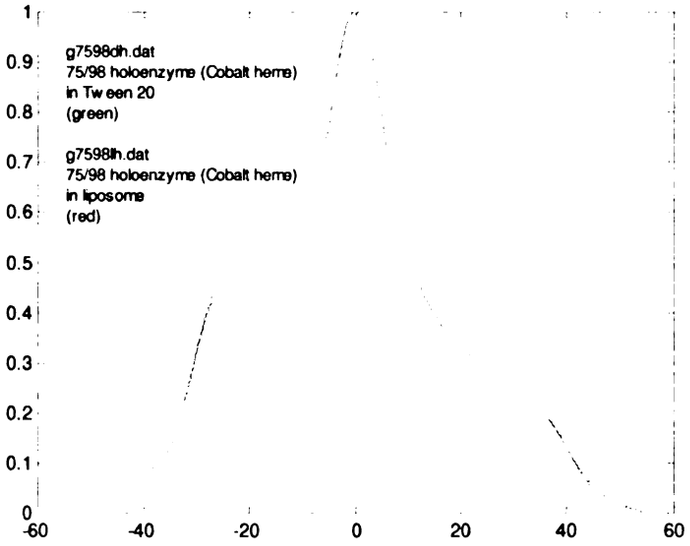
g7598dh.dat
75/98 holoenzyme (Cobalt heme)
in Tween 20
(green)
g7598lh.dat
75/98 holoenzyme (Cobalt heme)
in liposome
(red)
1
0.9
0.8
0.7
0.6
0.5
0.4
0.3
0.2
0.1
0
-60
-40
-20
0
20
40
60

**Figure 4C**. Absorbance EPR spectra of Y76C/I98C double mutant in detergent (Tween 20) and liposome and in the presence of Co-PPIX, arachidonic acid and various COX inhibitors.
Spectra were normalized to maximum absorbance and were uncorrected for any contribution by monoradical species.
Images in this dissertation are presented in color.

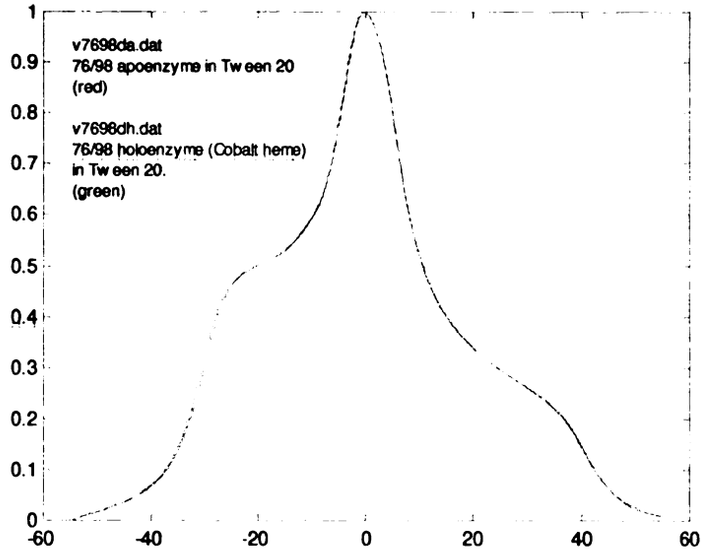
v7698da.dat
76/98 apoenzyme in Tween 20
(red)
v7698dh.dat
76/98 holoenzyme (Cobalt heme)
in Tween 20.
(green)

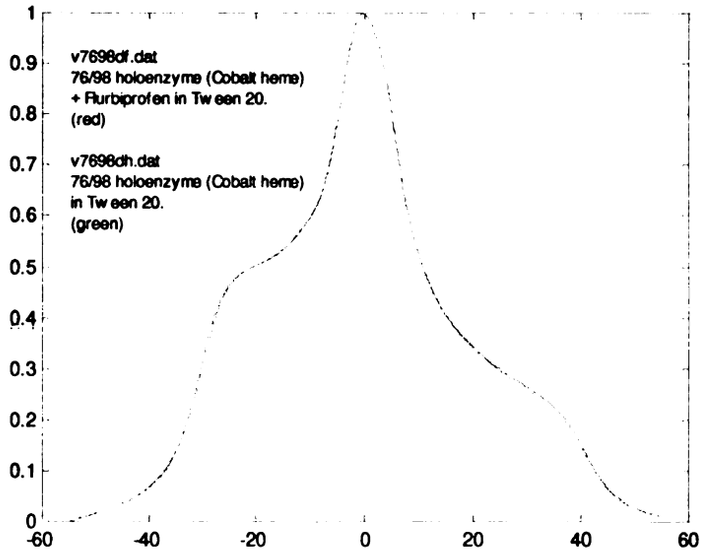
v7698df.dat
76/98 holoenzyme (Cobalt heme)
+ Flurbiprofen in Tween 20.
(red)
v7698dh.dat
76/98 holoenzyme (Cobalt heme)
in Tween 20.
(green)

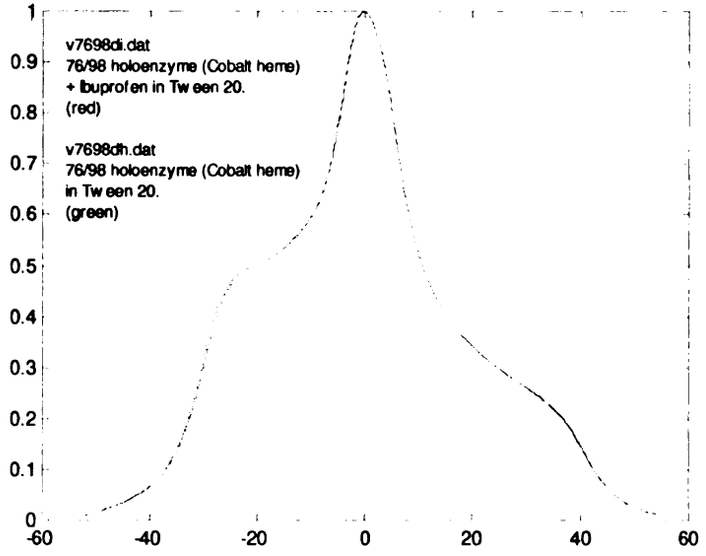
v7698di.dat
76/98 holoenzyme (Cobalt heme)
+ Ibuprofen in Tween 20.
(red)
v7698dh.dat
76/98 holoenzyme (Cobalt heme)
in Tween 20.
(green)

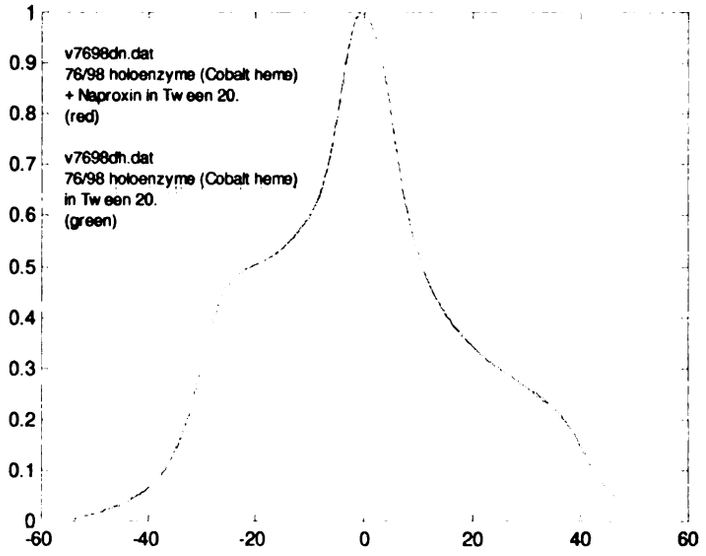
v7698dn.dat
76/98 holoenzyme (Cobalt heme)
+ Naproxin in Tween 20.
(red)
v7698dh.dat
76/98 holoenzyme (Cobalt heme)
in Tween 20.
(green)

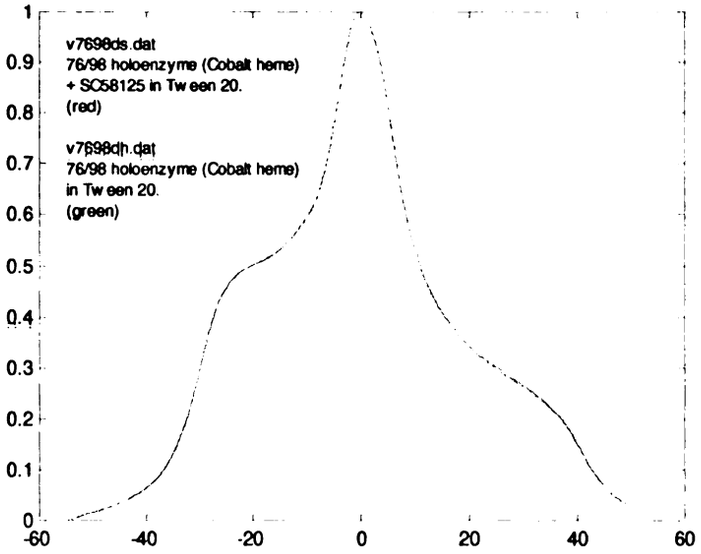
v7698ds.dat
76/98 holoenzyme (Cobalt heme)
+ SC58125 in Tween 20.
(red)
v7698dh.dat
76/98 holoenzyme (Cobalt heme)
in Tween 20.
(green)

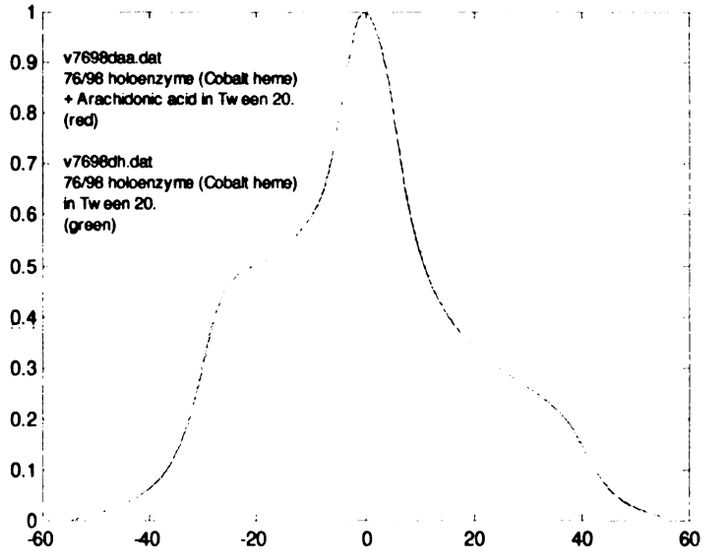
v7698daa.dat
76/98 holoenzyme (Cobalt heme)
+ Arachidonic acid in Tween 20.
(red)
v7698dh.dat
76/98 holoenzyme (Cobalt heme)
in Tween 20.
(green)

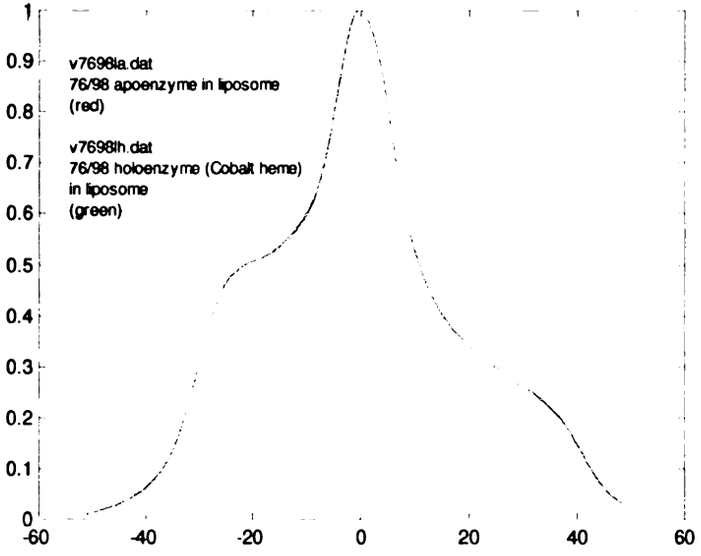
v7698la.dat
76/98 apoenzyme in liposome
(red)
v7698lh.dat
76/98 holoenzyme (Cobalt heme)
in liposome
(green)

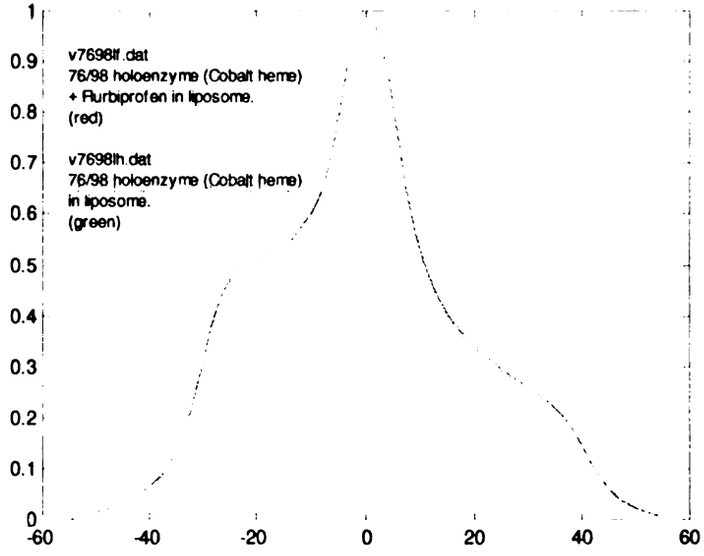
v7698lf.dat
76/98 holoenzyme (Cobalt heme)
+ Flurbiprofen in liposome.
(red)
v7698lh.dat
76/98 holoenzyme (Cobalt heme)
in liposome.
(green)

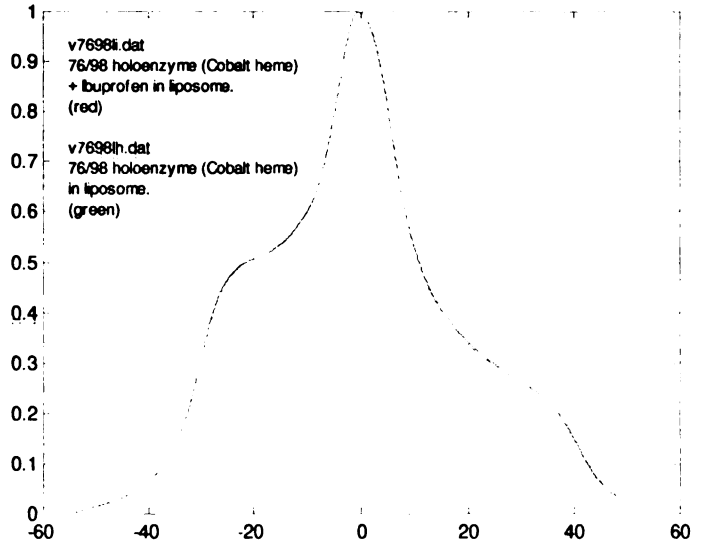
v7698li.dat
76/98 holoenzyme (Cobalt heme)
+ Ibuprofen in liposome.
(red)
v7698lh.dat
76/98 holoenzyme (Cobalt heme)
in liposome.
(green)
1
0.9
0.8
0.7
0.6
0.5
0.4
0.3
0.2
0.1
0
-60
-40
-20
0
20
40
60

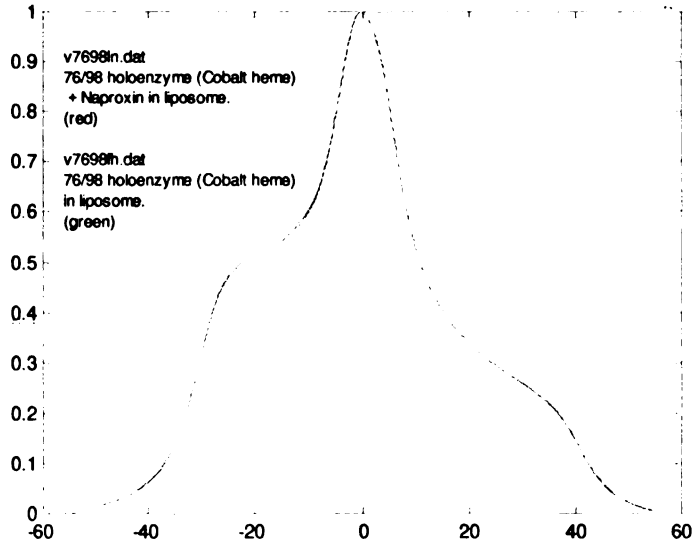
v7698ln.dat
76/98 holoenzyme (Cobalt heme)
+ Naproxin in liposome.
(red)
v7698lh.dat
76/98 holoenzyme (Cobalt heme)
in liposome.
(green)
1
0.9
0.8
0.7
0.6
0.5
0.4
0.3
0.2
0.1
0
-60
-40
-20
0
20
40
60

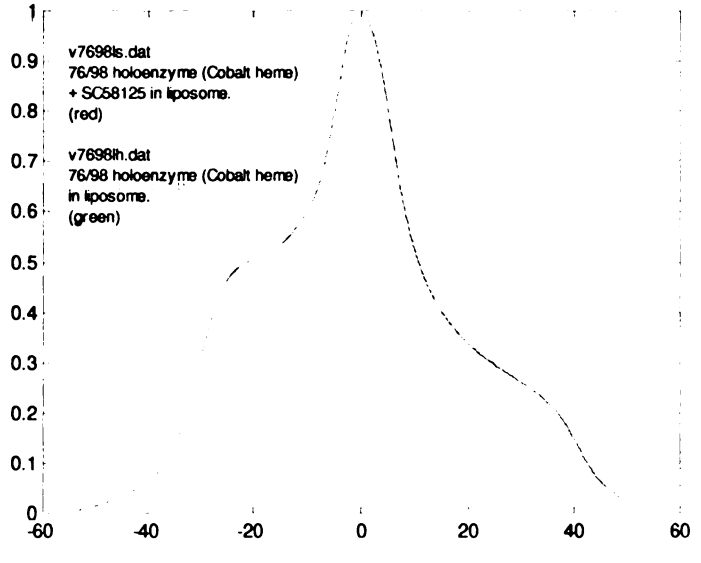
v7698ls.dat
76/98 holoenzyme (Cobalt heme)
+ SC58125 in liposome.
(red)
v7698lh.dat
76/98 holoenzyme (Cobalt heme)
in liposome.
(green)
1
0.9
0.8
0.7
0.6
0.5
0.4
0.3
0.2
0.1
0
-60
-40
-20
0
20
40
60

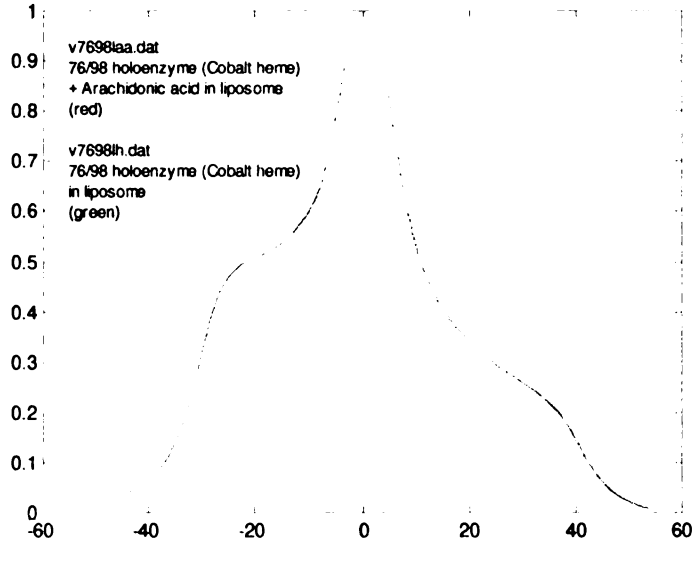
v7698laa.dat
76/98 holoenzyme (Cobalt heme)
+ Arachidonic acid in liposome
(red)
v7698lh.dat
76/98 holoenzyme (Cobalt heme)
in liposome
(green)
1
0.9
0.8
0.7
0.6
0.5
0.4
0.3
0.2
0.1
0
-60
-40
-20
0
20
40
60

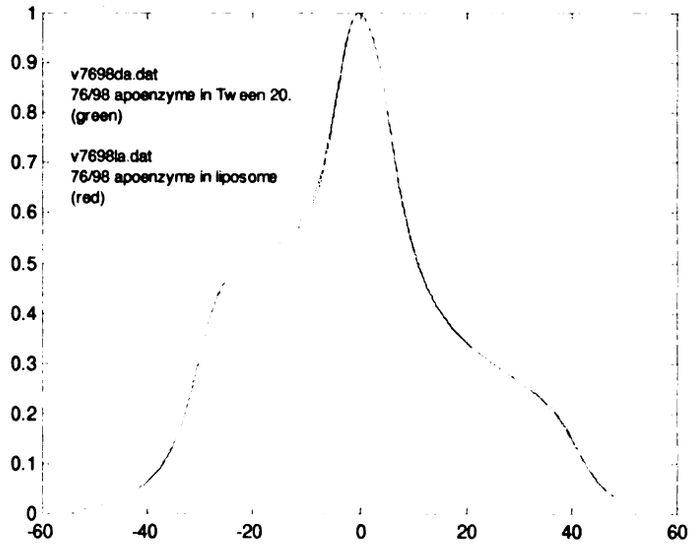
v7698da.dat
76/98 apoenzyme in Tween 20.
(green)
v7698la.dat
76/98 apoenzyme in liposome
(red)

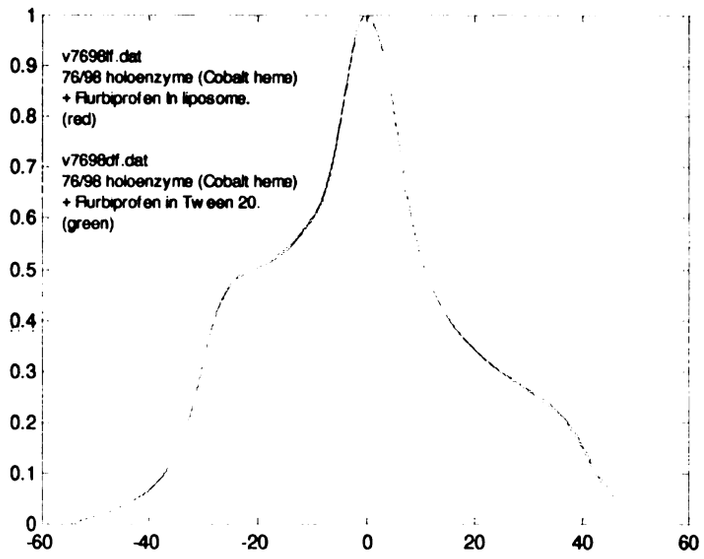
v7698lf.dat
76/98 holoenzyme (Cobalt heme)
+ Flurbiprofen in liposome.
(red)
v7698df.dat
76/98 holoenzyme (Cobalt heme)
+ Flurbiprofen in Tween 20.
(green)

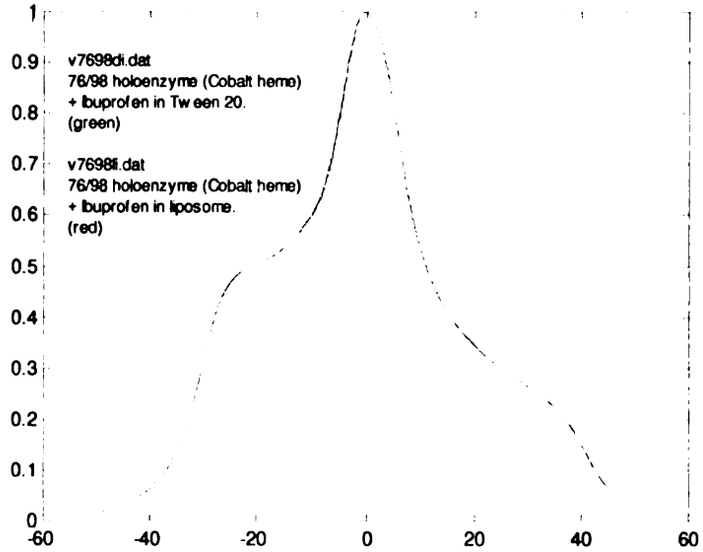
v7698di.dat
76/98 holoenzyme (Cobalt heme)
+ Ibuprofen in Tween 20.
(green)
v7698li.dat
76/98 holoenzyme (Cobalt heme)
+ Ibuprofen in liposome.
(red)

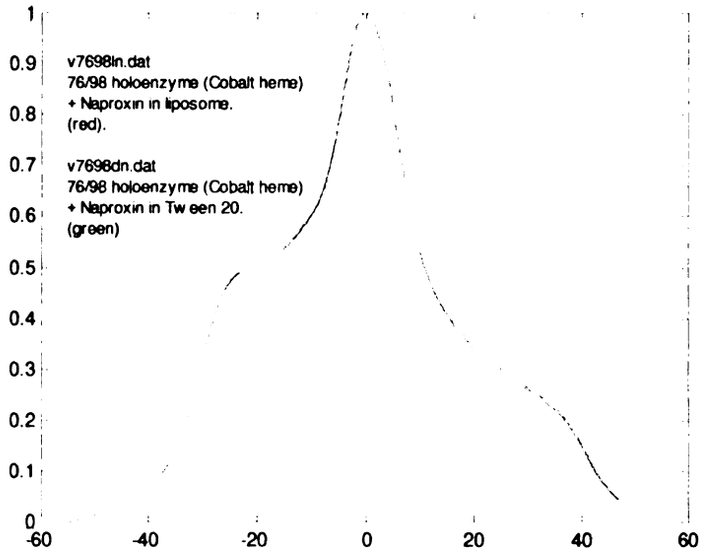
v7698ln.dat
76/98 holoenzyme (Cobalt heme)
+ Naproxin in liposome.
(red).
v7698dn.dat
76/98 holoenzyme (Cobalt heme)
+ Naproxin in Tween 20.
(green)

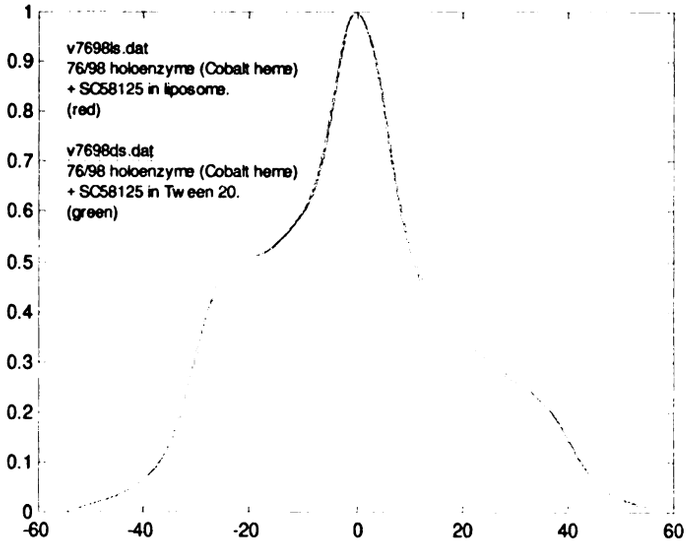
v7698ls.dat
76/98 holoenzyme (Cobalt heme)
+ SC58125 in liposome.
(red)
v7698ds.dat
76/98 holoenzyme (Cobalt heme)
+ SC58125 in Tween 20.
(green)
1
0.9
0.8
0.7
0.6
0.5
0.4
0.3
0.2
0.1
0
-60
-40
-20
0
20
40
60

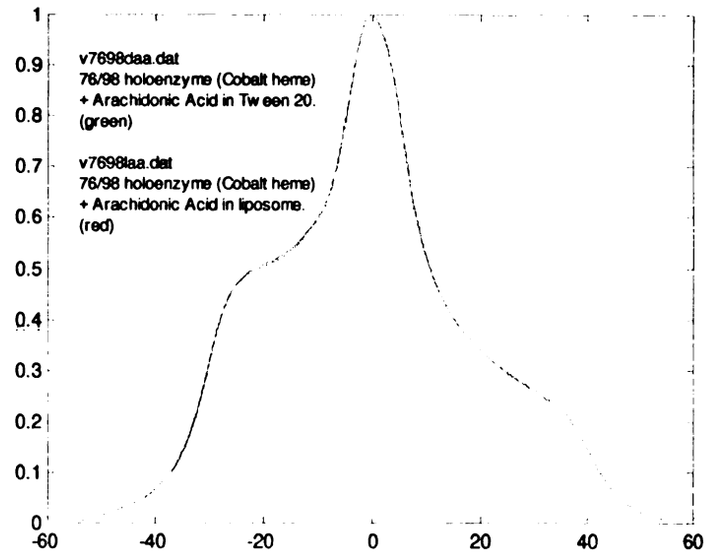
v7698daa.dat
76/98 holoenzyme (Cobalt heme)
+ Arachidonic Acid in Tween 20.
(green)
v7698laa.dat
76/98 holoenzyme (Cobalt heme)
+ Arachidonic Acid in liposome.
(red)
1
0.9
0.8
0.7
0.6
0.5
0.4
0.3
0.2
0.1
0
-60
-40
-20
0
20
40
60

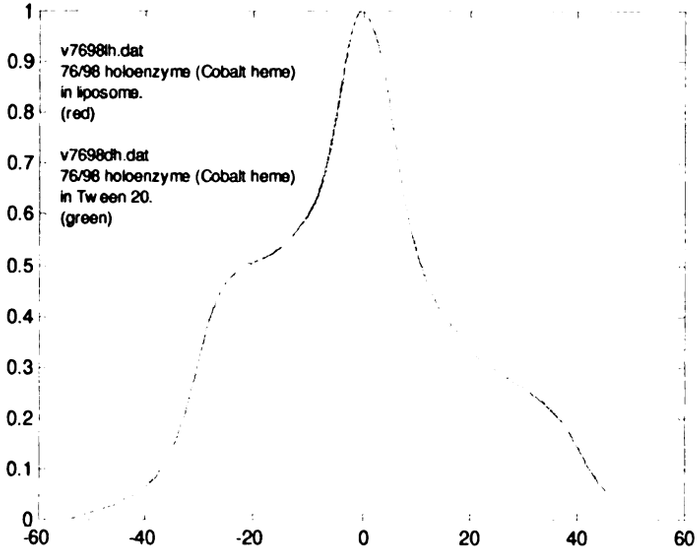
v7698lh.dat
76/98 holoenzyme (Cobalt heme)
in liposome.
(red)
v7698dh.dat
76/98 holoenzyme (Cobalt heme)
in Tween 20.
(green)
1
0.9
0.8
0.7
0.6
0.5
0.4
0.3
0.2
0.1
0
-60
-40
-20
0
20
40
60

**Figure 5C**. Absorbance EPR spectra of I77C/I98C double mutant in detergent (Tween 20) and liposome and in the presence of Co-PPIX, arachidonic acid and various COX inhibitors.
Spectra were normalized to maximum absorbance and were uncorrected for any contribution by monoradical species.
Images in this dissertation are presented in color.

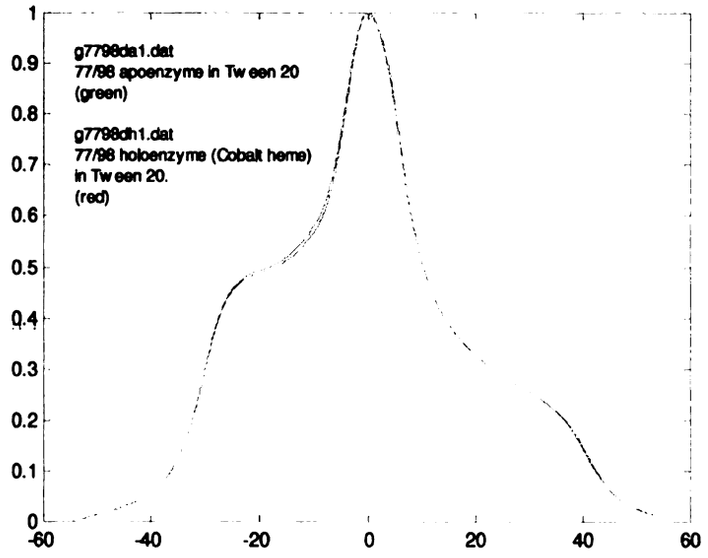
g7798da1.dat
77/98 apoenzyme in Tween 20
(green)
g7798dh1.dat
77/98 holoenzyme (Cobalt heme)
in Tween 20.
(red)

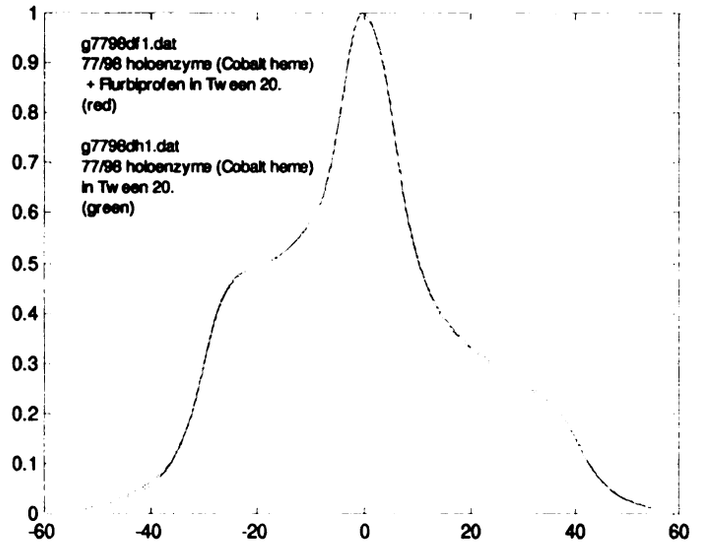
g7798df1.dat
77/98 holoenzyme (Cobalt heme)
+ Flurbiprofen in Tween 20.
(red)
g7798dh1.dat
77/98 holoenzyme (Cobalt heme)
in Tween 20.
(green)

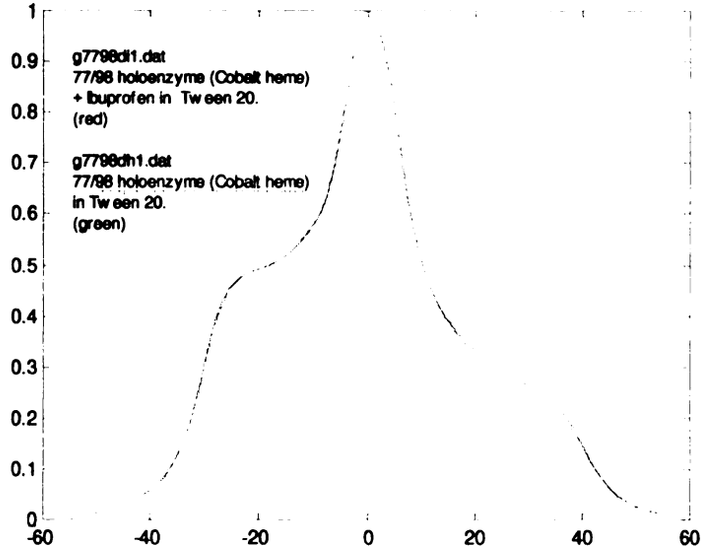
g7798di1.dat
77/98 holoenzyme (Cobalt heme)
+ Ibuprofen in Tween 20.
(red)
g7798dh1.dat
77/98 holoenzyme (Cobalt heme)
in Tween 20.
(green)

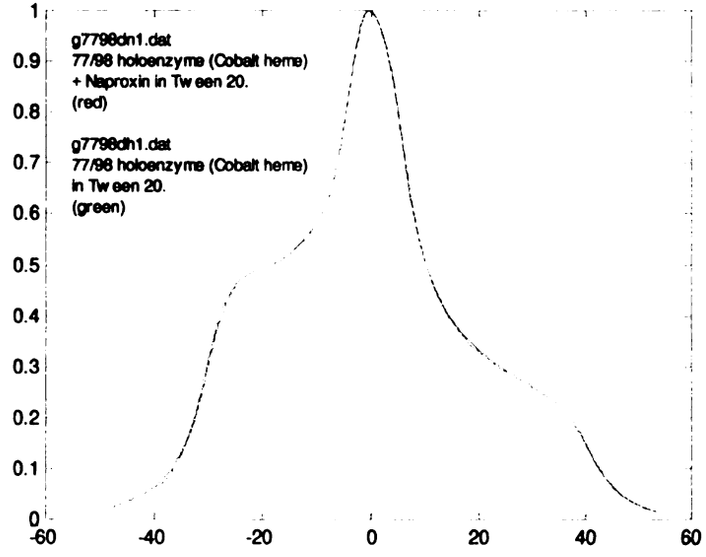
g7798dn1.dat
77/98 holoenzyme (Cobalt heme)
+ Naproxin in Tween 20.
(red)
g7798dh1.dat
77/98 holoenzyme (Cobalt heme)
in Tween 20.
(green)

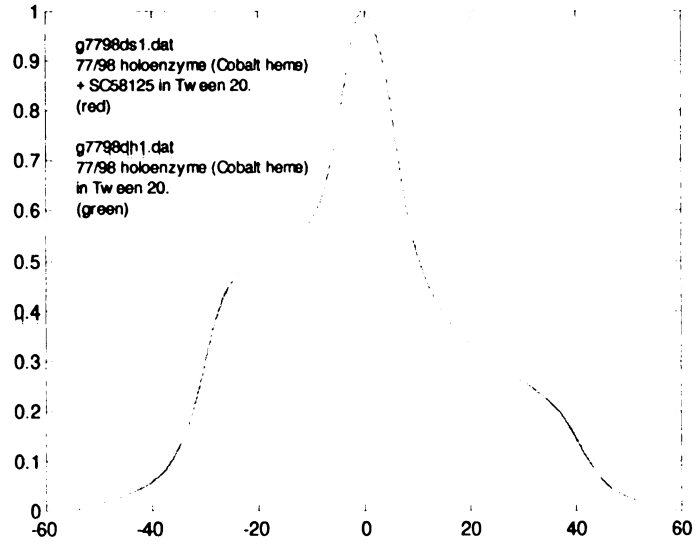
g7798ds1.dat
77/98 holoenzyme (Cobalt heme)
+ SC58125 in Tween 20.
(red)
g7798dh1.dat
77/98 holoenzyme (Cobalt heme)
in Tween 20.
(green)

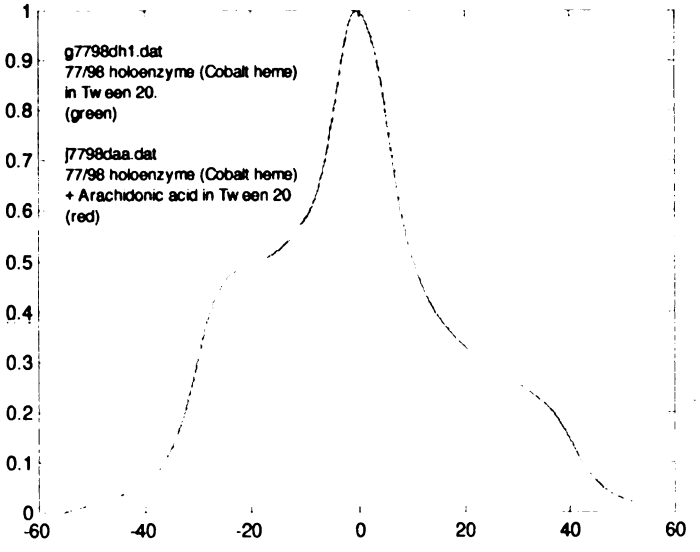
g7798dh1.dat
77/98 holoenzyme (Cobalt heme)
in Tween 20.
(green)
7798daa.dat
77/98 holoenzyme (Cobalt heme)
+ Arachidonic acid in Tween 20
(red)

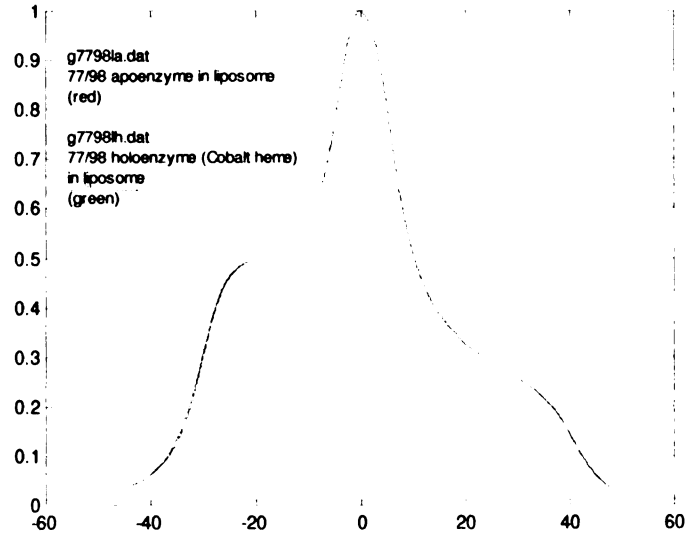
g7798la.dat
77/98 apoenzyme in liposome
(red)
g7798lh.dat
77/98 holoenzyme (Cobalt heme)
in liposome
(green)

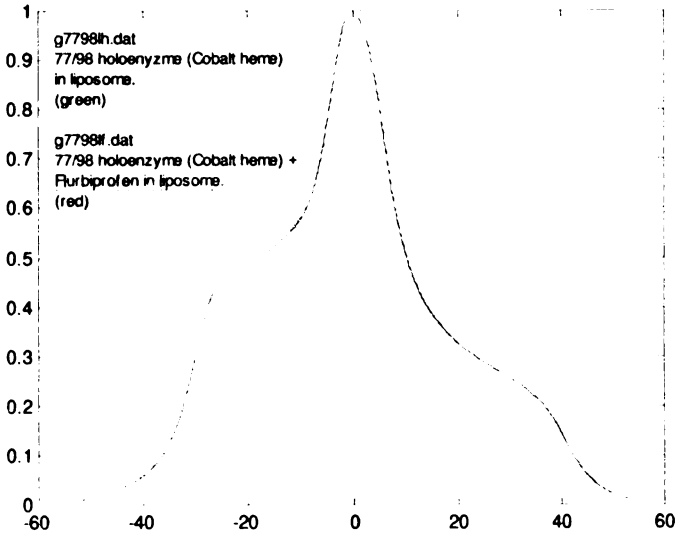
g7798lh.dat
77/98 holoenyzme (Cobalt heme)
in liposome.
(green)
g7798lf.dat
77/98 holoenzyme (Cobalt heme) +
Flurbiprofen in liposome.
(red)

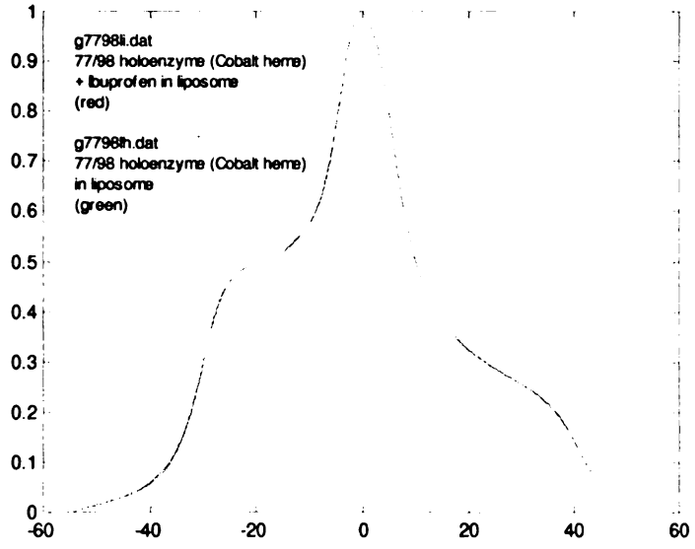
g7798li.dat
77/98 holoenzyme (Cobalt heme)
+ Ibuprofen in liposome
(red)
g7798lh.dat
77/98 holoenzyme (Cobalt heme)
in liposome
(green)
1
0.9
0.8
0.7
0.6
0.5
0.4
0.3
0.2
0.1
0
-60
-40
-20
0
20
40
60

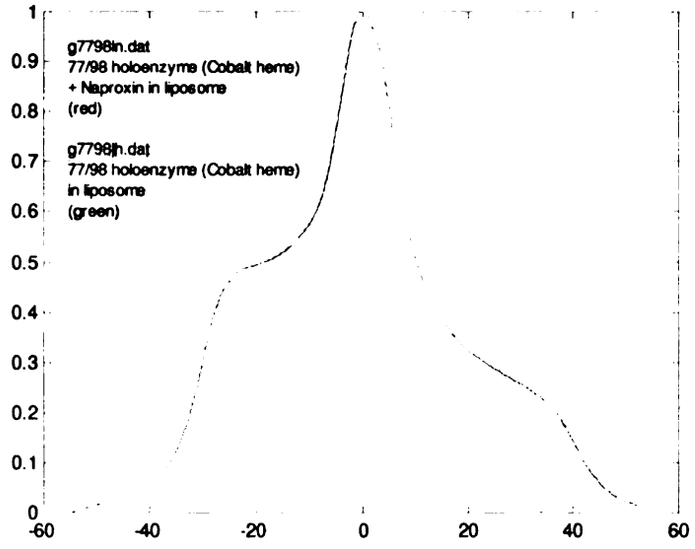
g7798ln.dat
77/98 holoenzyme (Cobalt heme)
+ Naproxin in liposome
(red)
g7798lh.dat
77/98 holoenzyme (Cobalt heme)
in liposome
(green)
1
0.9
0.8
0.7
0.6
0.5
0.4
0.3
0.2
0.1
0
-60
-40
-20
0
20
40
60

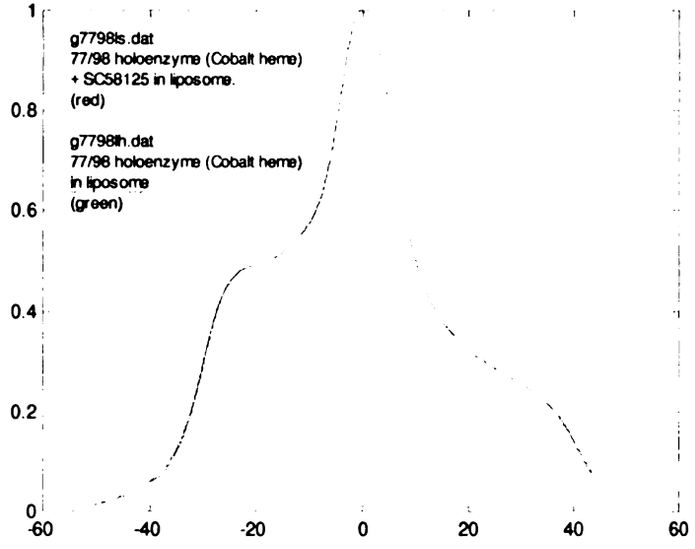
g7798ls.dat
77/98 holoenzyme (Cobalt heme)
+ SC58125 in liposome.
(red)
g7798lh.dat
77/98 holoenzyme (Cobalt heme)
in liposome
(green)
1
0.8
0.6
0.4
0.2
0
-60
-40
-20
0
20
40
60

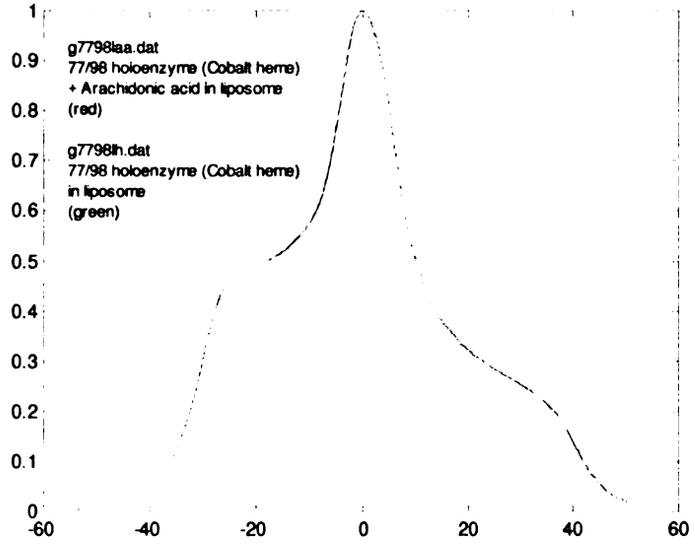
g7798laa.dat
77/98 holoenzyme (Cobalt heme)
+ Arachidonic acid in liposome
(red)
g7798lh.dat
77/98 holoenzyme (Cobalt heme)
in liposome
(green)
1
0.9
0.8
0.7
0.6
0.5
0.4
0.3
0.2
0.1
0
-60
-40
-20
0
20
40
60

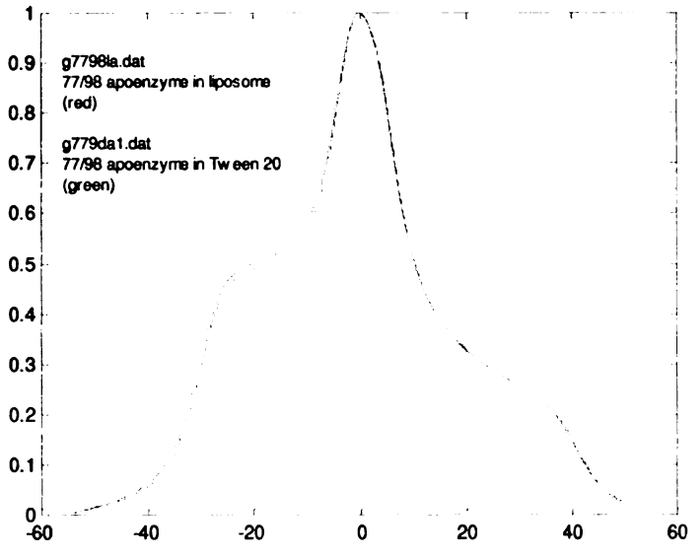
g7798la.dat
77/98 apoenzyme in liposome
(red)
g779da1.dat
77/98 apoenzyme in Tween 20
(green)

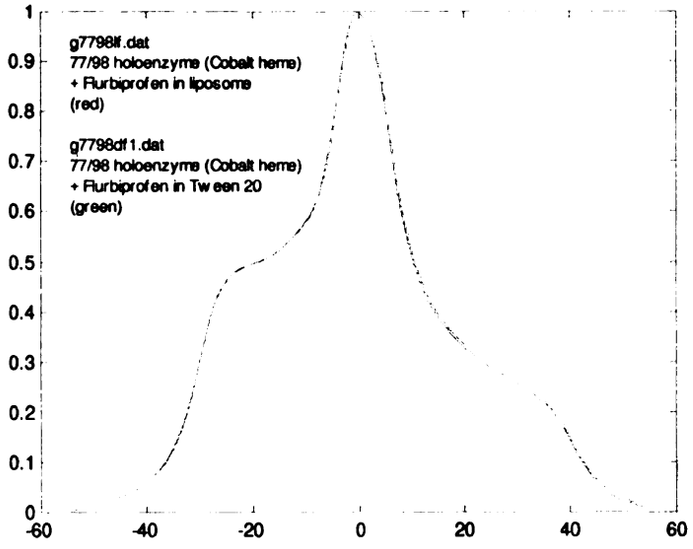
g7798lf.dat
77/98 holoenzyme (Cobalt heme)
+ Flurbiprofen in liposome
(red)
g7798df1.dat
77/98 holoenzyme (Cobalt heme)
+ Flurbiprofen in Tween 20
(green)

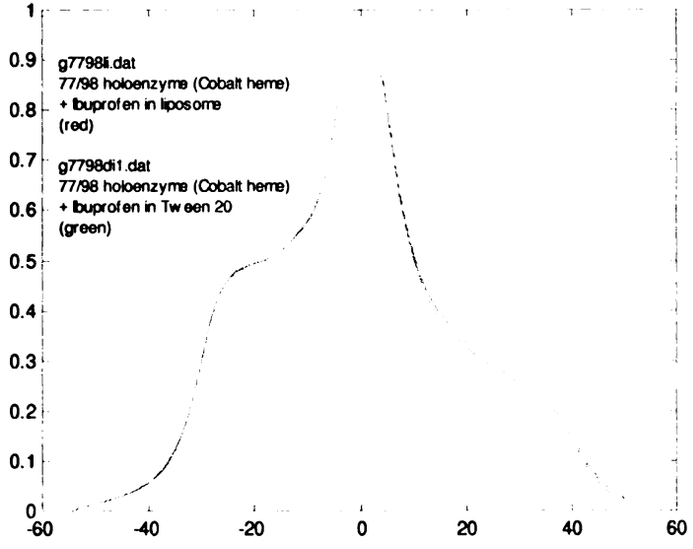
g7798li.dat
77/98 holoenzyme (Cobalt heme)
+ Ibuprofen in liposome
(red)
g7798di1.dat
77/98 holoenzyme (Cobalt heme)
+ Ibuprofen in Tween 20
(green)

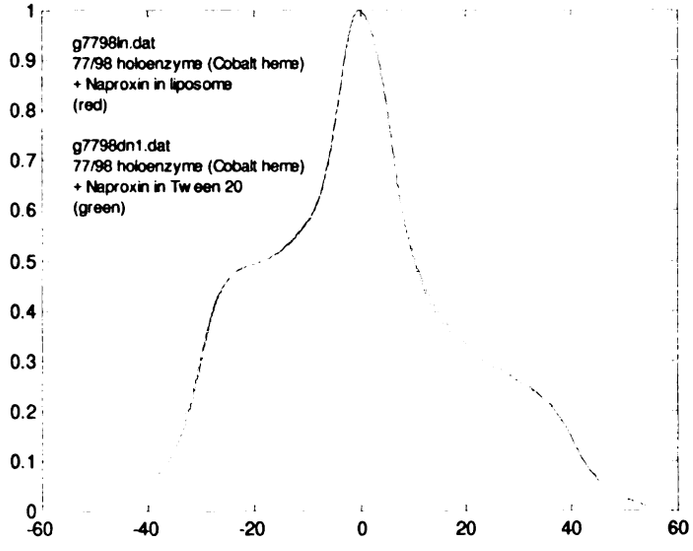
g7798ln.dat
77/98 holoenzyme (Cobalt heme)
+ Naproxin in liposome
(red)
g7798dn1.dat
77/98 holoenzyme (Cobalt heme)
+ Naproxin in Tween 20
(green)

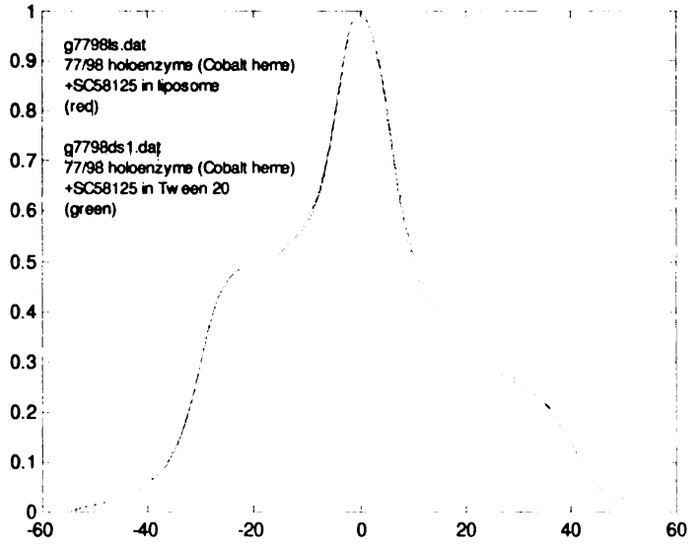
g7798ls.dat
77/98 holoenzyme (Cobalt heme)
+SC58125 in liposome
(red)
g7798ds1.dat
77/98 holoenzyme (Cobalt heme)
+SC58125 in Tween 20
(green)
1
0.9
0.8
0.7
0.6
0.5
0.4
0.3
0.2
0.1
0
-60
-40
-20
0
20
40
60

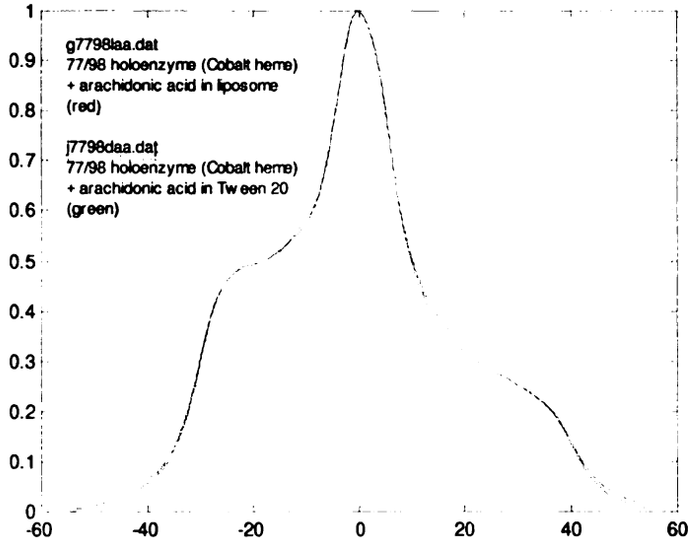
g7798laa.dat
77/98 holoenzyme (Cobalt heme)
+ arachidonic acid in liposome
(red)
j7798daa.dat
77/98 holoenzyme (Cobalt heme)
+ arachidonic acid in Tween 20
(green)
1
0.9
0.8
0.7
0.6
0.5
0.4
0.3
0.2
0.1
0
-60
-40
-20
0
20
40
60

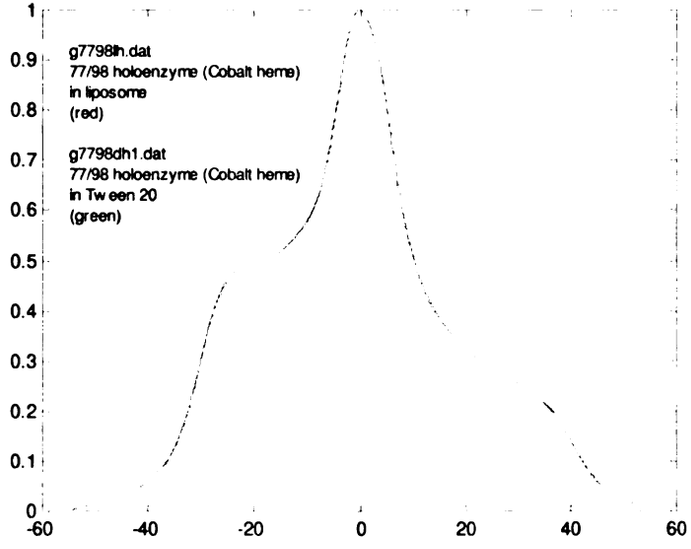
g7798lh.dat
77/98 holoenzyme (Cobalt heme)
in liposome
(red)
g7798dh1.dat
77/98 holoenzyme (Cobalt heme)
in Tween 20
(green)
1
0.9
0.8
0.7
0.6
0.5
0.4
0.3
0.2
0.1
0
-60
-40
-20
0
20
40
60

**Figure 6C**. Absorbance EPR spectra of F84C/I98C double mutant in detergent (Tween 20) and liposome and in the presence of Co-PPIX, arachidonic acid and various COX inhibitors.
Spectra were normalized to maximum absorbance and were uncorrected for any contribution by monoradical species.
Images in this dissertation are presented in color.

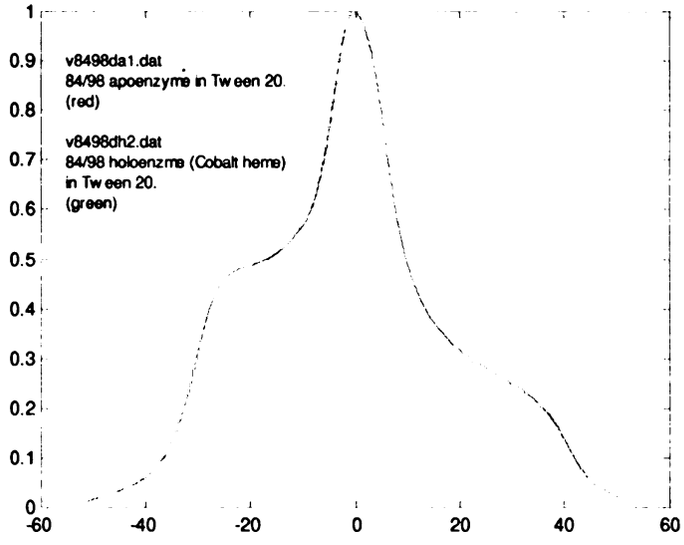
v8498da1.dat
84/98 apoenzyme in Tween 20.
(red)
v8498dh2.dat
84/98 holoenzme (Cobalt heme)
in Tween 20.
(green)

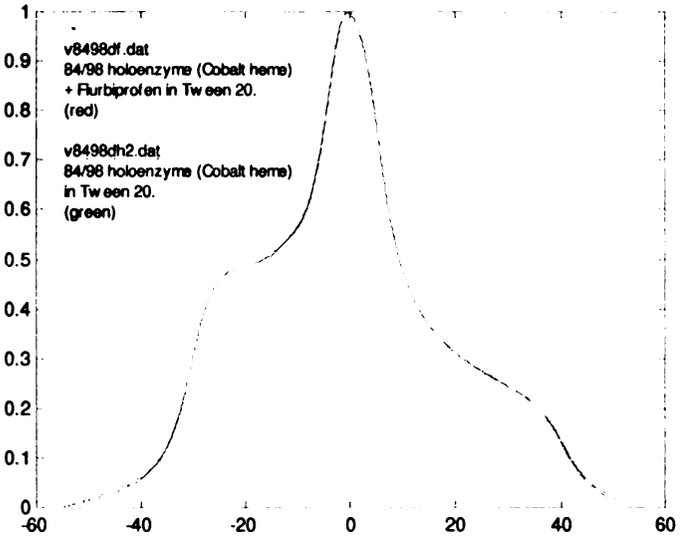
v8498df.dat
84/98 holoenzyme (Cobalt heme)
+ Flurbiprofen in Tween 20.
(red)
v8498dh2.dat
84/98 holoenzyme (Cobalt heme)
in Tween 20.
(green)

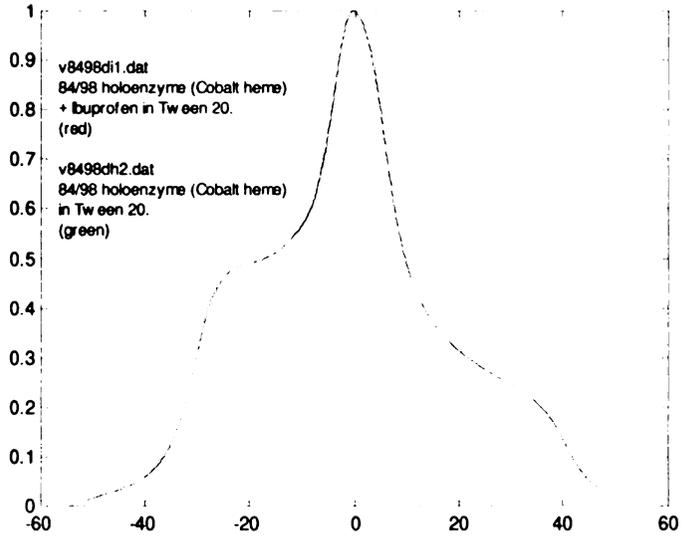
v8498di1.dat
84/98 holoenzyme (Cobalt heme)
+ Ibuprofen in Tween 20.
(red)
v8498dh2.dat
84/98 holoenzyme (Cobalt heme)
in Tween 20.
(green)

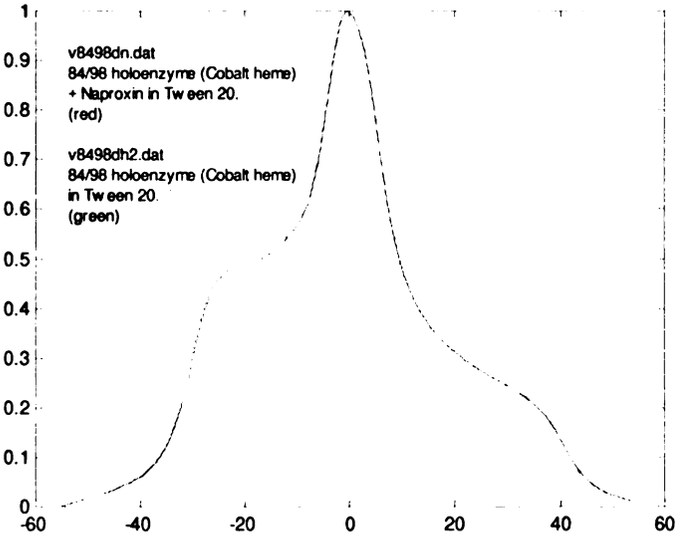
v8498dn.dat
84/98 holoenzyme (Cobalt heme)
+ Naproxin in Tween 20.
(red)
v8498dh2.dat
84/98 holoenzyme (Cobalt heme)
in Tween 20.
(green)

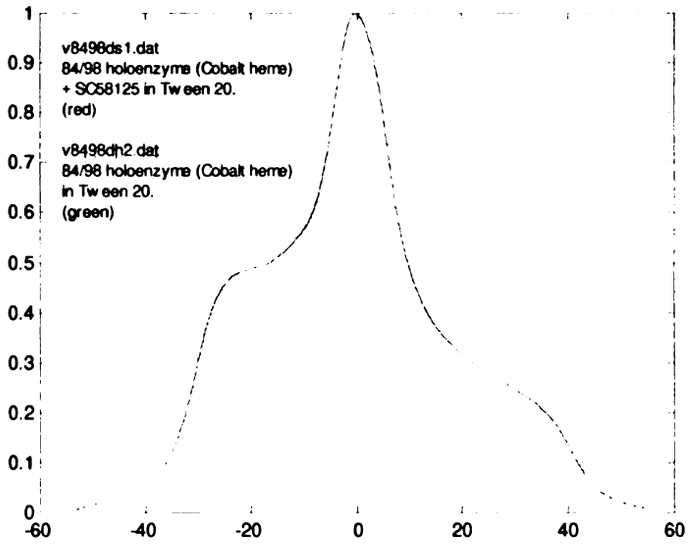
v8498ds1.dat
84/98 holoenzyme (Cobalt heme)
+ SC58125 in Tween 20.
(red)
v8498dh2.dat
84/98 holoenzyme (Cobalt heme)
in Tween 20.
(green)
1
0.9
0.8
0.7
0.6
0.5
0.4
0.3
0.2
0.1
0
-60
-40
-20
0
20
40
60

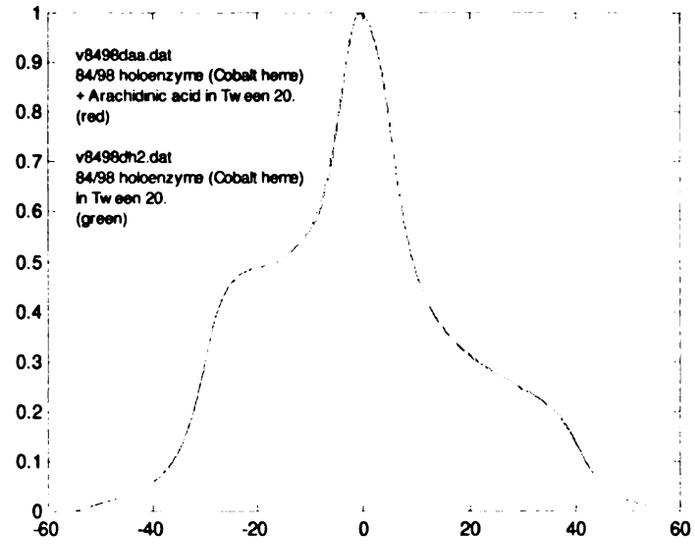
v8498daa.dat
84/98 holoenzyme (Cobalt heme)
+ Arachidinic acid in Tween 20.
(red)
v8498dh2.dat
84/98 holoenzyme (Cobalt heme)
in Tween 20.
(green)
1
0.9
0.8
0.7
0.6
0.5
0.4
0.3
0.2
0.1
0
-60
-40
-20
0
20
40
60

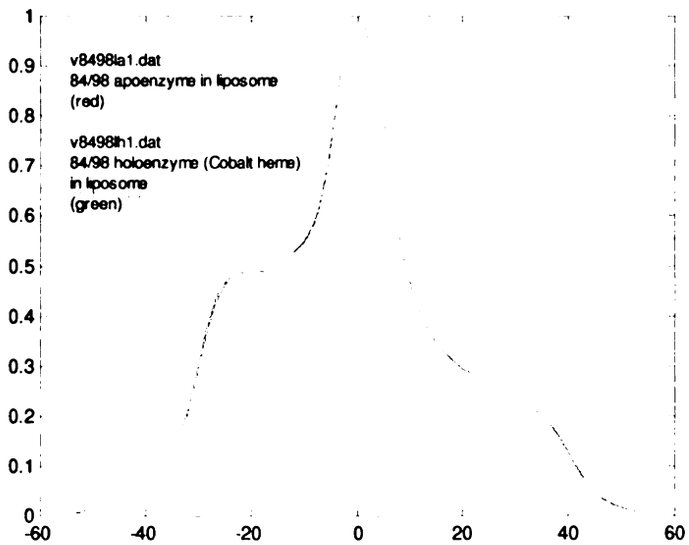
v8498la1.dat
84/98 apoenzyme in liposome
(red)
v8498lh1.dat
84/98 holoenzyme (Cobalt heme)
in liposome
(green)
1
0.9
0.8
0.7
0.6
0.5
0.4
0.3
0.2
0.1
0
-60
-40
-20
0
20
40
60

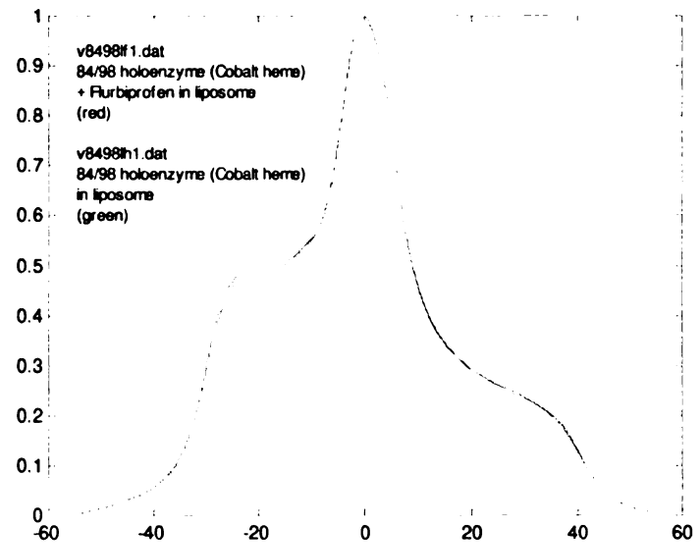
v8498lf1.dat
84/98 holoenzyme (Cobalt heme)
+ Flurbiprofen in liposome
(red)
v8498lh1.dat
84/98 holoenzyme (Cobalt heme)
in liposome
(green)
1
0.9
0.8
0.7
0.6
0.5
0.4
0.3
0.2
0.1
0
-60
-40
-20
0
20
40
60

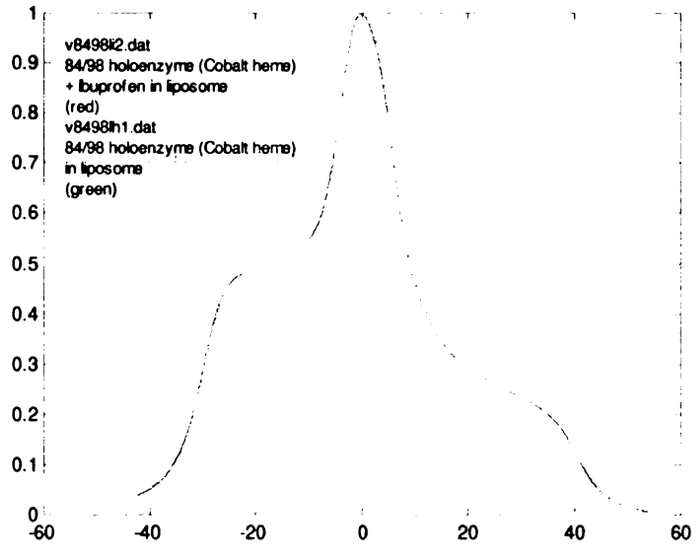
v8498ik2.dat
84/98 holoenzyme (Cobalt heme)
+ Ibuprofen in liposome
(red)
v8498lh1.dat
84/98 holoenzyme (Cobalt heme)
in liposome
(green)

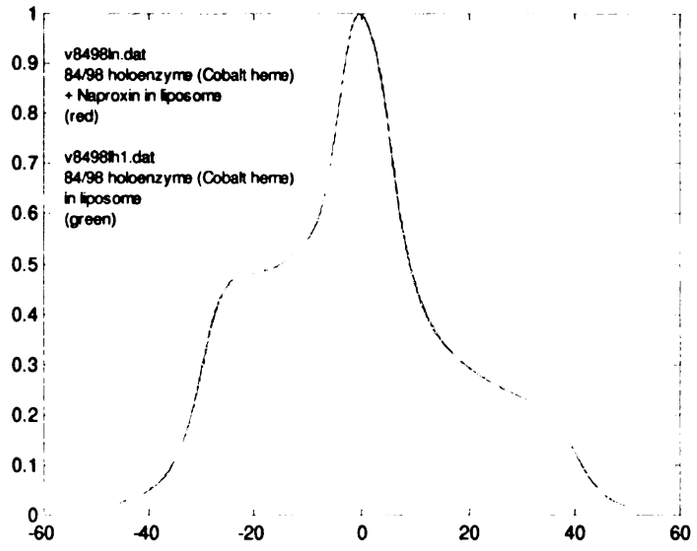
v8498in.dat
84/98 holoenzyme (Cobalt heme)
+ Naproxin in liposome
(red)
v8498lh1.dat
84/98 holoenzyme (Cobalt heme)
in liposome
(green)

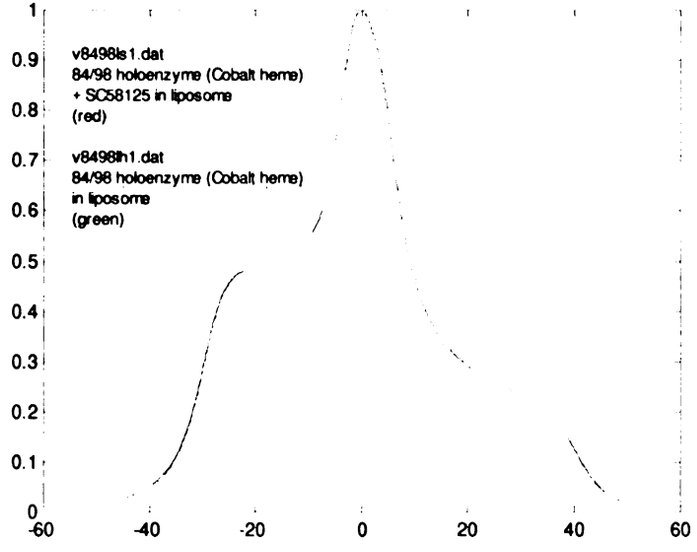
v8498is1.dat
84/98 holoenzyme (Cobalt heme)
+ SC58125 in liposome
(red)
v8498lh1.dat
84/98 holoenzyme (Cobalt heme)
in liposome
(green)

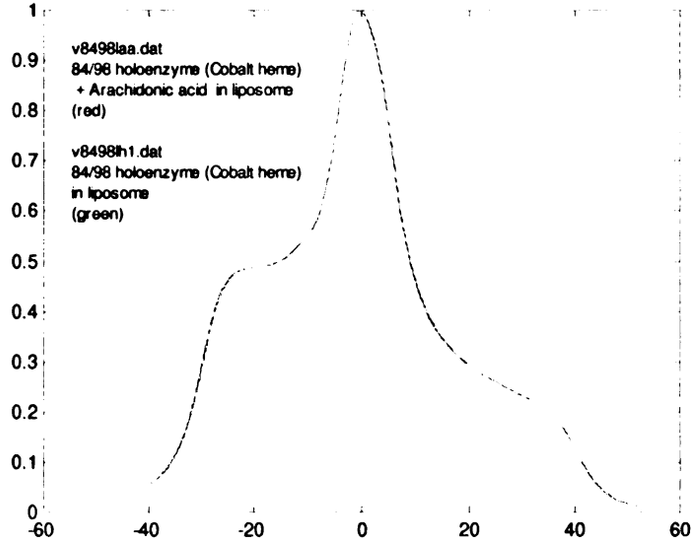
v8498iaa.dat
84/98 holoenzyme (Cobalt heme)
+ Arachidonic acid in liposome
(red)
v8498lh1.dat
84/98 holoenzyme (Cobalt heme)
in liposome
(green)

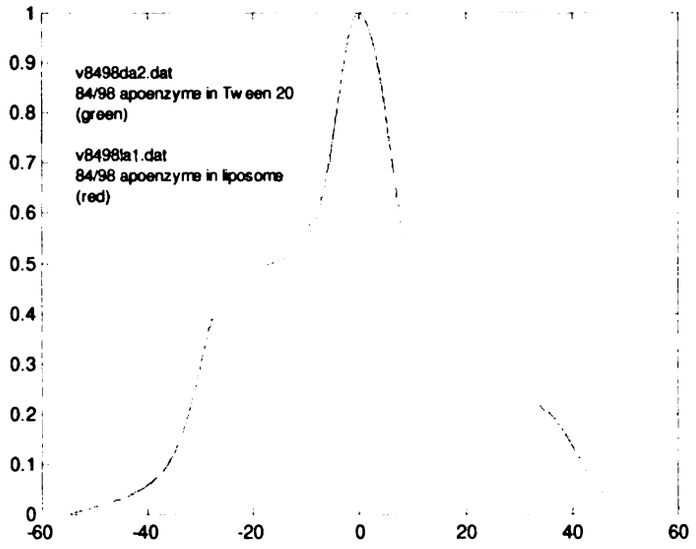
v8498da2.dat
84/98 apoenzyme in Tween 20
(green)
v8498la1.dat
84/98 apoenzyme in liposome
(red)

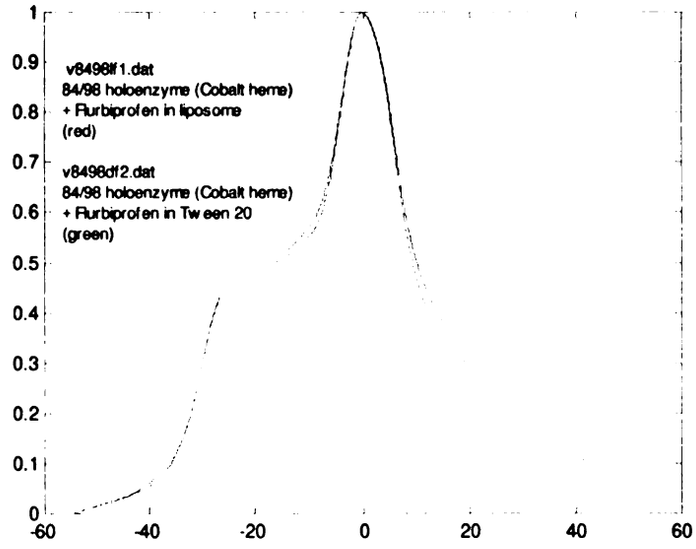
v8498lf1.dat
84/98 holoenzyme (Cobalt heme)
+ Flurbiprofen in liposome
(red)
v8498df2.dat
84/98 holoenzyme (Cobalt heme)
+ Flurbiprofen in Tween 20
(green)

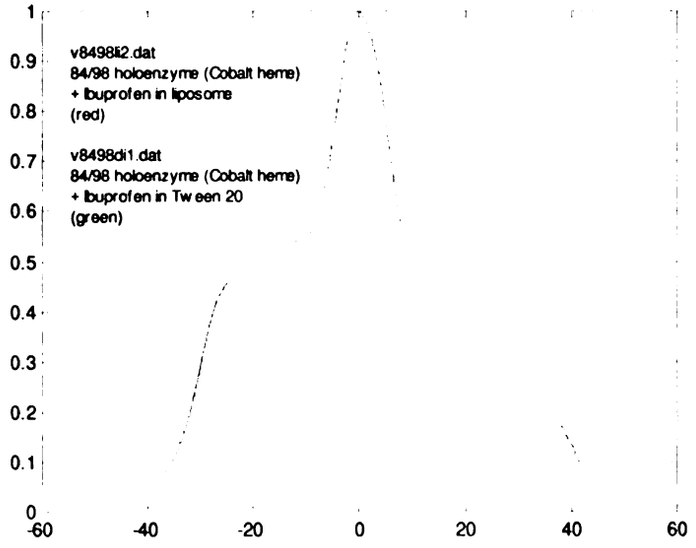
v8498li2.dat
84/98 holoenzyme (Cobalt heme)
+ Ibuprofen in liposome
(red)
v8498di1.dat
84/98 holoenzyme (Cobalt heme)
+ Ibuprofen in Tween 20
(green)

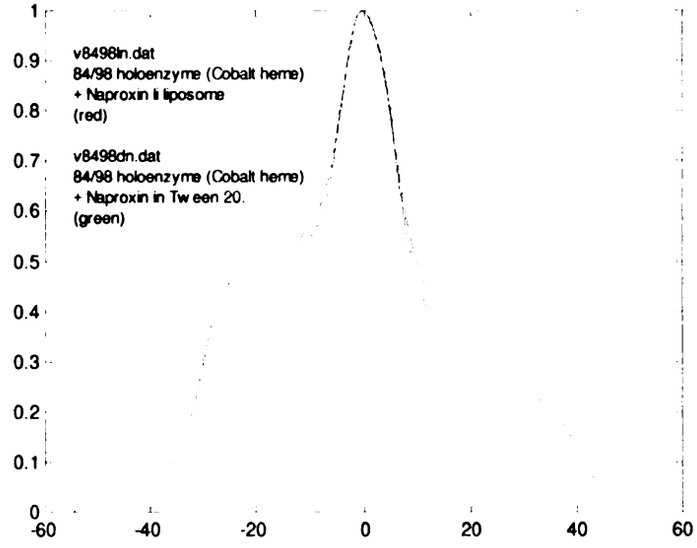
v8498ln.dat
84/98 holoenzyme (Cobalt heme)
+ Naproxin li liposome
(red)
v8498dn.dat
84/98 holoenzyme (Cobalt heme)
+ Naproxin in Tween 20.
(green)

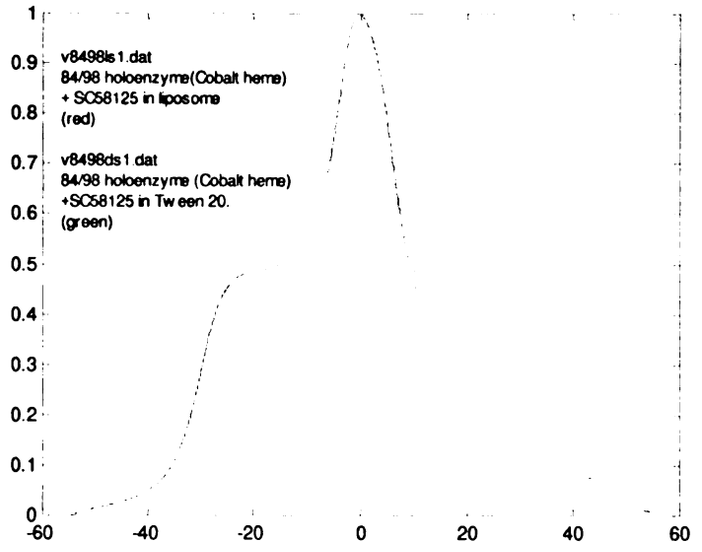
v8498ls1.dat
84/98 holoenzyme(Cobalt heme)
+ SC58125 in liposome
(red)
v8498ds1.dat
84/98 holoenzyme (Cobalt heme)
+SC58125 in Tween 20.
(green)
1
0.9
0.8
0.7
0.6
0.5
0.4
0.3
0.2
0.1
0
-60
-40
-20
0
20
40
60

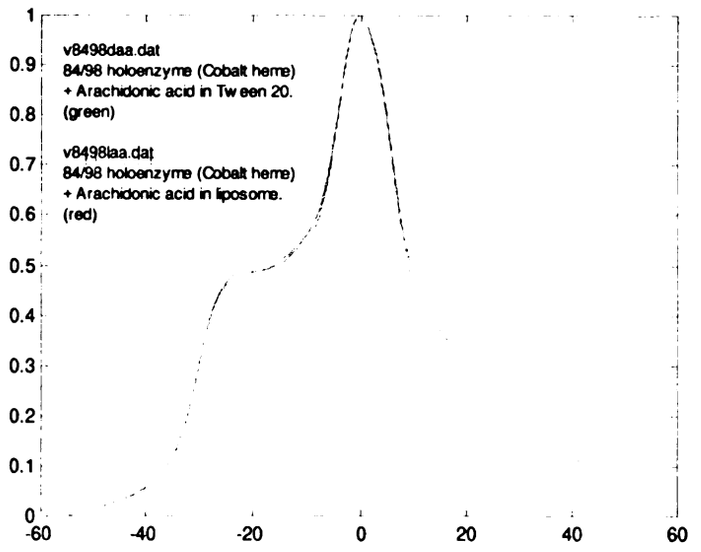
v8498daa.dat
84/98 holoenzyme (Cobalt heme)
+ Arachidonic acid in Tween 20.
(green)
v8498laa.dat
84/98 holoenzyme (Cobalt heme)
+ Arachidonic acid in liposome.
(red)
1
0.9
0.8
0.7
0.6
0.5
0.4
0.3
0.2
0.1
0
-60
-40
-20
0
20
40
60

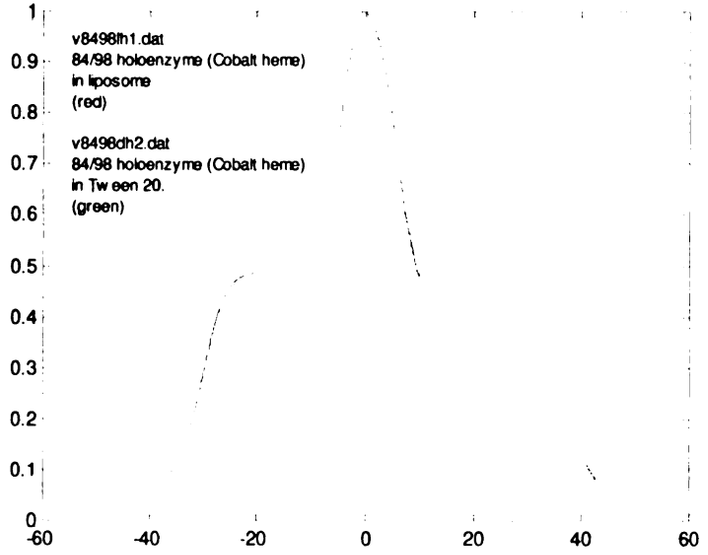
v8498lh1.dat
84/98 holoenzyme (Cobalt heme)
in liposome
(red)
v8498dh2.dat
84/98 holoenzyme (Cobalt heme)
in Tween 20.
(green)
1
0.9
0.8
0.7
0.6
0.5
0.4
0.3
0.2
0.1
0
-60
-40
-20
0
20
40
60

**Figure 7C**. Absorbance EPR spectra of W85C/I98C double mutant in detergent (Tween 20) and liposome and in the presence of Co-PPIX, arachidonic acid and various COX inhibitors.
Spectra were normalized to maximum absorbance and were uncorrected for any contribution by monoradical species.
Images in this dissertation are presented in color.

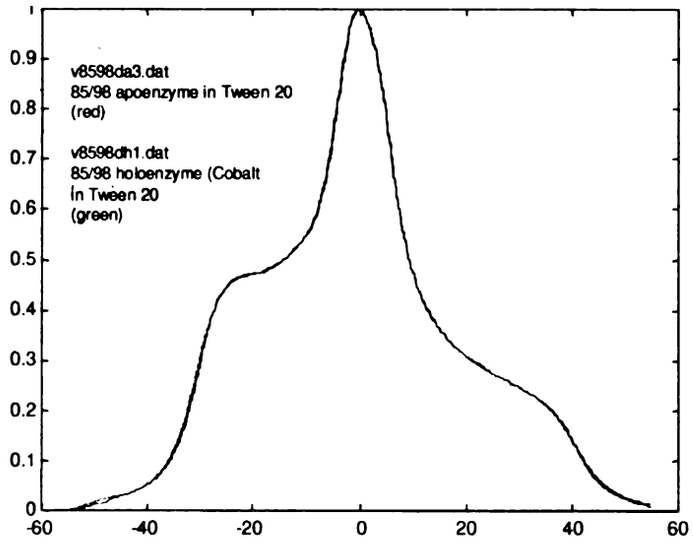
v8598da3.dat
85/98 apoenzyme in Tween 20
(red)
v8598dh1.dat
85/98 holoenzyme (Cobalt
In Tween 20
(green)

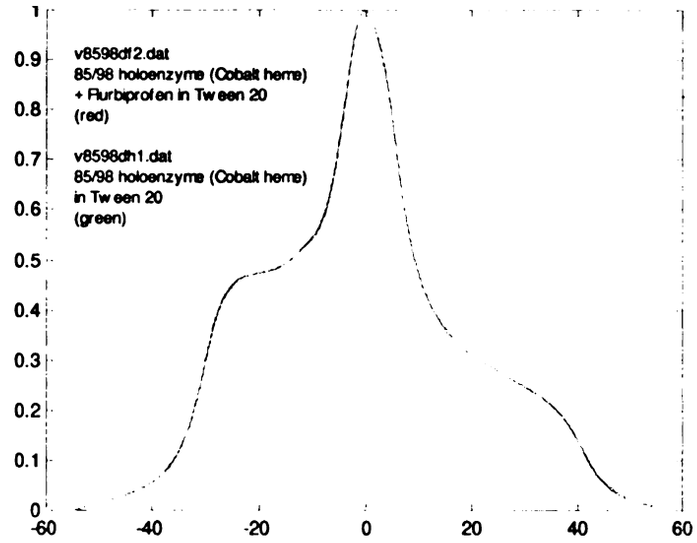
v8598df2.dat
85/98 holoenzyme (Cobalt heme)
+ Flurbiprofen in Tween 20
(red)
v8598dh1.dat
85/98 holoenzyme (Cobalt heme)
in Tween 20
(green)

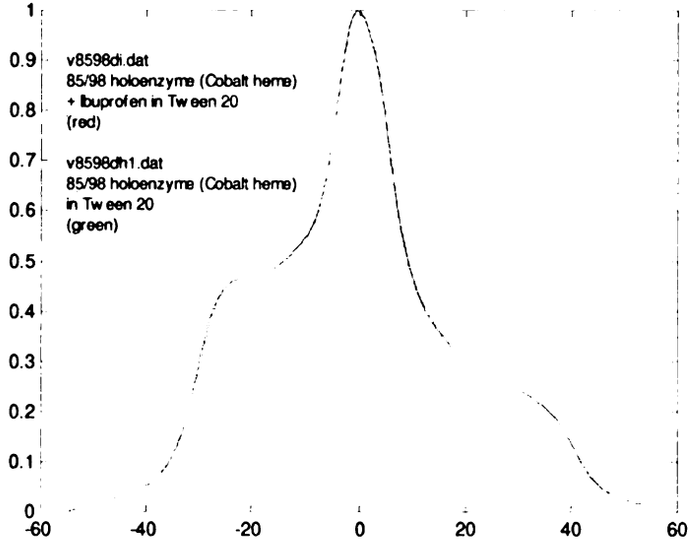
v8598di.dat
85/98 holoenzyme (Cobalt heme)
+ Ibuprofen in Tween 20
(red)
v8598dh1.dat
85/98 holoenzyme (Cobalt heme)
in Tween 20
(green)

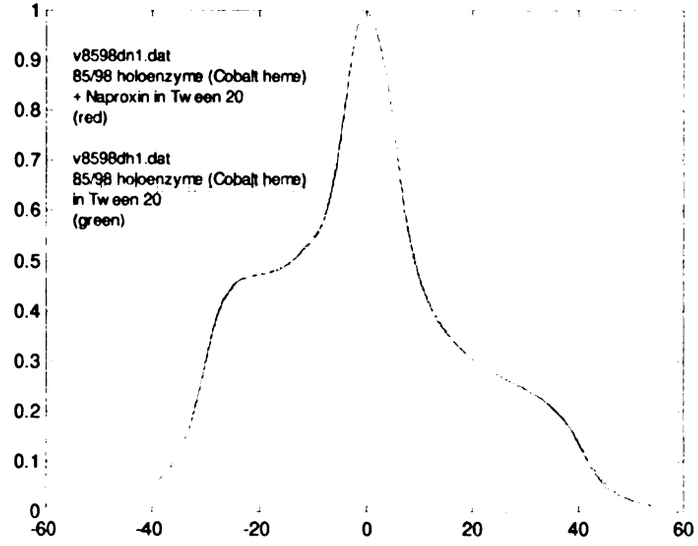
v8598dn1.dat
85/98 holoenzyme (Cobalt heme)
+ Naproxin in Tween 20
(red)
v8598dh1.dat
85/98 holoenzyme (Cobalt heme)
in Tween 20
(green)

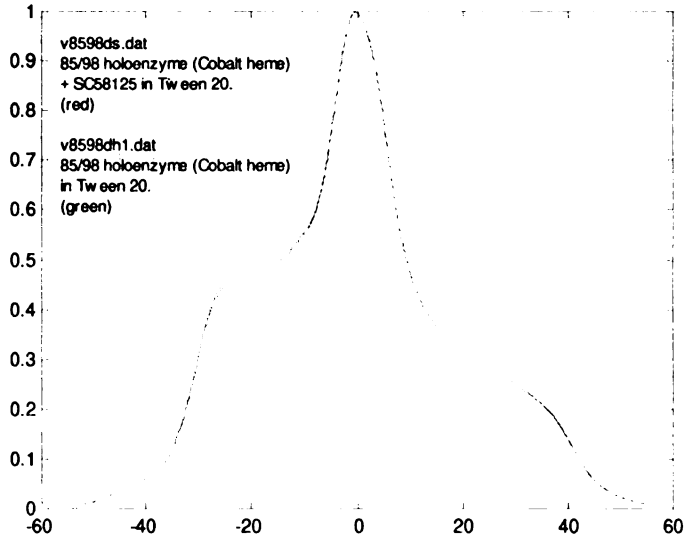
v8598ds.dat
85/98 holoenzyme (Cobalt heme)
+ SC58125 in Tween 20.
(red)
v8598dh1.dat
85/98 holoenzyme (Cobalt heme)
in Tween 20.
(green)

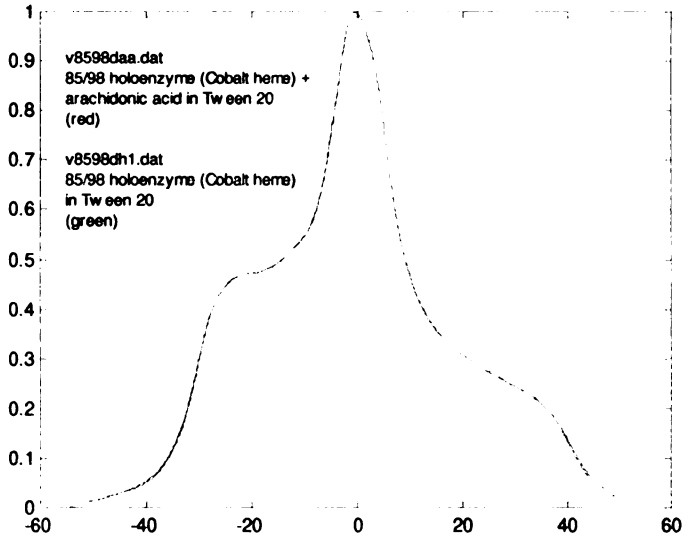
v8598daa.dat
85/98 holoenzyme (Cobalt heme) +
arachidonic acid in Tween 20
(red)
v8598dh1.dat
85/98 holoenzyme (Cobalt heme)
in Tween 20
(green)

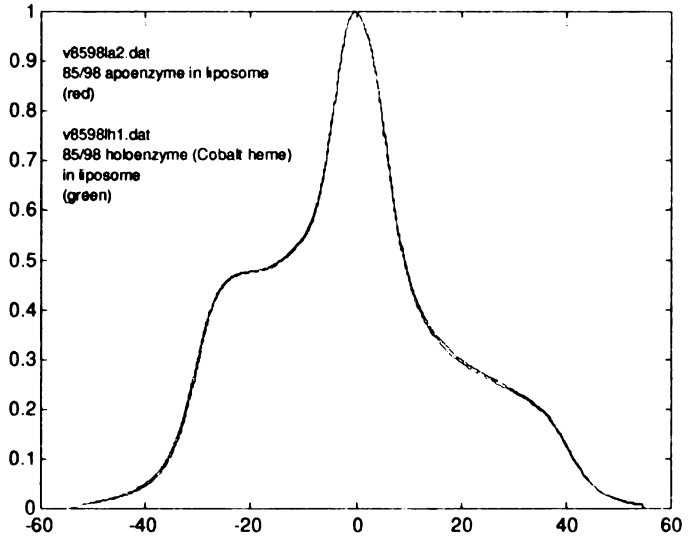
v8598la2.dat
85/98 apoenzyme in liposome
(red)
v8598lh1.dat
85/98 holoenzyme (Cobalt heme)
in liposome
(green)

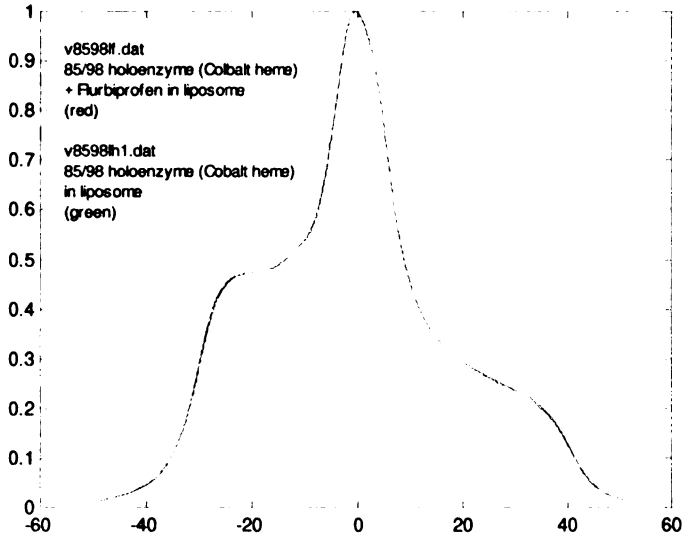
v8598lf.dat
85/98 holoenzyme (Colbalt heme)
+ Flurbiprofen in liposome
(red)
v8598lh1.dat
85/98 holoenzyme (Cobalt heme)
in liposome
(green)

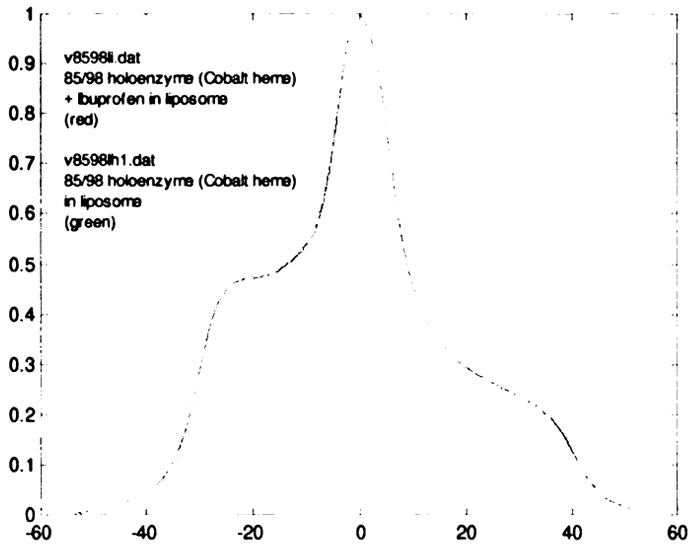
v8598il.dat
85/98 holoenzyme (Cobalt heme)
+ Ibuprofen in liposome
(red)
v8598ih1.dat
85/98 holoenzyme (Cobalt heme)
in liposome
(green)

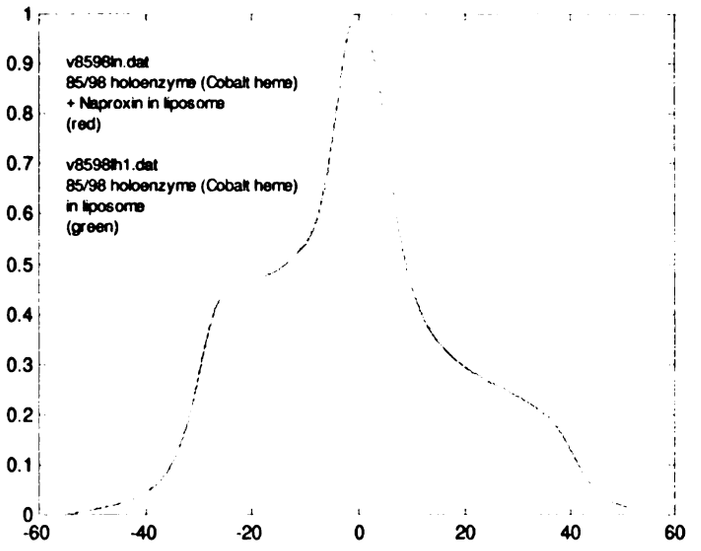
v8598in.dat
85/98 holoenzyme (Cobalt heme)
+ Naproxin in liposome
(red)
v8598ih1.dat
85/98 holoenzyme (Cobalt heme)
in liposome
(green)

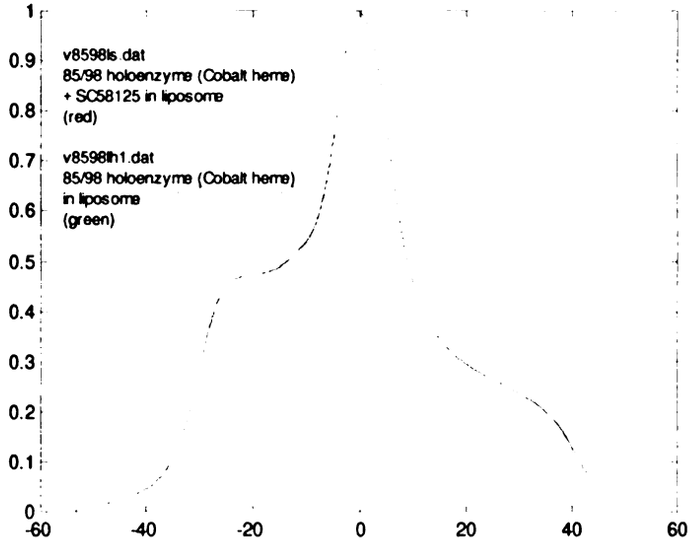
v8598is.dat
85/98 holoenzyme (Cobalt heme)
+ SC58125 in liposome
(red)
v8598ih1.dat
85/98 holoenzyme (Cobalt heme)
in liposome
(green)

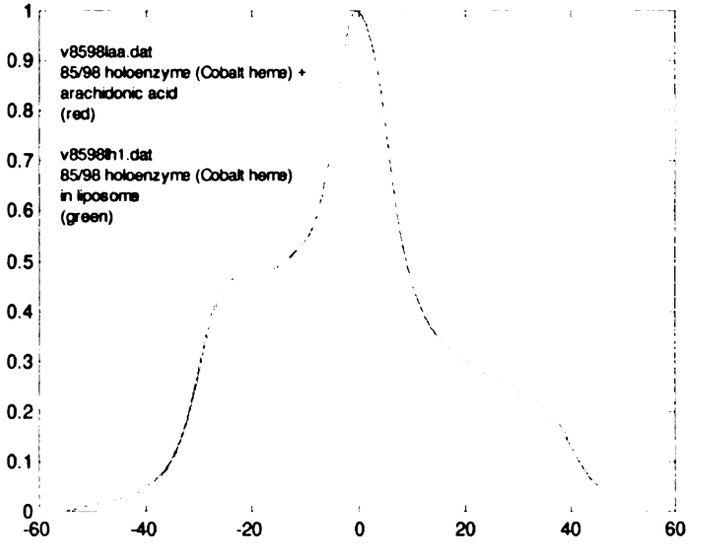
v8598iaa.dat
85/98 holoenzyme (Cobalt heme) +
arachidonic acid
(red)
v8598ih1.dat
85/98 holoenzyme (Cobalt heme)
in liposome
(green)

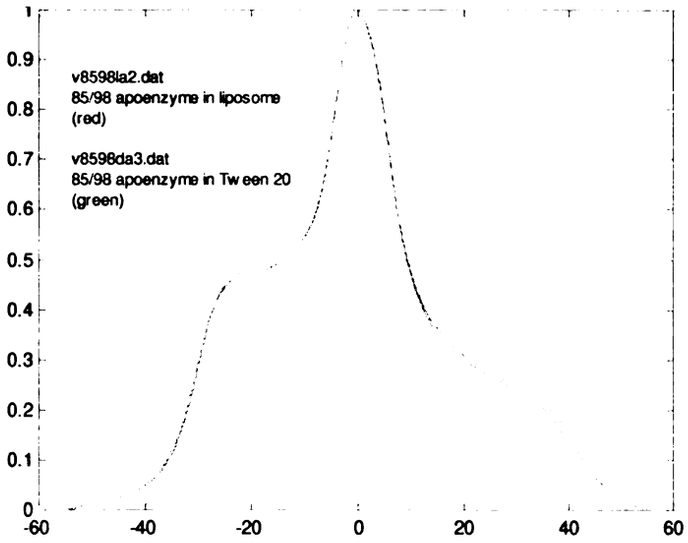
v8598la2.dat
85/98 apoenzyme in liposome
(red)
v8598da3.dat
85/98 apoenzyme in Tween 20
(green)

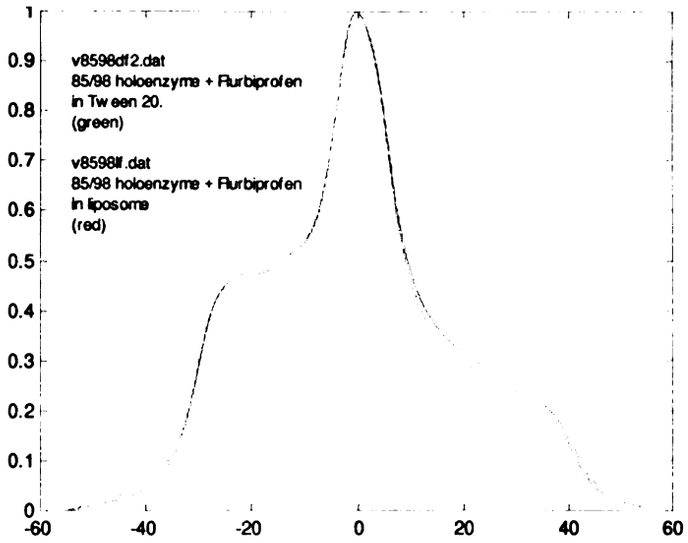
v8598df2.dat
85/98 holoenzyme + Flurbiprofen
in Tween 20.
(green)
v8598lf.dat
85/98 holoenzyme + Flurbiprofen
in liposome
(red)

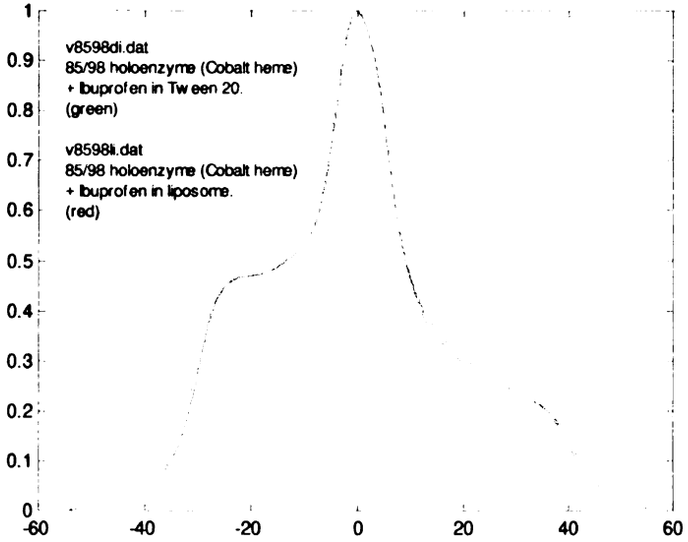
v8598di.dat
85/98 holoenzyme (Cobalt heme)
+ Ibuprofen in Tween 20.
(green)
v8598li.dat
85/98 holoenzyme (Cobalt heme)
+ Ibuprofen in liposome.
(red)

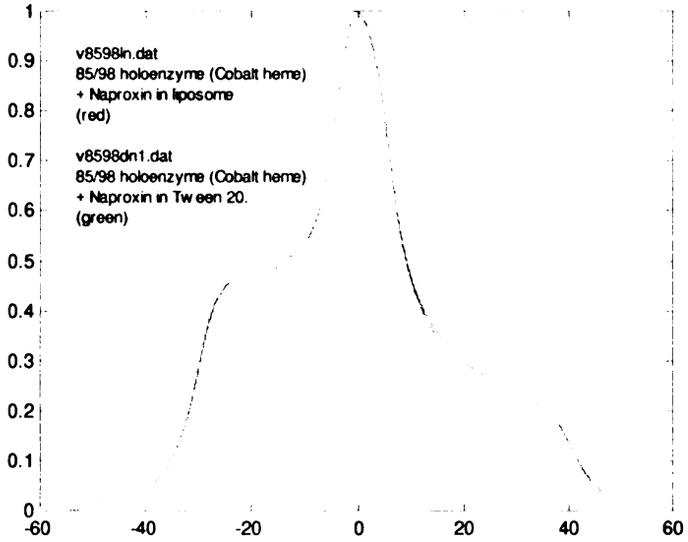
v8598ln.dat
85/98 holoenzyme (Cobalt heme)
+ Naproxin in liposome
(red)
v8598dn1.dat
85/98 holoenzyme (Cobalt heme)
+ Naproxin in Tween 20.
(green)

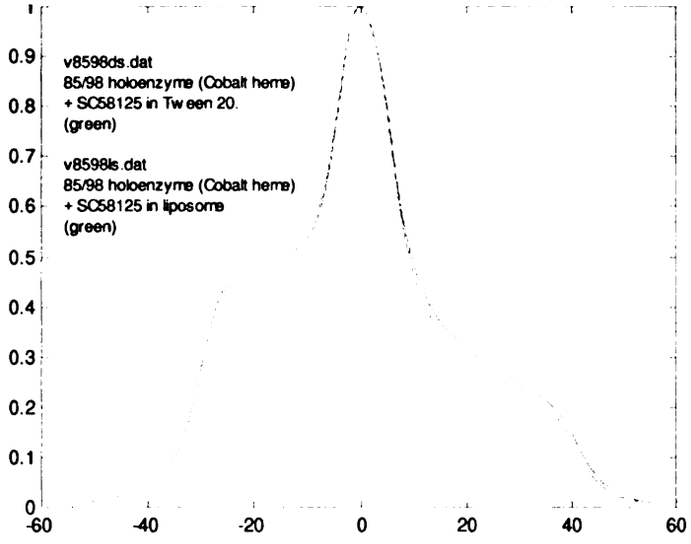
v8598ds.dat
85/98 holoenzyme (Cobalt heme)
+ SC58125 in Tween 20.
(green)
v8598ls.dat
85/98 holoenzyme (Cobalt heme)
+ SC58125 in liposome
(green)
0
0.1
0.2
0.3
0.4
0.5
0.6
0.7
0.8
0.9
-60
-40
-20
0
20
40
60

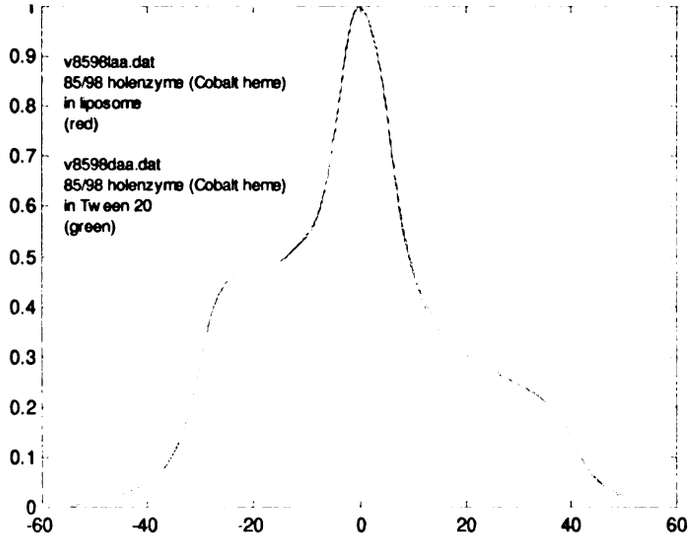
v8598laa.dat
85/98 holenzyme (Cobalt heme)
in liposome
(red)
v8598daa.dat
85/98 holenzyme (Cobalt heme)
in Tween 20
(green)
0
0.1
0.2
0.3
0.4
0.5
0.6
0.7
0.8
0.9
-60
-40
-20
0
20
40
60

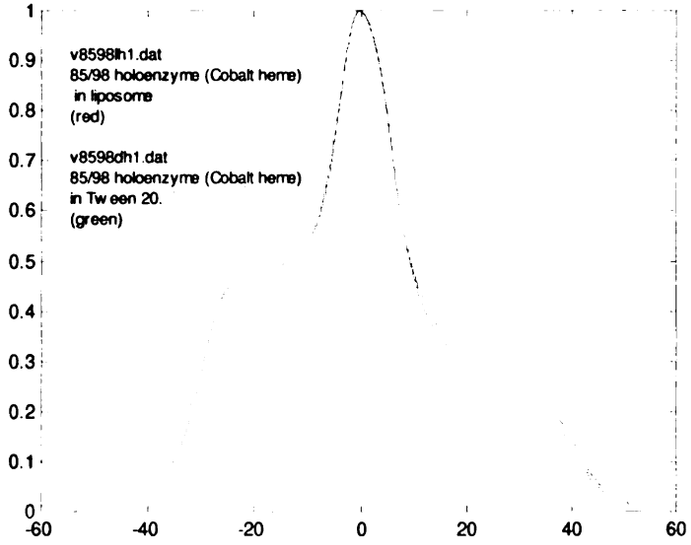
v8598lh1.dat
85/98 holoenzyme (Cobalt heme)
in liposome
(red)
v8598dh1.dat
85/98 holoenzyme (Cobalt heme)
in Tween 20.
(green)
0
0.1
0.2
0.3
0.4
0.5
0.6
0.7
0.8
0.9
1
-60
-40
-20
0
20
40
60

**Figure 8C**. Absorbance EPR spectra of N86C/I98C double mutant in detergent (Tween 20) and liposome and in the presence of Co-PPIX, arachidonic acid and various COX inhibitors.
Spectra were normalized to maximum absorbance and were uncorrected for any contribution by monoradical species.
Images in this dissertation are presented in color.

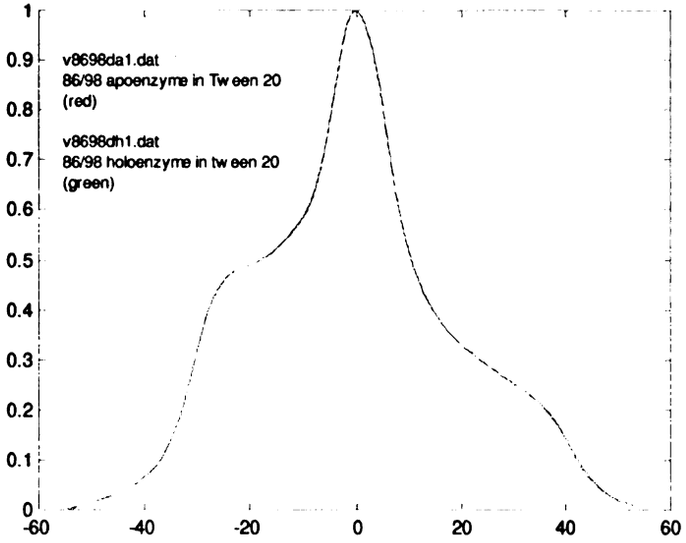
v8698da1.dat
86/98 apoenzyme in Tween 20
(red)
v8698dh1.dat
86/98 holoenzyme in tween 20
(green)

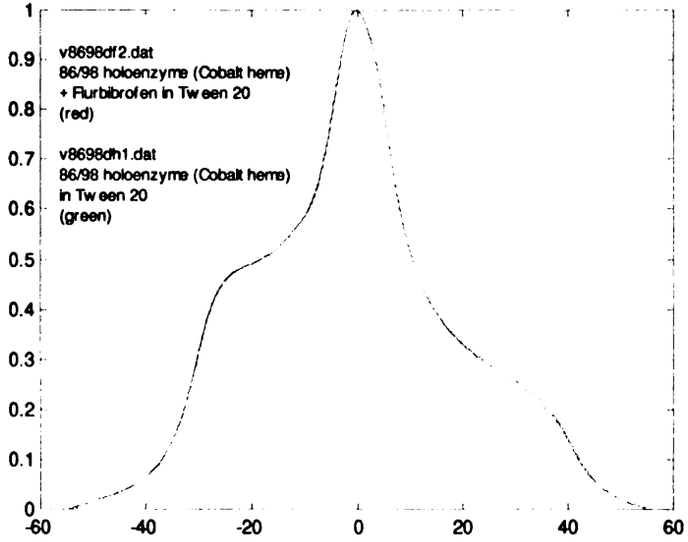
v8698df2.dat
86/98 holoenzyme (Cobalt heme)
+ Flurbibrofen in Tween 20
(red)
v8698dh1.dat
86/98 holoenzyme (Cobalt heme)
in Tween 20
(green)

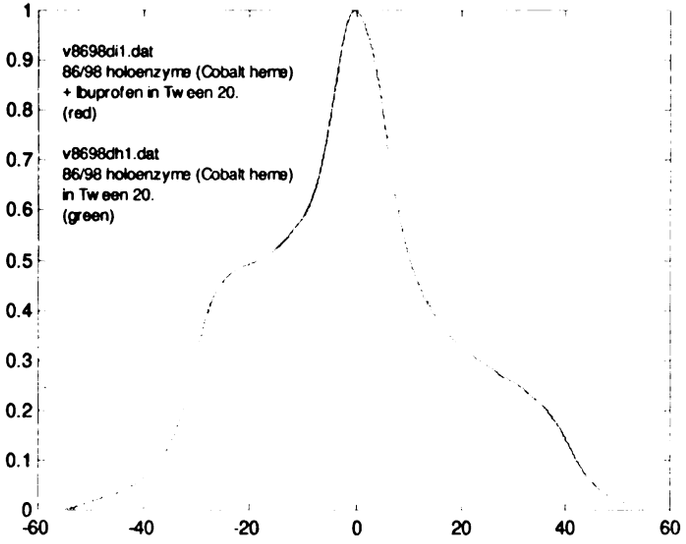
v8698di1.dat
86/98 holoenzyme (Cobalt heme)
+ Ibuprofen in Tween 20.
(red)
v8698dh1.dat
86/98 holoenzyme (Cobalt heme)
in Tween 20.
(green)

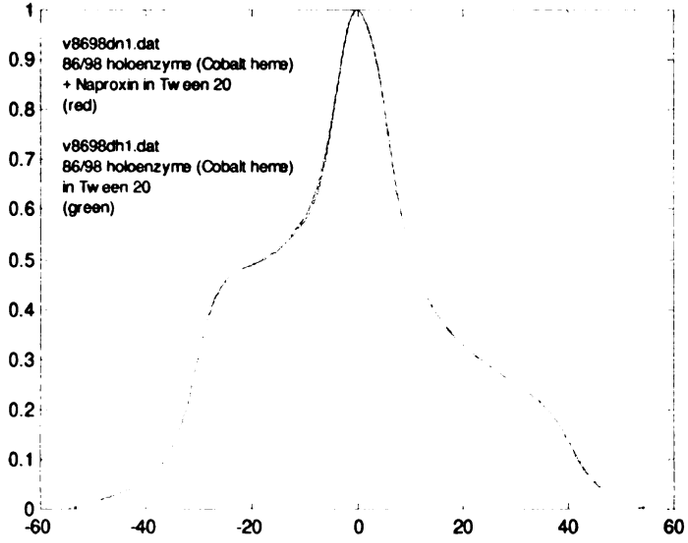
v8698dn1.dat
86/98 holoenzyme (Cobalt heme)
+ Naproxin in Tween 20
(red)
v8698dh1.dat
86/98 holoenzyme (Cobalt heme)
in Tween 20
(green)

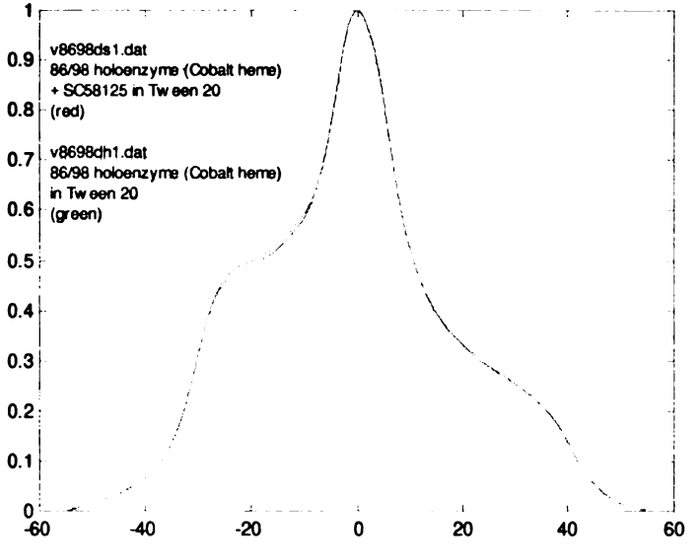
v8698ds1.dat
86/98 holoenzyme (Cobalt heme)
+ SC58125 in Tween 20
(red)
v8698dh1.dat
86/98 holoenzyme (Cobalt heme)
in Tween 20
(green)

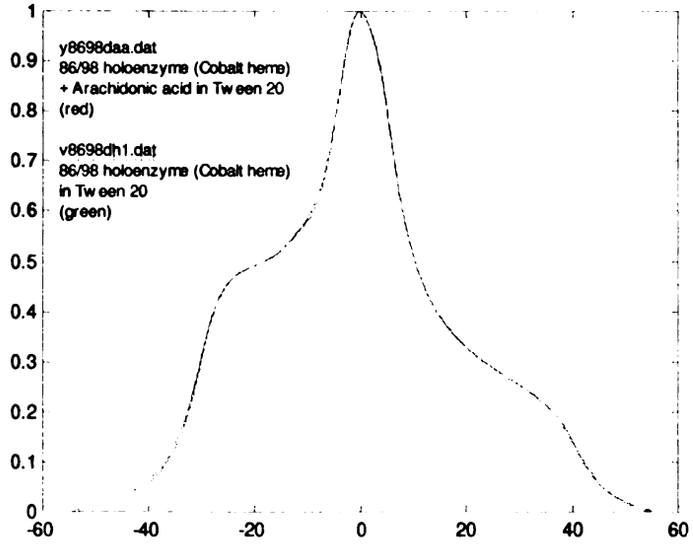
y8698daa.dat
86/98 holoenzyme (Cobalt heme)
+ Arachidonic acid in Tween 20
(red)
v8698dh1.dat
86/98 holoenzyme (Cobalt heme)
in Tween 20
(green)

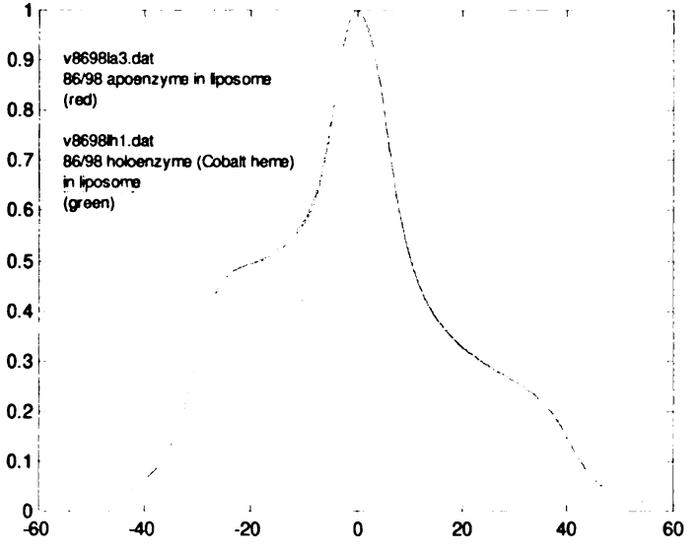
v8698la3.dat
86/98 apoenzyme in liposome
(red)
v8698lh1.dat
86/98 holoenzyme (Cobalt heme)
in liposome
(green)

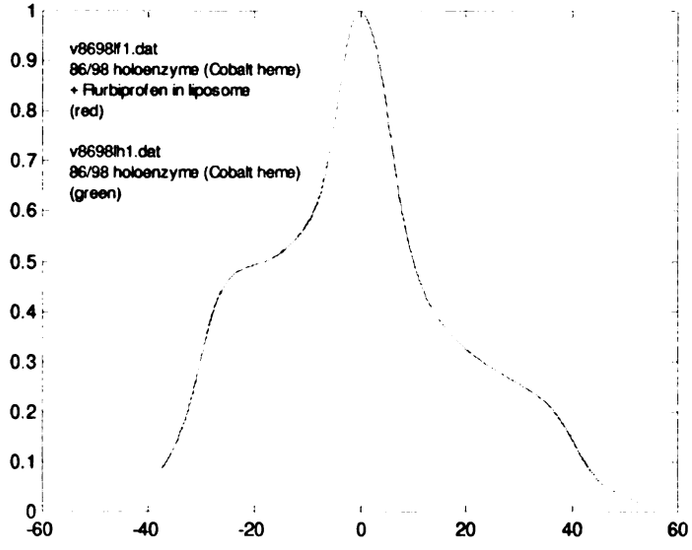
v8698lf1.dat
86/98 holoenzyme (Cobalt heme)
+ Flurbiprofen in liposome
(red)
v8698lh1.dat
86/98 holoenzyme (Cobalt heme)
(green)

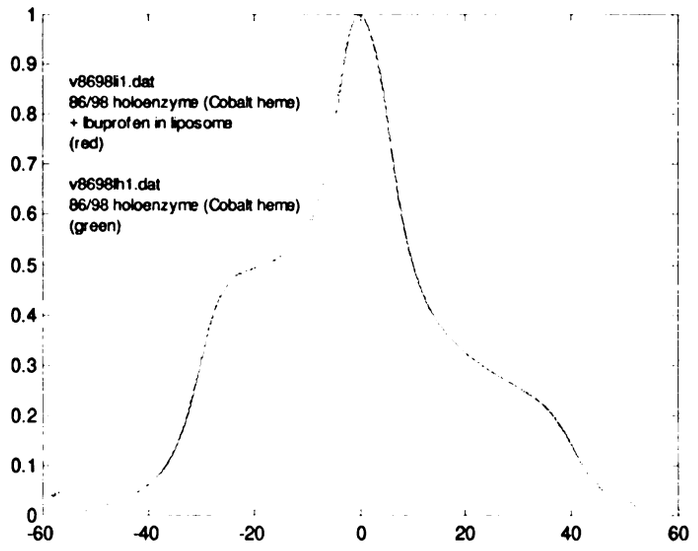
v8698li1.dat
86/98 holoenzyme (Cobalt heme)
+ Ibuprofen in liposome
(red)
v8698lh1.dat
86/98 holoenzyme (Cobalt heme)
(green)

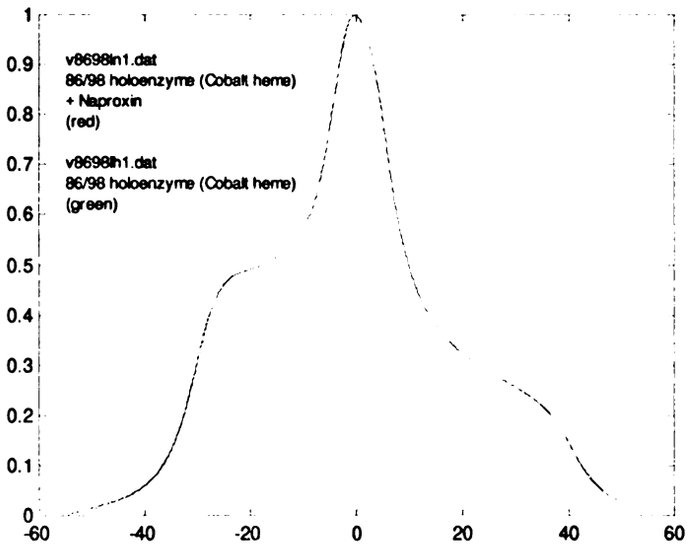
v8698ln1.dat
86/98 holoenzyme (Cobalt heme)
+ Naproxin
(red)
v8698lh1.dat
86/98 holoenzyme (Cobalt heme)
(green)

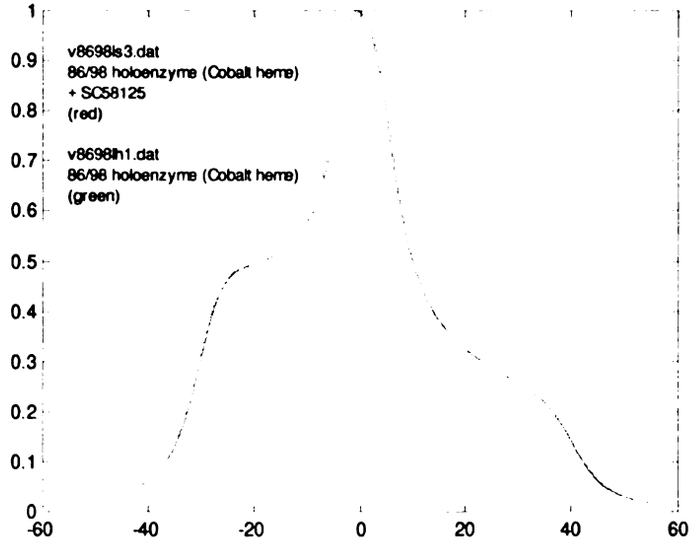
v8698ls3.dat
86/98 holoenzyme (Cobalt heme)
+ SC58125
(red)
v8698lh1.dat
86/98 holoenzyme (Cobalt heme)
(green)

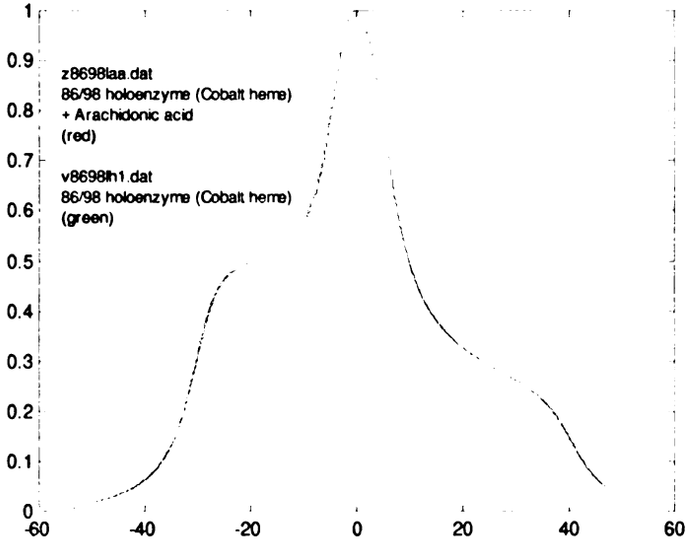
z8698laa.dat
86/98 holoenzyme (Cobalt heme)
+ Arachidonic acid
(red)
v8698lh1.dat
86/98 holoenzyme (Cobalt heme)
(green)

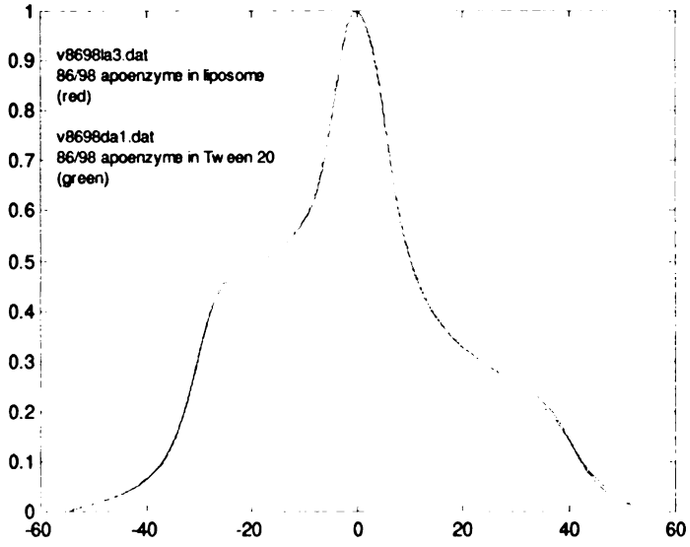
v8698la3.dat
86/98 apoenzyme in liposome
(red)
v8698da1.dat
86/98 apoenzyme in Tween 20
(green)

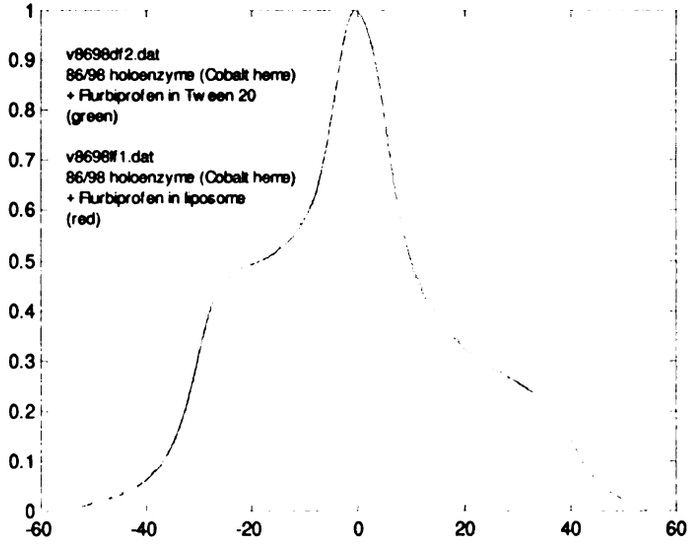
v8698df2.dat
86/98 holoenzyme (Cobalt heme)
+ Flurbiprofen in Tween 20
(green)
v8698lf1.dat
86/98 holoenzyme (Cobalt heme)
+ Flurbiprofen in liposome
(red)

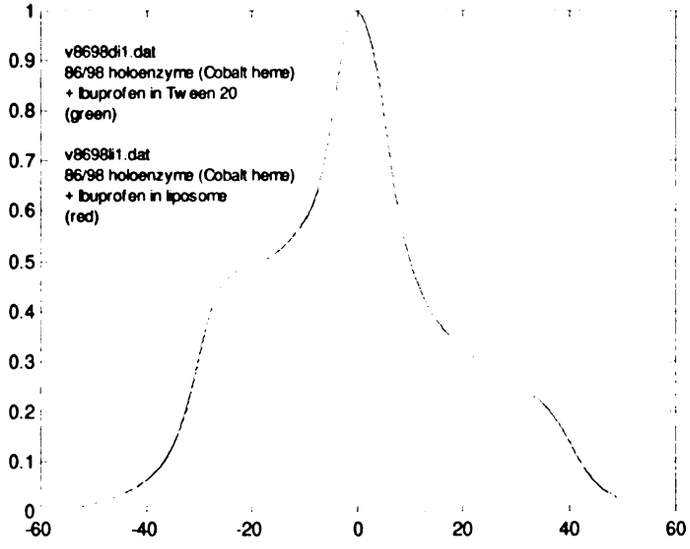
v8698di1.dat
86/98 holoenzyme (Cobalt heme)
+ Ibuprofen in Tween 20
(green)
v8698li1.dat
86/98 holoenzyme (Cobalt heme)
+ Ibuprofen in liposome
(red)

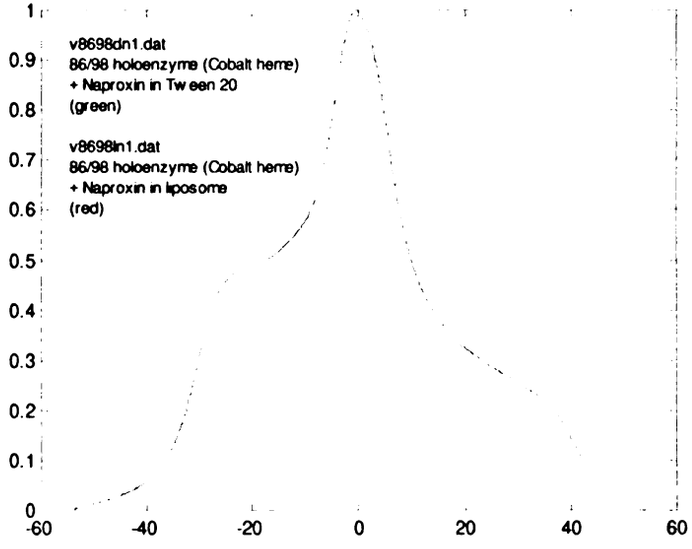
v8698dn1.dat
86/98 holoenzyme (Cobalt heme)
+ Naproxin in Tween 20
(green)
v8698ln1.dat
86/98 holoenzyme (Cobalt heme)
+ Naproxin in liposome
(red)

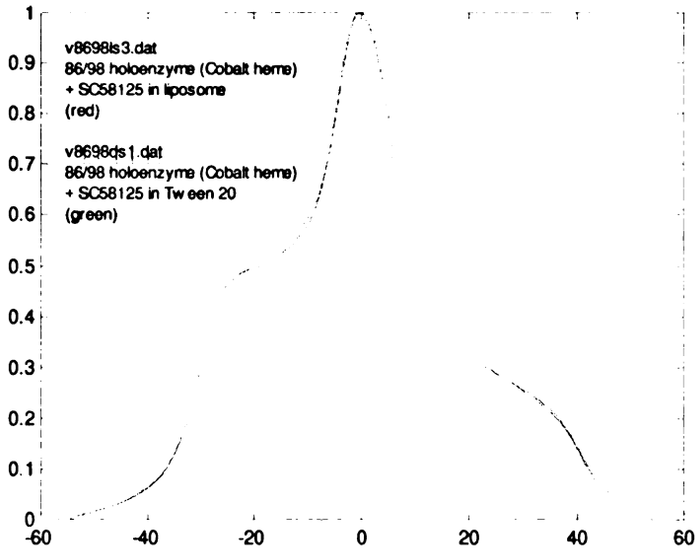
v8698ls3.dat
86/98 holoenzyme (Cobalt heme)
+ SC58125 in liposome
(red)
v8698ds1.dat
86/98 holoenzyme (Cobalt heme)
+ SC58125 in Tween 20
(green)
1
0.9
0.8
0.7
0.6
0.5
0.4
0.3
0.2
0.1
0
-60
-40
-20
0
20
40
60

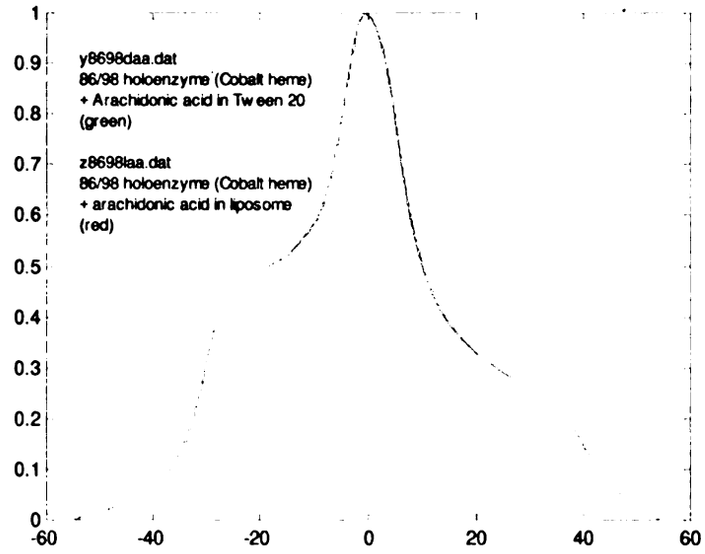
y8698daa.dat
86/98 holoenzyme (Cobalt heme)
+ Arachidonic acid in Tween 20
(green)
z8698laa.dat
86/98 holoenzyme (Cobalt heme)
+ arachidonic acid in liposome
(red)
1
0.9
0.8
0.7
0.6
0.5
0.4
0.3
0.2
0.1
0
-60
-40
-20
0
20
40
60

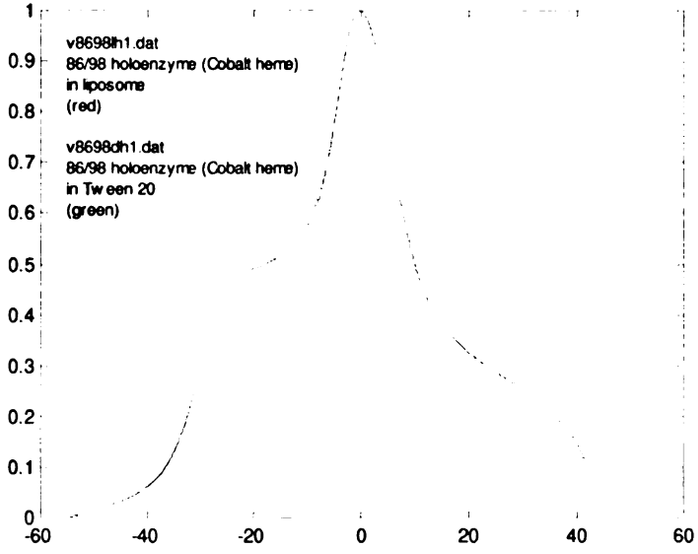
v8698lh1.dat
86/98 holoenzyme (Cobalt heme)
in liposome
(red)
v8698dh1.dat
86/98 holoenzyme (Cobalt heme)
in Tween 20
(green)
1
0.9
0.8
0.7
0.6
0.5
0.4
0.3
0.2
0.1
0
-60
-40
-20
0
20
40
60

**Figure 9C.** Absorbance EPR spectra of V87C/I98C double mutant in detergent (Tween 20) and liposome and in the presence of Co-PPIX, arachidonic acid and various COX inhibitors
Spectra were normalized to maximum absorbance and were uncorrected for any contribution by monoradical species.

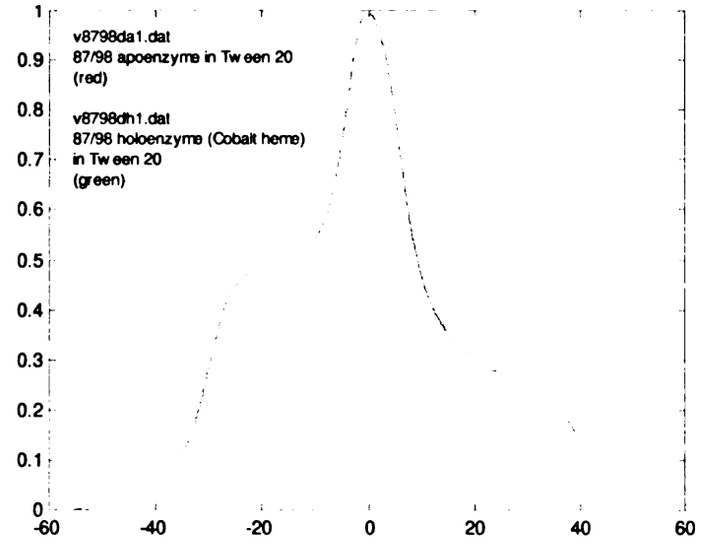
v8798da1.dat
87/98 apoenzyme in Tween 20
(red)
v8798dh1.dat
87/98 holoenzyme (Cobalt heme)
in Tween 20
(green)

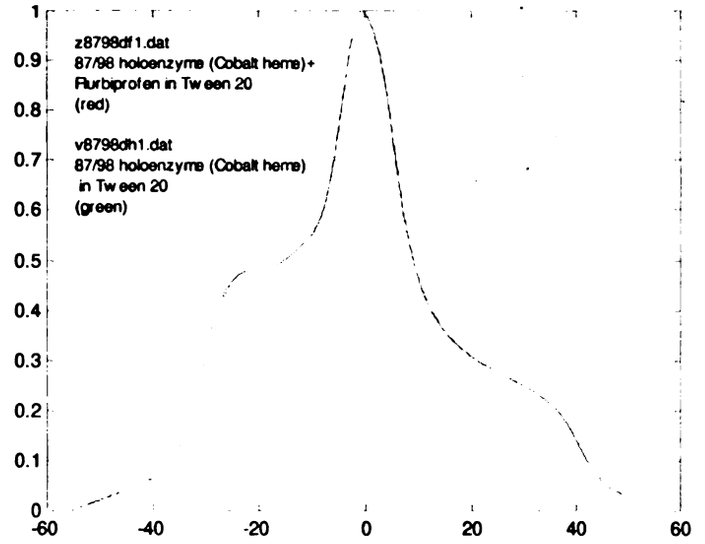
z8798df1.dat
87/98 holoenzyme (Cobalt heme)+
Flurbiprofen in Tween 20
(red)
v8798dh1.dat
87/98 holoenzyme (Cobalt heme)
in Tween 20
(green)

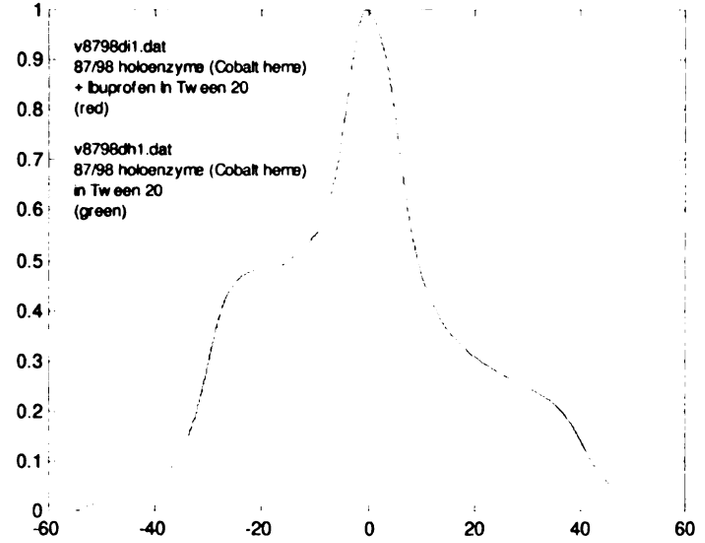
v8798di1.dat
87/98 holoenzyme (Cobalt heme)
+ Ibuprofen in Tween 20
(red)
v8798dh1.dat
87/98 holoenzyme (Cobalt heme)
in Tween 20
(green)

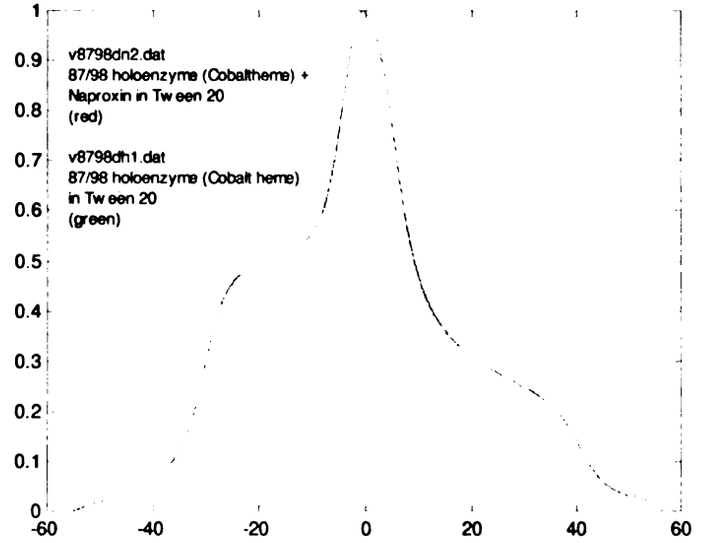
v8798dn2.dat
87/98 holoenzyme (Cobaltheme) +
Naproxin in Tween 20
(red)
v8798dh1.dat
87/98 holoenzyme (Cobalt heme)
in Tween 20
(green)

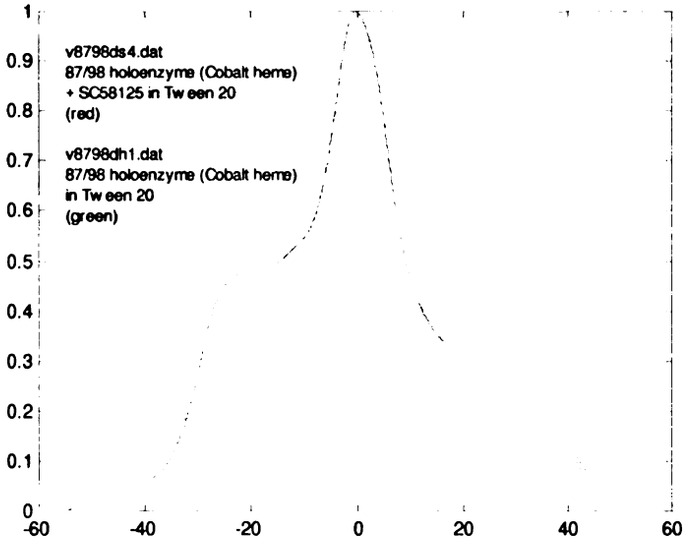
v8798ds4.dat
87/98 holoenzyme (Cobalt heme)
+ SC58125 in Tween 20
(red)
v8798dh1.dat
87/98 holoenzyme (Cobalt heme)
in Tween 20
(green)

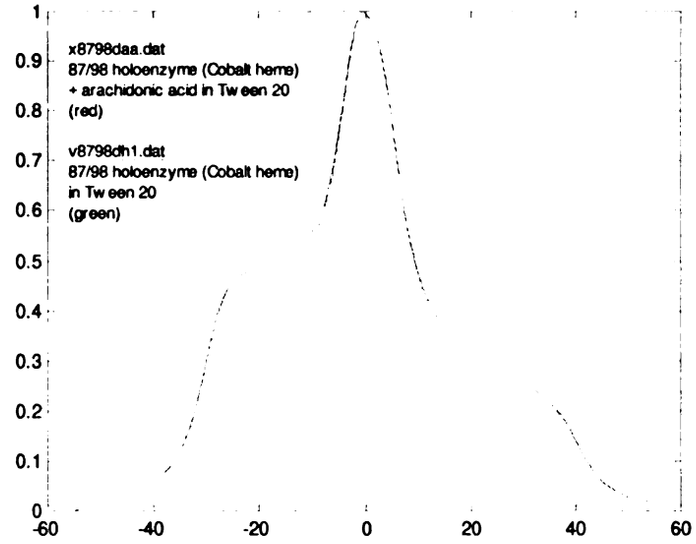
x8798daa.dat
87/98 holoenzyme (Cobalt heme)
+ arachidonic acid in Tween 20
(red)
v8798dh1.dat
87/98 holoenzyme (Cobalt heme)
in Tween 20
(green)

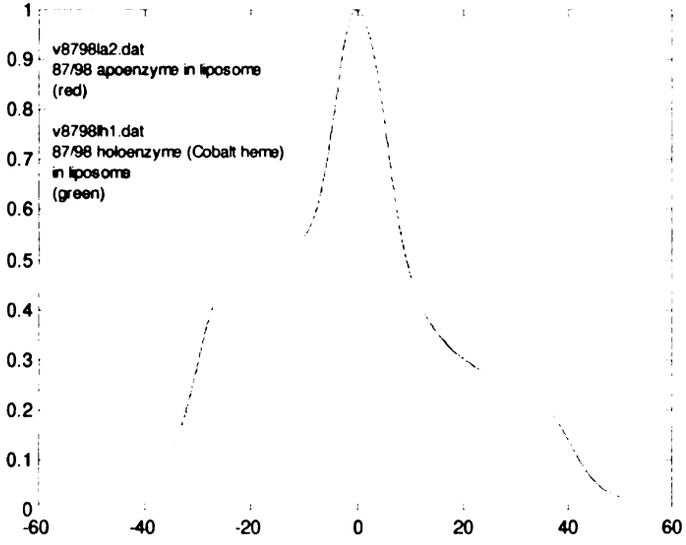
v8798la2.dat
87/98 apoenzyme in liposome
(red)
v8798lh1.dat
87/98 holoenzyme (Cobalt heme)
in liposome
(green)

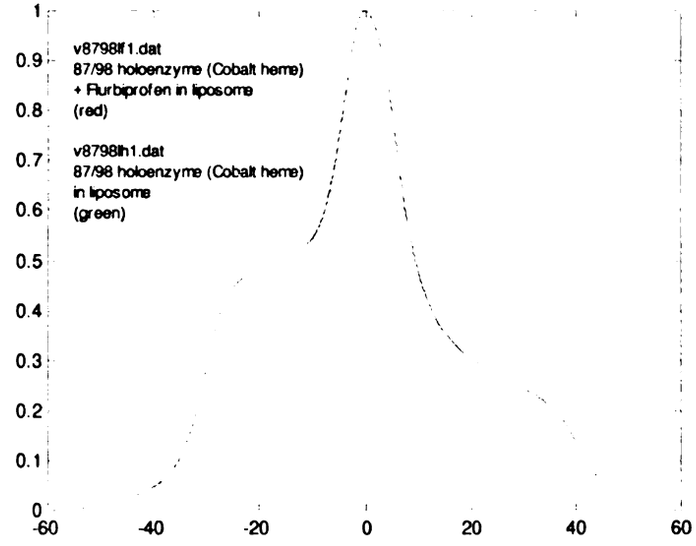
v8798lf1.dat
87/98 holoenzyme (Cobalt heme)
+ Flurbiprofen in liposome
(red)
v8798lh1.dat
87/98 holoenzyme (Cobalt heme)
in liposome
(green)

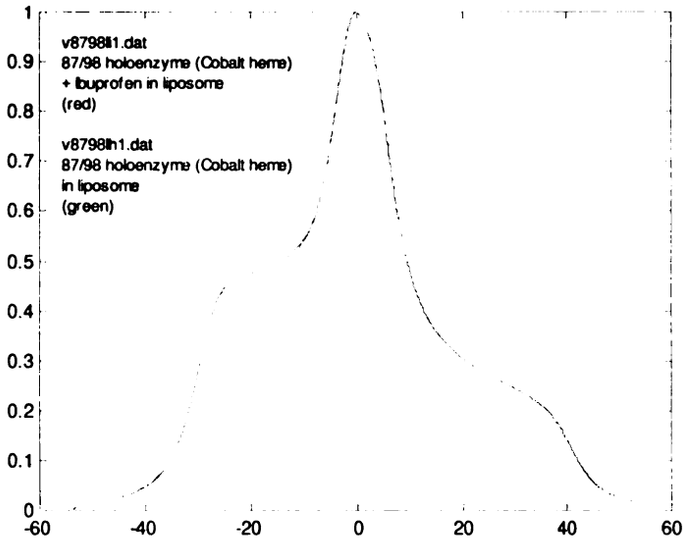
v8798il1.dat
87/98 holoenzyme (Cobalt heme)
+ Ibuprofen in liposome
(red)
v8798lh1.dat
87/98 holoenzyme (Cobalt heme)
in liposome
(green)

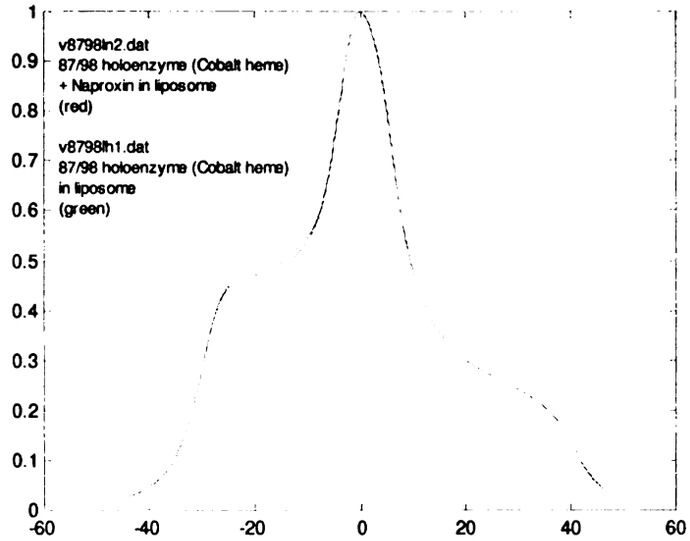
v8798ln2.dat
87/98 holoenzyme (Cobalt heme)
+ Naproxin in liposome
(red)
v8798lh1.dat
87/98 holoenzyme (Cobalt heme)
in liposome
(green)

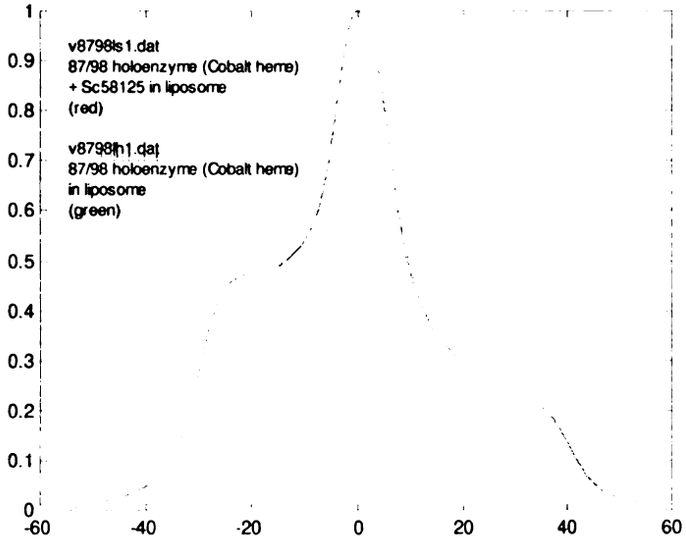
v8798ls1.dat
87/98 holoenzyme (Cobalt heme)
+ Sc58125 in liposome
(red)
v8798lh1.dat
87/98 holoenzyme (Cobalt heme)
in liposome
(green)

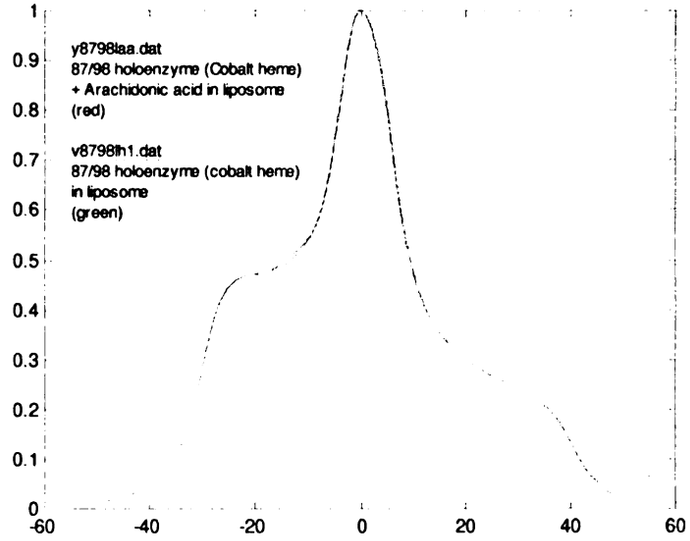
y8798laa.dat
87/98 holoenzyme (Cobalt heme)
+ Arachidonic acid in liposome
(red)
v8798lh1.dat
87/98 holoenzyme (cobalt heme)
in liposome
(green)

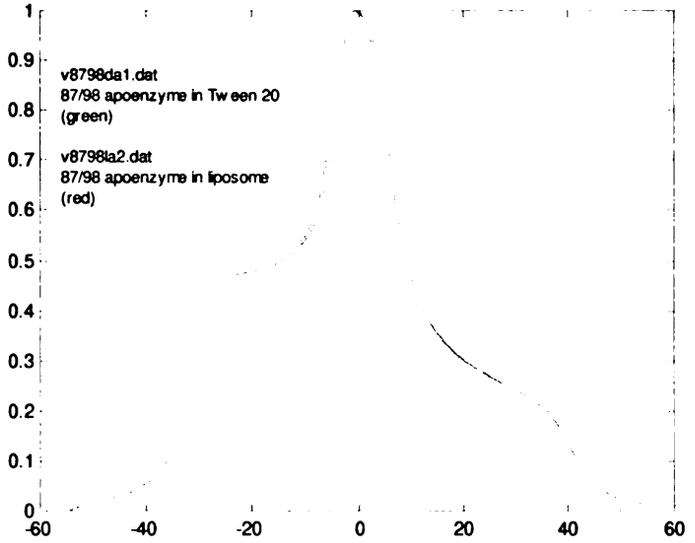
v8798da1.dat
87/98 apoenzyme in Tween 20
(green)
v8798la2.dat
87/98 apoenzyme in liposome
(red)

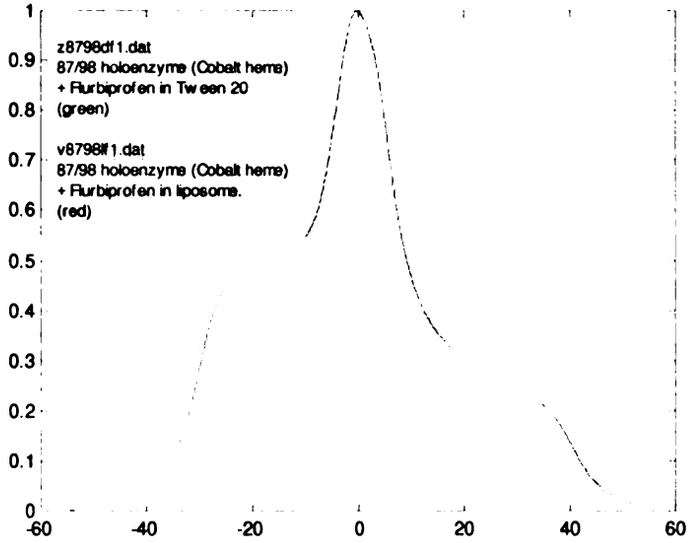
z8798df1.dat
87/98 holoenzyme (Cobalt heme)
+ Flurbiprofen in Tween 20
(green)
v8798lf1.dat
87/98 holoenzyme (Cobalt heme)
+ Flurbiprofen in liposome.
(red)

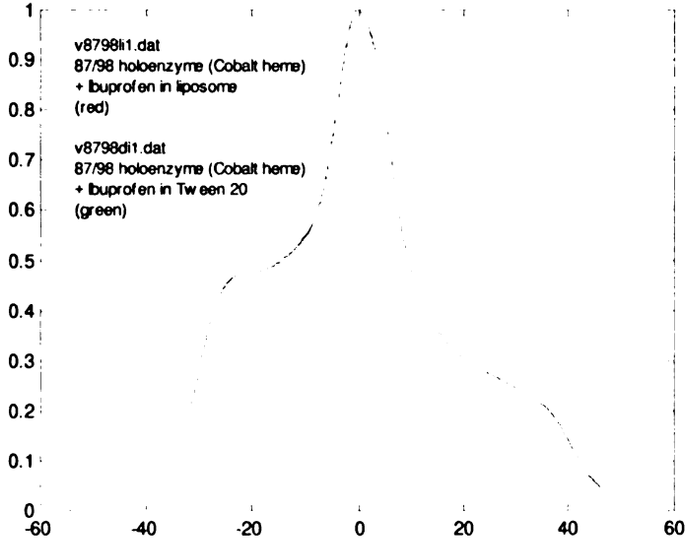
v8798li1.dat
87/98 holoenzyme (Cobalt heme)
+ Ibuprofen in liposome
(red)
v8798di1.dat
87/98 holoenzyme (Cobalt heme)
+ Ibuprofen in Tween 20
(green)

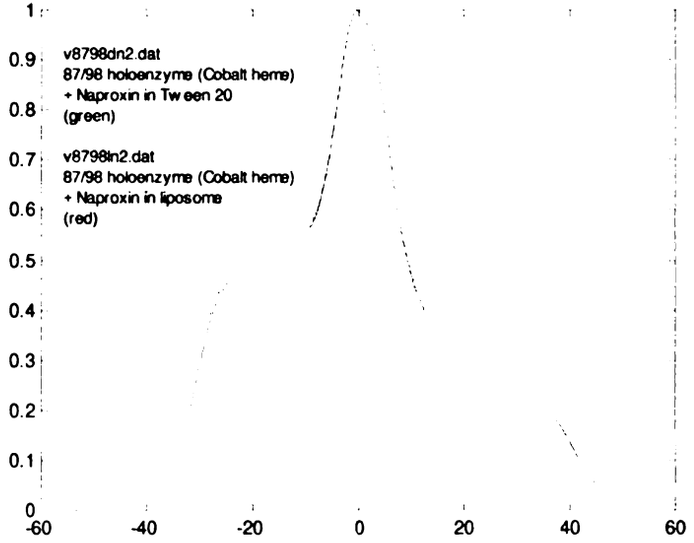
v8798dn2.dat
87/98 holoenzyme (Cobalt heme)
+ Naproxin in Tween 20
(green)
v8798ln2.dat
87/98 holoenzyme (Cobalt heme)
+ Naproxin in liposome
(red)

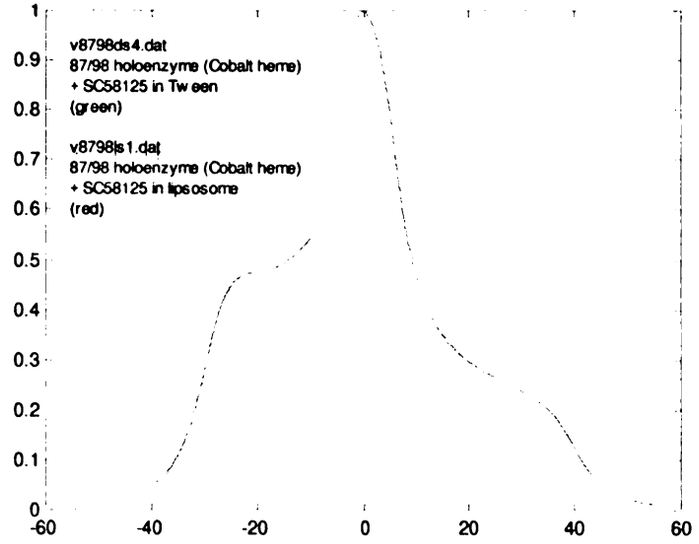
v8798ds4.dat
87/98 holoenzyme (Cobalt heme)
+ SC58125 in Tween
(green)
v8798ls1.dat
87/98 holoenzyme (Cobalt heme)
+ SC58125 in liposome
(red)
1
0.9
0.8
0.7
0.6
0.5
0.4
0.3
0.2
0.1
0
-60
-40
-20
0
20
40
60

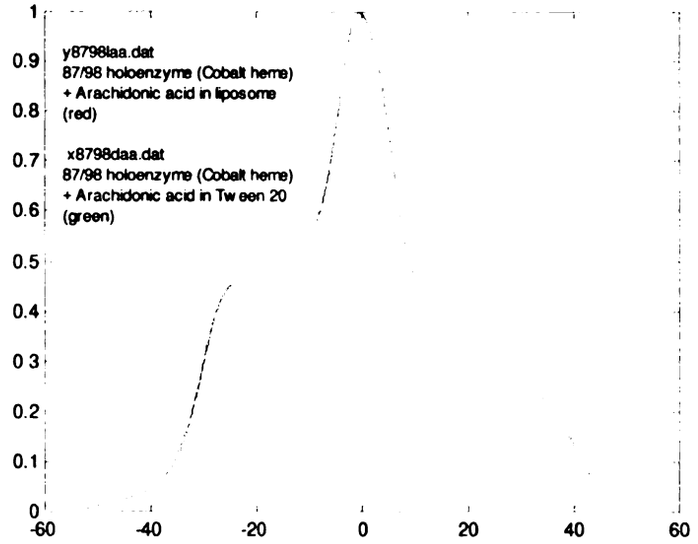
y8798laa.dat
87/98 holoenzyme (Cobalt heme)
+ Arachidonic acid in liposome
(red)
x8798daa.dat
87/98 holoenzyme (Cobalt heme)
+ Arachidonic acid in Tween 20
(green)
1
0.9
0.8
0.7
0.6
0.5
0.4
0.3
0.2
0.1
0
-60
-40
-20
0
20
40
60

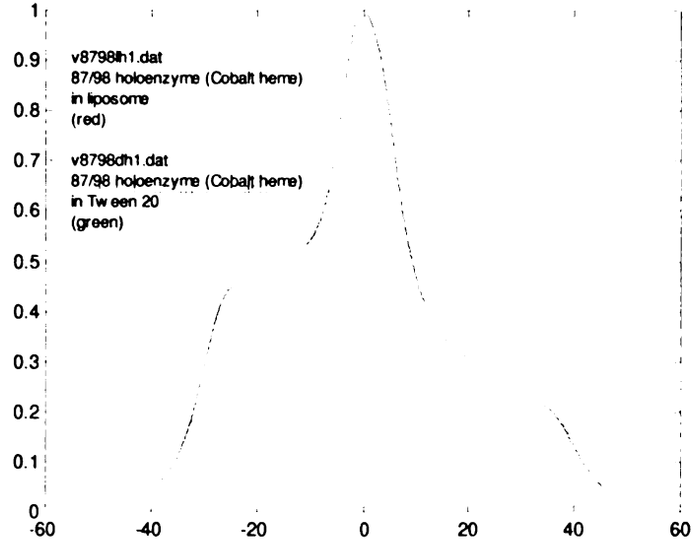
v8798lh1.dat
87/98 holoenzyme (Cobalt heme)
in liposome
(red)
v8798dh1.dat
87/98 holoenzyme (Cobalt heme)
in Tween 20
(green)
1
0.9
0.8
0.7
0.6
0.5
0.4
0.3
0.2
0.1
0
-60
-40
-20
0
20
40
60

**Figure 10C.** Absorbance EPR spectra of V88C/I98C double mutant in detergent (Tween 20) and liposome and in the presence of Co-PPIX, arachidonic acid and various COX inhibitors
Spectra were normalized to maximum absorbance and were uncorrected for any contribution by monoradical species.

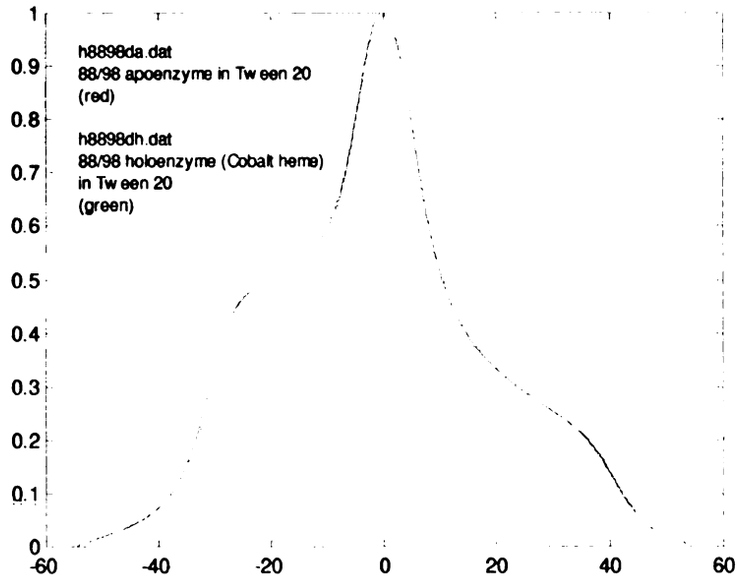
h8898da.dat
88/98 apoenzyme in Tween 20
(red)
h8898dh.dat
88/98 holoenzyme (Cobalt heme)
in Tween 20
(green)
1
0.9
0.8
0.7
0.6
0.5
0.4
0.3
0.2
0.1
0
-60
-40
-20
0
20
40
60

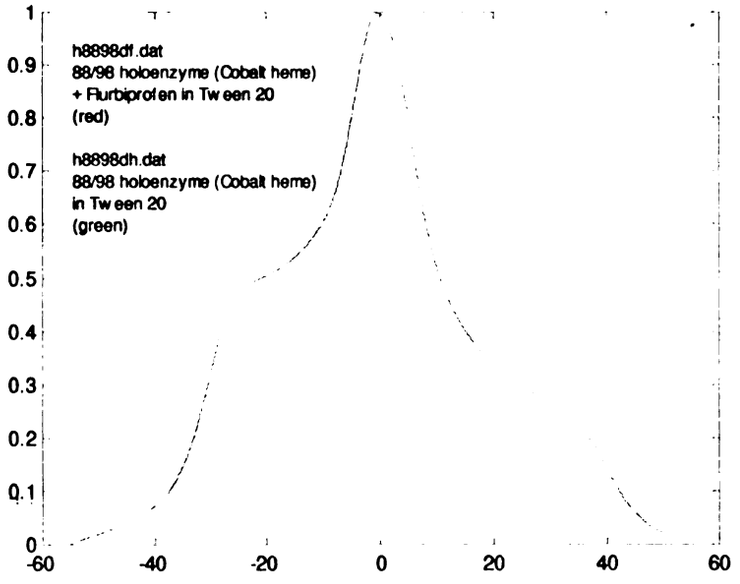
h8898df.dat
88/98 holoenzyme (Cobalt heme)
+ Flurbiprofen in Tween 20
(red)
h8898dh.dat
88/98 holoenzyme (Cobalt heme)
in Tween 20
(green)
1
0.9
0.8
0.7
0.6
0.5
0.4
0.3
0.2
0.1
0
-60
-40
-20
0
20
40
60

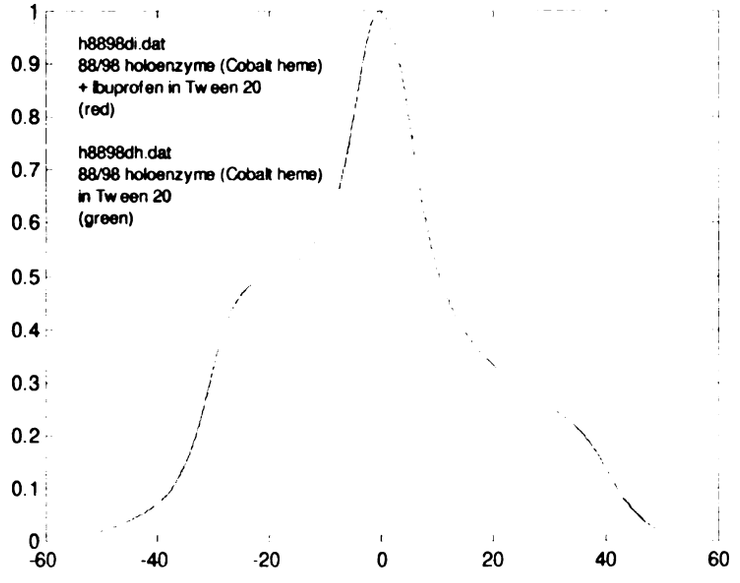
h8898di.dat
88/98 holoenzyme (Cobalt heme)
+ Ibuprofen in Tween 20
(red)
h8898dh.dat
88/98 holoenzyme (Cobalt heme)
in Tween 20
(green)
1
0.9
0.8
0.7
0.6
0.5
0.4
0.3
0.2
0.1
0
-60
-40
-20
0
20
40
60

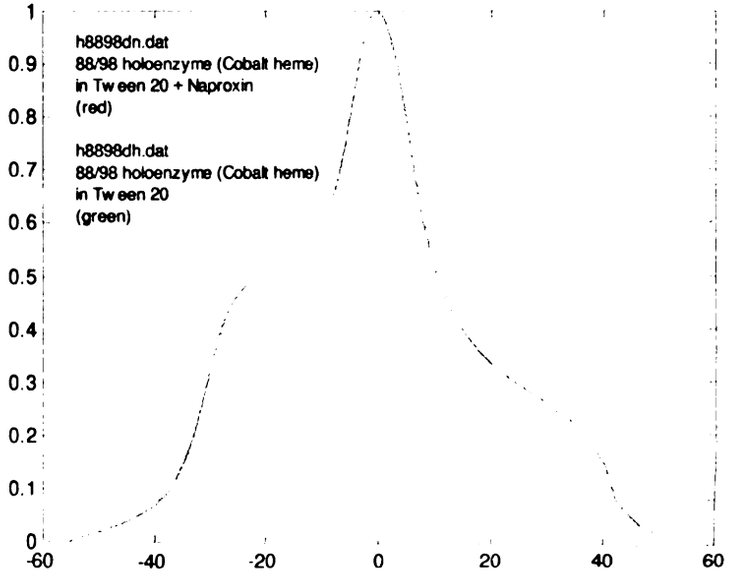
h8898dn.dat
88/98 holoenzyme (Cobalt heme)
in Tween 20 + Naproxin
(red)
h8898dh.dat
88/98 holoenzyme (Cobalt heme)
in Tween 20
(green)
1
0.9
0.8
0.7
0.6
0.5
0.4
0.3
0.2
0.1
0
-60
-40
-20
0
20
40
60

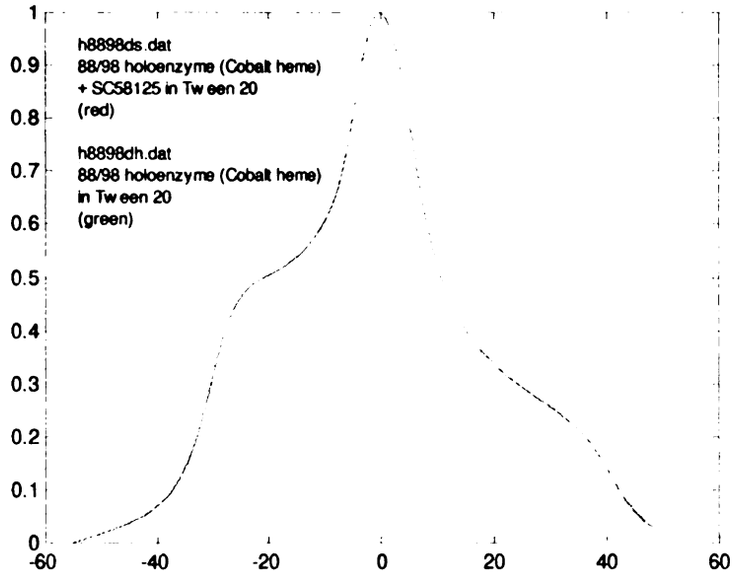
h8898ds.dat
88/98 holoenzyme (Cobalt heme)
+ SC58125 in Tween 20
(red)
h8898dh.dat
88/98 holoenzyme (Cobalt heme)
in Tween 20
(green)

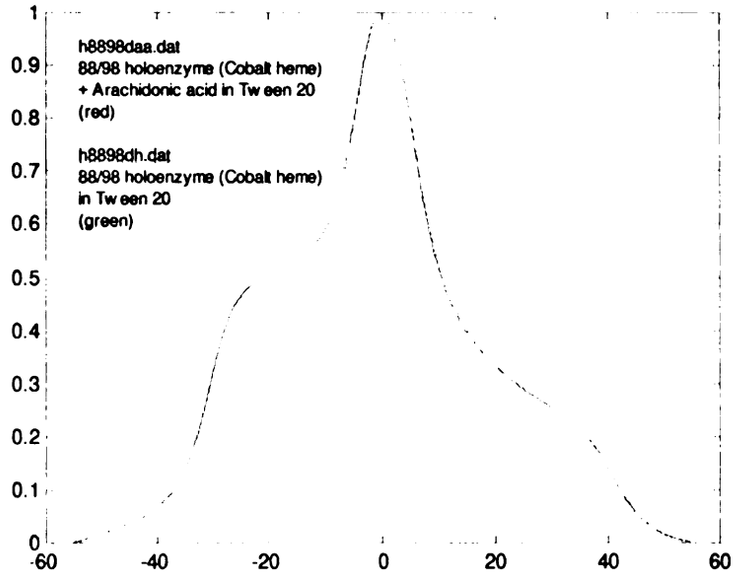
h8898daa.dat
88/98 holoenzyme (Cobalt heme)
+ Arachidonic acid in Tween 20
(red)
h8898dh.dat
88/98 holoenzyme (Cobalt heme)
in Tween 20
(green)

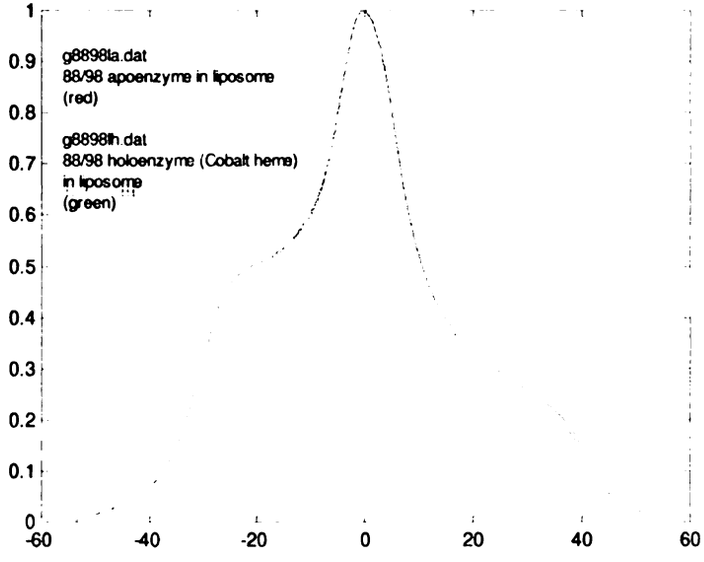
g8898la.dat
88/98 apoenzyme in liposome
(red)
g8898lh.dat
88/98 holoenzyme (Cobalt heme)
in liposome
(green)

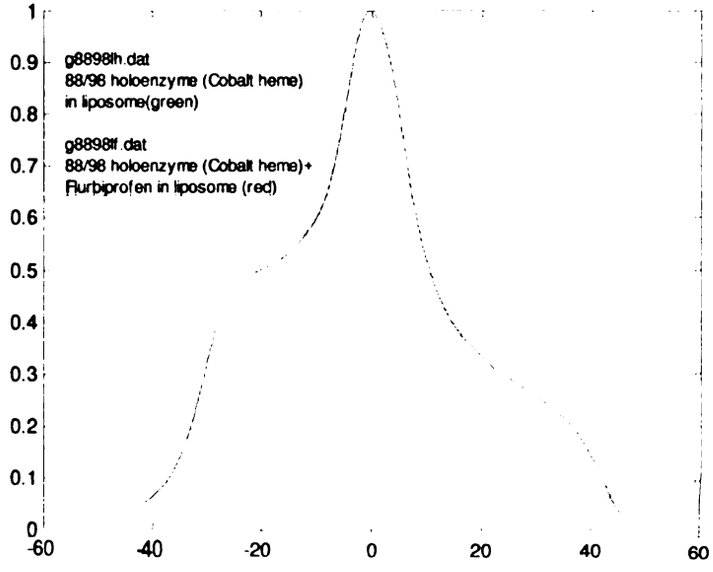
g8898lh.dat
88/98 holoenzyme (Cobalt heme)
in liposome(green)
g8898lf.dat
88/98 holoenzyme (Cobalt heme)+
Flurbiprofen in liposome (red)

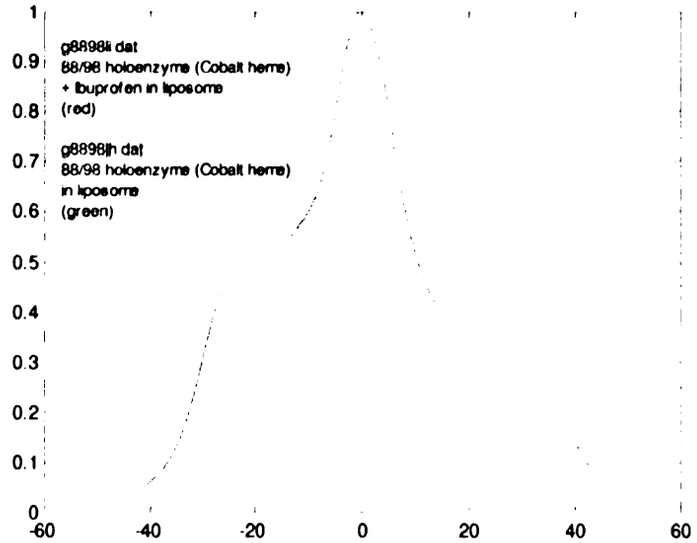
g8898ii.dat
88/98 holoenzyme (Cobalt heme)
+ Ibuprofen in liposome
(red)
g8898ih.dat
88/98 holoenzyme (Cobalt heme)
in liposome
(green)

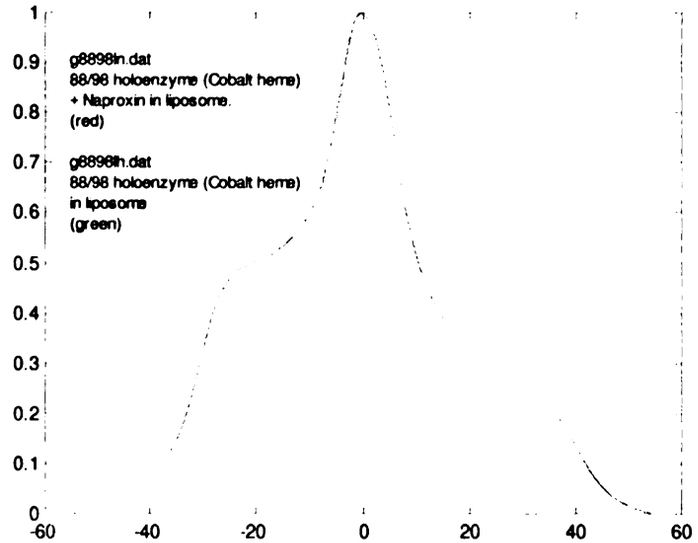
g8898in.dat
88/98 holoenzyme (Cobalt heme)
+ Naproxin in liposome.
(red)
g8898ih.dat
88/98 holoenzyme (Cobalt heme)
in liposome
(green)

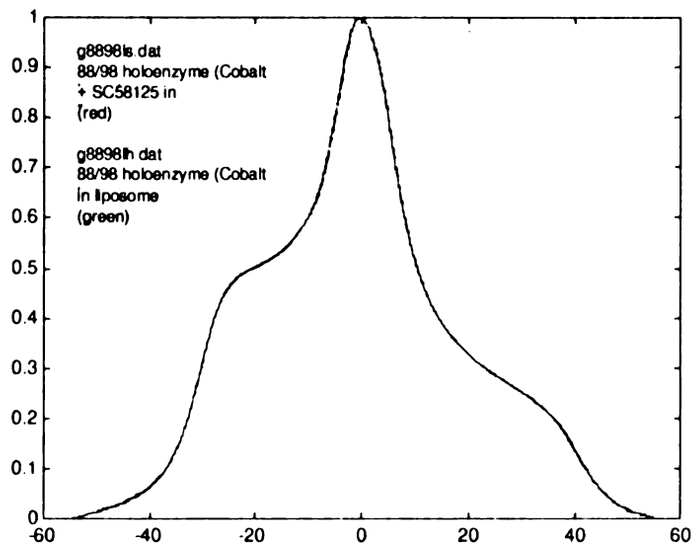
g8898is.dat
88/98 holoenzyme (Cobalt
+ SC58125 in
(red)
g8898ih.dat
88/98 holoenzyme (Cobalt
in liposome
(green)

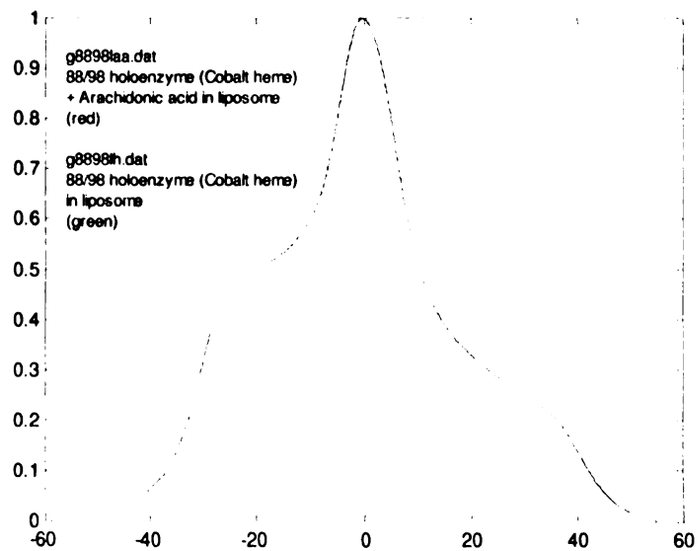
g8898iaa.dat
88/98 holoenzyme (Cobalt heme)
+ Arachidonic acid in liposome
(red)
g8898ih.dat
88/98 holoenzyme (Cobalt heme)
in liposome
(green)

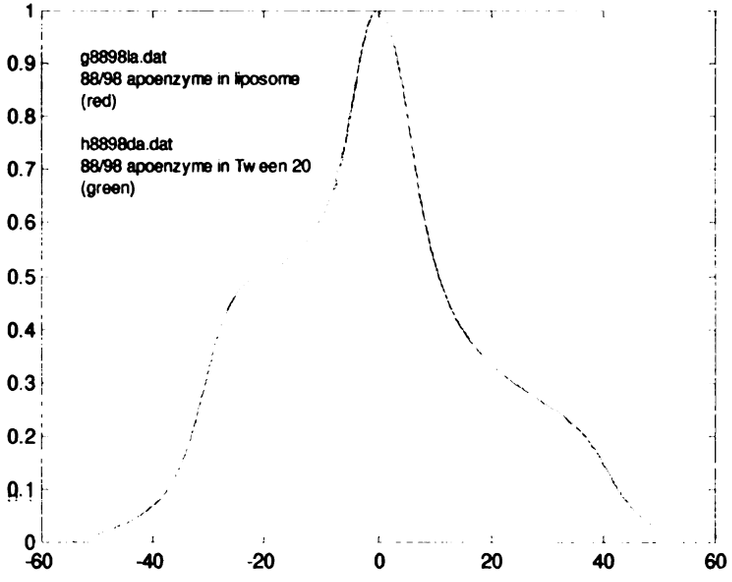
g8898la.dat
88/98 apoenzyme in liposome
(red)
h8898da.dat
88/98 apoenzyme in Tween 20
(green)

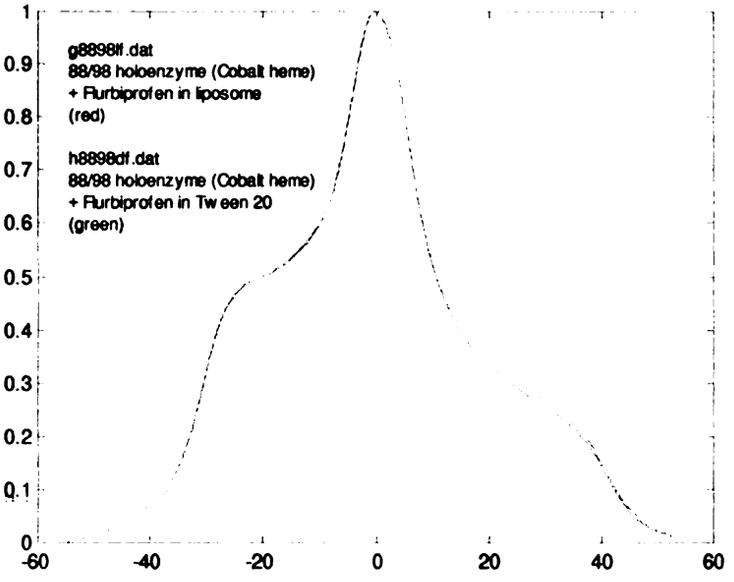
g8898lf.dat
88/98 holoenzyme (Cobalt heme)
+ Flurbiprofen in liposome
(red)
h8898df.dat
88/98 holoenzyme (Cobalt heme)
+ Flurbiprofen in Tween 20
(green)

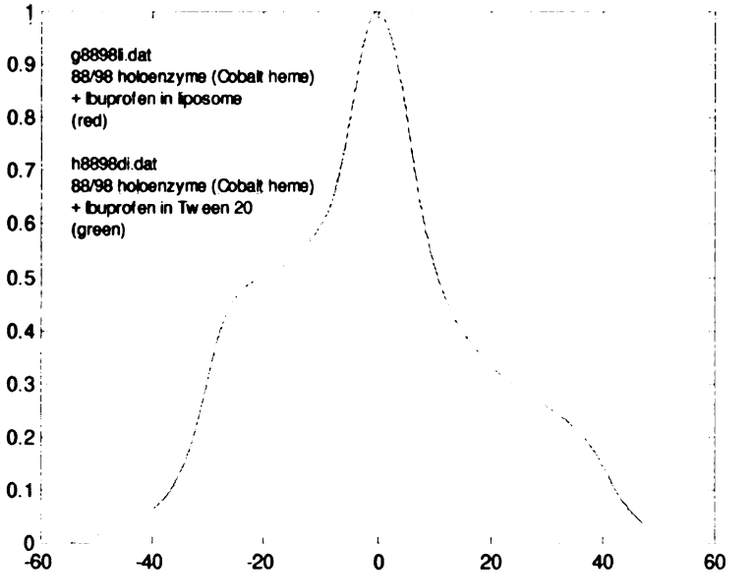
g8898li.dat
88/98 holoenzyme (Cobalt heme)
+ Ibuprofen in liposome
(red)
h8898di.dat
88/98 holoenzyme (Cobalt heme)
+ Ibuprofen in Tween 20
(green)

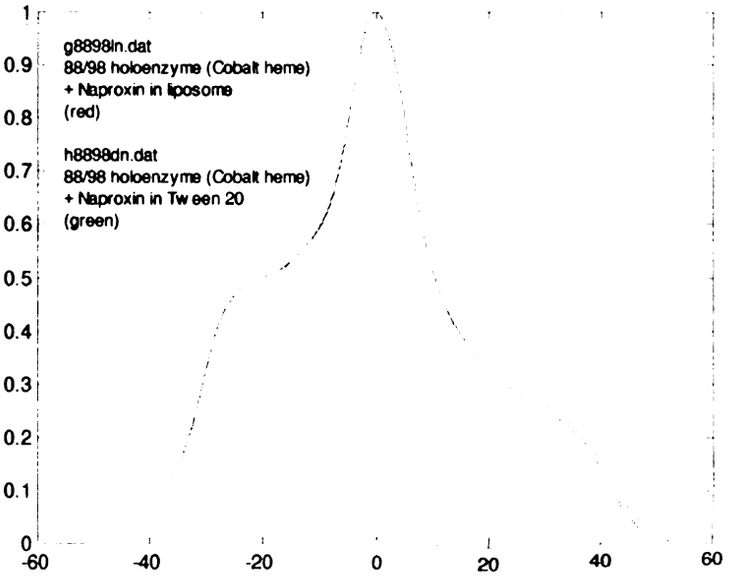
g8898ln.dat
88/98 holoenzyme (Cobalt heme)
+ Naproxin in liposome
(red)
h8898dn.dat
88/98 holoenzyme (Cobalt heme)
+ Naproxin in Tween 20
(green)

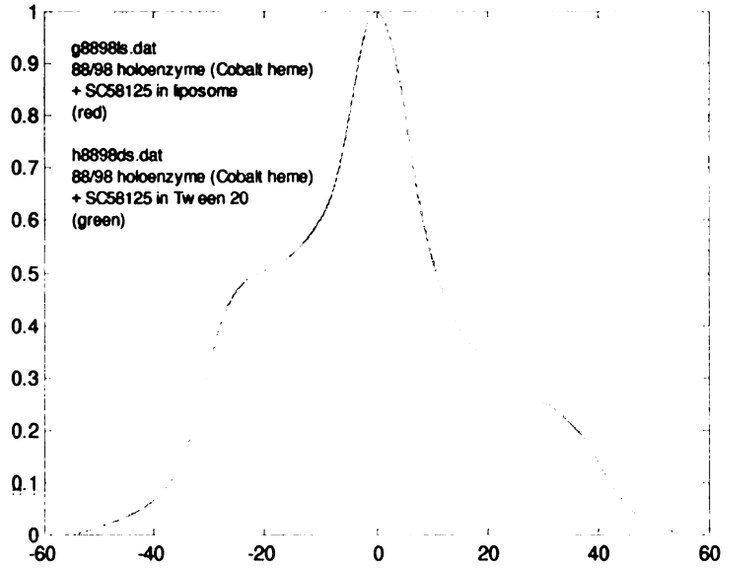
g8898ls.dat
88/98 holoenzyme (Cobalt heme)
+ SC58125 in liposome
(red)
h8898ds.dat
88/98 holoenzyme (Cobalt heme)
+ SC58125 in Tween 20
(green)
1
0.9
0.8
0.7
0.6
0.5
0.4
0.3
0.2
0.1
0
-60
-40
-20
0
20
40
60

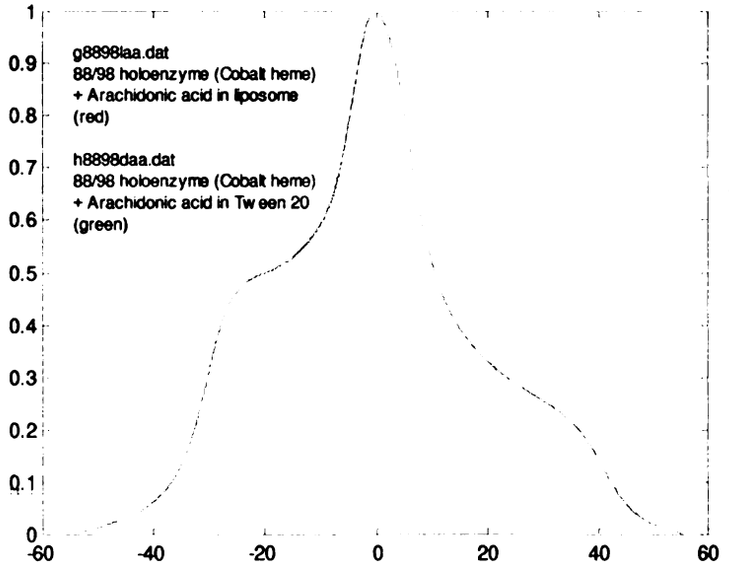
g8898laa.dat
88/98 holoenzyme (Cobalt heme)
+ Arachidonic acid in liposome
(red)
h8898daa.dat
88/98 holoenzyme (Cobalt heme)
+ Arachidonic acid in Tween 20
(green)
1
0.9
0.8
0.7
0.6
0.5
0.4
0.3
0.2
0.1
0
-60
-40
-20
0
20
40
60

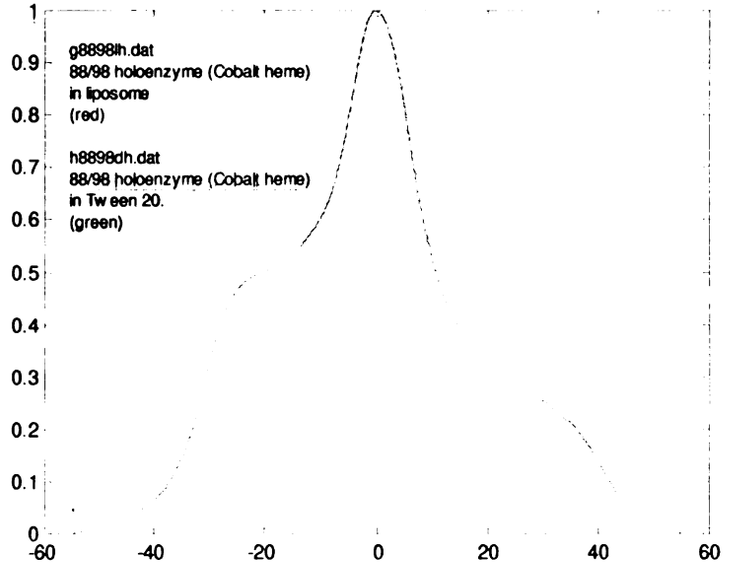
g8898lh.dat
88/98 holoenzyme (Cobalt heme)
in liposome
(red)
h8898dh.dat
88/98 holoenzyme (Cobalt heme)
in Tween 20.
(green)
1
0.9
0.8
0.7
0.6
0.5
0.4
0.3
0.2
0.1
0
-60
-40
-20
0
20
40
60